Czech Technical University in Prague

Faculty of Electrical Engineering

Department of Measurement

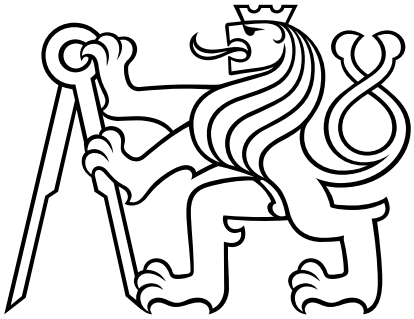

Precise magnetometers for geophysics and metrology

Habilitation thesis

Ing. Michal Janošek, Ph.D.

Prague, May 2024

Abstract

This habilitation thesis is a commented collection of author's post-doctoral publications on the topic of improving the precision (and accuracy) of magnetometers in the geomagnetic field range with their prospective use in geophysics and exploration, and their metrology. The author focused on room-temperature magnetometers (parallel and orthogonal fluxgate) and a high-temperature-superconductor quantum magnetometer (SQUID). The author's research is presented and organized in two fundamental branches: establishing and improving magnetometer precision and accuracy, and its application and performance in geophysical observations. The first topic is addressed by research in establishing and improving magnetometer parameters, such as their (ultra-) low-frequency noise and offset, and by researching magnetometer calibration methods which can compensate for the effects of anthropogenous noise. The second topic deals with applications of such precise and accurate, i.e. low-noise and well calibrated magnetometers in geophysics – the developed orthogonal fluxgate magnetometer is shown to have a perspective of replacing search-coils and even SQUIDs for geophysical exploration due to its noise below 1 pT/√Hz at 1 Hz.

Authorship statement

As most of the presented publications resulted from a collective effort, the author's contribution is defined and presented in the commentaries before each publication.

Keywords

Magnetic sensors; magnetometers; fluxgate; SQUID; magnetometer noise; calibrations; geophysics; magnetic metrology.

Table of contents

Glossary of symbols and abbreviations

Symbol	Description	Unit
B	Magnetic flux density vector	T
F	Total value of B (B scalar magnitude)	T
Φ_0	Quantum of magnetic flux („fluxon“)	Wb

Abbreviation	
SQUID	Superconducting Quantum Interference Device
AMR	Anisotropic Magneto-Resistance (-Resistor)
ASD	Amplitude Spectral Density
HTS	High-Temperature Superconductor
LTS	Low-Temperature Superconductor
TEM	Transient-Electromagnetics (exploration method)
MCG	Magneto-Cardiography
OFM	Orthogonal, fundamental-mode (fluxgate/magnetometer)
CMI	Czech Metrology Institute
ASCR	Academy of Sciences of the Czech Republic
DUT	Device under test (calibrated device)
VGHMUr	Office of Military Geography and Hydrometeorology
PTB	Physikalisch-Technische Bundesanstalt
INTERMAGNET	International Real-time Magnetic Observatory Network
SANSA	South African National Space Agency
PPM	Proton-precession magnetometer
ULF	Ultra-Low-Frequency (<< 1 Hz)
OVM	Overhauser magnetometer

Introduction

Magnetometers are instruments used to measure *an estimate* of the magnetic flux density vector **B** and are used in a variety of scientific and socio-economic applications. In this thesis, the author presents his post-dissertation [Q1] contribution to the research of highly accurate −i.e. precise and well-calibrated [1]− vectorial magnetometers of fluxgate and also SQUID type. Two topics are addressed:

1. research in improving magnetometer resolution and accuracy by improving their noise parameters and calibrations, respectively, and
2. their subsequent application in precise geophysical observations.

The need for a precise and accurate, i.e. a low-noise and calibrated magnetometer is mostly stressed in metrology applications, this can be the magnetometer itself as a part of magnetic flux density standard, traceable [2] magnetic calibrating system [3]-[8] or an auxiliary device used to calibrate magnetic instruments. For example, a *nulling magnetometer* is used for indirect calibrations of coils or coil systems with respect to a secondary magnetic flux density standard, typically established as a wire-wound solenoid with high homogeneity [9][10]. It is required to be of high precision (low noise) with low short-term (temperature) drift of its offset; but the gain calibration is not important since the desired value is near zero. On the other hand, a fluxgate magnetometer used as a reference for a coil system [3]-[6] needs all of its nine parameters calibrated; magnetometer calibration, together with its stability and noise adds to the calibrating coil system accuracy.

Lowering the magnetometer noise is not an easy and straightforward task. The author focused on fluxgate magnetometer technology where he presents research in reducing the noise of a parallel and orthogonal [11] fluxgate – see Chapter 2.1. There are other low-noise, room-temperature, vectorial sensors than fluxgate [11], however with larger low-frequency noise. The most sensitive of magneto-resistive sensors –the HMC 1001 AMR– is limited to about 100 pT/√Hz at 1 Hz [12], even with a “set-reset” modulation / demodulation technique [13]. A room-temperature quantum magnetometer utilizing diamond nitrogen-vacancy center [14] shows promising results in measurements requiring high spatial resolution, however even the recent laboratory results show about 10 pT/√Hz noise amplitude spectral density (ASD) at 1 Hz. Vectorial, optically-pumped magnetometers have a limited field range (~tens of nT) suitable for biomagnetic measurements in shielded rooms [15]; for fields in the micro-tesla range (i.e. geomagnetic measurements), field-nulling has to employed. Another

approach is utilizing a rotating field around a scalar sensor with wider range, using field modulation and demodulation in the three axes [16]. In both of these techniques, the overall magnetometer performance is dominated by the noise limits of room-temperature semiconductors, and yield in units of pT ASD at 1 Hz [17], hindering the actual fT-level performance.As the 1/f noise level in a parallel, second harmonic fluxgate, reaches about 2.5 pT/√Hz at 1 Hz, it is increasingly difficult to reduce it further by means of magnetic material annealing and sensor design [18]. Only a few articles regarding state-of-the-art sensors claim noise levels around 1 pT − results of Marusenkov [17] and of Koch [19] remain isolated reports, indicating low reproducibility for parallel, second harmonic fluxgates. Moreover, these results were achieved for optimum laboratory conditions - they indicate noise of the sensor with minimal dynamic range, but embedding the sensors in a magnetometer would bring further challenges. The author's focus thus later shifted from parallel fluxgates –Chapter 2.1.2− to the relatively new technology of fundamental-mode orthogonal fluxgate [20] where finally the "1-pT/√Hz @ 1 Hz barrier" was crossed [21] and state-of-the-art noise level below 1 pT was reached even in a practical geomagnetic magnetometer – see Chapters 2.1.3 and 2.1.4.

A low noise magnetometer alone is not enough for a precise estimate of the magnetic flux density vector orientation and magnitude. The author presents his research in magnetometer calibrations –see Chapter 2.2– covering two topics: calibrations using off-the-shelf instruments under the presence of magnetic disturbances; and a metrologically rigorous calibration of magnetometer parameters. Although the topic on well-defined, traceable magnetometer calibration might seem well developed and achieve low uncertainties, mainly when using complex systems utilizing atomic magnetometers [7][8][10], it faces one substantial challenge. The already established infrastructure (calibrating coils, workplaces), which was magnetically „quiet and clean" i.e. free of static and dynamic disturbances, is challenged by a steady increase of magnetic disturbances due to urbanization, increased usage of DC inverter technology and DC power in transportation and industry [22]. Because of the gradient nature of anthropogenous disturbances, compensating them with a remote reference is not effective. One solution is a feedback-operated coil system with reference magnetometer in the homogeneous area [23], prohibiting calibrations for devices which create (disturb) magnetic fields; another one (and effective) is „running away", which is increasingly difficult. New methods of (numerical) compensation for such disturbing magnetic fields were researched, with the ultimate aim of a magnetometer calibration procedure with a uncertainty below 100 ppm in the geomagnetic range – Chapter 2.2.1.

Out of all the various magnetometer applications in industry and research, the author's focus lies in geomagnetism/geophysics [24] – magnetometer feasibility as a precise magnetic observatory instrument and its prospective use in geophysical exploration where inductions coils and/or SQUIDs are used – see Chapter 3. Geomagnetic observations are used in research of the geodynamo, Earth's field modeling and space weather effects [25]; a world-wide network of magnetic stations under the umbrella of INTERMAGNET association [27] provides such data quasi real-time. To further improve the models and predictions based on observations (e.g. of low-level pulsations [28],[29]), the requirements on resolution of the instruments have recently risen substantially: the INTERMAGNET standard for 1-second geomagnetic data requires a noise ASD less than 10 pT/√Hz at 0.1 Hz [30] which is difficult, if not impossible, to achieve with instruments deployed currently [17] [31]. As in the case of calibrations facilities, there is a global interest in identifying and possibly suppressing the man-made magnetic noise due to urban development [22][32].

The interest of the exploration industry in research towards lowering the ultra-low-frequency (ULF) noise of magnetometers lies in the geophysical principle of one the exploration methods: in magnetotellurics (MT) /transient electromagnetics (TEM) [33], the penetration depth at ultra-low frequencies (tens of μHz to units of Hz) theoretically allows for conductivity profiling from up to hundreds of km's in depth. At the same time, however, when utilizing the „natural" ULF excitation by geomagnetic pulsations and storms, the excitation amplitude is only in nT-level with a response several magnitudes below. Magnetometer noise floor is thus a hindering parameter to further increase depth and/or sensitivity of the method [34][35]. The state-of-the-art of ULF noise in magnetometers used for MT is 10 pT/√Hz at 10 mHz, which is achieved by search-coils with no less than 10 kg / 1.5 m in mass and dimensions, respectively [36]. The HTS SQUID with relatively cheap liquid nitrogen cryostat exhibits 1/f noise in the ULF region when operated unshielded due to flux trapping and is difficult to produce it in substantial quantities [37]. LTS SQUID seems like an ideal candidate [34][38], but is still prohibitably expensive and impractical for long-term operation in large numbers due to the He-filled cryostat. SQUID is also sensitive up to radio-frequency (RF), EMC/EMI and RF shields may further increase its noise [39].

Research on lowering the OFM fluxgate magnetometer noise is presented in Chapter 3. Noise ASD below 0.1 Hz was same or better when compared to an HTS SQUID or a search-coil. As the fluxgate has an advantage of reduced size and mass and response down to DC when compared to a search coil, and a cheap as well as room-temperature operation when compared to a SQUID, it allows for its potential use in geophysical exploration [34].

1 The parallel- and OFM-fluxgate magnetometer

Substantial part of the author's focus in non-cryogenic magnetometers was towards the fluxgate magnetometer, either of parallel or orthogonal type [9].

In the following, introductory book chapter *„Parallel Fluxgate Magnetometers"* [B1], the author described the fundamental principles, noise limits and state-of-the-art in parallel fluxgate magnetometers and gradiometers, summarizing his own research in the topic [Q1] and the state-of-the-art (as of 2015). The limitations of a parallel fluxgate basically lie in its mode of operation: during the alternating saturation cycles, any residual Barkhausen noise and non-reproducibility of hysteresis loop between the excitation cycles [40] will directly affect the low frequency noise performance due to the domain wall movements. This implies the need for extensive research in ferromagnetic core material selection, treatment and proper, noise-less excitation techniques. Author's further research in parallel fluxgate [J18],[J19],[J22] brought a conclusion that a different principle, although still fluxgate, is needed to consistently achieve an 1-Hz ASD below 1 pT/√Hz at room temperature.

To address the abovementioned limitation, the author was involved in collaborative research towards noise reduction of a fundamental mode, orthogonal (OFM) fluxgate, based on an annealed or as-cast amorphous, Cobalt-rich ferromagnetic wire [20][21]. The OFM fluxgate has been researched and developed at the CTU since 2010's and its theory is well described in [41]. The main advantage of the OFM fluxgate as compared to the second harmonic fluxgate is its largely static operation point on the B-H curve with a minimum (ideally zero) influence from Barkhausen noise of the ferromagnetic material. The orthogonal mode further simplifies the sensor to only one (pick-up) coil. However, there are peculiarities to address: power requirements are significant due to the sinusoidal excitation with a large DC component [41], and any residual (e.g. capacitive or inductive) coupling of the excitation signal affects sensor noise, since the excitation and detection occur at the same frequency. Also, the sensor offset and mainly offset drift are 1−2 order of magnitudes higher than with a parallel fluxgate [J25]. Despite these limitations, however, we were able to reduce the noise ASD of an OFM fluxgate below 1 pT/√Hz at 1 Hz [21] − see Chapter 2.1.

[B1] *Parallel fluxgate magnetometers (2016).*

Author contribution: 100%. **Citations:** 23

Parallel Fluxgate Magnetometers

Michal Janosek

Abstract This chapter gives a brief overview of parallel fluxgate development, technology and performance. Starting from theoretical background through derivation of fluxgate gating curves, the fluxgate sensor is explained on its typical examples, including sensors with rod-, ring- and race-track core. The effects of geometry, construction and magnetic material treatment on parallel fluxgate noise are discussed in detail–noise levels as low as 2 $pT_{rms} \cdot Hz^{-0.5}$ are possible with state-of-the-art devices. Basic applications of fluxgate magnetometers are given and a quick overview of commercial devices is presented, concluded with recent advances in bulk, miniature, digital and aerospace devices.

1 Background

The parallel fluxgate sensor dates back to the 1930s [1] and most of this early knowledge remains valid until today, although refined by recent findings in the field of sensor noise, core magnetic materials and new principles of signal extraction. Since the early times, the noise level of several nanoteslas has continuously decreased due to evolution in electronic circuits and core materials to units of pT in a 10-Hz bandwidth.

The parallel fluxgate sensor in its simplest form is sketched on Fig. 1 (left)—the time-varying excitation flux Φ_E created in the ferromagnetic core via the excitation field intensity H_E (produced by the excitation coil) and the "measured" field H_M are in *parallel*.

A fluxgate sensor is basically a magnetic field sensor relying on induction law. For its simplest form of Fig. 1 (left), its output voltage U_i present at the pick-up coil terminal P is approximated by the following equation:

$$U_i = -N \cdot S \cdot \left(\frac{dB_E}{dt} + K \cdot \mu_0 \mu_r \cdot \frac{dH_M}{dt} + K \cdot \mu_0 \cdot H_M \frac{d\mu_r}{dt} \right) \quad (1)$$

M. Janosek (✉)
Department of Measurement, Faculty of Electrical Engineering,
Czech Technical University in Prague, Technicka 2, Prague, Czech Republic
e-mail: janosem@fel.cvut.cz

A. Grosz et al. (eds.), *High Sensitivity Magnetometers*, Smart Sensors,
Measurement and Instrumentation 19, DOI 10.1007/978-3-319-34070-8_2

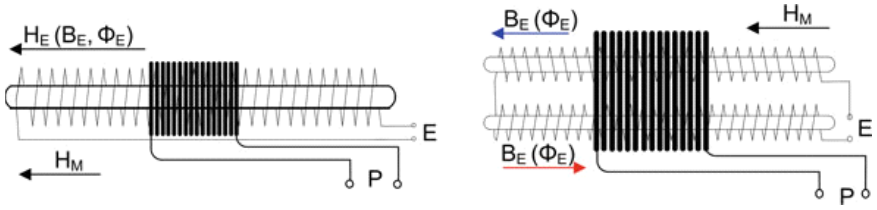

Fig. 1 (*Left*) Simplest parallel fluxgate with a rod-core. (*Right*) Modification with two cores

where H_M is the measured external magnetic field intensity with an eventual time-varying component, B_E is the alternating excitation flux density in the ferromagnetic core due to the excitation field intensity H_E, N is the number of turns of the pick-up coil, S is the core cross-sectional area, μ_0 is the permeability of vacuum and K is a dimension-less coupling coefficient of the core to the field H_M (real core geometry is far from an ellipsoid). The first term in parentheses is present because this simple sensor directly transforms also the excitation flux Φ_E to the pick-up coil, which is the basic disadvantage of this design. The second term is due to the eventually time-varying measured field H_M. However the key principle of a fluxgate sensor is in the last term of the equation—the alternating excitation ("drive") field H_E, which periodically causes the saturation of the magnetic material used in the fluxgate core, modulates the core permeability which has in turn a non-zero time derivative.

The sensor presented in Fig. 1 (left) is however impractical, although sometimes used in low-cost devices. Two cores can be used instead of one core, with each core having an opposite direction of the excitation flux, whereas the pick-up coil shares both of the cores—see Fig. 1 (right). If the core magnetic properties are same for both of them, the first term of Eq. 1—with eventually large disturbing amplitude—is effectively suppressed by the common pick-up coil.

If the measured magnetic field H_M is constant, the second term is also zero and only the third term of Eq. 1 remains as fluxgate output. In agreement with [2] and [3] we can then write for the fluxgate output voltage:

$$U_i(t) = -NS \cdot \mu_0 H_M \cdot \frac{d\mu_r}{dt} \frac{1-D}{[1+D(\mu_r - 1)]^2} \tag{2}$$

The "coupling coefficient" K in Eq. 1 was replaced by an equation introducing the dimension-less demagnetization factor D of a ferromagnetic body (fluxgate core).

2 The Physical Model

2.1 Fluxgate Transfer Function

The sensor depicted in Fig. 1 (right) can be used for deriving the parallel fluxgate operation principle. As we have two core slabs sharing the same, but opposite-in-direction excitation field H_E (yielding in time-varying $\Phi_E(B_E)$ in the

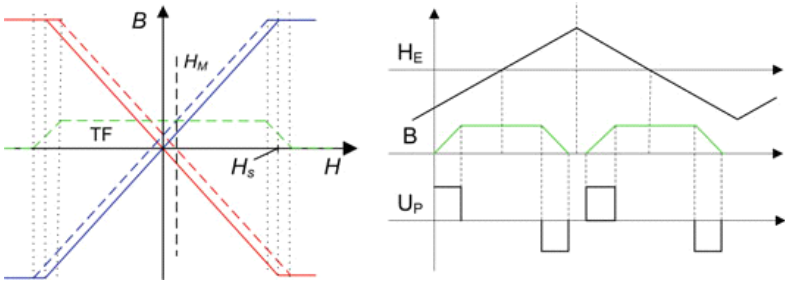

Fig. 2 (*Left*) Transfer function—ideal BH curve. (*Right*) Output voltage derivation with triangular excitation

core), we can draw the corresponding B-H loops for each core (which correspond to one-half of the magnetizing cycle) as seen in Fig. 2 (left). The core B-H loop was simplified to an ideal one with no magnetic hysteresis with H_S standing for the field intensity where it becomes saturated; the red curve corresponds to the lower core of Fig. 1 (right) and the blue one to the upper core. Without any external field H_M (solid curves), if both characteristics are summed, the net change of B during the half excitation cycle is zero. A non-zero external measured field H_M however effectively adds to the exciting field H_E and the resulting B-H loops are shifted (dashed curve). After their summation for both cores we obtain an effective "B-H transfer function" TF or "gating-function": the flux in the core (core flux density) is being periodically gated by the excitation field, the threshold is set by the H_S value and size of the external field H_M.

Now considering a triangular waveform of the excitation field H_E as in Fig. 2 (right) and applying the transfer function TF to it, we can derive the output voltage at the pick-up coil U_P as the core flux density B derivative. It can be seen that the output voltage is at twice the frequency of H_E and its magnitude and also phase lag would be proportional to the measured field H_M.

When taking into account also the material hysteresis, the transfer function will modify accordingly [2] as shown in Fig. 3 (left). However the approach-to-saturation

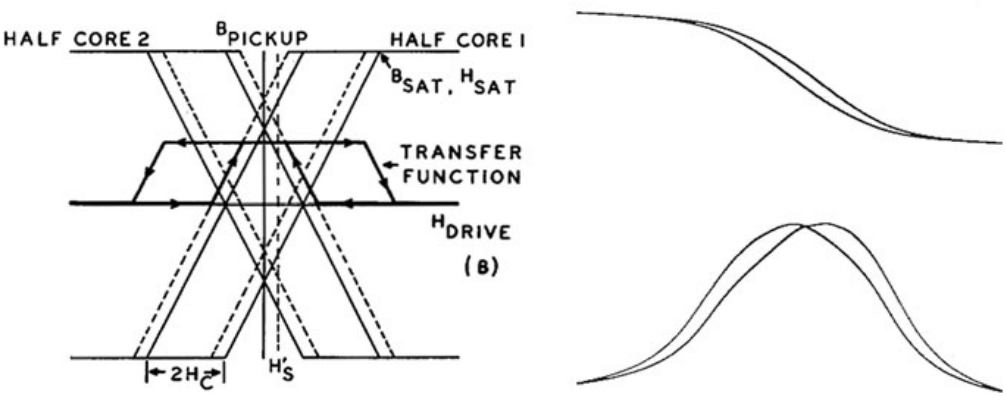

Fig. 3 (*Left*) Gating function with hysteresis from [2]. (*Right*) Real gating function from [3]

shown in Figs. 2 (right) and 3 (left) is not realistic—in Fig. 3 (right) a real BH loop and the corresponding gating function are shown.

An analytical approach to derive the fluxgate output signal was done as early in 1936 [1] and since then many improvements in the model were achieved, also by applying a Fourier-transform to the pulse-train shown in Fig. 2 (right), see [2–5]. However the original Aschenbrenner's approach is shown below since it gives a simple analytical demonstration of the origin of second harmonic in the fluxgate output signal.

Let's have a very simple approximation of the BH magnetizing curve [1], assuming the coefficients $a > 0$, $b > 0$:

$$B = a \cdot H - b \cdot H^3 \tag{3}$$

At each of the magnetic cores of Fig. 1 (right), the measured field H_M and the harmonic excitation field $H_E = A \sin \omega t$ are summed up:

$$H_{1,2} = H_M \pm H_E = H_M \pm A \sin \omega t \tag{4}$$

The corresponding flux density B in each of the two cores is then expressed using Eq. 3:

$$B_{1,2} = a(H_M \pm A \sin \omega t) - b(H_M \pm A \sin \omega t)^3 \tag{5}$$

$$\begin{aligned} B_{1,2} = {} & a \cdot H_M - b \cdot H_M^3 - \frac{3}{2} b \cdot A^2 \cdot H_M \\ & \pm \left(a \cdot A - 3b \cdot A \cdot H_M^2 - \frac{3}{4} b \cdot A^3 \right) \sin \omega t \\ & + \frac{3}{2} b \cdot A^2 H_M \cos 2\omega t \pm \frac{1}{4} b \cdot A^3 \sin 3\omega t \end{aligned} \tag{6}$$

If both cores are of equal cross-section S, the flux is then added by the means of common pick-up coil and after summing we get the remaining terms:

$$\begin{aligned} \Phi &= S \cdot (B_1 + B_2) \\ &= 2S \cdot \left(a \cdot H_M - b \cdot H_M^3 - \frac{3}{2} b \cdot A^2 \cdot H_M + \frac{3}{2} b \cdot A^2 H_M \cos 2\omega t \right) \end{aligned} \tag{7}$$

The only time-varying component is at the second harmonic of excitation field frequency:

$$\Phi(t) = 3S \cdot b \cdot A^2 \cdot H_M \cos 2\omega t \tag{8}$$

Again we see that the time-varying output is at the second harmonics of the excitation frequency and its amplitude is directly proportional to the measured, static field H_M. If H_M was time-varying, there would be also a signal at the fundamental frequency. In reality, however, also higher-order even harmonics are

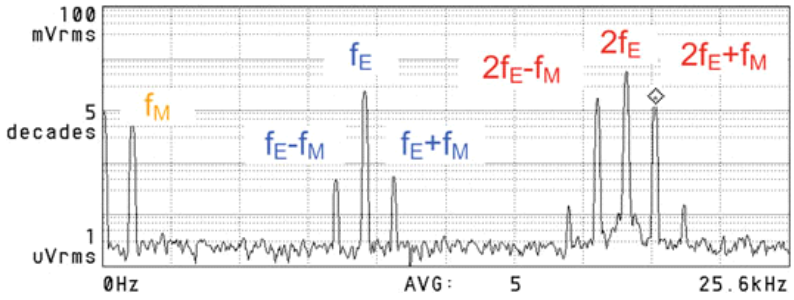

Fig. 4 The ac-driven fluxgate output spectrum

present, due to the nature of the B-H loop (hysteresis, approach to saturation) and non-sinusoidal excitation waveforms with higher harmonics. These effects are taken into account by the modern fluxgate models [2–5].

2.2 *The Fluxgate as a Modulator*

A real-world output of a fluxgate sensing a field H_M with both ac and dc component can be seen in Fig. 4—f_M is the frequency of alternating component and f_E is the excitation signal frequency. Signal at f_E which is present due to non-ideal symmetry of the sensor: i.e. the complementary terms of Eq. 6 are not exactly of the same amplitude and phase, so they do not subtract completely. The signal exactly at the second harmonics $2f_\mathrm{E}$ is due to the dc component of H_M. The measured field H_M is thus modulated on the excitation second harmonics. However due to the non-ideal symmetry of the sensor, it appears modulated also on the fundamental excitation frequency f_E. This applies not only to dc but also to the ac signal at f_M, which appears at $2f_E \pm f_M$ and $f_E \pm f_M$.

It can be concluded from the spectrum in Fig. 4 that an alternating signal is amplitude-modulated with a carrier on the 2nd harmonics of fluxgate excitation frequency, while the amplitude of the carrier is proportional to the dc component of the signal. This can be proven by substituting $H_M + B{\cdot}\cos(\psi t)$ for H_M in Eq. 8. If the excitation field would contain higher harmonics, there will be also higher modulation harmonics present in the spectra and the higher-order even harmonics will contain the information about the measured magnetic field.

3 The Parallel Fluxgate Noise

The fluxgate noise generally exhibits a $1/f$ behavior with a noise amplitude spectral density $(\mathrm{ASD} = \sqrt{\mathrm{PSD}})$ as low as 2–3 $\mathrm{pT_{rms}\ Hz^{-0.5}}$ @ 1 Hz, typically $\sim$10 $\mathrm{pT_{rms}\ Hz^{-0.5}}$. However, the noise due to the magnetometer electronic circuitry mostly limits at least the white noise floor (amplifier noise, detector phase

noise etc.), which makes measuring the fluxgate noise difficult and subject to large statistical errors.

The actual fluxgate noise can be related to three effects—stochastic behavior of the Barkhausen noise, or better explained as irreversible rotation and domain wall-displacement process during the fluxgate magnetizing cycle [6–8], thermal white noise [9] and an excessive, small-scale noise [10] which is seen at many fluxgates with supposedly low Barkhausen noise. The latter is believed to originate from inhomogeneous, stochastic magnetoelastic coupling of the non-zero magnetostrictive core to external stresses [11] rather to magnetostrictive movement itself [12]. The white noise of the pick-up coil does not have much influence, since although with increasing coil turns resistance increases but also the voltage sensitivity increases.

An important factor is the coupling of the "internal" fluxgate core noise to the actual sensor noise via the core demagnetization factor D. It can be written [13]:

$$B_{SensorNoise} \cong DB_{CoreNoise} \tag{9}$$

For Barkhausen noise, it was shown by van Bree [6], that minimum detectable signal H_0, which is equal to noise for SNR 0 dB, can be expressed as

$$H_{0(Bh)} = \frac{B_S}{\mu_0 \mu_r} \sqrt{\frac{\tau}{N_B \cdot t_m}} \tag{10}$$

where τ is the magnetization period lower limit (inverse of excitation frequency), t_m is the measurement time, B_s is the saturation flux density and N_B is the density of Barkhausen volumes after Bittel and Storm [8]. For the lower limit of $N_\mathrm{B} = 10^4$, $\tau = 10^{-6}$ s, $t_\mathrm{m} = 1$ s and $\mu_\mathrm{r} = 8000$ [6], H_0 yields in about 2×10^{-6} A/m (2 pT in air) which corresponds to the state-of-the art materials with low Barkhausen noise [14].

The white noise is usually estimated according to the (thermal) fluctuating current in the core: the component perpendicular to the core axis creates magnetic field noise, which couples to the pick-up coil [9]—Eq. 11.

$$I_{core}\left[\frac{A_{rms}}{\sqrt{\mathrm{Hz}}}\right] = \sqrt{\frac{4kT}{R_{core}}} \tag{11}$$

This "white-noise current" is also present at the 2nd harmonics. In this case, Eq. 11 should take into account the core "effective resistance" Re{Z} due to the skin-effect. However, since now we are considering only the correlated component at the 2nd harmonics, the noise couples to the pick-up coil only by the (low) residual transformer term of Eq. 1.

For usual core volumes, the predicted white noise is at least an order of magnitude below the observed fluxgate noise: for the race-track sensor [9] with 2 $\mathrm{pT_{rms}\ Hz^{-0.5}}$ @ 1 Hz the white noise was about 0.39 $\mathrm{pT_{rms}\ Hz^{-0.5}}$. In a single-domain fluxgate [14], white noise about 50 fT was reported utilizing a cross-spectral measurement technique.

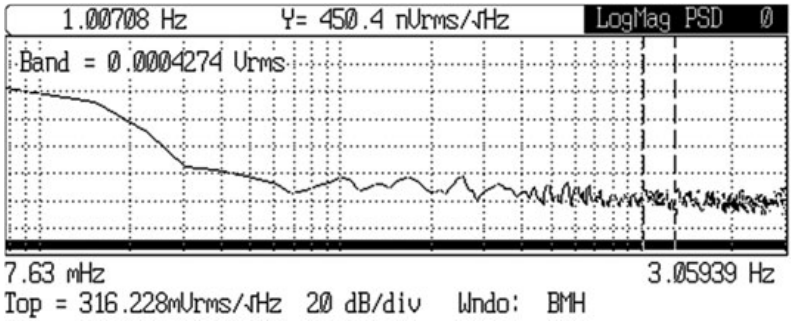

Fig. 5 Typical fluxgate magnetometer noise (TFM100G2, 100 kV/T, SR770)

A typical fluxgate noise is depicted below in Fig. 5—the low-noise TFM100G2 magnetometer of Billingsley A&D exhibits approximately 1/f character between 10 and 300 mHz and almost white response starting at 1 Hz with ASD about 4.5 pT_{rms} $Hz^{-0.5}$, which is a limit of the electronics, not the sensor itself.

4 Fluxgate Geometry and Construction

The core geometry plays an important role in constructing the parallel fluxgate sensor: the sensors can be roughly divided in two families according to core geometry. Rod sensors utilize cores with open magnetic path, ring-cores and race-tracks use closed path cores.

4.1 Rod Sensors

The design using two magnetic rods as in Fig. 1 (right) with a common pick-up coil was used already in 1936 by Aschenbrenner and it is also often referred as "Förster configuration" after the researcher and manufacturer F. Förster who utilized it. An example is in Fig. 6 with two thin Permalloy cores in glass tubes, on top of which the excitation coils are wound [compare to Fig. 1 (right)]. Alternatively, there can be two pick-up coils anti-serially connected which would be wound directly on the excitation coils—the so-called "Vacquier configuration" patented by V. Vacquier in 1941.

The advantage of rod sensors is low demagnetization factor due to the favorable ratio of cross-section and length which is in the direction of measured field. The disadvantage is that due to the open magnetic path the level of saturation is different across the core length, causing problems with sensor offset. The pick-up coil is then placed not to cover the noisy, unsaturated core ends [15].

Fig. 6 The rod fluxgate (Förster type) before assembly

4.2 Ring-Core and Race-Track

As stated previously, the construction of a parallel fluxgate should assure good symmetry to suppress unwanted excitation signal and also possibly to reduce the noise by strong excitation field: this can be obtained with a closed-path magnetic core. In terms of Eq. 4, the sensor can be virtually divided to two "core halves" with opposite excitation field direction—see Fig. 7. The key advantage of the ring-core [Fig. 7 (left)] is the possibility to rotate the pick-up coil in order to obtain best suppression of the residual excitation signal (due to transformer term in Eq. 1). Its disadvantage is the relatively large demagnetization factor decreasing its sensitivity when compared to the rod designs. To decrease the demagnetization factor, a sensor with an oval, race-track shape of ferromagnetic core [Fig. 7 (right)] is often designed. However its balance is not easily achieved as for ring-cores.

4.3 Bulk Sensors and Micro-fluxgates

The classical parallel fluxgate is a bulk-type, i.e. it uses magnetic core material from magnetic tape/wire or even a bulk material with wire-wound excitation and pick-up

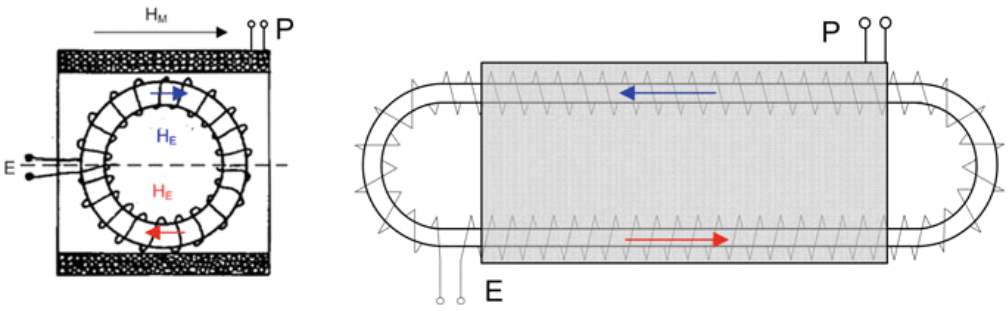

Fig. 7 (*Left*) The ring-core with H_E in "core halves." (*Right*) The race-track sensor

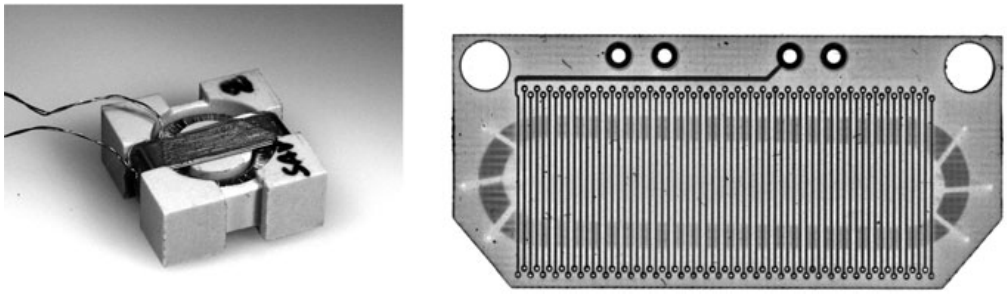

Fig. 8 (*Left*) The real 12-mm-dia ring-core is a typical bulk sensor. (*Right*) The 30-mm long race-track is created in PCB technology

coils. The final core shape in larger sensors is then obtained by winding the magnetic tape [16] or the annealed wire [14] to a core holder [Fig. 8 (left)]; a stress-free alternative is etching or arc-cutting the final core shape from a wide magnetic tape [17]. The advantage of bulk fluxgates is their high sensitivity due to large cross-section and high number of pick-up coil turns, and also low demagnetization factor achievable with long sensors. Disadvantages are their cost and mass which start to be a limiting factor even in aerospace applications where bulk fluxgates still find use [18]. An approach to at least simplify the manufacturing design has been done with PCB fluxgate sensors [19]—Fig. 8 (right), however despite the comparable size their parameters are inferior to that of classical ones mostly due to residual stresses after manufacturing (bonding of the ferromagnetic core) [20]. Electroplated ring-core fluxgates on PCB substrates have been presented by Butta [11], the thin layer was advantageous for high-frequency performance of the sensor.

Fluxgate micro-sensors appear since the end of 1980s. Their limitation is mostly very low sensitivity, resulting in 1-Hz ASD about 1 nT_{rms} $Hz^{-0.5}$ even when using excitation frequencies in the range of 1 MHz. The way of magnetic core manufacturing is often limited by desired sensor design: the need for solenoid coils and integrating the core mostly leads to MEMS devices; CMOS devices rely on flat-coils with worse coupling to the ferromagnetic core. An integrated micro-sensor core would require electrolytic deposition [21], integrating the etched tape [22] or sputtering [23].

5 Fluxgate Noise and Ferromagnetic Core

During the 80 years of fluxgate development, it has been finally understood that the core parameters are the key for a low-noise, high-sensitivity sensor [14, 16, 24]. The ferromagnetic core for a parallel fluxgate should fulfill several requirements arising from Eq. 2 and the principle of operation; these requirements affect several different parameters. Table 1 shows the list of required parameters and the most affected property.

Table 1 Influence of core parameter on fluxgate performance

Core parameter	Primary effect	Secondary
Low demagnetization factor	Sensitivity	Noise
Low Barkhausen noise	Noise	–
Low magnetostriction, low applied stresses	Offset	Noise
High permeability	Sensitivity	Power consump.
Approach to saturation	Noise	–
Thickness/resistivity	Losses	High *f* operation
Curie temperature	Operating range	Noise

5.1 Core Shape—Demagnetization Factor

Keeping the core demagnetization factor D low (lowest for rod-type sensors) not only allows for high sensitivity to external fields (Eq. 2) but also provides better ratio to the "core noise"—see Eq. 9. Thus a common practice to decrease sensor noise, if the limits of improving the magnetic material are reached, is to decrease D.

The demagnetization factor of a ring-core with a diameter d and effective core thickness T was estimated from a number of calculations and measurements [13]:

$$D \cong 0.223\ (T/d) \tag{12}$$

However it is relatively easy to model D it in today's FEM packages for arbitrary shapes. In Fig. 9 (left), the demagnetization factor of a 10-mm ring-core was calculated using ANSYS and also FLUX 3D software. The ferromagnetic tape was 20 μm thick and 2.6 mm wide with μ_r = 15,000. The resulting demagnetization factors for 5, 18 and 46 tape turns agree well with that calculated by Eq. 12. The relation between fluxgate noise and the demagnetizing factor due to Eq. 9 as proposed by Primdahl was later proved for large ring-core sensors [25]—the typical dependence is depicted in Fig. 9 (right). The increased noise at very low D values appears due to the fact that a smaller cross-section causes loss of SNR, assuming the existence of external induced noise coherent to the 2nd harmonic.

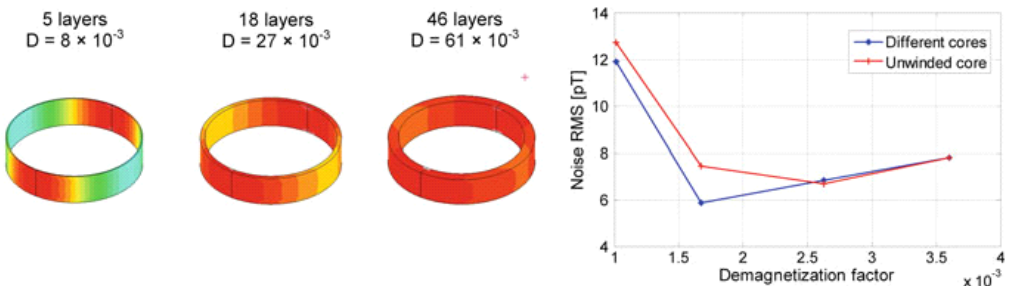

Fig. 9 (*Left*) Calculated demag. factor D of 10-mm ring [25]. (*Right*) Noise versus D for 50-mm rings

5.2 Core Material and Processing

Historically, the core materials were iron [1] or ferrites [3]. Later crystalline Ni-Fe started to be used in the form of tapes or rods ending up with specially annealed Molybdenum-Permalloy tapes [26] which are still being utilized in space research [18]. With these crystalline materials, the cores have to be annealed with the material already in its final shape. The inherent advantage of Permalloys is their high Curie temperature, allowing for high temperature operation, however special care of the material composition is necessary to achieve near-zero magnetostriction. Since 1980s there is a widespread use of amorphous materials, mostly in form of thin tapes and wires, which do not require hydrogen annealing in the final form and are less mechanically sensitive. Cobalt-based amorphous materials tend to be the best candidates for the sensors [16] however also in this case sufficient annealing process is necessary to obtain the same or better performance than the heritage Mo-Py cores.

Low Barkhausen noise is generally obtained in materials with very low area of the hysteresis loop with prevalent domain-wall rotations rather than domain-wall movements. This is achieved usually by perpendicular-field or stress annealing of the magnetic material to introduce perpendicular anisotropy, thus promoting domain-wall motion rather than sudden jumps due to the domain wall movement [16, 24]. Influence of Curie temperature on noise was studied by Shirae for various amorphous compositions [27]—a strong correlation between low Curie temperature and low fluxgate noise was found.

Since the end of the 20th century, nanocrystalline materials receive great attention because of their good thermal stability and stable phase, which makes them suitable for down-hole drilling [28] and possibly in space research. However their disadvantage is the relatively high saturation induction, requiring high excitation power and higher noise even after proper annealing.

6 The Feedback Compensated Magnetometer

The diagram of a typical feedback-compensated fluxgate magnetometer is on Fig. 10. The magnetometer usually uses feedback in order to achieve better stability and linearity of the device: the measured field is zeroed by an artificial field with opposite sign, created either by a coil shared for also for voltage pick-up, or by a separate compensating coil. The standard means of achieving the compensation field is using an integrating regulator feeding a feedback resistor or driving an active current source.

Alternatively, for full-vector magnetometers, the feedback coils can be integrated to a triaxial coil system where the orthogonal sensor triplet is placed, assuring high homogeneity of the compensating field and suppressing the parasitic sensitivity to perpendicular fields [30]. Also the mutual influence of feedback fields of the closely located sensors is suppressed.

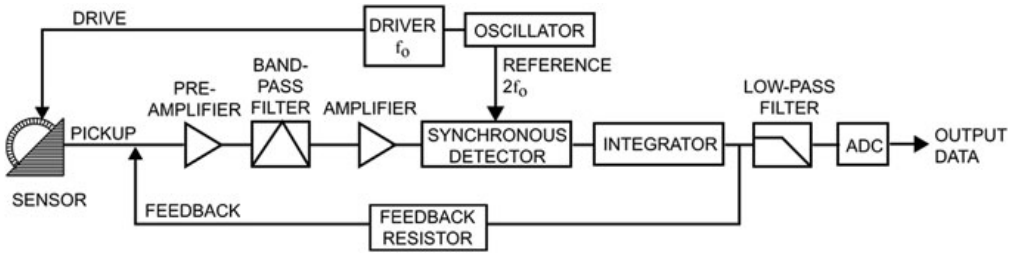

Fig. 10 The feedback compensated magnetometer from [29]

The sensitivity of the compensated magnetometer depends—by its operating principle—only on the coil constant of the compensating coil. The open-loop sensitivity (given by number of pick-up coil turns, core volume, demagnetization factor, permeability, drive waveform etc.) then affects the noise or resolution of the magnetometer, which ideally remains the same as in open-loop. The magnetometer linearity can be in tens of ppm and its gain stability better than 20 ppm/K, which in a good design is limited by the thermal expansion of the compensating coil (and its support) rather than by the electronics itself [30]. However, even for best magnetometers, the real-world limiting factor affecting the magnetometer resolution is the sensor offset and its temperature drift, which are not suppressed by the feedback loop. The offset is frequently caused by the non-ideal excitation waveform, which may contain parasitic signal at second-harmonic, which is not suppressed due to finite balance of the pick-up coil and the two ferromagnetic cores (or core halves). The core itself can be further affected by perming (i.e. large field shock, which causes change in the core remanence). Another significant contribution to the offset is the core in-homogeneity and its magnetostrictive coupling to inhomogeneous external stresses [12]; much lower contribution is to be expected from the electronics, such as amplifier non-linearity and detector offset. A detailed study of influence of the electronics on magnetometer parameters was presented by Piel [31].

6.1 Magnetometer Electronics

6.1.1 Analog

Signal processing of the pick-up voltage in an analog design normally uses an appropriate circuit for phase-sensitivite, dc-coupled down-conversion of the modulated signal on 2nd excitation harmonics (synchronous detector—phase sensitive detector/mixer)—this is done mainly when the fluxgate output signal at the pickup-coil can be “tuned” by a resonant capacitor to suppress higher-order even harmonics. Another detection possibility is “in time-domain” by integrating the output voltage [20]. Alternatively, it is possible to “short-circuit” the output

fluxgate terminals by a current-to-voltage converter and then process the pulse-like signal proportional to the gated flux [32]. Other techniques use the information of time-lag of the fluxgate output pulses in a special detector circuit [33, 34].

After the detector circuit, the feedback regulator (integrator) stage assures the feedback current, which is sensed, filtered and its value processed in an A/D converter. The fluxgate excitation (oscillator + driver in Fig. 10) in reality does not use sine-wave or triangular excitation signals, as shown in the derivation of the fluxgate output function. In order to save power, either pulse excitation using H-bridge is used [20] or the excitation circuit is "tuned", i.e. the excitation waveform is generated by switches and the non-linear inductance of the excitation circuit is tuned to serial-parallel resonance obtaining sharp excitation peaks. In that way the losses in the excitation circuit can be lowered only to ohmic losses of the excitation winding, moreover it was shown that the amplitude of the excitation signal has an inverse proportional effect on sensor noise [35].

6.1.2 Digital

Early digital magnetometer designs ended up with higher noise than the analog fluxgate with its D/A converter, however at least in space applications the trend is to integrate the electronics to an ASIC which can be further radiation-hardened for aerospace applications. The signal path historically utilized appropriate analog-to-digital converters and signal processing in DSP/FPGA together with D/A converters for feedback [36].

Recently, the fluxgate sensor was successfully integrated in an higher-order delta-sigma feedback loop electronics [37]—the power consumption of the corresponding ASIC (Fig. 11), which carries out the signal demodulation, feedback compensation and digital readout, was only 60 mW and the magnetometer performance was at least equivalent to 20-bit+ analog magnetometers with delta-sigma ADC's [38].

7 Applications

The first fluxgate applications appeared in the field of geomagnetic studies [1] and later also in the military or defense sector—"flux-valves" served for detection of ships or submarines [39]. After WWII, fluxgates have been extensively used in compasses/gyrocompasses in shipping and aviation [40], they have also found their use in attitude control of rockets or missiles and later they started to be used also on satellites [41]. Fluxgate sensors have been used in planetary studies since the early Apollo missions [26] and remained in their form almost unchanged—despite improved electronics—in the aerospace segment up to today [18]. Geophysical prospecting used aircraft-mounted fluxgates from the very beginning, and since

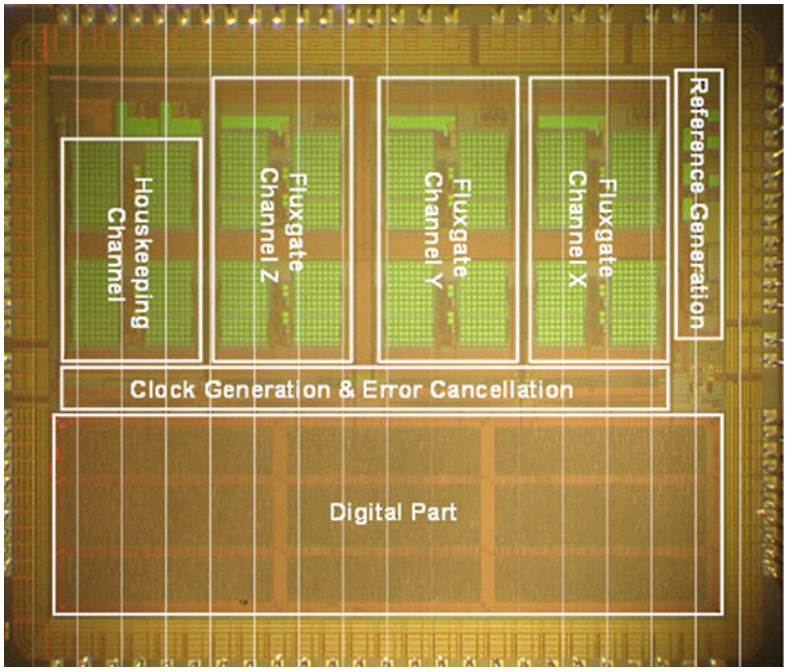

Fig. 11 Microphotograph of the MFA fluxgate ASIC. Reprinted from [37] with kind permission of the author

1980s, sufficient methods appeared to precisely calibrate the sensors, which allowed their use even onboard spacecraft for satellite-based geophysical research [42, 43].

One of the most common applications of a fluxgate for ground-based surveys is a magnetic gradiometer, consisting mostly of two aligned uniaxial sensors or two triaxial sensor heads. For a single-axis gradiometer, the estimated gradient dB_x/dx would be an approximation from two sensor readings B_{x1} and B_{x2} in a distance d:

$$\frac{\partial B_x}{\partial x} = \lim_{d \to 0} \frac{B_{x1} - B_{x2}}{(x_1 - x_2)} \cong \frac{B_{x1} - B_{x2}}{d} = \frac{\Delta B_x}{\Delta x} \tag{13}$$

Equation 13 implies the high requirements on individual fluxgate sensor noise if the sensor spacing d should be reasonable, i.e. below 1 m. Metal or UXO (Unexploded Ordnance) detectors using fluxgate find application also in underwater mine-hunting [44] and because of the cheap computational power now available, they are even constructed as full-tensor gradiometers which allow for localizing the magnetic dipole.

There also exist fields in biomedicine where fluxgate (gradiometers) have found their application: magneto-relaxometry (MRX) [45] and magneto-pneumography (MPG) [46]. Parallel fluxgate—or at least their principle—are also used for contact-less, precise dc/ac current measurements [34, 47].

8 Commercial Fluxgates

8.1 Magnetometers

There are actually very few suppliers who would sell good-quality fluxgate sensors separately—complete magnetometers are mostly offered. One common configuration is a triaxial magnetometer with analog outputs, the transfer constant (sensitivity) is mostly 100,000 V/T. Such instruments are for example of TFM100G2 (Billingsley Aerospace & Defense, USA), MAG03 (Bartington, UK), FGM3D (Sensys, Germany), TAM-1 or LEMI 024 of Laboratory of Electromagnetic Innovations (Lviv, Ukraine). Digitalization of these analog instrument outputs is upon the user or a special hardware is available from the manufacturers. Magnetometers which feature digital outputs (d-) are e.g. the Billingsley DFMG24, LEMI-029, the 3-axis magnetometer of Förster, Germany and FVM-400 of MEDA, USA. Table 2 summarizes most important parameters of the mentioned magnetometers.

8.2 Fluxgate Gradiometers/UXO Detectors

Table. 3 shows parameters of several commercially available gradiometers (UXO detectors), as manufactured by Schonsted (WV, USA), Förster (Germany), Geoscan (UK) or Bartington (UK). Although the gradiometer noise can be a parameter for selecting the best instrument, in reality, the gradiometer resolution is given by gradiometer calibration (astatization) which limits its real-world performance: the large, homogeneous Earth's field will cause false response unless the gradiometer is perfectly aligned or calibrated.

Table 2 Parameters of several commercial magnetometers

Magnetometer type	Range (±μT)	Noise (1 Hz) ($pT_{rms}/\sqrt{Hz}$)	3-dB BW (kHz)	Offset drift (nT/K)	Power (W)
TFM100G2	100	5–10	0.5/4	0.6	0.4
MAG03	70	6–10–20	3	0.1	0.5
FGM3D	100	15	2	0.3	0.6
LEMI 024	80	6	0.5	N/A	0.35
d—FVM-400	100	N/A	0.05/0.1	N/A	0.55
d—DFMG24	65	20	0.05	0.6	0.75
d—LEMI-029	78	6 (w/comp)	0.18	N/A	0.5
d—Förster 3-Axis	100	35	1	1	3.6

Table 3 Parameters of several commercial gradiometers

Gradiometer type	Base (m)	Resolution (nT/m)	Mass (kg)	Power (W)
Schonsted GA52Cx	0.5	N/A	1.1	0.2
Förster Ferex (0.6 m, w/logger)	0.65	1.5	4.9	2
Geoscan FM256	0.5	2	2.5	0.5
Bartington GRAD601 (w/logger)	1	<1	1.3	1.1

9 State of the Art—Recent Results

Recent achievements, either in the field of sensors, or in final magnetometers/gradiometers, are mainly determined by improving the ferromagnetic core material and sensing technologies.

9.1 Bulk Sensors, Magnetometers and Gradiometers

A fluxgate magnetometer with high-temperature rating of +250 °C was presented by Rühmer [28], the sensor core utilized nanocrystalline Vitroperm VP800R. Similar study was done before by Nishio [48] for Mercury exploration satellite, where the sensor characteristics were measured in −160 to +200 °C range.

Noise of a miniature, 10-mm diameter amorphous ring-core fluxgate was shown to decrease by field-annealing down to 6 pT_{rms} $Hz^{-0.5}$ @ 1 Hz [24] which is comparable to the state-of-the-art 17-mm aerospace sensors of the Danish Technical University [30] and also crystalline Mo-Py sensors used by the Geophysics and Extraterrestrial Physics group of the Technical University Braunschweig, Germany [18]. By decreasing the demagnetization factor by optimizing core geometry and the core cross-section of large ring-cores, it was shown by the author that 2 pT_{rms} $Hz^{-0.5}$ can be achieved even with an as-cast tape [25]. The problem with low sensitivity of miniature fluxgates was addressed by Jeng [49] who showed an improvement of 2× in the miniature magnetometer noise by using information from multiple even harmonics.

A study relating the magnetostrictive coupling of fluxgate core to external stresses with fluxgate noise was done by Butta [11]. The origin of the fluxgate offset was recently studied by Ripka [12] and it is—together with excessive noise—believed to be the effect of (local) magnetoelastic coupling, if other sources like perming or offset due to electronics are excluded.

In the field of gradiometers, the state-of-the art in axial devices is still the construction of DTU [50] with two triaxial vectorially-compensated heads, separated by 60 cm: the achieved resolution was 0.1 nT_{rms} m^{-1}. An underwater "real-time-tracking autonomous vehicle" developed at Naval Surface Warfare

Center, FL, USA [51] exhibited noise below 0.3 nT m^{-1} $Hz^{-0.5}$ @ 1 Hz, after compensating the vehicle noise. Recently, a similar full-tensor gradiometer vectorially compensated by a compact-spherical-coil was shown by Sui [52], which has the perspective to further decrease the gradiometer error and increase its sensitivity due to common compensation of the homogeneous field for all the 4 × 3 sensors.

9.2 *Micro-fluxgates*

A low-noise MEMS microfluxgate with nanocrystalline core embedded by chemical etching and with 3D solenoid coils was presented by Lei [22]. The sensor size was 6 × 5 mm^2 and the noise was as low as 0.5 nT $Hz^{-0.5}$ @ 1 Hz. Texas Instruments has recently published a CMOS-integrated Förster-type micro-fluxgate for contactless current sensing using a gradiometric arrangement [53]. It is also intended for closed-loop current measurement, where it replaces the common Hall-probe in the yoke gap. Its microphotograph is in Fig. 12: the Förster sensor is shown together with the excitation and signal-processing electronics. The microfluxgate operates at 1 MHz, achieves 0.2 mA resolution and was released as "DRV421". Recently, also a standalone micro-fluxgate in a 4 × 4 mm^2 QFN chip was released, with a noise of 1.5 nT $Hz^{-0.5}$ @ 1 kHz [54].

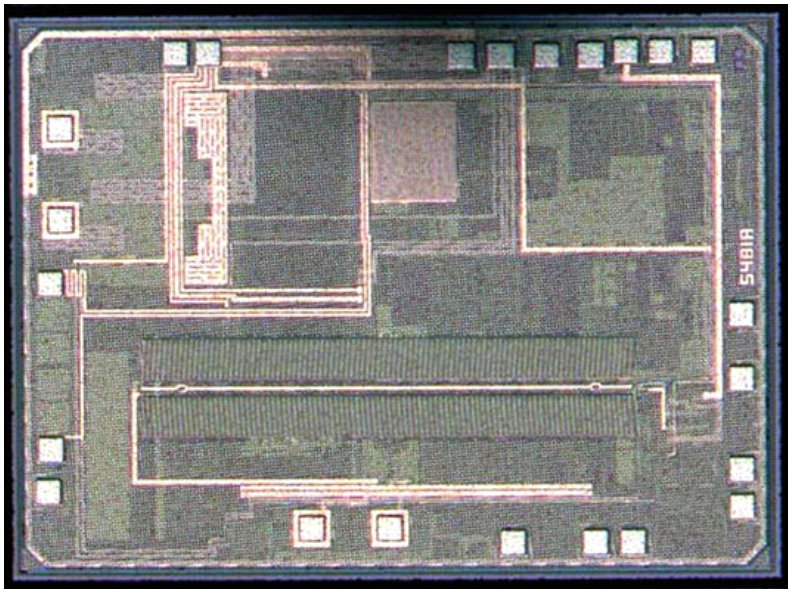

Fig. 12 The CMOS integrated Förster fluxgate, reproduced with kind permission of Texas Instruments, Inc

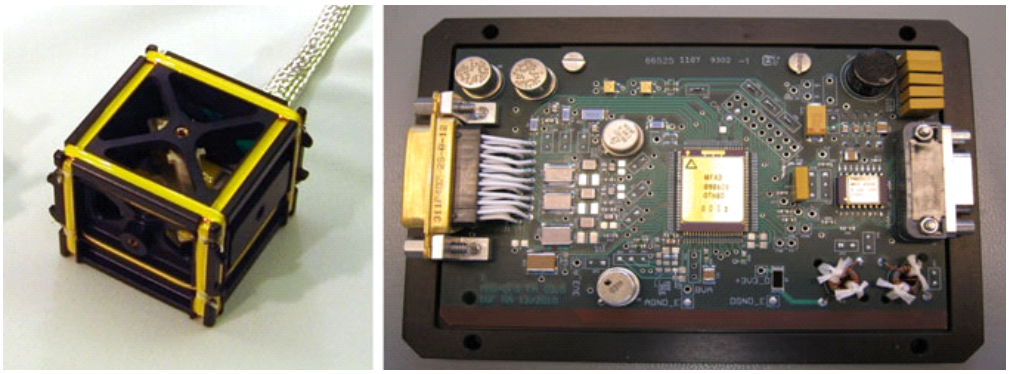

Fig. 13 The magnetic sensor and digital electronics of MMM mission (flight model, not to scale) —reproduced with kind permission of Werner Magnes /IWF Graz

9.3 Space Applications

An offset-reduction technique proposed by DTU for satellite missions [55] allowed to decrease offset drift of the heritage analog magnetometer design [30] to ±0.5 nT in a 73 °C range—the temperature changes in the excitation resonant circuit were compensated by an adaptive control of the detector phase. The digital-detection delta-sigma magnetometer of the THEMIS mission (launched 2007, still active) achieved offset stability of approximately 0.05 nT/K in the −55 to 60 °C temperature range [18]. These parameters became the state-of-the art in space fluxgate magnetometers.

The recently successful ROSETTA Explorer and its lander PHILAE used fluxgate magnetometers; the instrument noise was about 22 pT_{rms} in 0.1–10 Hz band [56]. The SWARM multi-satellite mission, launched in 2013, carries onboard several atomic magnetometers and also traditional fluxgates from DTU Denmark, and is now producing valuable data for a new Earth's field model and other geophysical observations [43]. A similar NASA "Magnetospheric Multiscale Mission" was launched in March 2015; the spacecraft carries analog and also delta-sigma-loop-integrated magnetometers with custom ASIC developed at the IWF Graz, Austria [37]—see Fig. 13. Multiple magnetometers have been used and large effort was made to achieve magnetic cleanliness [38].

References

1. H. Aschenbrenner, G. Goubau, Eine Anordnung zur Registrierung rascher magnetischer Störungen. Hochfrequenztechnik und Elektroakustik **47**(6), 177–181 (1936)
2. D.I. Gordon, R.H. Lundsten, R. Chiarodo, Factors affecting the sensitivity of gamma-level ring-core magnetometers. IEEE Trans. Magn. **1**(4), 330–337 (1965)
3. F Primdahl, The fluxgate mechanism, part I: the gating curves of parallel and orthogonal fluxgates. IEEE Trans. Magn. **6**(2), 376–383 (1970)

4. J.R. Burger, The theoretical output of a ring core fluxgate sensor. IEEE Trans. Magn. **8**(4), 791–796 (1972)
5. A.L. Geiler et al., A quantitative model for the nonlinear response of fluxgate magnetometers. J. Appl. Phys. **99**(8), 08B316 (2006)
6. J.L.M.J. van Bree, J.A. Poulis, F.N. Hooge, Barkhausen noise in fluxgate magnetometers. Appl. Sci. Res. **29**(1), 59–68 (1974)
7. M. Tejedor, B. Hernando, M.L. Sánchez, Reversible permeability for perpendicularly superposed induction in metallic glasses for fluxgate sensors. J. Magn. Magn. Mater. **133**(1), 338–341 (1994)
8. H. Bittel, L. Storm, *Rauschen. Eine Einfuehrung zum Verstaendnis elektrischer Schwankungserscheinungen*. (Springer, Berlin, 1971) (1)
9. C. Hinnrichs et al., Dependence of sensitivity and noise of fluxgate sensors on racetrack geometry. IEEE Trans. Magn. **37**(4), 1983–1985 (2001)
10. D. Scouten, Sensor noise in low-level flux-gate magnetometers. IEEE Trans. Magn. **8**(2), 223–231 (1972)
11. M. Butta et al., Influence of magnetostriction of NiFe electroplated film on the noise of fluxgate. IEEE Trans. Magn. **50**(11), 1–4 (2014)
12. P. Ripka, M. Pribil, M. Butta, Fluxgate Offset Study. IEEE Trans. Magn. **50**(11), 1–4 (2014)
13. F. Primdahl et al., Demagnetising factor and noise in the fluxgate ring-core sensor. J. Phys. E: Sci. Instrum. **22**(12), 1004 (1989)
14. R.H. Koch, J.R. Rozen, Low-noise flux-gate magnetic-field sensors using ring-and rod-core geometries. Appl. Phys. Lett. **78**(13), 1897–1899 (2001)
15. C. Moldovanu et al., The noise of the Vacquier type sensors referred to changes of the sensor geometrical dimensions. Sens. Actuators A **81**(1), 197–199 (2000)
16. O.V. Nielsen et al., Analysis of a fluxgate magnetometer based on metallic glass sensors. Meas. Sci. Technol. **2**(5), 435 (1991)
17. P. Ripka, Race-track fluxgate sensors. Sens. Actuators, A **37**, 417–421 (1993)
18. H.U. Auster et al., in *The THEMIS fluxgate magnetometer.* The THEMIS Mission (Springer, New York, 2009), pp. 235–264
19. O. Dezuari et al., Printed circuit board integrated fluxgate sensor. Sens. Actuators, A **81**(1), 200–203 (2000)
20. J. Kubik, M. Janosek, P. Ripka, Low-power fluxgate sensor signal processing using gated differential integrator. Sens. Lett. **5**(1), 149–152 (2007)
21. O. Zorlu, P. Kejik, W. Teppan, A closed core microfluxgate sensor with cascaded planar FeNi rings. Sens. Actuators A **162**(2), 241–247 (2010)
22. J. Lei, C. Lei, Y. Zhou, Micro fluxgate sensor using solenoid coils fabricated by MEMS technology. Meas. Sci. Rev. **12**(6), 286–289 (2012)
23. E. Delevoye et al., Microfluxgate sensors for high frequency and low power applications. Sens. Actuators A **145**, 271–277 (2008)
24. P. Butvin et al., Field annealed closed-path fluxgate sensors made of metallic-glass ribbons. Sens. Actuators A Phys. **184**, 72–77 (2012)
25. M. Janosek et al., Effects of core dimensions and manufacturing procedure on fluxgate noise. Acta Phys. Pol. A **126**(1), 104–105 (2014)
26. M.H. Acuna, Fluxgate magnetometers for outer planets exploration. IEEE Trans. Magn. **10**, 519–523 (1974)
27. K. Shirae, Noise in amorphous magnetic materials. IEEE Trans. Magn. **20**(5), 1299–1301 (1984)
28. D. Rühmer et al., Vector fluxgate magnetometer for high operation temperatures up to 250 °C. Sens. Actuators A Phys. **228**, 118–124 (2015)
29. A. Matsuoka et al., Development of fluxgate magnetometers and applications to the space science missions. Sci. Instrum. Sound. Rocket Satell. (2012)
30. O.V. Nielsen et al., Development, construction and analysis of the "Oersted" fluxgate magnetometer. Meas. Sci. Technol. **6**(8), 1099 (1995)

31. R. Piel, F. Ludwig, M. Schilling, Noise optimization of racetrack fluxgate sensors. Sens. Lett. **7**(3), 317–321 (2009)
32. F. Primdahl et al., The short-circuited fluxgate output current. J. Phys. E Sci. Instrum. **22**(6), 349 (1989)
33. B. Andò et al., in *Experimental investigations on the spatial resolution in RTD-fluxgates*. IEEE Instrumentation and Measurement Technology Conference, 2009 (IEEE 2009), pp. 1542–1545
34. D. High, Sensor Signal Conditioning IC for Closed-Loop Magnetic Current Sensor (Texas Instruments, 2006)
35. P. Ripka, W.G. Hurley, Excitation efficiency of fluxgate sensors. Sens. Actuators A **129**(1), 75–79 (2006)
36. J. Piil-Henriksen et al., Digital detection and feedback fluxgate magnetometer. Meas. Sci. Technol. **7**(6), 897 (1996)
37. W. Magnes et al., in *Magnetometer Front End ASIC*. Proceedings of 2nd International Workshop on Analog and Mixed Signal Integrated Circuits for Space Applications, (Noordwijk, 2008) pp. 99–106
38. C.T. Russell et al., The magnetospheric multiscale magnetometers. Space Sci. Rev. 1–68 (2014)
39. D.T. Germain-Jones, Post-war developments in geophysical instrumentation for oil prospecting. J. Sci. Instrum. **34**(1), 1 (1957)
40. W.L. Webb, Aircraft navigation instruments. Electr. Eng. **70**(5), 384–389 (1951)
41. S.F. Singer, in *Measurements of the Earth's Magnetic Field from a Satellite Vehicle*. Scientific uses of earth satellites (Univ. Michigan Press, Ann Arbor,1956), pp. 215–233
42. M.H. Acuna et al., in *The MAGSAT Vector Magnetometer: a Precision Fluxgate Magnetometer for the Measurement of the Geomagnetic Field*. NASA Technical Memorandum (1978)
43. T.J. Sabaka et al., CM5, a pre-Swarm comprehensive geomagnetic field model derived from over 12 yr of CHAMP, Ørsted, SAC-C and observatory data. Geophys. J. Int. **200**(3), 1596–1626 (2015)
44. Y.H. Pei, H.G. YEO, in *UXO Survey Using Vector Magnetic Gradiometer on Autonomous Underwater Vehicle*. OCEANS 2009, MTS/IEEE Biloxi-Marine Technology for Our Future: Global and Local Challenges (2009), pp. 1–8
45. F. Ludwig et al., Magnetorelaxometry of magnetic nanoparticles with fluxgate magnetometers for the analysis of biological targets. J. Magn. Magn. Mater. **293**(1), 690–695 (2005)
46. J. Tomek et al., Application of fluxgate gradiometer in magnetopneumography. Sens. Actuators A **132**(1), 214–217 (2006)
47. T. Kudo, S. Kuribara, Y. in *Takahashi, Wide-range ac/dc Earth Leakage Current Sensor Using Fluxgate with Self-excitation System*. IEEE Sensors (2011), pp. 512–515
48. Y. Nishio, F. Tohyama, N. Onishi, The sensor temperature characteristics of a fluxgate magnetometer by a wide-range temperature test for a Mercury exploration satellite. Meas. Sci. Technol. **18**(8), 2721 (2007)
49. J. Jeng, J. Chen, C. Lu, Enhancement in sensitivity using multiple harmonics for miniature fluxgates. IEEE Trans. Magn. **48**(11), 3696–3699 (2012)
50. J.M.G. Merayo, P. Brauer, F. Primdahl, Triaxial fluxgate gradiometer of high stability and linearity. Sens. Actuators A **120**(1), 71–77 (2005)
51. G. Sulzberger et al., in *Demonstration of the Real-time Tracking Gradiometer for Buried Mine Hunting while Operating from a Small Unmanned Underwater Vehicle*. IEEE Oceans (2006)
52. Y. Sui et al., Compact fluxgate magnetic full-tensor gradiometer with spherical feedback coil. Rev. Sci. Instrum. **85**(1), 014701 (2014)
53. M. Kashmiri et al., in *A 200kS/s 13.5 b Integrated-fluxgate Differential-magnetic-to-digital Converter with an Oversampling Compensation Loop for Contactless Current Sensing*. IEEE International Solid-State Circuits Conference-(ISSCC), 2015 (IEEE, 2015), pp. 1–3

54. Texas Instruments Inc., DRV425—Fluxgate Magnetic-Field Sensor (2015), http://www.ti.com/lit/ds/symlink/drv425.pdf
55. A. Cerman et al., in *Self-compensating Excitation of Fluxgate Sensors for Space Magnetometers.* IEEE Instrumentation and Measurement Technology Conference Proceedings, 2008 (IEEE, 2008), pp. 2059–2064
56. K.-H. Glassmeier et al., RPC-MAG the fluxgate magnetometer in the ROSETTA plasma consortium. Space Sci. Rev. **128**(1–4), 649–670 (2007)

2 Improving magnetometer precision and accuracy

Improving the magnetometer precision (resolution) is directly connected with lowering the magnetometer noise. Improving the magnetometer accuracy means not only improving its precision (which is part of the overall accuracy [1]), but also the uncertainty of magnetometer calibration and long-term stability of its parameters. Given the considered applications (geophysics and metrology), the author focused mainly on establishing and decreasing the ultra-low-frequency (ULF) magnetometer noise − between 1 mHz and 1 Hz.

2.1 Precision: noise and offset instability

The precision of a magnetometer reading is largely affected by its noise parameters and instability of its offset, which can be either corrected numerically, or is a random variable increasing the ULF noise. The author focused on establishing and improving the parameters of two types of Earth's-field-range magnetometers: the in-house developed parallel [44] and orthogonal fluxgate [41], and a commercial HTS SQUID. As the noise of a magnetometer sensor is improved, the noise contribution of the electronic has to be considered too: the additional sources to the actual fluxgate / SQUID sensor noise include and are not limited to the (pre-) amplifier, feedback loop, excitation and/or bias current [40] and digitizer noise.

2.1.1 Establishing and decreasing noise during magnetometer deployment

The following article *„Low frequency noise investigation of pT-level magnetic sensors by cross-spectral method"* [P2], presented at IEEE Sensors 2021 conference, deals with estimation of magnetic noise of fluxgate and SQUID sensors while in operation i.e. during geomagnetic measurements. As opposed to establishing the noise in a magnetic shield, this method shows the actual noise performance of the whole system including digitizer noise, as the noise of a typically used delta-sigma ADC near zero-voltage does not contain the voltage reference noise which dominates in high-resolution systems. Also, for HTS SQUID sensors, the noise strongly depends on the amount of flux „frozen" in the ring material: due to impurities of the superconducting material, flux vortices are pinned in normal areas of the superconducting film and their distribution is unstable in time, increasing the 1/f noise [42].

[P2] *Low frequency noise investigation of pT-level magnetic sensors by cross-spectral method (2021).* **Author contribution:** 40%. Fundamentals of methodology, data collection and processing, article structuration and finalization.

Low frequency noise investigation of pT-level magnetic sensors by cross-spectral method

Michal Janošek[1], David Novotný[1], Michal Dressler[1] and Elda Saunderson[2,3]
[1]Dept. of Measurement, Czech Technical University in Prague, Prague, Czech Republic
[2]Directorate Space Science, South African National Space Agency, Hermanus, South Africa
[3]Stellenbosch University, Stellenbosch, South Africa

2021 IEEE Sensors | 978-1-7281-9501-8/21/$31.00 ©2021 IEEE | DOI: 10.1109/SENSORS47087.2021.9639875

***Abstract*— We present a simple method to estimate the noise of magnetic sensors running in the Earth's field range by establishing the cross-power spectrum density during ambient field operation and performing spectral subtraction. This method has advantages to the usual subtraction of two sensors outputs, mainly in requirements for synchronization of the sample rate and gain calibration. With this method, verified in simulation and measurements with AMR magnetometers, we could use a fluxgate as a second sensor in order to estimate the low-frequency noise of an HTS SQUID in the ambient field.**

Keywords—magnetic sensor; noise; SQUID; fluxgate; AMR; correlation

I. INTRODUCTION

Estimating the ultralow frequency (ULF, 0.01-1 Hz) noise levels of magnetic sensors in a laboratory is not a straightforward task once the expected noise levels of the sensor are in the order of pT. The first option is to use a magnetic shielding cylinder ("zero-field cylinder") [1]. An even better option is a shielded room with large dimensions and "active shielding". The state-of-the-art "BMSR-2" with 8 layers states about 1×10^4 to 1×10^5 shielding factor between 0.01 and 1 Hz [2]; however, such an establishment is out of reach of a typical laboratory. We have estimated the shielding factor of a compact 6-layer magnetic shielding cylinder (length 0.75 m, inner diameter 17 cm) available at the CTU as approx. $1x10^4$ between 10 and 100 mHz and 2×10^4 at 20 Hz [3]. For a typical laboratory noise of 10 nT/√Hz @ 1 Hz, the transverse shield attenuation would yield about 1 pT/√Hz "residual" noise at 100 mHz.

The problem with finite shielding factors can be mitigated by doing the noise measurements with the shield in a low noise environment. However, for the HTS DC SQUID (High-temperature-superconductor Superconducting Quantum Interference Device) magnetometer, the noise obtained in a zero-field environment might be much smaller than when exposed to the Earth's magnetic field (~20 - 60 μT) during geomagnetic observations [4]. Although the SQUID sensor design can be optimized to reduce the effect of "flux trapping" and subsequent ULF noise due to exposure to large magnetic fields [5], the researchers and manufacturers almost exclusively claim the sensor noise "in zero field", and rarely show noise figures at frequencies below 1 Hz [6], [7] because of its dependence on the electronics, setup and location.

An alternative to magnetic shields for estimating the sensor noise is measuring its output in a quiet ambient (Earth's) field [8]. The method is cheap and benefits from the real-world operation of the sensor, i.e., it is not artificially exposed to zero magnetic field. If ambient noise is lower than the predicted sensor noise, direct measurements can be performed, however, the ambient field cancellation method with two sensors, as described below, is utilized mostly.

A. Out of the shield – difference measurement

The most common method to reject ambient magnetic field and its noise is subtracting the outputs of two identical magnetic sensors; although more advanced methods might yield better results [9]. If we assume that the two sensors exhibit sensor noise $n_1(t)$ and $n_2(t)$, then it follows for the two noisy observations $y_1(t)$ and $y_2(t)$ of the ambient field $a(t)$:

$$y_1(t) = n_1(t) + a(t) \quad \text{and} \quad y_2(t) = n_2(t) + a(t) \qquad (1)$$

If observations are subtracted, the common (correlated) noisy ambient field $a(t)$ is removed. The basic condition is that $a(t)$ is the same at the two sensors. This can be met where the noise gradient is negligible (i.e. sufficiently far away from anthropogenic noise). Natural ambient field fluctuations (diurnal changes of the Earth's magnetic field, magnetic storms / field oscillations induced by Sun activity, thunderstorm discharges etc. - [8]) can be regarded as homogeneous on a local scale and thus $a(t)$ for two aligned and calibrated sensors will be the same.

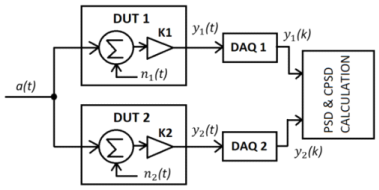

Fig. 1. Difference measurement method

If the condition that $n_1(t)$ and $n_2(t)$ are uncorrelated is met, and both signals are of the same magnitude and distribution, we can then write for Amplitude Spectral Density (ASD=√PSD, T/√Hz) of the individual sensor noise:

$$ASD\big(n_{1,2}(t)\big) = \frac{1}{\sqrt{2}} \cdot ASD\big(y_1(t) - y_2(t)\big) \qquad (2)$$

This method is convenient, however suffers from drawbacks. First, the two sensors have to be of similar noise performance, otherwise the estimation yields more towards the noise of the inferior sensor. Also, the noise floor is limited by coherent sampling, alignment and perfect calibration of the two sensors, i.e. $k_1a(t) \neq k_2a(t)$. Further, any gradient or de-correlation (i.e. due to the presence of ferrous objects) in the

ambient noise is not suppressed, requiring lowering the sensor-to-sensor distance [9] and/or using a low-gradient environment.

B. *Proposed method – cross-spectrum subtraction*

To overcome the first two limitations of the difference method, we propose to use a modified cross-spectrum method, as described i.e. in [10]-[12]. The cross-spectrum method was used to suppress the noise of the preamplifiers for magnetoresistive sensors [13] - here the uncorrelated noise was suppressed and noise of the magnetoresistors, far less than the noise floor of the preamplifiers, was revealed. In our case, we will however assume that the ambient magnetic noise is the only correlated component when logging the ambient field with two magnetic sensors. By calculating the cross-spectra and using the spectral subtraction method [14], however, we do not reconstruct the signal our case and stay in the frequency domain.

II. Cross-Spectral Noise Estimation in Ambient Magnetic Field

With the "modified cross-spectrum method", we can calculate individual sensor noise while overcoming the drawbacks of the direct-subtraction method. Specifically, we can estimate the noise when using two sensors with different noise characteristics, which will be illustrated below even in the case of more than one order of magnitude difference (fluxgate vs SQUID sensors). Also, this method allows us to estimate the noise of a single SQUID sensor, as the ULF noise can differ significantly from sensor to sensor. In our setup [18] we have only one SQUID axis running; therefore the difference method cannot be used.

A. *Method description*

Firstly we have to obtain power spectrum densities (PSD) for measured signals and cross power spectrum densities (CPSD) for DUTs. As the PSD/CPSD is a Fourier transform of auto/cross correlation $R(k)$ of sampled signals [15], we can write for the first observation $y_1(k)$ - using the notation of equation (1) and skipping some mathematical operations after substituting $y_1(k) = n_1(k) + a(k)$:

$$R_{y_1}(k) = \frac{1}{N}\sum_{n=1}^{N} y_1(n)y_1(n-k) = \cdots = \\ = R_a(k) + R_{an_1}(k) + R_{n_{1a}}(k) + R_{n_1}(k) \quad (3)$$

Because $R_{an1} = R_{n1a}$, we can write:

$$R_{y_1}(k) = R_a(k) + 2R_{an_1}(k) + R_{n_1}(k) \quad (4)$$

The same applies for observation y_2(k):

$$R_{y_2}(k) = R_2(k) = R_a(k) + 2R_{an_2}(k) + R_{n_1}(k) \quad (5)$$

Cross-correlation between the two observations is then:

$$R_{y_1y_2}(k) = \frac{1}{N}\sum_{n=1}^{N} y_1(n)y_2(n-k) = \ldots = \\ = R_a(k) + 2R_{an_2}(k) + R_{n_1n_2}(k) \quad (6)$$

When subtracting the cross-correlation (4) from $R_{y1}(k)$:

$$R_{y_1}(k) - R_{y_1y_2}(k) = R_a(k) + 2R_{an_1}(k) + \ldots \\ \ldots + R_{n_1}(k) - \left(R_a(k) + 2R_{an_2}(k) + R_{n_1n_2}(k)\right) \quad (7)$$

If we can assume that $2R_{an_1}(k) = 0$ and $2R_{an_2}(k) = 0$ due to no correlation between DUT intrinsic noise and external noise, and that also $R_{n_1n_2}(k) = 0$ due to no correlation between the noise of both DUTs, it is left that:

$$R_{y_1}(k) - R_{y_1y_2}(k) = R_{n_1}(k) \quad (8)$$

which proves our method to be correct. Conversion between correlations $R(k)$ and power spectral density $S(f)$ can be expressed using Fourier transform F:

$$S(f) = F\{R(k)\} = \sum_{k=1}^{N} R(k)e^{-i2\pi fk} \quad (9)$$

The Welch's periodogram [15] estimates the averaged $S(f)$ with number of averages m, defined by window length and overlap. The number of averages influences the variance of the spectrum – $PSD = S(f)$ variance is approximately inversely proportional to m. During the estimation of $a(t)$ noise by calculating the CPSD, we need to suppress the non-correlated part of the y_1 and y_2 observations. The suppression further depends on the number of averages available, and is inversely proportional to $\sqrt{m}$ [10]. The minimum number of averages for Gaussian signals was shown to depend on the inverse coherence function γ^2 [16]: $m_{min} = 1/\gamma^2$.

B. *Verification with synthetic data*

For the initial testing of the proposed method, we generated synthetic data in MATLAB (white noise with additional pink noise). Using three arrays $n_1(k)$, $n_2(k)$, $a(k)$ of uncorrelated noise we obtained two "composite noise" observations $y_1(k)$, $y_2(k)$ - see equation (1). We simulated a frequent scenario with one "good" low-noise sensor and one "poor" sensor with higher noise. In this case the subtraction method cannot be used as it automatically leads to the noise of "poor" sensor. Results can be seen in Fig. 2.

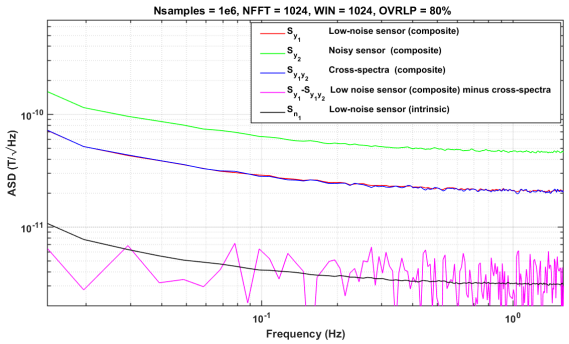

Fig. 2. Verification with simulated data – 1×10^6 samples, m ~4900

C. *Effects of imperfections – alignment, sample rate, gain*

For practical use of the method, multiple imperfect scenarios have been tested to verify its usability. Since we are doing computations in the frequency domain instead of the

time domain, and the process can be assumed ergodic, it gives us inherent independence to time alignment (lead/lag has no effect on the CPSD subtraction method). Errors in sampling rate leads to worsening of results as shown in Fig.3 for real data. Error in gains (>10%) caused by imperfect calibration also lead to worse results, however, we have verified that even a 1% gain error is acceptable.

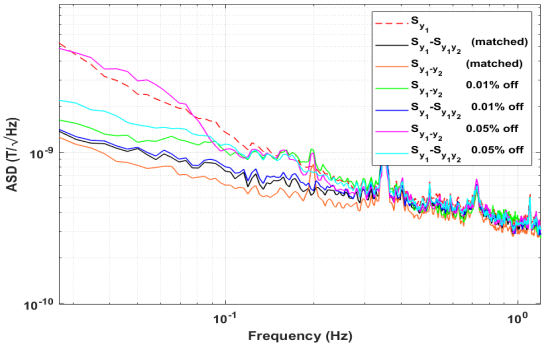

Fig. 3. Samplerate error simulation - effect on CPSD subtraction

D. AMR magnetometer noise estimation

The real-world measurement has been done using two identical AMR magnetometers [17] mounted on a wooden desk with 18 cm spacing, shown in Fig. 4. Both magnetometers streamed data over a serial link with the same sampling rate, and the data were recorded on a PC. Even at such a small distance, crosstalk between compensation windings of AMR sensors is negligible, as the compensation windings are on the AMR chip, and thus yield negligible magnetic moments. In Fig. 4 we see that the calculated noise of AMR#1 (black trace) matches the direct measurement of S_{n1} in a 6-layer shield (magenta) closely.

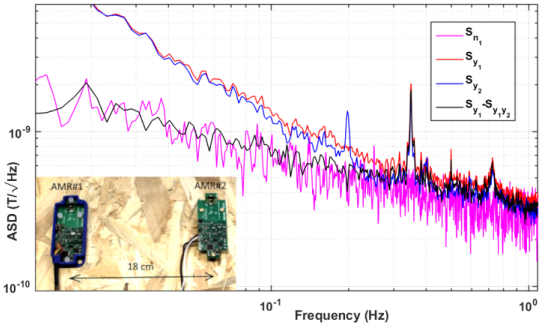

Fig. 4. AMR – noise measurement results and photo of the setup

III. Field Estimation of SQUID Noise

At SANSA Space Science, we are operating an unshielded HTS SQUID for geomagnetic observations [18]. A single Z-axis sensor type M2700 (StarCryo, USA), is connected to flux-feedback-loop electronics type SEL-1 (Magnicon, Germany) - see Fig. 5. The analog output is digitized with two 24-bit cards, NI-9252 and AD24-ETH. For this study we used the latter, as it offers lower noise at the expense of bandwidth. The ULF noise of the SQUID could not be estimated yet as it is masked by ambient noise and we are lacking a second sensor performing equally well.

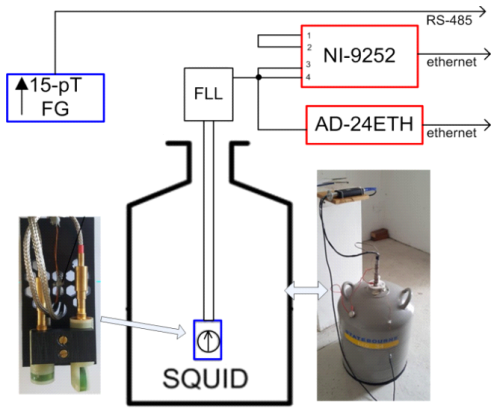

Fig. 5. HTS SQUID and fluxgate sensor setup

The AMR fluxgate and SQUID do not share a common ADC (the fluxgate output is digital). The only possible correlation would be from a noisy power supply, which is 12V DC buffered by lead-acid batteries. Fig. 6 shows a short record of sampled data and resulting spectra. Correlation between the fluxgate and SQUID data is evident from the time record; we also see that the "composite" fluxgate noise is also almost order of magnitude higher than of the SQUID.

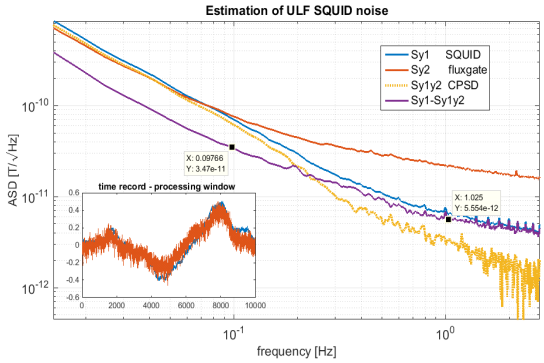

Fig. 6. SQUID and fluxgate data - time domain and noise estimation

The level of correlated ambient field noise of about 3 pT/√Hz at 1 Hz is reasonable since we observed similar values before with a 1-pT fluxgate magnetometer [19]. We can see that above approximately 200 mHz, the SQUID noise is dominating, with about 5 pT/√Hz at 1 Hz. Below 100 mHz the coherent ambient field noise dominates. The SQUID noise at 100 mHz (upper limit estimation) was established as about 30 pT/√Hz. A future measurement with the 1-pT fluxgate [19] as a third instrument will bring us more confidence in the potential of the presented method and reliability of the established SQUID noise.

Acknowledgment

M.J. and D.N. acknowledge the support of the Grant Agency of the Czech Republic, under grant No. 20-19686S. E.S. and M.D. acknowledge the support of the IEEE Magnetics Society through 2021 IEEE Educational Seed Funding. D.N. was also supported through the internal grant of the CTU Prague, No. SGS19/177/OHK3/3T/13.

REFERENCES

[1] E. Baum and J. Bork, "Systematic design of magnetic shields", Journal of Magnetism and Magnetic Materials, 101(1-3), 1991, pp 69-74.

[2] J. Bork., H. D. Hahlbohm, R. Klein and A. Schnabel, "The 8-layered magnetically shielded room of the PTB: Design and construction", Biomag2000, Proc. 12th Int. Conf. on Biomagnetism. Espoo, Finland, 2001. pp. 970-73.

[3] M. Janosek, A. Zikmund and P. Ripka, "Tensor behaviour of magnetic shielding factor", 2011 INTERMAG Conference, April 25–29, 2011, Taipei, Taiwan, unpublished.

[4] C. P. Foley, et al., "Geophysical exploration using magnetic gradiometry based on HTS SQUIDs", IEEE Transactions on Applied Superconductivity, Vol 11, No 1, 2001, 1375-1378.

[5] R. Stolz, et al., "Superconducting sensors and methods in geophysical applications" Supercond. Sci. Technol., Vol. 34, 2021, 033001

[6] M. I. Faley, Y. V. Maslennikov, V. P. Koshelets, and R. E. Dunin-Borkowski, "Flip-Chip High-Tc DC SQUID Magnetometer with a Ferromagnetic Flux Antenna", IEEE Transactions on Applied Superconductivity, 28(4), 2018, pp. 1-5.

[7] S. Keenan, CSIRO Manufacturing, HTS SQUID magnetometers and gradiometers, available from www.csiro.au, accessed on 2/7/2021

[8] G. C. Constable and S. C. Constable, "Satellite magnetic field measurements: applications in studying the deep earth", The State of the Planet: Frontiers and Challenges in Geophysics, 2004, 150: pp. 147-159.

[9] P. J. M. Wőltgens, R. H. Koch, "Magnetic background noise cancellation in real-world environments", Review of Scientific Instruments, 2000, 71.3: pp. 1529-1533.

[10] E. Rubiola, F. Vernotte, "The cross-spectrum experimental method", arXiv preprint arXiv:1003.0113, 2010

[11] M. Sampietro, L. Fasoli, and G. Ferrari, "Spectrum analyzer with noise reduction by cross-correlation technique on two channels", Review of Scientific Instruments, 70.5, 1999 pp. 2520-2525.

[12] A. C. Cárdenas-Olaya, et al., "Noise characterization of analog to digital converters for amplitude and phase noise measurements", Review of Scientific Instruments, 2017, 88.6: 065108.

[13] N. A. Stutzke, S. E. Russek, D. P. Pappas, and M. Tondra, "Low-frequency noise measurements on commercial magnetoresistive magnetic field sensors", J. Appl. Phys., 97, 10Q107, 2005.

[14] S. V. Vaseghi, Advanced digital signal processing and noise reduction. John Wiley & Sons, 2008, pp. 333, ISBN: 0-471-62692-9.

[15] A. V. Oppenheim, R. W. Schafer and J. R. Buck, Discrete-Time Signal Processing, 2nd Ed., Prentice Hall, NJ, 1999, p.737-738.

[16] J. Biaire, L. K. J. Vandamme, "Uncertainty in Gaussian noise generalized for cross-correlation spectra", Journal of Applied Physics, 1998, 84.8: pp. 4370-4374.

[17] D. Novotny, V. Petrucha, M. Dressler and A. Platil, "Characterization of a Digital AMR Magnetometer for Space Applications", in IEEE Transactions on Instrumentation and Measurement, vol. 70, pp. 1-9, 2021, Art no. 9504309, doi: 10.1109/TIM.2020.3043867.

[18] T. Matladi, et al., "Correlation between fluxgate and SQUID magnetometer data sets for geomagnetic storms". In: E3S Web of Conferences. EDP Sciences, 2014, p. 02002.

[19] M. Janosek, et al., "1-pT noise fluxgate magnetometer for geomagnetic measurements and unshielded magnetocardiography", IEEE Transactions on Instrumentation and Measurement, vol. 69, No 5, 2019, pp. 2552-2560.

2.1.2 Parallel fluxgate noise reduction - demagnetization factor

During 2012-2014, the author was involved in a collaborative project with the exploration industry aimed at reaching parallel fluxgate magnetometer noise ASD of 1 pT/√Hz @ 1 Hz, which has been reported in the state-of-the-art only twice − in [17] and [19].

The results with a 50-mm tape-wound ring-core (cobalt-rich amorphous tape), as shown in the article "*Effects of Core Dimensions and Manufacturing Procedure on Fluxgate Noise"* [J23], were promising, although consistently only 2 pT/√Hz 1-Hz ASD was reached. The aim of the research was to verify the dependence of fluxgate noise on the demagnetization factor of its core [43], i.e. that by reducing the demagnetization factor the noise should decrease towards the actual limits of the material. (More detailed results, mainly regarding the core-annealing were not published due to non-disclosure agreements.)

From the data shown in [J23], Fig. 4, there was an indication that the excitation noise at 2^{nd} harmonic plays a significant role: excitation noise does not change as the demagnetization factor improves, so there will be a limitation on the noise improvement with decreasing demagnetization factor. Unfortunately, this will be more pronounced for larger cores with lower demagnetization factors, which require more excitation energy for the same levels of saturation (increased winding resistance due to larger core circumference, in our case). Theoretically, excitation noise would be cancelled for a perfect parallel fluxgate but the there is always a residual coupling to the excitation field due to imperfect geometry and core and winding inhomogeneity [44]. Another limitation, when decreasing the demagnetizing factor simply by decreasing the material cross-section, would be the decreased sensitivity, however this can be compensated for with increased number of turns of the secondary winding, and did not pose a problem in our study.

The requirement for excitation field "purity" is even more pronounced if the Barkhausen noise was further reduced with perpendicular annealing (field-, stress-, Joule-heat-) of the magnetic material: the excitation levels for deep saturation [40] need to be even higher – the author reported up to 10 kA/m p-p in [J27] for a field-annealed amorphous ring-core.

[J23] *Effects of Core Dimensions and Manufacturing Procedure on Fluxgate Noise (2014).*

Author contribution: 60%. Theory, data collection (minus simulations), processing and article composition. **Citations:** 2

Proceedings of the 15th Czech and Slovak Conference on Magnetism, Košice, Slovakia, June 17–21 2013

Effects of Core Dimensions and Manufacturing Procedure on Fluxgate Noise

M. Janošek[a,*], J. Vyhnánek[a], A. Zikmund[a], P. Butvin[b], B. Butvinová[b]

[a]Dept. of Measurement, FEE, Czech Technical University in Prague, Technická 2, 166 27 Praha, Czech Republic

[b]Institute of Physics, Slovak Academy of Sciences, Dúbravská cesta 9, 84511 Bratislava , Slovakia

The effect of demagnetizing factor and manufacturing procedure on noise of the fluxgate probes, manufactured from metallic glasses, is presented. The fluxgate probes were either tape-wound, or flat, wet-etched ringcore and race-track geometries. When combining low demagnetizing factor and high enough cross-section of the probe, a minimum in the noise dependence can be found. For 50 mm ringcores, in such minimum the noise value as low as 7 pT_{RMS} in 0.1-10 Hz frequency band was achieved, which is very low for an as-cast tape, and has not been reported before.

DOI: 10.12693/APhysPolA.126.104

PACS: 75.75.–c, 75.30.-m, 75.50.–y, 07.55.–w, 75.70.-i

1. Introduction

The coupling of internal noise of the magnetic material to the noise of fluxgate sensors, manufactured from that material is ruled according to the commonly agreed practice, by the so called demagnetizing factor of the probe. This factor can be altered by changing the geometry of the probe (Fig. 1). For tape-wound sensors, core radius can be modified or the number of tape-turns can be altered. For ring-core and race-track geometries etched from tapes, changing the width of the annulus or stacking of the cores brings similar results.

The effect of the demagnetizing factor on noise was shown by Primdahl [1] for a given ringcore diameter of 17 mm. Tape-wound racetracks, studied in [2], were also optimized by altering the race-track geometry.

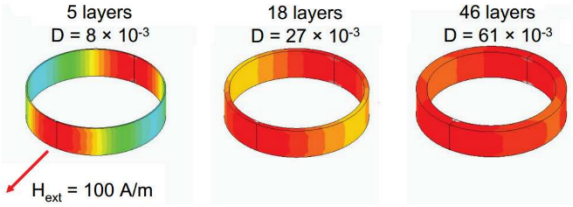

Fig. 1. Demagnetizing factor as a function of ring-core thickness (3D FEM simulation, the outer diameter (12 mm) is fixed).

However, mainly for ringcores with various diameters, the comparison is not straightforward: the bending stress, which becomes higher with smaller core diameter, is worsening the fluxgate probe noise. This can be handled either by appropriate zero-magnetostriction annealing [3], or at least by partially releasing the stresses during field annealing of the tape-wound core in its final form [4].

A different situation exists for flat cores wet-etched from a wide amorphous tape. In this case the bending stress does not affect the probe noise, however the smoothness of etching process and mainly the art of fixing the core to the bobbin influence the noise. Fluxgate probes with etched race-track cores were previously studied in printed-circuit-board (PCB) sensors; however the internal stresses due to embedding the core in the PCB laminate affected probe performance [5]. In [4] the authors have shown noise figure also for the race-track core which was not embedded in the laminate, however its performance was limited by excitation electronics. In this study, the working conditions were all the same for all studied sensors in order to facilitate the comparison of results.

2. Material and geometry selection

In this work, Vitrokov 8116 – a Co-Cr-Fe-B-Si metallic glass tape was used, with an average thickness of 20 μm and with tape widths of 2.6 mm (wound cores) and 20 mm (etched race-tracks).

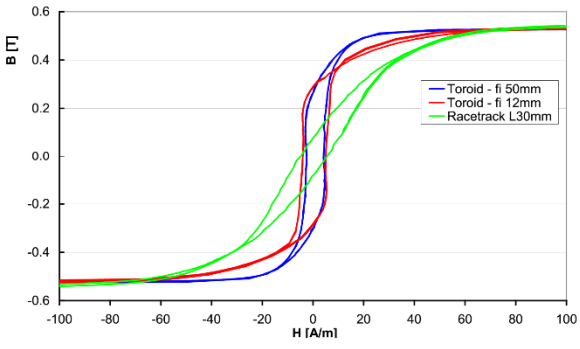

Fig. 2. *B-H* loops of the 3 core geometries.

*corresponding author; e-mail: janosem@fel.cvut.cz

For the tape-wound cores, the magnetoelastic effects can be seen by using the same material for 12 mm and 50 mm diameter (Fig. 2). From the *B-H* loops it is evident, that even for these tapes with magnetostriction of $\sim 1 \times 10^{-7}$ this effect is present.

As for the 2.6 mm tape width, the material did not show any appreciable macroscopic heterogeneity, which otherwise causes poorly reproducible inhomogeneous magnetic anisotropy, brought about by macroscopic stress between surfaces and interior of many Fe-based ribbons (e.g. Finemets). The absence of this heterogeneity in Co-Cr-Fe-B-Si has been verified by comparing hysteresis loops prior to and after surfaces removal when the ribbon thickness was reduced by $10 \div 15\%$ ($2 \div 3$ μm).

In the 20 mm tape however, the heterogeneity was present but still acceptable. The different *B-H* loop shape of the race-track in the comparison is evident but not caused by the tape macroscopic heterogeneity: the explanation lies in the as-cast anisotropy of the amorphous tape due to the manufacturing process, which is in the case of longitudinally etched race-tracks combined in both of the perpendicular branches of the race-track. An evidence for this behavior was shown in the MOKE pictures in [4].

4. Noise measurements – setup and results

The setup of electronics and operating conditions of the fluxgate probe were almost identical to that used in [4]. The resulting noise spectra for various tape thicknesses in the case of 50 mm ringcores obtained in a 6-layer magnetic shielding can, are shown in Fig. 3. To decrease the statistical error, an integral value of the noise in the frequency band of 0.1 to 10 Hz was calculated.

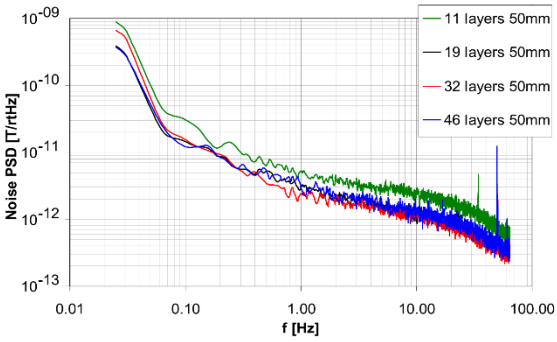

Fig. 3. Noise spectra of the 50 mm ringcore sensors.

The spectrum clearly maintains $1/f$ behaviour with lowpass filtering visible for frequencies above 12 Hz. The measuring procedure was done for the 50 mm cores in two tracks: 4 cores with different number of turns were produced and also one core was sequentially re-wound with decreased number of turns of the tape. The almost identical 50 mm results shown in Fig. 4 are thus independently obtained.

For 12 mm cores, there was a manufacturing problem of the bobbins, so only values for two demagnetizing factors are shown (5 and 10 turns). Although no dependence can be deducted, the overall increased noise, due to the bending stress is evident. This was further confirmed by the one-layer, 30 mm long race-track noise: absence of the bending stress and relatively low demagnetizing factor resulted in a noise comparable to that of 50 mm wound cores.

The results are in agreement with the behaviour found by Primdahl [1]. The noise for a given geometry slowly decreases with the decreasing demagnetizing factor up to a given minimum, from which it increases much faster.

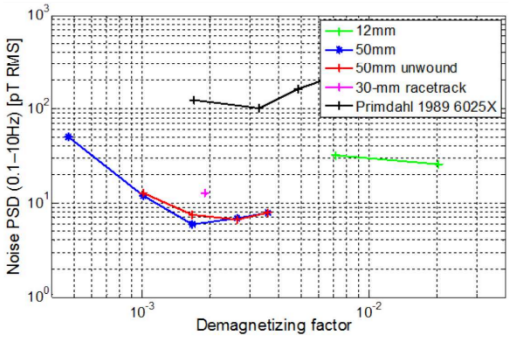

Fig. 4. Noise vs. demagnetizing factor for three geometries, including results of Primdahl for reference (he used 5, 10, 15 and 20 turns, respectively, on 17 mm diameter).

The authors offer the following explanation: as the cross-section of the magnetic material decreases in this case, also the signal-to-noise ratio of the whole sensor-electronics setup decreases, so the lower demagnetizing factor cannot bring a benefit anymore. Here the limitation was not the 5 nV lock-in amplifier noise, but rather remanent parasitic signal from unwanted even harmonics in the excitation current, which does not change when the core cross-section (and thus demagnetizing factor) is altered.

Acknowledgments

The authors are grateful for partial financial support by APVV grant SK-CZ-0078-11.

References

[1] F. Primdahl, B.Hernando, O.V. Nielsen, J.R. Petersen, *J. Phys. E: Sci. Instrum.* **22**, 1004 (1989).

[2] C. Hinnrichs, J. Stahl, K. Kuchenbrandt, M. Schilling, *IEEE Trans. Mag.* **37**, 1983 (2001).

[3] F. Primdahl, P. Brauer, J.M.G. Merayo, O.V. Nielsen, *Meas. Sci. Technol.* **13**, 1248 (2002).

[4] P. Butvin, M. Janošek, P. Ripka, B. Butvinová, P. Švec sr., M. Kuzminski, P. Švec jr., D. Janičkovič, G. Vlasák, *Sens. Act. A* **184**, 72 (2012).

[5] J. Kubík, L. Pavel, P. Ripka, *Sens. Act. A* **130-131**, 184 (2006).

2.1.3 Noise reduction in an OFM fluxgate

The article „ *Reduction of magnetic noise limits of orthogonal fluxgate sensor*“ [J4] focuses on addressing the limitations of signal electronics for an OFM fluxgate. Demands are higher than for a parallel fluxgate: the corresponding ~1 pT/√Hz voltage levels of a properly annealed sensor are already reaching the 1 nV/√Hz region; moreover, the signal and excitation of the sensor occur at the same frequency, so common-mode rejection of the amplifier is of great importance. By redesigning the electronic; we were able to lower the 1 Hz noise ASD to 0.7 pT/√Hz and the white noise ASD below 0.3 pT/√Hz. This result has been since a new state-of-the art for a room-temperature, vectorial sensor.

The next article *„Very low frequency noise reduction in orthogonal fluxgate“* [J12**]** shows significant reduction of ULF 1/f noise with the means of thermal damping of the sensor core. Care was taken to research the material parameters in order not to influence the sensor by mechanical stresses during curing and operation due to non-zero magnetostriction of the ferromagnetic core. We have found that the 0.1 Hz noise dropped almost three times − down to 8 pT/√Hz. The principle has been patented - [X1], [X3].

[J4] *Reduction of magnetic noise limits of orthogonal fluxgate sensor (2021)*
Author contribution: 30%. MOKE image processing, noise theory and results review, article finalization. **Citations:** 4

[J12] *Very low frequency noise reduction in orthogonal fluxgate (2018)*
Author contribution: 30%. Proposal of testing methodology, setup of experiments, results review and interpretation. **Citations:** 4

2.1.4 OFM – field-induced excess offset drift

The article „ *Offset drift in orthogonal fluxgate and importance of closed-loop operation“* [J2] is an outcome of collaborative research in the OFM fluxgate offset drift. During extensive experiments trying to identify and link offset drift and ULF noise, we have discovered a previously unknown phenomena: the OFM fluxgate, when exposed to non-zero fields, suffers from an induced, excess offset-drift, similar to „perming“ [44] in parallel fluxgate, however the sensor state (original offset) recovers. The settling slope / settling time was found as proportional to the magnitude of applied field and also its duration.

[J2] *Offset drift in orthogonal fluxgate and importance of closed-loop operation (2022)*
Author contribution: 20%. Effect observation, proposal of experiments and methodology, data review and interpretation **Citations:** 2

AIP Advances ARTICLE scitation.org/journal/adv

Reduction of magnetic noise limits of orthogonal fluxgate sensor

Cite as: AIP Advances 11, 015347 (2021); doi: 10.1063/9.0000231
Presented: 5 November 2020 • Submitted: 15 October 2020 •
Accepted: 29 December 2020 • Published Online: 27 January 2021

Michal Dressler,[a] Michal Janosek, and Mattia Butta

AFFILIATIONS

Department of Measurement-Faculty of Electrical Engineering, Czech Technical University in Prague, Technicka 2, 16627 Prague, Czech Republic

Note: This paper was presented at the 65th Annual Conference on Magnetism and Magnetic Materials.
[a]**Author to whom correspondence should be addressed:** dressmic@fel.cvut.cz

ABSTRACT

We have further lowered the white noise of an orthogonal fluxgate to about 0.3 pT/$\sqrt{}$Hz @ 8 Hz. So far, this is the lowest noise reported for a fluxgate magnetometer. The noise reduction was achieved by introducing a JFET input stage, embedded directly to the sensor head, allowing for high common-mode rejection and negligible loading of the resonant circuit. The origin of the noise was investigated by correlation measurements and we concluded that, at least in the white noise region, we observe the magnetic noise of the sensor, with about 0.1 pT/$\sqrt{}$Hz white noise contribution by the electronics. We were finally able to obtain sensor noise floor below 1 pT/$\sqrt{}$Hz @ 1 Hz also in a feedback-compensated closed-loop. Closed-loop operation allows for higher magnetometer stability and operation in Earth's magnetic field without deteriorating its noise performance.

INTRODUCTION

The orthogonal fluxgate sensors based on magnetic microwires, when operated in fundamental mode with DC bias,[1,2] show perspective for sub pT-level vectorial magnetic sensors at room-temperature. However, decreasing the magnetic noise values close or below 1 pT puts strong demands not only on manufacturing the sensor,[3,4] but also on the performance of its conditioning electronics. So far, the lowest noise was achieved using fluxgates with Π-shaped magnetic core made from amorphous wires.[5,6] Specifically, we used a sensor head with four Co-rich AC20 Unitika^{TM} wires with 120 μm diameter - see Fig. 1a. The wires have been annealed for 6 minutes by Joule heating with a 2 second polarity switch.[7] The process of annealing is necessary to increase the circular anisotropy, which leads to lower energy of the minor loops for a given excitation current. The effect of annealing is also visible in the MOKE images we have obtained with a Kerr Microscope and KerrLab software (evico-magnetics, Dresden, Germany) - see Fig. 1b. The as-cast (C) and annealed (A) wires were fed by the same current with two different values - 0.2 and 2 mA. While the as cast wire is still composed of multiple bamboo-like domains with the 2-mA excitation, the annealed wire already exhibits a single, large domain which flips polarity between those two levels.

The optimization of the wire core however pushed the design of our magnetometer to its limits. Recently, we were able to achieve about 0.8 pT/$\sqrt{}$Hz noise density at 1 Hz and 0.8 pT/$\sqrt{}$Hz noise floor with an open-loop operated magnetometer.[5] The electronic unit consisted of a multichannel DDS, a stable current source for magnetic wire excitation[8] and two independent pickup preamplifiers and demodulators - see Fig. 1c. The limiting factor in terms of noise was found as the pickup coil preamplifier and the rejection of excitation feed-through and other EMI signals. Also, we experienced an increase of the noise to 1.5 pT/$\sqrt{}$Hz when operated in the feedback loop.

If we want to achieve further noise reduction, we should then reduce the noise of the input stage (amplifier), which is a crucial component of the magnetometer. In this paper we address this noise and we propose a new circuit which reduces the noise by removing the loading of the pick-up coil.

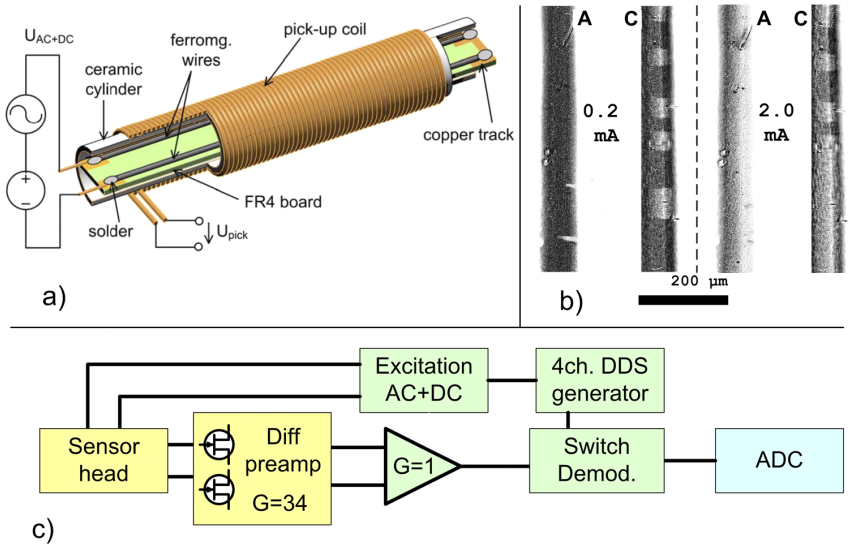

FIG. 1. a) The orthogonal fluxgate sensor head structure.[5] Reproduced with permission from IEEE Trans. Inst. Meas. 69, 2552 (2020). Copyright 2020 IEEE. b) Superimposed topology and MOKE image of microwire magnetic domains on as-cast and Joule annealed wire. c) Simplified magnetometer circuit block diagram.

IDENTIFYING THE LIMITATIONS

We have investigated the limitations of our initial design.[5,6] Here, a simple difference amplifier with LT6234 op-amp was used – the equation for its equivalent voltage noise e_{out} is following:

$$e_{out} = \sqrt{2(i_n R_2)^2 + (e_n(NG+1))^2 + 8kT\left(R_2 + R_1 \cdot NG^2\right)}, \quad (1)$$

$$NG = \frac{2 \cdot R_2}{2 \cdot R_1 + Z_c}. \quad (2)$$

The gain of 30 was set with two feedback resistors R_1 = 1 kΩ and R_2 = 30 kΩ, the opamp input voltage noise density was e_n = 2 nV/√Hz and its current noise was i_n = 0.8 pA/√Hz. In addition, we need to take into the account the effect of coil impedance Z_c at resonance on the noise-gain NG of the amplifier in Eq. 2. Taking into account all noise contributions of Eq. 1, the resulting noise e_{out} is equal to 240 nV/√Hz or 8 nV/√Hz when referred to input.

Moreover, the low input resistance of the differential amplifier (~2 kΩ) dampens the pickup resonant circuit (about 5 kΩ equivalent LC tank impedance Z_c at 40 kHz), resulting in lowering magnetometer sensitivity approx. to ¼. The noise contribution of a switching-type demodulator adds another 12 nV/√Hz RTI (measured with its input shorted). All these noise sources combined together create a hardware noise limit of 14.4 nV/√Hz. If we know the sensor sensitivity (before amplification) - about 22 kV/T - we end up with approx. 0.65 pT/√Hz white noise, which was the noise limit presented.[5] However, having the noise of the electronics at the same level of the total noise of the magnetometer does not allow to reveal the actual noise of the sensor, and this is the ultimate limit to reduce the total noise.

CIRCUITRY IMPROVEMENTS

In order to reduce the capacitively-coupled excitation feedthrough, at the cost of lower sensitivity, we have decreased the pick-up coil number of turns from 2000 (4-layers) to approximately 1000 (2-layers). This also allowed to decrease the pickup coil impedance from 5 kΩ to 2 kΩ. We could also use higher gain in the input stage to minimize noise contribution of following stages (demodulator and acquisition circuits).

J-FET input stage

In order to avoid loading of the resonant circuit and thus maximize the sensitivity, we have added a J-FET differential amplifier stage before the difference amplifier (Fig. 2). This stage consists of a low-noise LSK389 matched transistor pair with 1.9 nV/√Hz white input voltage noise density and negligible input current noise. The gain of the J-FET pre-amplifier stage was set to 34 and it is followed by a differential to single-ended receiver with gain 1. The JFET preamplifier is built on a PCB together with the sensor, in order to obtain high common-mode-rejection ratio and avoid long cabling with high impedance signals Fig. 2.

Since the J-FET amplifier does not load the LC tank, we observe a significant sensitivity increase at the resonance frequency – see Fig. 3a. The magnetometer sensitivity with the same excitation parameters (48 mA AC at 44 kHz) is five times higher than with

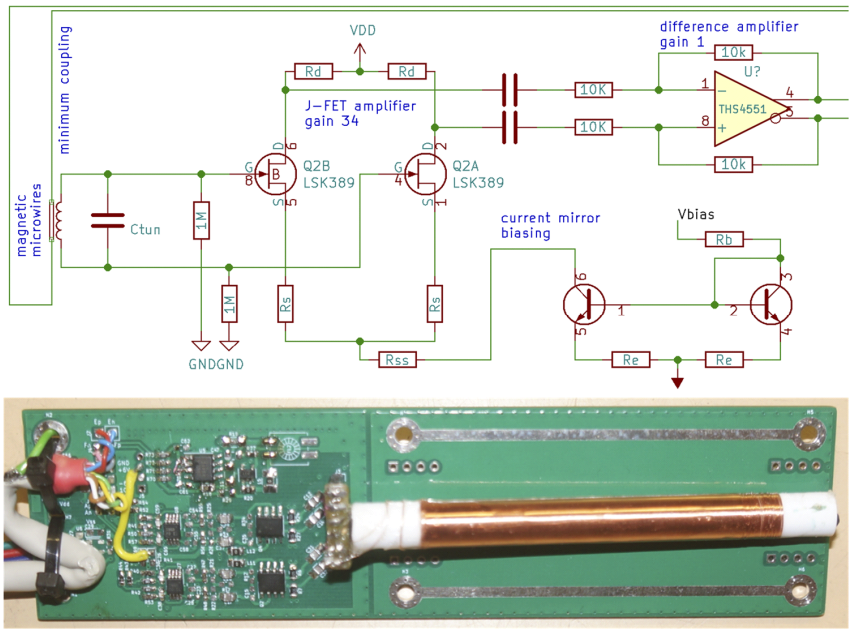

FIG. 2. Simplified schematics of pickup coil input stage (top) and a photo of finished board including two independent input channels (bottom) connected directly to sensor head.

the simple diff op-amp - 30-35 kV/T. Higher sensitivity leads to an expected decrease of the measurable sensor noise floor, which dropped from 0.6 pT/$\sqrt{}$Hz to 0.15 pT/$\sqrt{}$Hz - Fig. 3b. More importantly, we achieved a noise reduction also in the 1/f region; the noise density at 1 Hz measured on the sensor dropped from 1 pT/$\sqrt{}$Hz to 0.7 pT/$\sqrt{}$Hz. We can also see the effect of increased CMRR and noise suppression by having the preamplifier stage close to the sensor - the spikes seen with the previous design completely disappeared.

INVESTIGATING THE NOISE ORIGIN

To further distinguish the noise of the electronics from the noise of the sensor, we have utilized both magnetometer input

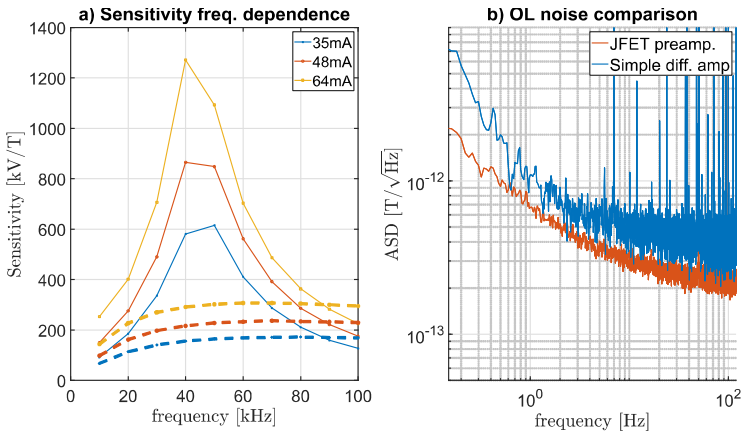

FIG. 3. a) Comparison of magnetometer sensitivity frequency dependence using simple diff-amp (dashed) and an improved JFET amplifier stage (solid). b) Magnetic noise spectrum density measured in a 6-layer Mu-metal shield.

channels and two sensors for correlation measurements. We have measured the cross-spectrum density using only one sensor connected to two independent inputs and acquisition channels in parallel. Later, we measured with two individual sensor heads, placed several centimeters apart, pointing to the same direction and again connected to independent inputs, but sharing common excitation current. The measurements shown in this chapter were done in a 6-layer Mu-metal shield, and the sensors were operated in open loop mode to eliminate the possibility of feedback compensation cross-talk.

Assuming no correlation in the amplifier stages of the input channels, the possible remaining origins of correlation are:

- Common excitation current noise.[8]
- Demodulators reference jitter correlation (reference is driven from single four-channel DDS IC).
- Shielding remanence noise (which is however in fT range[9]).
- Magnetic field noise (residual noise in the shielding due to finite shielding factor).
- Magnetic coupling of closely placed sensors.[10]
- Noisy feed-through signal (by capacitive and transformer coupling from excitation).

From the theory, the DIFF (noise density of time-domain difference of CH1 and CH2) values in Fig. 4 should either increase for uncorrelated noise signals CH1 and CH2 by a factor of $\sqrt{2}$, or for correlated signals it should drop down to the noise floor limit of the acquisition. Similarly, the CROSS (cross-spectrum density) value should drop for uncorrelated noise sources and should not change for correlated signals.

From the cross-spectrum measurement on a single sensor connected to two independent channels (Fig. 4a), we conclude that the observed noise is fully correlated (no change of CROSS density and DIFF density drops to 150 fT/$\sqrt{}$Hz floor).

The correlation measurement of two independent sensor heads placed side by side about 5 cm apart – see Fig. 4b – gives evidence that the measured noise limit is truly a property of the given sensors, as the noise at higher frequencies is not correlated (DIFF increases, CROSS drops). On the opposite, the noise in 1/f section below 1 Hz seems to be correlated, most likely because it is actually the Earth's magnetic field noise not sufficiently attenuated by the Mu-metal magnetic shielding. To use the two sensor heads as a gradiometer, also a proper astatization (sensors axes numerical alignment) would be necessary.

CLOSING THE LOOP

Feedback loop operation of a magnetometer is advantageous not only for increasing the measurement range but also for decreasing the effects of gain instability with time and temperature. In order to close the feedback loop, we added a V/I converter with ADA4004-1 to our sensor head electronic; the V/I converter is driven by a differential receiver-amplifier. In this manner, we could design the integrator (feedback I-controller) circuit as a part of the remote electronic box and still achieve large suppression of noise even with long cabling to the sensor head. Rather than using the pick-up coil also for the generation of the compensating field, we decided to add a separate feedback coil (1-layer, 500 turns) on top of the pick-up coil. Thus, we did not create any additional common-mode by asymmetrical loading the pick-up.

Ideally, our feedback range would be ± 50 μT in order to cover the Earth's magnetic field. When recalculated with the estimated feedback coil constant (about 108 μA/μT) and the supply voltage available (±2.5V), the feedback current sense resistor would be 500Ω maximum. We also used 1 kΩ and 4.7 kΩ, which however limited the feedback range to ±25 μT and ±4 μT, respectively, in order to show the effect of V/I opamp noise on the feedback noise-field generated in the compensating coil.

Fig. 5a depicts an open-loop measurement, whereas the feedback V/I converter input has been shorted, thus effectively only generating magnetic noise by the feedback coil. We can see that the noise increased with the 500R resistor when compared to the lower range with 4k7. Fig. 5b shows the closed-loop noise, i.e., with the complete feedback loop running. Also, in this case, the lowest noise is with the lowest range. The peaks are related to the power grid frequency

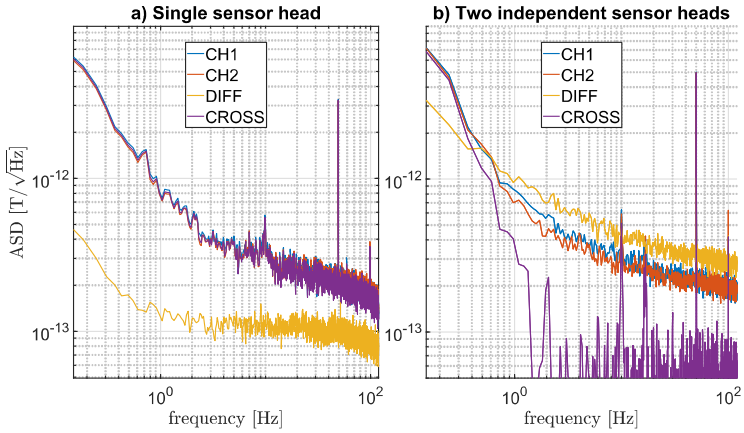

FIG. 4. Noise density of simultaneously measured independent input channels CH1 and CH2. DIFF is CH1-CH2 difference and CROSS is their cross-spectrum density. a) Correlation measurement of single sensor head connected to both input channels. b) Correlation measurement of independent sensor heads with common excitation.

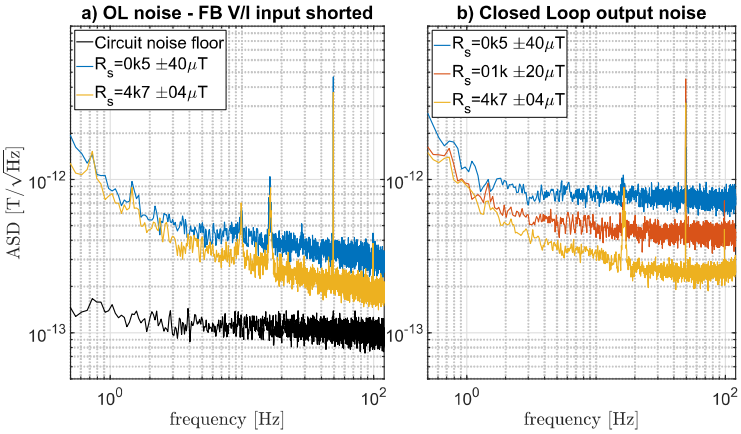

FIG. 5. Trade-off between achievable feedback range and output noise density. a) The effect of feedback V/I converter sense resistor selection on the open loop noise. b) The effect of resistor selection on closed-loop noise parameters.

50 Hz and its 1/3 subharmonic created by the powertrain of a nearby tramway line.

CONCLUSIONS

We have managed to further lower the white noise of a microwire based magnetometer below 0.3 pT/$\sqrt{}$Hz @ 8 Hz by optimizing the preamplifier stage and integrating the circuitry and sensor on one PCB board. So far, this is the lowest noise reported for a fluxgate magnetometer. By investigating cross-spectral measurements with multiple sensors/electronic channels, we have verified that the noise of 0.7 pT/$\sqrt{}$Hz @ 1 Hz is the sensor magnetic noise. Closed-loop operation was also optimized and it finally allowed for sub-pT measurements in compensated feedback loop even for full-field magnetometry.

ACKNOWLEDGMENTS

This work was supported by the Czech Science Foundation, Grant No. 20-19686S and CTU Student Grant Competition Grant No. SGS20/182/OHK3/3T/13.

DATA AVAILABILITY

The data that support the findings of this study are available from the corresponding author upon reasonable request.

REFERENCES

[1] I. Sasada, J. Appl. Phys. **91**, 7789 (2002).
[2] R. Bazinet, A. Jacas, G. A. B. Confalonieri, and M. Vazquez, IEEE Trans. Magn. **50**, 6500103 (2014).
[3] A. Plotkin, E. Paperno, and A. Samohin, J. Appl. Phys. **99**, 08B305 (2006).
[4] M. Butta and M. Janosek, AIP Advances **8**, 047203 (2018).
[5] M. Janosek, M. Butta, M. Dressler, E. Saunderson, D. Novotny, and C. Fourie, IEEE Trans. Inst. Meas. **69**, 2552 (2020).
[6] M. Janosek, M. Butta, M. Dressler, E. Saunderson, D. Novotny, C. Fourie *et al.*, "1 pT-noise fluxgate magnetometer design and its performance in geomagnetic measurements," in *2019 IEEE International Instrumentation and Measurement Technology Conference*, edited by IEEE (IEEE, NY, 2019).
[7] M. Butta and B. P. Schutte, IEEE Trans. Magn. **55**, 4002906 (2019).
[8] M. Butta, S. Yamashita, and I. Sasada, IEEE Trans. Magn. **47**, 3748 (2011).
[9] S.-K. Lee and M. V. Romalis, J. Appl. Phys. **103**, 084904 (2008).
[10] F. Han, S. Harada, and I. Sasada, IEEE Trans. Magn. **50**, 4100305 (2014).

AIP ADVANCES **8**, 047203 (2018)

Very low frequency noise reduction in orthogonal fluxgate

Mattia Butta[1,a] and Michal Janosek[1]
[1]*Department of Measurement, Faculty of Electrical Engineering, Czech Technical University in Prague, 16627 Prague, The Czech Republic*

(Received 4 July 2017; accepted 7 September 2017; published online 17 October 2017)

In this paper we present a simple, cheap and effective method to obtain reduction of very low frequency noise in an orthogonal fluxgate in fundamental mode. This method consists in the application of a layer of silicone over the magnetic core of the sensor filling the whole space inside the pick-up coil. In this way we avoid fast variations of temperature to affect the offset of the sensor (which is very sensitive to temperature changes). Eventually the offset will still drift to the same value, but it will do it slower, thus reducing the component of the noise in the sub-Hz region. Using this method we could simply reduce the noise at 100 mHz from 23 to 8 pT/$\sqrt{\text{Hz}}$, with no additional hardware on the excitation or signal conditioning circuits.
https://doi.org/10.1063/1.4994208

I. INTRODUCTION

One of the main problems of the orthogonal fluxgate in fundamental mode[1] is its large offset dependence on temperature.[2] This problem can be easily solved by periodical flipping the polarity of the excitation current.[3] This system however, while providing an excellent suppression of the offset drift (0.012 nT/°C)[4] requires an additional electronic circuit to erase the few periods of the signal after every flipping to avoid the noise introduced by the transient following the flipping. Moreover, it was found that the polarity flipping caused a slight deteriorating of sensor noise.

The offset dependence on the temperature does not involve only the offset itself. In normal working environments the temperature changes in time: while at high frequency such variations of temperature are negligible (due to thermal inertia), at sub-Hz frequency we can see the effect of the slow change of offset as a low-frequency component of the noise spectrum. In some cases we want to have the lowest possible noise a 100 mHz or lower frequency, e.g. when using the sensors for geophysical or biomedical measurements.[5] In this case we are effectively interested in reducing the variation of the offset at such low frequencies. In other words, we need a thermal low-pass filter, which suppresses the relatively fast variations of temperature (which cause variations of the offset) while we can tolerate a slight change of the overall dc offset.

For this purpose we propose an orthogonal fluxgate with the core embedded in a layer of silicone, which also fills the space in the pick-up coil.[6] The purpose of the silicone layer is to avoid that a fast change of temperature applied to the sensor will immediately change the temperature the core; the silicone introduces thermal inertia, which in turn introduces damping of the sensor low-frequency noise.

II. STRUCTURE OF THE SENSOR

We manufactured an orthogonal fluxgate sensor using Unitika AC-20 magnetic wires mounted on a FR-4 fiberglass 2-mm thick support. This magnetic core was then surrounded by Dow Corning

[a]Corresponding author: buttamat@fel.cvut.cz, mattia@butta.org

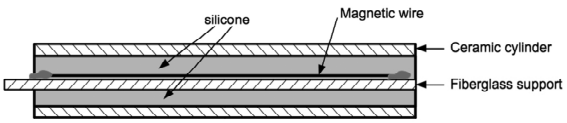

FIG. 1. Structure of the sensor.

® 744 silicone and then inserted in a ceramic cylinder with 5 mm internal diameter and 1 mm thick wall (Figure 1).

In order to avoid displacement of the magnetic wires during the insertion of the core in the ceramic cylinder, the silicone was added in two steps. First we added a small amount of material which was large enough to bond the magnetic wires to the fiberglass support but yet small enough to allow us to check that the wire was not bent. We left this first layer of silicone cure for 6 hours and then we applied another layer on both sides of the core (including the side with no magnetic wires mounted on) and we inserted it in the ceramic cylinder. Also, we applied silicone on the internal walls of the ceramic cylinder to assure that the whole cylinder was filled by silicone (without doing so some empty spots could be created). Finally we left the silicone cure for 24 hours.

A 1600 turns coil made of copper wire was wound on the ceramic coil to serve as the pick-up coil for the sensor.

III. EFFECT OF THE SILICONE ON MECHANICAL STRESS

The Co-rich alloy of the amorphous magnetic wires used for this sensor shows very low magnetostriction. Nevertheless introduction of mechanical stress to the magnetic core of a fluxgate sensor should always be avoided, as it could result in introduction of magnetic noise of the sensor.[7] This is particularly true when aiming for very low noise sensors, where any source of noise should be possibly avoided.

Therefore, we tested the effect silicone curing in order to verify if it could potentially introduce any mechanical stress to the magnetic core, especially considering that the core was inserted in a ceramic tube which serves as mechanical constrain for the deformation of the silicone. We inserted two 120 ohm metallic strain gauges (k=2) in the opposite terminations of the same kind of ceramic tube used for the sensors, and we connected them in a bridge powered by 10 Vdc (Figure 2). One of the two strain gauges was immersed in silicone while the second one was not. We logged the output voltage of the bridge for the following 18 hours while the silicone was curing, in order to see any strain developing on the strain gauge immersed in silicone (the strain gauge without silicone served as a reference, in order to compensate for common temperature effects). The output voltage moved from 3 mV (effect of non perfectly balanced bridge) up to 3.25 mV during curing, but then it decreased back to 3 mV. This shows that basically no mechanical stress will be introduced by the silicone to the magnetic core of the sensor (Figure 3).

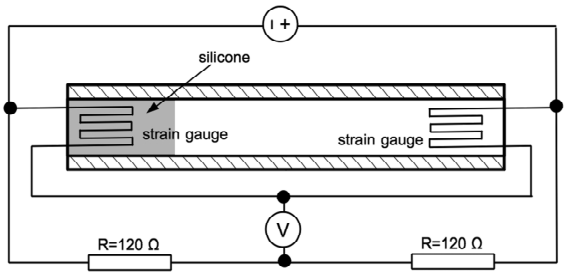

FIG. 2. Set-up for measurement of the mechanical stress introduced by the silicone.

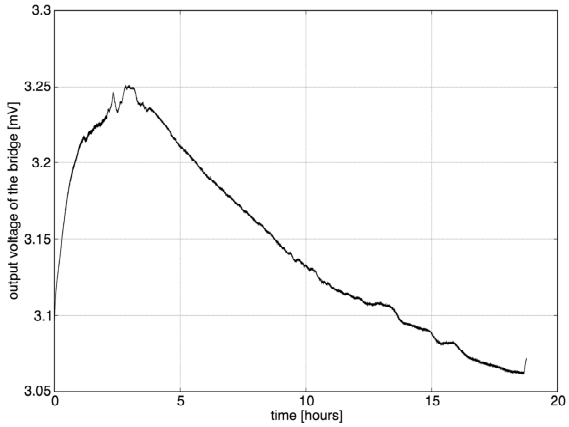

FIG. 3. Output voltage of the bridge of Fig. 2 during the curing of the silicone.

We also tested thermal expansion of the silicone using the same configuration as of Figure 2, inserting the system in a heated oven. First me measured the output of the bridge for temperature changing from 25 °C to 65 °C without silicone: in this way we could record how the output changes because of slight mismatch between the temperature coefficients of the two strain gauges resistances. The output voltage changed from 2.14 mV to 2.43 mV, corresponding to a 0.29 mV variation. Then, we recorded again the output voltage vs. temperature after curing of the silicone embedding one of the strain gauges: the temperature changed from 22 °C to 70 °C and we obtained a variation of about 0.34 mV, which is comparable to the value obtained without silicone.

This confirms that adding silicone to the magnetic core does not introduce any significant mechanical stress to the core, even if the temperature changes after curing.

IV. THERMAL EFFECT OF THE SILICONE LAYER

We also tested the thermal inertia introduced by the silicone layer by exposing to Pt100 sensors to 50 °C temperature step. One of the sensors was covered by 3 mm thick layer or silicone while the second was not. In Figure 4 we see how the output resistance of the sensor finally converges to the same value, but for the sensor covered by silicone this process is much slower due to the added thermal mass. In particular, the transient of the sensor without silicone has a 12 s time constant, while

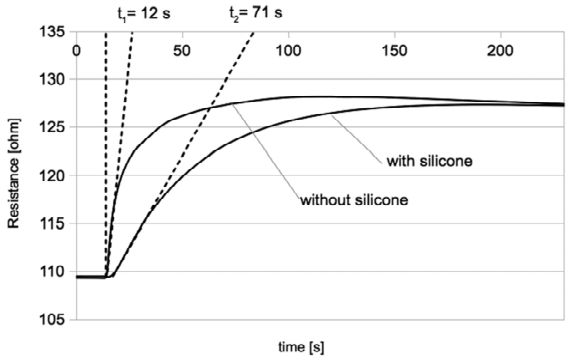

FIG. 4. Resistance of two Pt100 sensor exposed to a 50°C temperature range, with and without 3mm thick layer of silicone.

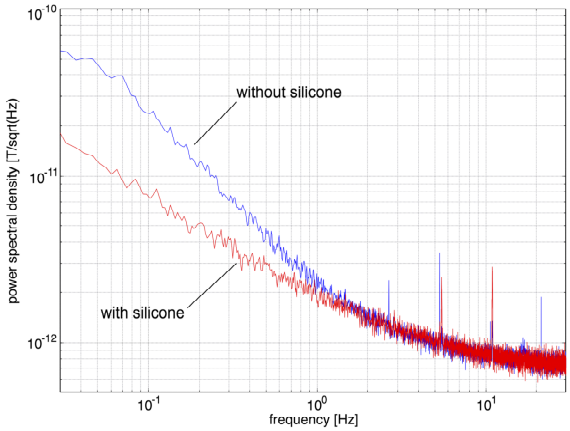

FIG. 5. Noise spectra of the sensor before and after the application of the silicone.

with silicone this value increases to 71 s. This time constant is expected to be large enough to be effective at sub-Hz frequency.

V. NOISE REDUCTION

Figure 5 shows the spectrum of an orthogonal fluxgate operated in fundamental mode with Idc=50 mA and Iac=40 mA at 100 kHz, before and after the application of the silicone to the magnetic core. The output voltage of the respective pick-up coil was demodulated by a SR865A lock-in amplifier. We clearly observe that the noise is basically the same for frequencies larger than 15 Hz. For lower frequencies, however, we clearly notice that the noise after the application of silicone is significantly lower. At 100 mHz the noise dropped from 23 pT·Hz$^{-1/2}$ to 8 pT·Hz$^{-1/2}$. Also at 1 Hz we notice a reduction of noise but not so pronounced.

This frequency range, where the noise was significantly reduced by the application of silicone, is considered to correspond to the frequency range where the noise is affected by variations of offset due to temperature ranges. For higher frequencies, this effect becomes negligible because the temperature cannot change at such speed. We should also note, that despite the ferromagnetic wire is a good thermal conductor, without any silicone or other thermal compound surrounding it, there will be a temperature inhomogeneity due to different heat transfer coefficients across its length (given by the surrounding objects, air movement etc). This is even more pronounced by the fact, that for this type of orthogonal fluxgate the current passes directly through the ferromagnetic wire and heats it mainly via resistive losses. Since the current is DC, also the Peltier effect should be theoretically considered, which could further cause a temperature gradient across the wire.

Interestingly we notice in Figure 5 that before the application of the silicone the noise spectrum had two slopes, a first slope between 1.2 Hz and 20 Hz and a more pronounced slope for frequencies lower than 12 Hz. However, after the application of the silicone, the noise spectrum shows only one slope - the same observed for higher frequency before application of silicone. This indicates that without silicone there were two distinct sources of noise, a magnetic one (due to Barkhausen noise) and a thermal one (due to the change of offset caused by temperature variations): the application of silicone effectively resulted in only the magnetic noise in the low frequency region.

VI. MAGNETOELASTIC COUPLING

A second possible explanation for the noise reduction shown in the previous paragraph could be however the magnetoelastic coupling between the silicone and the magnetic wires used as fluxgate

core. To exclude this effect, we performed two experiments to verify if there was any signif cant magneto-elastic coupling effect between the silicone and the core. First of all, if such effect were present we would see a signif cant change of the open-loop sensitivity. The silicone in fact would affect the mobility the magnetic domains on the outer shell of the wire resulting in sensitivity drop. However, we observed only a minor decrement of the sensitivity (within 2% and in some cases even lower than 1%). This minor change can be attributed to the different capacitance between the pick-up coil and the magnetic core because of the silicone which has a different dielectric permittivity than air, and is even on the border of measurement uncertainty.

The second experiment regarded the offset. As a matter of fact, the magneto-elastic effect would change the offset temperature coeff cient of the sensor (its thermal offset drift). In such case, the low-frequency noise reduction would simply be cause by the fact that the offset drift was lower after silicone application. On the contrary, if the cause were the effect previously described (the silicone acting as thermal inertia), the offset drift would be eventually the same (the offset would change slower due to slower temperature changes in the core but it would reach the same f nal level for steady-state core temperature).

In order to verify the theory as above, we exposed the coated and uncoated sensor to a step of temperature and we recorded the resulting offset change. We did so by inserting the sensor in a Dewar f ask put in a 4-layer magnetic shielding. We quickly f lled the glass jar with 200 ml of vegetal oil warmed up to 75 °C. The temperature therefore changed by 50 °C with the respect of 25 °C of room temperature. The sensor was protected in both cases by a latex bag to avoid direct contact of the oil with the sensor, which would drastically change the stray capacitance of the coil and therefore also the sensor output.

The offset drift obtained for such temperature step of 50 °C is shown in Figure 6. In order to facilitate the comparison of the curves we subtracted the value of the offset at room temperature, which was in any case very similar (87 nT without silicone vs. 169 nT with silicone). The 50 °C temperature step caused a very similar drift with of without silicone: 870 nT and 700 nT respectively.

This minor difference could be caused simply by the fact that in case of the core with silicone it takes longer to warm-up (this is also visible from the transient of the offset); during this time more heat is transferred from the oil to the jar and the air, thus, the also the f nal temperature of the oil is few degrees lower (unfortunately we could not control the temperature of the oil once in the shielding as we had no means to keep it at constant 75 °C without affecting the offset measurement).

This experiment however brings conf dence that the main effect, causing the noise reduction at low frequencies, is slowing down the thermal changes of the core as we have expected.

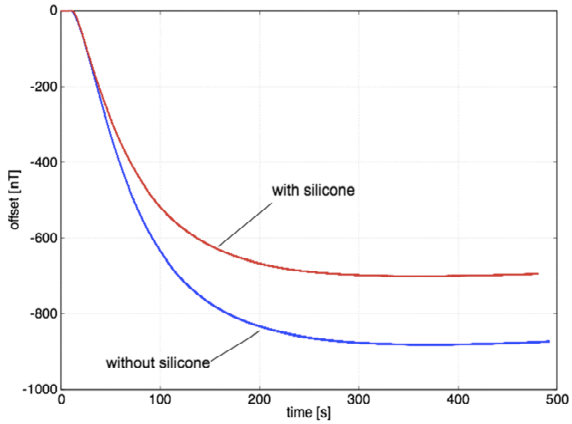

FIG. 6. Offset drift of the sensor when exposed to a temperature change from 25°C to 75°C with and without silicone (the offset at 25°C was substracted).

VII. CONCLUSIONS

In this paper we presented a method to reduce the low-frequency noise of an orthogonal fluxgate in fundamental mode, consisting of application of a layer of silicone to the magnetic core, which in turn reduces the speed of variation of its temperature and helps homogenizing it across the core length. This method is simple, cheap and requires no additional hardware for signal conditioning. Clearly, it cannot suppress the sensor offset drift which is basically unchanged, however it is effective in reducing the sub-Hz noise – we show an improvement of 100 mHz noise from 23 down to 8 $pT \cdot Hz^{-1/2}$.

ACKNOWLEDGMENTS

This work was funded by resources provided by the Czech Science Foundation (GA ČR) under Grant No. 16-10591Y, "Magnetic gradiometer based on fundamental mode orthogonal fluxgate". Fundamentals of the presented invention are subject of Patent Application No PV 2017-386 at the Czech Patent Office.

[1] I. Sasada, "Orthogonal fluxgate mechanism operated with dc biased excitation," J. Appl. Phys. **91**(10), 7789–7791 (2002).
[2] M. Butta *et al.*, "Temperature dependence of offset and sensitivity in orthogonal fluxgate operated in fundamental mode," IEEE Trans. Magn. **48**(11), (2012).
[3] I. Sasada, "Symmetric response obtained with an orthogonal fluxgate operating in fundamental mode," IEEE Trans. Magn. **38**(5 I), 3377–3379 (2002).
[4] M. Butta *et al.*, "Low offset drift–low noise orthogonal fluxgate with synchronized polarity flipping," IEEE Trans. Magn. **53**(4), (2017).
[5] H. Karo *et al.*, "Magnetocardiogram measured by fundamental mode orthogonal fluxgate array," J. Appl. Phys. **117**(17), 17B322 (2015).
[6] Patent Application No PV 2017-386 at the Czech Patent Office.
[7] M. Butta *et al.*, "Influence of magnetostriction of NiFe electroplated film on the noise of fluxgate," IEEE Trans. Magn. **50**(11), (2014).

Sensors & Actuators: A. Physical 342 (2022) 113583

Contents lists available at ScienceDirect

Sensors and Actuators: A. Physical

journal homepage: www.journals.elsevier.com/sensors-and-actuators-a-physical

Offset drift in orthogonal fluxgate and importance of closed-loop operation

M. Butta [a,*], M. Dressler [a], M. Janosek [a]

[a] Faculty of Electrical Engineering, Czech Technical University in Prague, Czech Republic

ARTICLE INFO

Keywords:
Fluxgate
Offset
Stability
Magnetometer
Amorphous microwires

ABSTRACT

In this paper we show an up-to-now unexplained source of offset drift affecting the fundamental mode orthogonal fluxgate. After a sudden change or removal of the magnetic field, we observe an offset transient which lasts units to hundreds of seconds. We exclude the thermal origin of such transient as well as the electric origin in the pick-up coil resonance circuit or sensing amplifiers. We prove that this transient has magnetic origin, since it depends on both the amplitude and the duration of the pulse of magnetic field applied to the sensor which can be expressed as magnetic energy. We conclude that operating the fundamental mode orthogonal fluxgate in a closed feedback-loop is useful by suppressing this transient behavior by keeping the core in a (almost) zero field, however when switching the magnetometer sensor on/off, this transient has to be taken into account.

1. Introduction

Orthogonal fluxgates in fundamental mode [1] have been shown since early 2000 s to provide very low-noise [2–5,6] vectorial measurements of quasi-static magnetic fields. Magnetometers based on annealed wire core [7,8] with precisely designed excitation and signal conditioning circuits have shown noise levels below $1\,pT/\sqrt{\mathrm{Hz}}$ at $1Hz$ and a noise floor which can reach $350\,fT/\sqrt{\mathrm{Hz}}$. Such low noise makes it possible to measure very weak magnetic fields, such as those generated by the human heart [9,10]. However, in all cases, these noise levels were achieved some time after the magnetometer started up, while its output has a first order transient until reaching a stable value. The same transient has been observed when the sensor is placed in magnetic shielding for noise measurements. This is not uncommon for fluxgate magnetometers, but it seems more pronounced for the orthogonal fluxgate. In this paper, we investigate the origin of such a transient, since it could lead us to a more detailed understanding of the mechanism underlying the performance of orthogonal fluxgate in fundamental mode. Moreover, since the effect is in the scale of seconds to a minute, it might give us more insight into the origin of the excess ultra-low-frequency noise of the orthogonal fluxgate in fundamental mode.

2. Excluding the thermal response of the amorphous wire

For our fluxgate, we have used Co-rich amorphous wire ($[Co_{94}Fe_6]_{72.5}Si_{12.5}B_{15}$) (CoFeSiB) with $120\mu m$ diameter. Our first reasonable assumption was based on the fact that the saturation magnetization M_S of this type of material depends on temperature. In an orthogonal fluxgate, the excitation current flows through the wire and could lead to a non-negligible increase in its temperature due to the Joule effect, leading to a drop in saturation magnetization M_S. If we consider the working principle of the orthogonal fluxgate in fundamental mode [11], we find that the voltage is proportional to the derivative of the projection of saturation magnetization M_S on the axis of the wire core; thus:

$$v_{out} = -N\cdot\frac{\partial\phi_Z}{\partial t} = -N\cdot\frac{\partial}{\partial t}S_w\mu_0 M_S sin\left(atan\left(\frac{H_Z}{H_{exc}}\right)\right). \quad (1)$$

where N is the number of turns of the pick-up coil, S_w is the axial cross-section of the wire at the active part of the wire core where the fluxgate mechanism occurs, M_S is the saturation magnetization, H_Z is the axial field, and H_{exc} is the circumferential field generated by the excitation current.

As the temperature changes, either because of the Joule effect of the wire's excitation current or because the sensor is moved to another location (e.g., shielding) with a different temperature, we can expect a change in the output of the magnetometer because of temperature-dependent M_S. To investigate this hypothesis, we must first analyze the dependence of M_S on temperature. To do so, we measured the amorphous wire's circumferential hysteresis loop at 1 kHz in an oven wherein the temperature was monitored by a Pt100 sensor. The hysteresis loop was obtained by averaging the loop for 20 s. The wire reached saturation state for a current as low as 40 mA. We measured the

* Corresponding author.
E-mail address: buttamat@fel.cvut.cz (M. Butta).

https://doi.org/10.1016/j.sna.2022.113583
Received 29 November 2021; Received in revised form 18 April 2022; Accepted 21 April 2022
Available online 21 May 2022
0924-4247/

hysteresis loop both while the temperature rose from 27°C to 62°C and while it fell, which took place over a much longer time period (about 6 h). This length of measurement is necessary to homogenize the temperature in the oven and minimize the temperature gradient between the Pt100 sensor and the amorphous wire. The temperature should also not significantly change while the hysteresis loop is averaged for 20 s; indeed, the fastest rate temperature of change was 0.08°C in 20 s, which was sufficiently low.

Fig. 1 shows the dependence of the saturation flux Φ_S (which is proportional to the saturation magnetization M_S by a geometrical factor) on the temperature for both the warming and the cooling process. We can observe a small hysteresis, probably due to the fact that the warming curve is faster.

In terms of the cooling curve, we obtained a rate of change of M_S of $-0.133\%/K$. The next step is to determine the temperature rise caused by the excitation current in the wire. To do so, we first characterized the dependence of the resistance of the wire R_{wire} on the temperature. This was done simultaneously with the measurement of the hysteresis loop, albeit indirectly. We used the value of the resistance that is necessary to suppress the resistive component of the voltage on the wire before integration to obtain the magnetic flux [12]. As the temperature rises, the value necessary to obtain a correct hysteresis loop also increases. Fig. 2 shows the dependence of R_{wire} on temperature: it is linear, as expected, and we estimate the rate of change to be $0.02\%/K$. Then we measured the actual effect, i.e., the dependence of the resistance on the current, by injecting a current into the wire and measuring its resistance. As expected, the dependance of R_{wire} on the current was parabolic (Fig. 3). Knowing the dependence of resistance on temperature from the previous experiment, we can estimate the mean temperature rise of the wire for the actual excitation parameters, and thus the change of saturation magnetization M_S. A typical excitation current for our fluxgates is $40mA$ AC added to $50mA$ DC, which results in just over $57mA$ RMS value (which should be considered for thermal effects). In the worst-case scenario, when turning the magnetometer on, we experienced a change of current from 0 to $57mA$ RMS, which, according to Fig. 2, brings a change of resistance of 0.0157%. Since R_{wire} has a rate of change of $0.02\%/K$, this means that the excitation current in the wire itself causes an increase in temperature of less than $0.8°C$. Such a change of temperature causes a change in the saturation magnetization of -0.1%. Such change is, however, two orders of magnitude lower than what we had observed in the transient of the magnetometer output (units and up to 10% of the offset). While the excitation current actually warmed up the wire, causing a drop in M_S, we derived that thermal effects were not the cause of such large transient.

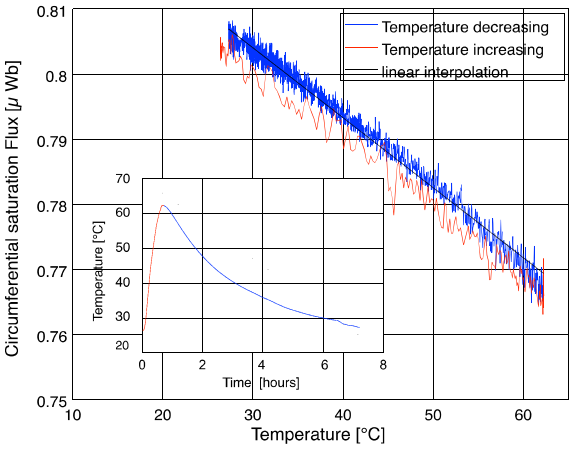

Fig. 1. Dependence of the circumferential saturation flux (proportional to M_S) on the temperature. In the inset: temperature vs. time during the measurement.

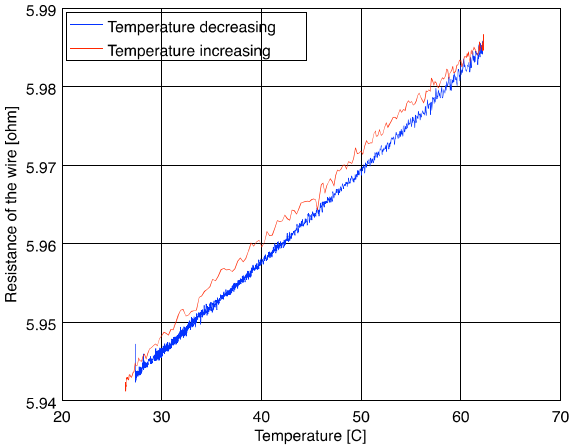

Fig. 2. Dependence of the amorphous magnetic wire resistance on the temperature.

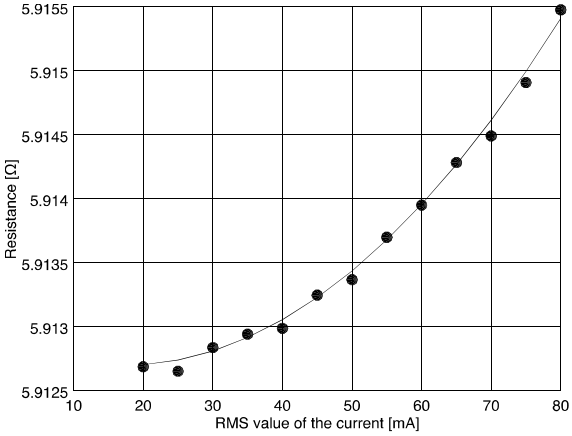

Fig. 3. Dependence of the amorphous magnetic wire resistance on the current.

3. The effect of exposure to large axial field

Having ruled out the thermal effects, we now investigate another possible cause of the transient on the magnetometer output, which may be the presence of a large magnetic field in the wire core of the fluxgate that can magnetize the inner section of the wire, which is not saturated by the excitation current [13]). To test this hypothesis, we performed two experiments. First, we exposed the sensor to a geomagnetic field of approximately $+20\mu$T. We turned the (open-loop) magnetometer on and allowed it to stabilize for about 50 min. Then we moved the sensor to a four-layer shielding, and the output voltage of the magnetometer showed a very slow transient that appeared to stabilize at a voltage of 0.2 V (corresponding to 183 nT). Then we extracted the sensor from the shielding and exposed it again to the geomagnetic field for just 4 min, albeit this time in the opposite direction, namely to -20μT. After inserting the sensor into the shielding again, we noticed that the transient, aiming once more at 0.2 V, was now reversed (Fig. 4). Not only that, but the transient appeared faster. This indicates that the transient had a magnetic origin depending on the value of the magnetic field that was applied to the magnetic wire and on the duration of that exposure.

The second experiment was performed to confirm any residual thermal effects on the transient. Previously, we had found from the dependence of M_S on temperature that the thermal effect should be

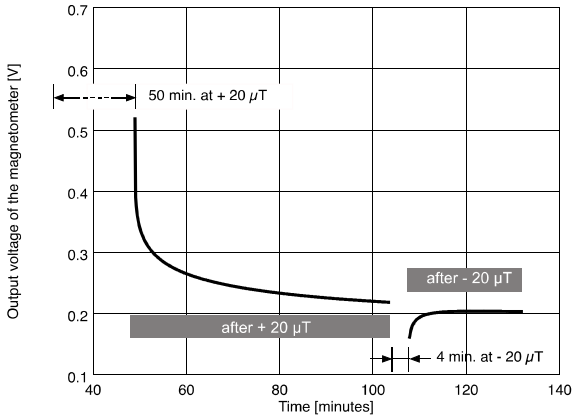

Fig. 4. Transient of the output voltage magnetometer when the sensor is in the shielding after exposing the sensor to $+20\mu$T (in the sensitive direction) for 50 min, and after exposing it to -20μT for 4 min.

negligible. We inserted the fluxgate sensor into the shielding and allowed it to stabilize until the transient was almost exhausted. Then we preheated a block of copper and inserted it into the shielding in the proximity of the sensor to increase its temperature. The temperature was monitored by measuring the voltage on a diode located in close proximity to the wire core and fed by an approximately $10\mu A$ current source (the magnetic field due to such a small current was negligible). In Fig. 5, we can see the results of this experiment. The temperature, which is almost stabilized at $24.7^{\circ}C$, rises to over $27^{\circ}C$ due to the heat provided by the block of copper, and from the time scale, we can reasonably assume that the temperature of the wire core has settled to the same value. However, the output voltage of the magnetometer does not appear to be affected by the temperature, and it continues its initial magnetic transient induced trend. This confirms that the origin of the transient has to be found in the magnetic field applied to the sensor and not in the effect of the saturation magnetization temperature of the fluxgate's amorphous wire core [14].

This magnetic phenomenon can also explain the transient we observed when the magnetometer was turned on. Also, in that case, the magnetic field applied to the wire core changed. When no excitation current is present in the wire, its whole cross-section is exposed to the axial field. However, once the magnetometer is switched on, the circumferential field generated by the excitation current will reorient

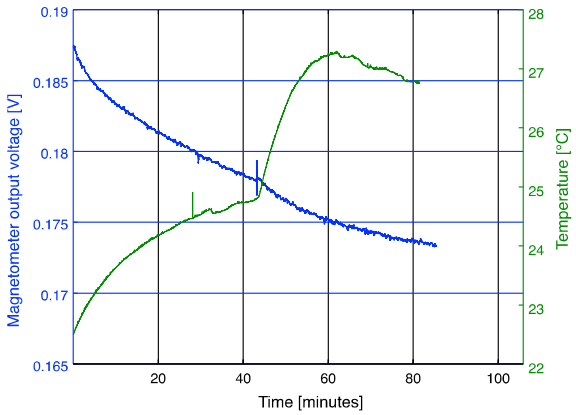

Fig. 5. Output voltage of the magnetometer after the sensor was placed in the shielding. At time= 42 min the temperature is increased by inserting a block of pre-heated copper in the proximity of the sensor.

the magnetic domains to this direction, although this does not happen instantly. This change in amplitude and direction of the magnetic field can cause a similar transient in the output of the magnetometer.

4. Dependence of the settling time on axial field amplitude and duration

In the previous section, we showed that the origin of the reported transient is in fact magnetic and not thermal, as originally supposed. To understand this phenomenon better, we study this effect by exposing the sensor to different magnetic field pulses of well-defined amplitude and duration. To do so, we placed the sensor inside the shielding and created an artificial axial field B_{ax} in the axial direction of the sensor using an additional coil coaxial with the sense winding (Fig. 6). With a current source, we can control both the amplitude and duration of the applied field B_{ax}.

We again needed to exclude the auxiliary coil that produces B_{ax} from creating sufficient heat to affect the sensor thermally. Therefore, we initially used a large Helmholtz coil (600 mm diameter) far enough to exclude any possible heating of the sensor, and we measured the transient of the output after exposing the sensor to B_{ax}. After that, the experiment was repeated by creating B_{ax} using a coil wound directly on the sensor, and the transient was identical. From this, we can derive that the transient was not affected by any possible heat generated by the auxiliary coil producing B_{ax}. Another possible source of artifact arises from the magnetization of the shielding where the experiment is performed. In that case, we would rather observe the effect of changing the shielding remanence. To rule out this possible source of error, we repeated the experiment outside the shielding while exposing the sensor in an east-west direction to minimize the geomagnetic field applied to it. Once we moved the sensor back to the shielding, we obtained the same transient, proving that the source of the transient was not the magnetization of the shielding. Yet another possible problem could arise from the fact that the sensor is exposed to a field larger than the maximum field measurable by the magnetometer (in open-loop operation, our range is approximately $1\mu T$). This could lead to saturation of the input stage of the electronics, causing a transient of the magnetometer output due to the protection diodes' recovery time (which would then have electric and not magnetic origin). Therefore, during our experiments we added a switch that would automatically short the input of the

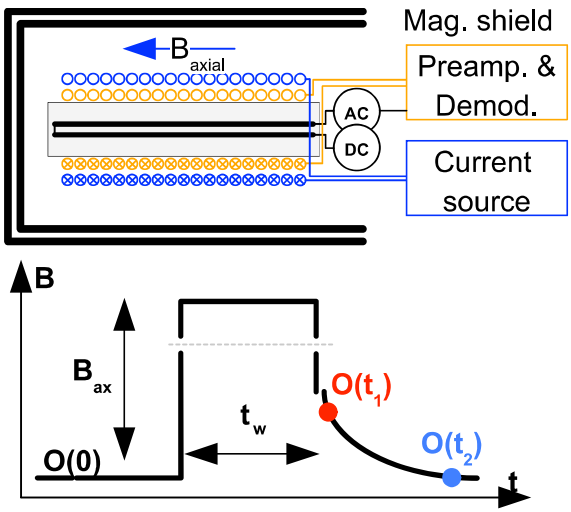

Fig. 6. Set-up for the measurement of the settling time (not to scale). The field B_{ax} was applied for the time t_w, and the two points O(t1) and O(t2) were later used to describe the transient.

preamplifier when a large field is applied to the sensor.

5. Study of the transient behavior- duration and amplitude of the field pulse

The sensor was tuned at the resonance frequency with an additional capacitor so that we achieved about 1 MV/T sensitivity in the open-loop magnetometer operation. We measured the transient of the magnetometer output after applying $B_{ax} = 8\mu T$ and $-8\mu T$ for $t_w = 1$, 2, 3, and 4 s. The results are shown in Fig. 7 for both positive and negative fields, from which we have removed the offset value once it stabilized (around 40 nT for positive pulses and $-100nT$ for negative pulses), to highlight the transient. We must point out that after applying a pulse of $\pm 8\mu T$, the offset always returned to the same value ($40nT$ or $-100nT$, depending on the polarity) regardless the duration of the pulse. First, we observed that in the case of a negative field, the transient was reversed, once again confirming the magnetic origin of this phenomenon (any temperature effect would yield the same change). Next, we measured once again the transient after exposure of the sensor to $B_{ax} = 8\mu T$, albeit after adding a 330 Ω damping resistor connected in parallel to the pick-up coil. The purpose of this resistor was to change the quality factor of the resonance circuit to see if this had any effect of the transient. In Fig. 8, we can see that the transient is not affected by the damping resistor, showing that the transient is not even in the relaxation of the tuned circuit.

In Fig. 7, we have plotted not only the transient of the output of the magnetometer for different pulse durations but also the slope vs. time. From a physical point of view, we are interested in the time necessary for the offset to reach a stable condition, and this can be identified as a the time when the derivative of the offset becomes lower than a certain threshold. Since an offset drift corresponds to a low-frequency noise, a different threshold of the derivative of the offset can be chosen as a parameter to define the offset as "stable" when interested in the noise at a different frequency. As we can see in Fig. 7, the longer the time of exposure of the sensor to the $B_{ax} = 8\mu T$ field, the longer the settling time, which is defined as the time required to reach a value below a specific threshold. This leads us to study the dependence of the settling time on both the amplitude of B_{ax} and its duration. Specifically, we defined as the settling time the time necessary for the offset transient to reach a derivative in time less than 0.1 nT/s after exposure to B_{ax}. We tested fields from $1\mu T$ to $30\mu T$ and duration times of the pulses t_w from 0.1 to 10 s. We observed that the settling time depends on both amplitude and duration of B_{ax}. These results are summarized in Fig. 9, where we can observe the dependence of the settling time on the duration of B_{ax} with the amplitude of the pulse as a parameter.

To better understand this phenomenon, we plotted the values of

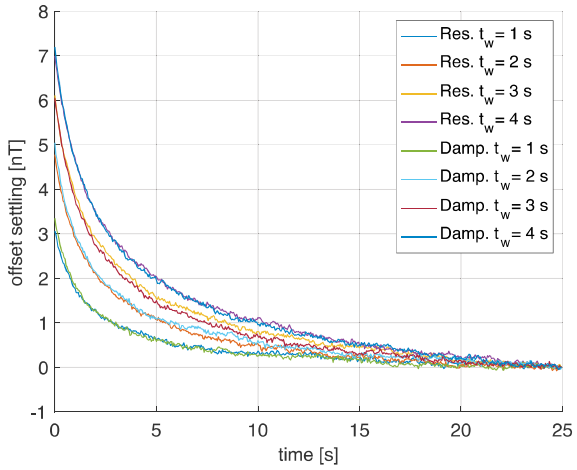

Fig. 8. Offset drift after the application of $B_{ax} = 8\mu T$ for 1, 2, 3 and 4 s without (Res.) and with (Damp.) a 330 Ω damping resistance parallel to the pick-up coil to artificially modify the resonance circuit (the transients have been normalized by removing the final DC offset from each trend.).

settling time as a function on a quantity calculated as $\sqrt{t_w \cdot B_{ax}}$, which can be regarded as "magnetic energy". Interestingly, we observed a linear behavior that was consistent for t_w up to 1 s (Fig. 10). This means that for a short time exposure to the axial field, the settling time depends only on the product of t_w and B_{ax}, regardless of the respective amplitude of the factors. This phenomenon deviated, however, especially for t_w of 5 and 10 s. The possible reason for this is that the settling time had not yet been reached, since the energy in this case was high.

6. Towards the origin of the phenomenon

Although we have proved that the origin of the transient is magnetic, the actual mechanism that gives rise to such a transient after the removal of an axial field it is still open to question. A similar process of reversal magnetization in amorphous microwires has been studied by Vazquez on iron-rich wires [15]. The effect described in that paper also applies to CoFeSiB wires, such as the one used in this study, under specific circumstances, such as thermal treatment or the application of tensile stress. In our case, the wire had a natural curvature from the manufacturing process that was made straight and soldered to the sensor head holder. The residual stress therefore provided a tensile component

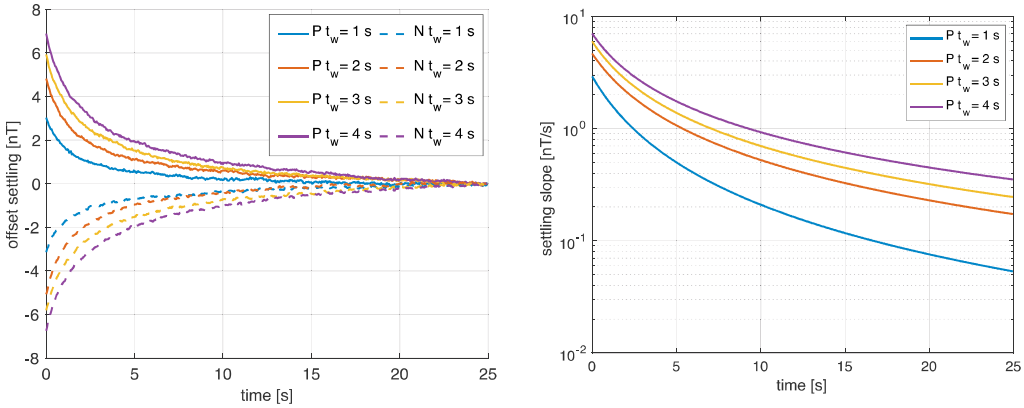

Fig. 7. Left: Offset drift after the application of $B_{ax} = 8\mu T$ (P) and $-8\mu T$ (N) for 1, 2, 3 and 4 s (the transients have been normalized by removing the final DC offset from each trend). Right: amplitude of the derivative of the offset transients vs. time (for simplicity only for the negative pulses and with filtering).

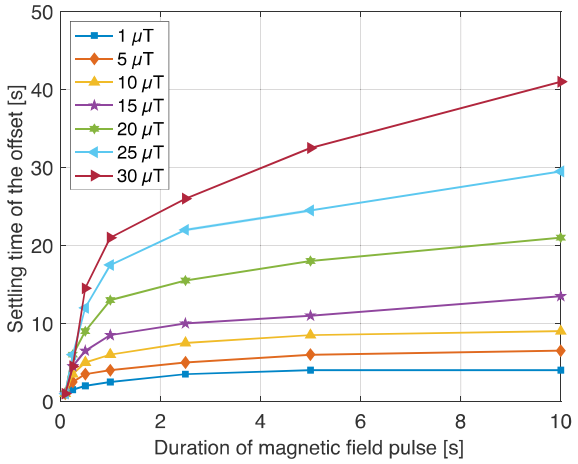

Fig. 9. Settling time of the offset after removal of B_{ax} as a function of the duration t_w of the B_{ax} for different values of the field.

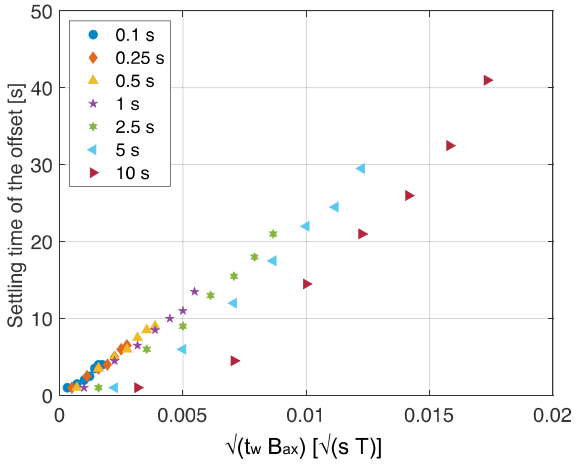

Fig. 10. Settling time of the offset after removal of B_{ax} as a function of $\sqrt{t_w \cdot B_{ax}}$ for different duration of t_w [s].

to the wire. The application of tensile stress gives rise to a variable switching field of the magnetization that depends both on the stress and length of the wire (due to the demagnetization factor). Vazquez then modeled the total energy of the wire, taking into account the Zeeman, reversed domain walls, and stray field energy. Then it was shown that, after removal of the applied field, some closure domains appeared at the ends of the wire to minimize the energy, and they progressively collapsed along the length of the wire. This effect may sound similar to what we had observed; however, there was a substantial difference, namely that the velocity of propagation was too large (hundreds of m/s) to explain our reported phenomenon. A probable cause in our case may lie in the fact that ferromagnetic wire can actually be regarded as having two different regions. During the operational mode, the wire core is not only exposed to the axial field B_{ax} but also to the circumferential excitation field generated by the excitation current. The wire's outer shell is thus saturated in a circumferential direction, and only the inner part of the wire, which is progressively less saturated as we approach the wire center, is magnetized in an axial direction. There is no clear-cut separation between these two regions of the wire, since the circumferential field monotonically increases as the radius increases. We can at this point speculate that there may be a transitional region between the inner core and the outer shell, where the domains slowly reverse and reorient to minimize the energy after removing the magnetic field from the wire, giving rise to the observed transient. As a preliminary test to verify this hypothesis, we again measured the transient of the output after applying $10\mu T$ for 1 s, but we changed the excitation current. We performed three experiments, each using 33 mA as the AC component of the excitation current, while the DC component used 34, 50, and 72 mA. The purpose of increasing the DC component of the current was to increase the portion of the wire that was saturated (the depth of the shell), and therefore we should change the volume of the transition region where this phenomenon could occur. Fig. 11 shows that to some extent the transient is indeed faster when the DC component of the excitation current is increased, but our results are not conclusive. More detailed investigation is clearly needed to fully understand this phenomenon.

7. The importance of a compensating feedback-loop operation

Operating a fluxgate in a closed-loop feedback is a common method used to improve the linearity of a sensor, mainly to extend its linear range when open-loop sensitivity is very high. This study shows that in the case of an orthogonal fluxgate in fundamental mode, it is important to operate the sensor in the closed loop also to minimize the reported effect. As we have already seen, even a small variation in magnetic field (e.g., quickly rotating the sensor on the horizontal plane of the Earth's field) does affect the output of magnetometers by creating decaying transients from one field value to another. This causes a delay in the response of the sensor, which might not be acceptable in some applications. If we operate the sensor in feedback mode, however, the wire core is always exposed to the same value of the magnetic field (ideally zero), even if the measured field changes. Thus, the core of the fluxgate should not experience any transient.

To verify that this problem is solved by operating the sensor in feedback mode, we performed the following experiments, and their results are shown in Fig. 12. First, we exposed a sensor to 20 μT for 120 s on its axial direction while operated in open loop and then removed the axial field and observed a typical transient of the output of the magnetometer. Next, we repeated the same experiment while operating the sensor in feedback mode by choosing the closed-loop option of the magnetometer. The compensating field was created by a 500 turn, single-layer coil wound directly over the pick-up coil. A layer of Kapton tape was used between the pick-up coil and compensating coil. The total length of the compensating coil was 80 mm. In this case, the magnetic core of the fluxgate was constantly exposed to zero field, since the sensor

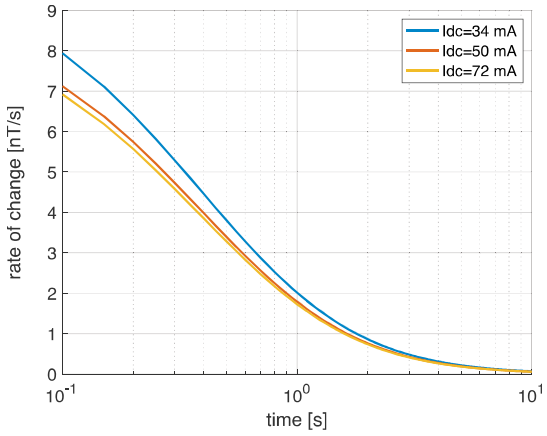

Fig. 11. Settling of the offset vs. time for I_{ac} = 33 mA and different values of dc current after exposing the wire to 10 μT for 1 s.

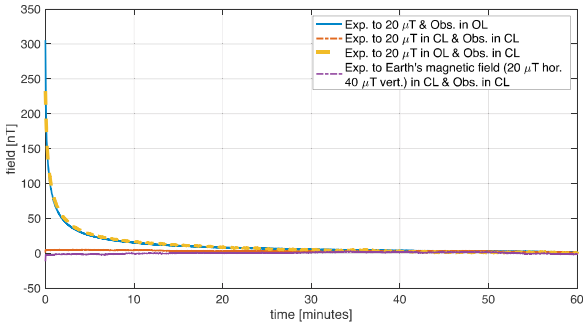

Fig. 12. Offset transient of the magnetometer observed after exposing it to 20 μT for 120 s in open-loop [OL] (blue curve), in closed-loop [CL] (orange curve), in open-loop while applying the magnetic field and then in closed-loop after removing it (yellow curve). The purple curves shows the output of the magnetometer operated in close-loop after exposing it to the Earth magnetic field.

was being operated in closed loop. We exposed the sensor again to 20 μT for 120 s and observed the output of the magnetometer after the removal of the axial field. In this case, the transient of the output disappeared. This shows that operating the sensor in feedback mode does indeed suppress this phenomenon.

To provide additional evidence of the role of the feedback in suppressing the transient of the output, we performed the following experiment. We exposed the sensor one more time to 20 μT for 120 s while operating in open-loop. Then we removed this field and simultaneously switched the magnetometer to closed-loop. In this case, we again observed the typical large offset transient. This confirmed that the transient of the offset had been caused by the fact that the field was exposed to an axial field when left in open-loop, and the feedback could no longer compensate for the problem once the offset had been generated because the closed-loop would simply follow the offset transient. With this experiment, we show that the feedback mode, when constantly applied, suppresses the offset transient because it nulls the magnetic field applied to the sensor when the axial field is 20 μT.

We then performed a final experiment whereby we operated the sensor in closed-loop and exposed it to the Earth's magnetic field (with a horizontal component of 20 μT and a vertical component of 40 μT). Then we inserted the sensor in shielding, still keeping the magnetometer in closed-loop. Again, in this case, we did not observe a large transient of the offset. This result indicates that it is enough to compensate for the magnetic field in the axial direction to suppress the problem of the large offset transient, and it is not necessary to have a three-axial feedback system.

This experiment proves the importance of using the feedback mode operated magnetometer with this type of orthogonal fluxgate, even if no improvement in linearity is required.

8. Conclusions

In this paper we have proved that the offset drift in an orthogonal fluxgate operated in fundamental mode when the magnetometer is turned on is not due to change of temperature as initially assumed but, on the contrary, it has magnetic origin. We have proven it by showing that the current flowing in the wire does not increase the temperature of the wire enough to cause a change of offset due to temperature. We have also excluded external sources of temperature change (for instance when moving the sensor to the shielding) since they don't change the transient of the offset. On the contrary, we have shown that the transient of the offset is caused by the magnetic field applied in axial direction, most probably because the inner part of the magnetic wire is not saturated by the excitation current and it the external axial field can magnetize it. Finally we have shown that this problem is solved by operating the sensor in feedback mode, since the total magnetic field applied to the core of the sensor in axial direction is kept at zero and the core of the wire has no opportunity to be magnetized in axial direction.

Declaration of Competing Interest

The authors declare that they have no known competing financial interests or personal relationships that could have appeared to influence the work reported in this paper.

Acknowledgments

This work has been supported by the Grant Agency of the Czech Republic under the standard grant n. 20–19686S, "To the origin of the fluxgate noise".

References

[1] I. Sasada, Orthogonal fluxgate mechanism operated with dc biased excitation, J. Appl. Phys. 91 (2002) 7789–7791.
[2] M. Dressler, M. Janosek, M. Butta, Reduction of magnetic noise limits of orthogonal fluxgate sensor, AIP Adv. 11 (2021).
[3] M. Tibu, S. Corodeanu, C. Hlenschi, H. Chiriac, N. Lupu, New aspects on the performance of a fundamental mode orthogonal fluxgate magnetometer based on amorphous wire cores, AIP Adv. 11 (2021).
[4] Z. Yuan, Y. Zhang, D. Wang, Y. Jiang, R. Guo, Research on the orthogonal fundamental mode fluxgate sensor circuit, IEEE Access 8 (2020) 150665–150671.
[5] H. Jiang, J. Zhang, Z. Xu, Y. Xu, K. Chen, G. Li, P. Zeng, T. Qu, Modeling and performances of the orthogonal fluxgate sensor operated in fundamental mode, IEEE Trans. Magn. 56 (2020).
[6] I. Sasada, Low-noise fundamental-mode orthogonal fluxgate magnetometer built with an amorphous ribbon core, IEEE Trans. Magn. 54 (2018).
[7] M. Butta, B. Schutte, Low-noise orthogonal fluxgate using flipped current joule annealing, IEEE Trans. Magn. 55 (2019).
[8] N. Murata, R. Nomura, A. Matsuoka, Current annealing of amorphous wire core for performance improvement of fundamental mode orthogonal fluxgate, J. Mag. Mag. Mater. 484 (2019) 497–503.
[9] M. Janosek, M. Butta, M. Dressler, E. Saunderson, D. Novotny, C. Fourie, 1-pt noise fluxgate magnetometer for geomagnetic measurements and unshielded magnetocardiography, IEEE Trans. Instrum. Measur. 69 (2020) 2552–2560.
[10] H. Karo, I. Sasada, Magnetocardiogram measured by fundamental mode orthogonal fluxgate array, J. Appl. Phys. 117 (2015).
[11] I., Coroli, Excitation unit for orthogonal fluxgate with dc bias flipping, Master's thesis, Czech Technical University in Prague, 2016.
[12] P. Ripka, M. Butta, M. Malatek, S. Atalay, F. Atalay, Characterisation of magnetic wires for fluxgate cores, Sens. Actuat., A: Phys. 145–146 (2008) 23–28.
[13] M. Butta, P. Ripka, G. Infante, G. Badini-Confalonieri, M. Vazquez, Bi-metallic magnetic wire with insulating layer as core for orthogonal fluxgate, IEEE Trans. Magn. 45 (2009) 4443–4446.
[14] A. Plotkin, E. Paperno, A. Samohin, I. Sasada, Compensation of the thermal drift in the sensitivity of fundamental-mode orthogonal fluxgates, J. Appl. Phys. 99 (2006).
[15] M. Vazquez, D.-X. Chen, The magnetization reversal process in amorphous wires, IEEE Trans. Magn. 31 (1995) 1229–1238.

Mattia Butta was born in Lecco (Lombardy) in 1980. He received a MSc. in Electrical Engineering from Politecnico di Milano in 2005 and a Ph.D. degree from Czech Tecnical University in Prague in 2010. From 2010 and 2012 he was JSPS fellow at Kyushu University. From 2012 he his a researcher at the Magnetic laboratory of department of measurement at FEE-CTU in Prague. From 2017 he is an associate professor at the same faculty.

Michal Janošek, born in Varnsdorf in 1980, graduated from the Faculty of Electrical Engineering, Czech Technical University in Prague in 2007 at the Dept. of Measurement. He finished his PhD under the supervision in 2014 in the field of magnetic gradiometers and since 2015 he is Assistant professor at the same department. His main research activity is the application of magnetic sensors (mainly fluxgate) in magnetometers and gradiometers for detection of low amplitude magnetic fields in the scope of geophysics and magnetic metrology. During 2019 and 2020, he was a postdoc research fellow at the Stellenbosch University and SANSA Space Science, South Africa, where he became also involved in geomagnetic applications of HTS SQUID sensors. He is an author or co-author of 40 + journal publications, the first from 2007 mentioning miniaturised fluxgate sensors. Url: https://meas.fel.cvut.cz/janosek

Michal Dressler graduated at the Faculty of Electrical Engineering of the Czech Technical University in Prague where he is currently a Ph.D. student. His main research field is low-noise magnetometers.

2.2 Accuracy: calibration methods

2.2.1 Suppression of anthropogenous noise effects

The existing calibration methods of magnetometers in the presence of anthropogenous noise mostly rely on two principles. One is to reduce the field disturbances in a coil system by utilizing a compensating magnetometer in a large distance [3]; this does not work well in the case of gradient, man-made noise. Another solution is placing a reference sensor inside of the feedback-operated coil system, slightly off-centre to allow for device-under-test (DUT) placement [23]. However, these approaches are not feasible for every DUT: a magnetometer can produce substantial stray fields (e.g. by large feedback coils), influencing the reference sensor. Another example is the calibration of coil-based magnetic flux density standards with a field-subtraction method [10]. The author has researched two alternative possibilities of suppressing the effect of man-made disturbances − [J7] and [J17].

The first option is utilizing a closely (units of meters) co-located vectorial magnetometer, whose alignment with the respect to the coil system is established numerically using actual field disturbances. The software of the coil system keeps track of the baseline value of the vector which is measured by the reference magnetometer and “locked-in” at the beginning, and is subsequently updated before and after each measurement point. During the acquisition of the DUT response at one measurement point, the field disturbances are actively compensated – see *Magnetic Calibration System With Interference Compensation* [J7].

The second option was numerical: we did not employ any field compensation, we used a co-located Overhauser magnetometer and a specific calibration method [45], which allowed for compensation of noise and field drift without the need for a vectorial magnetometer, which would have to be aligned to the coil system. The article *Precise calibration method for triaxial magnetometers not requiring Earth's field compensation* [J17] is an extended version of the proceedings article [P12].

[J7] *Magnetic Calibration System With Interference Compensation (2019).* **Author contribution:** 50%. Principle proposal, methodology, defining and overseeing experiments, article composition. **Citations:** 2

[J17] *Precise calibration method for triaxial magnetometers not requiring Earth's field compensation (2015).* **Author contribution:** 25%. Experiment and methodology oversight, data review, interpretation. **Citations:** 49

Magnetic Calibration System With Interference Compensation

Michal Janosek, Michal Dressler, Vojtech Petrucha, and Andrey Chirtsov

Faculty of Electrical Engineering, Czech Technical University in Prague, 16000 Prague, Czech Republic

This paper describes a novel method for calibrating dc-precise magnetometers in the low field range (±100 μT), which gives acceptable results even in laboratory conditions with significant magnetic interference. By introducing a closely mounted reference magnetometer and a specific calibration procedure, it is possible to compensate for the external magnetic field disturbances caused, e.g., by the local transportation operated with dc power supplies. The field compensation occurs only shortly after the calibrating coils are energized. In this case, the leakage of the coil's magnetic flux to the reference sensor due to the cancelation of the time-varying compensating field was negligible. When using 60 cm coils and reference sensor in 2.5 m distance, we were able to calculate magnetometer gains with a standard deviation of 91 ppm. We show that an overall uncertainty of 0.1% can be achieved.

Index Terms—**Calibration, coil system, interference, magnetometer.**

I. Introduction

PRECISE calibrations of Earth's field range (±100 μT) magnetic field sensors (or magnetometers) are challenging not only due to the Earth's field variations but also by anthropogenic noise, caused, e.g., by traffic or nearby uncompensated direct currents. In the literature, three basic calibrating methods are described.

The first method is the so-called "scalar calibration," where the triaxial magnetometer is rotated in (preferably all) spherical directions in a highly homogeneous and stable Earth's magnetic field [1]. For this purpose, it is often required to travel far away from the city to a place with the lowest possible magnetic field gradient. The advantage is that only a precise knowledge of the field amplitude is required–this is provided, e.g., by an Overhauser scalar magnetometer. Another disadvantage is that the calibration sensor frame is arbitrary. This method is also not much suitable for sensors with high cross-field error [2], [3].

The second possibility is using a precisely calibrated coil system and a stable, calibrated current source. If the sensor is small, magnetic field gradient can be tolerated. Usually, the "exciting" field is being alternated in every direction, and its magnitude is changed to check for linearity and range errors. If the coil system is calibrated, a reference frame can be provided with respect to the device-under-test (DUT) casing. This technique can be also used for uniaxial sensors and can provide a traceable calibration with the uncertainty derivation.

The third calibration method is a mixture of both the scalar and vector one: the so-called "thin-shell" method utilizes a fixed sensor head in the triaxial coil system, but the field is artificially rotated and its scalar magnitude is calculated [4]. From a large set of equations, all parameters can be established, as in the scalar method. The main benefit is a fixed sensor and, thus, tolerance to field inhomogeneity.

Manuscript received July 15, 2018; revised September 7, 2018 and September 25, 2018; accepted September 25, 2018. Date of publication October 25, 2018; date of current version December 18, 2018. Corresponding author: M. Janosek (e-mail: janosem@fel.cvut.cz).

Color versions of one or more of the figures in this paper are available online at http://ieeexplore.ieee.org.

Digital Object Identifier 10.1109/TMAG.2018.2874169

A usual way of disturbance canceling with coil systems is to place a reference fluxgate magnetometer very far from the coil facility–tens to hundreds of meters, in order not to be influenced by the mutual crosstalk [5], [6]. It is also possible to monitor the ambient field changes with a distant Overhauser magnetometer [7] without the active cancelation; however, any gradient in the disturbance will deteriorate the results.

The disturbances can be also suppressed if the coil system is running in a closed loop. The closed-loop systems utilize a precise magnetic field sensor, which governs the system precision [8]–[12]. The feedback loop systems, in general, suffer from possible mutual influence between the DUT and the feedback sensor (both can generate disturbing magnetic fields), so off-center placement and gradient estimation are necessary.

In this contribution, we focused on a low-cost calibrating system with 0.6 m triaxial coils, which is usable for the direct vectorial or thin-shell calibration procedure and allows for the calibration of sensors and magnetometers which could otherwise disturb, or could be disturbed, by any intra-coil closed-loop sensor. The setup was running in a laboratory heavily influenced by neighboring dc-traction traffic and other sources of anthropogenic noise. The sensor used for disturbance cancelation was placed just 2.5 m away from the coil system given by our laboratory constraints.

II. Coil-System Calibration

A. Available Methods

The most accurate calibrations can be provided by a scalar calibration of the coil system [13], [14] which can provide also its non-orthogonalities. Another option is using nuclear magnetic resonance (NMR), mainly with flowing water [15], [16] which allows for very small measurement volume of the pickup coil. A disadvantage of calibration with scalar sensor lies in the required coil-system size—its inhomogeneity across the sensor volume is another source of uncertainty for large scalar sensor volume.

Another option is to use a magnetic flux density standard based on a solenoid precisely wound on a quartz support [17]; in this case, the achievable accuracy is about 60 ppm.

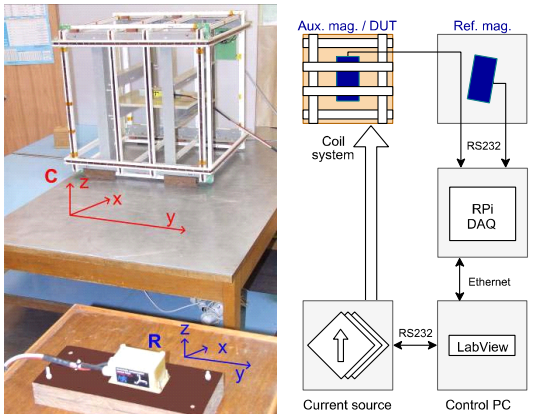

Fig. 1. Coils are wound on fiberglass supports to achieve high temporal and thermal stability. The Merritt quaternion is located in the y-direction (E–W) (left). Block diagram of the calibration system (right).

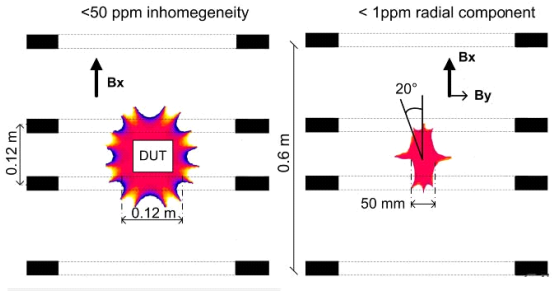

Fig. 2. Red—inhomogeneity below 50 ppm in a 0.12×0.12 m^2 area where DUT is placed (left). Red—area of 0.05×0.12 m^2 where the error due to the radial field component is below 1 ppm, allowing for up to 20° DUT rotation—see (2) and (3) (right).

B. Calibration of the 60 cm Coil System

Our coil system (Fig. 1) with overall 60 cm dimensions comprises of one Merritt-coil quaternion [18] with high homogeneity and two Helmholtz coils. We have done a 3-D finite-element model (FEM) simulation (Cedrat FLUX3D) of the Merritt coils showing that in an area of 12×12 cm^2, the inhomogeneity is below 50 ppm—see Fig. 2. Due to size constraints, we calibrated the individual coils with a flowing-water NMR magnetometer. The uncertainty of 70 ppm ($1\ \sigma$) was mainly due to field instability–about 30 ppm can be achieved [19].

III. Calibration Procedure

A. Principle

Although we cannot actively compensate for the Earth's magnetic field (~48 000 nT in Europe) because of the coupling to the 2.5 m distant reference sensor, we show that it is possible to compensate only for the magnetic field variations and/or disturbances. The static value of the Earth's magnetic field is then suppressed by performing two or more measurements with different applied fields. We performed a 3-D FEM simulation and have verified by measurements that a 250 nT field in the coils will create a field of 1 nT at the reference sensor. This weak back coupling results in a slight degradation of the disturbance compensation effectiveness.

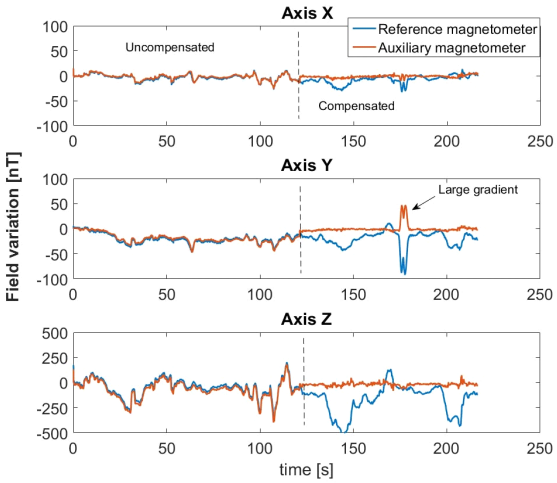

Fig. 3. Field variations sensed by the reference magnetometer (blue—bottom trace) and in the coil system (orange—top trace). The reference magnetometer and the one in the coils have been numerically aligned. The large uncompensated peak was due to the steel door opening (large gradient).

B. Reference Sensor and Its Alignment

The reference sensor (a triaxial fluxgate with 200 samples/s digital output and an effective 20 Hz bandwidth after filtering) is placed just 2.5 m away from the coils.

The reference sensor is roughly oriented in the coil-system direction before each calibration. It is difficult to align it precisely with the coil system—for this purpose, we use numerical alignment with another, well-calibrated triaxial fluxgate, which is temporarily placed in the coil system and aligned with its axes. A recording of 10 minutes of both magnetometer outputs is enough to calculate 3×3 transformation matrix $\mathbf{F}$ between reference sensor readings $\mathbf{R}$ and magnetic field vector $\mathbf{C}$ in the coil-system coordinates (Fig. 1)– $\mathbf{C} = \mathbf{FR}$. To obtain matrix $\mathbf{F}$, we utilize magnetic disturbances $\Delta\mathbf{C}$, which are assumed to be homogeneous on the 2.5 m distance, i.e., we try to solve

$$\begin{bmatrix} F_{11} & F_{12} & F_{13} \\ F_{21} & F_{22} & F_{23} \\ F_{31} & F_{32} & F_{33} \end{bmatrix} \begin{bmatrix} \Delta R_x \\ \Delta R_y \\ \Delta R_z \end{bmatrix} - \begin{bmatrix} \Delta C_x \\ \Delta C_y \\ \Delta C_z \end{bmatrix} = \min . \qquad (1)$$

Matrix $\mathbf{F}$ was obtained by least-squares inversion of the recording in MATLAB, i.e., $\mathbf{F} = \Delta\mathbf{R}/\Delta\mathbf{C}$. The efficiency of the procedure is shown in Fig. 3—after finding $\mathbf{F}$, we first calculated and compared the two aligned sensor—see Fig. 3 left (uncompensated). After that, the current source has been switched-on and only the compensating field values were fed to the coil system, effectively suppressing the external field disturbances—see Fig. 3 right (compensated). The field variations, which exceeded 500 nT p–p in the vertical z-axis, were suppressed by a factor of ~10. We can also see that the disturbance in the vertical axis is almost unipolar: averaging would not bring a significant improvement of the calibration quality.

C. DUT Placement and Alignment

The DUT should be generally well-aligned with the coil-system axes. For triaxial sensor heads, this is commonly achieved by observing the orthogonal sensor output crossing zero and relying on the sensor orthogonality, since the readings of an aligned sensor exhibit a flat maximum. The residual misalignment, which can be either due to imperfect coil calibrations or due to the sensor non-orthogonalities, causes, however, an additional error: 1° of misalignment (or sensor pair non-orthogonality) causes about 150 ppm error. However, it is not really necessary to align the sensor precisely, if the coil system is well-calibrated. (Also, coil-system non-orthogonalities are usually below 0.1° [7], [13].) If two orthogonal coils are subsequently energized creating fields B_x and B_y, the sensor with a sensitivity S_x, misaligned by an angle α, will produce uncalibrated outputs O_{xx} and O_{yy}

$$\Delta O_{xx} = \Delta B_x \cdot \cos\alpha \cdot S_x\,[V, T, °, V/T] \tag{2}$$

$$\Delta O_{yy} = \Delta B_y \cdot \sin\alpha \cdot S_x\,[V, T, °, V/T]. \tag{3}$$

From the equations (2) and (3), it is obviously possible to cancel out the constant misalignment angle and obtain the true, "aligned" sensitivity S_x. It is, however, necessary to take into account any orthogonal component of the magnetic field which could occur in the area where the sensor is placed; from our 3-D simulation, we see that up to 20° rotation is theoretically possible. If the sensor casing is mechanically pre-aligned with one of the coil axes, the angular deviations are obtained for a defined frame, as opposed to thin-shell and scalar calibrations. This applies also for the two remaining (vertical) misalignment angles.

D. Current Sequencing and Disturbance Compensation

As a very basic calibration method, the currents in the coil systems are sequenced and magnetometer output is recorded, preferably in a bipolar way to suppress the external field variations as much as possible. As shown in Fig. 3, the noise in our laboratory can exceed 500 nT p–p and manifests itself as a unipolar disturbance for most of the time, thus not allowing for efficient averaging. Also, DUT settling time is significant: a magnetometer with 1 Hz bandwidth and first-order response settles to 100 ppm in 9 s, achieving 100 ppm stability during this time with a 50 000 nT field equals 5 nT.

Let us describe the calibration procedure for magnetometer gain in the x-axis, assuming the value of α to be zero, Earth's field x-component B_{Ex} to be static, and experiencing time-varying disturbance $B_{\mathrm{Dx}}(t)$ while acquiring O_x

$$O_{x1} = [B_{x1} + B_{\mathrm{Ex}} + B_{\mathrm{Dx}}(t + t_1)] \cdot S_x \tag{4}$$

$$O_{x2} = [B_{x2} + B_{\mathrm{Ex}} + B_{\mathrm{Dx}}(t + t_2)] \cdot S_x. \tag{5}$$

Obviously, when able to cancel out the time-varying B_{Dx} term, we can obtain S_x after subtracting (4) and (5), which effectively cancels out B_{Ex}

$$O_{x1} - O_{x2} = [B_{x1} - B_{x2}] \cdot S_x. \tag{6}$$

In detail, the calibrating sequence for S_x is as follows.

1) Energize the x-axis coil, creating a calibrating field B_{x1}.

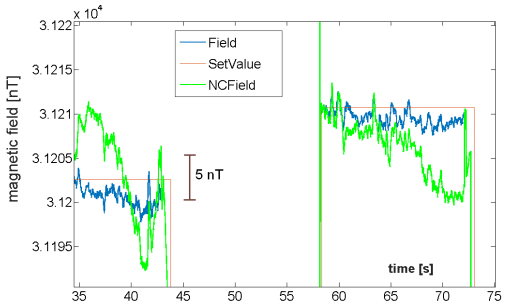

Fig. 4. Uncompensated (green) and compensated (blue) field variations during a calibration sequence with ~30 000 nT field step.

2) Wait for the settling of the reference magnetometer.
3) In time $t = 1$, record the vector $\mathbf{R}_{(t=1)}$ measured with the reference magnetometer and recalculate it to $\mathbf{C}_{(t=1)}$ in the coil frame using the matrix $\mathbf{F}$ obtained previously: $\mathbf{C}_{(t=1)} = \mathbf{F}\mathbf{R}_{(t=1)}$. The component $C_{x(t=1)}$ is a superposition of the calibrating field, Earth's field x-projection, and the actual value of disturbance in the x-axis: $C_{x(t=1)} = B_{x1} + B_{\mathrm{Ex}} + B_{\mathrm{Dx}(t=1)}$.
4) Continually compensate the applied field B_x on the value $C_x(t) - C_{x(t=1)}$, which is in turn only the time-varying disturbance $B_{\mathrm{Dx}}(t)$ since B_x and B_{Ex} are constant—see (4) and (5). Measure O_{x1} during this time.
5) Repeat for B_{x2} and O_{x2} and obtain S_x using (6).

The current sequencing is done with a precise 20 bit three-channel current source [20], which is commanded with the calibrating field minus the recalculated disturbance. In Fig. 4, we show one sequence with the zoomed-in short "constant-current" region—the actual disturbance and the residua after suppression are visible.

IV. Calibration Results

We have performed several calibration runs where the DUT was a digital triaxial fluxgate magnetometer of our own construction which has been precisely aligned with one of its axis along the y-axis coil. The calibrating steps were ±50 μT, and the sensitivity was calculated using (4)–(6).

A. Standard Deviation of the Results

By numerically adding the uncompensated magnetic noise, we were able to estimate the improvement of the calibration when using our compensating system—in Fig. 5, the z-axis differences from mean sensitivity estimation are plotted for both cases–with and without compensations. The improvement is different for different axes—see Table I; in the vertical axis, the standard deviation dropped from 1640 down to 311 ppm with compensation switched ON. However, for x- and y-axes, only ±50 nT p–p disturbance was observed, so averaging was already effective to suppress the disturbances.

B. Uncertainty Estimation

The abovementioned standard deviation of the results is only a small part of the overall calibration uncertainty—see

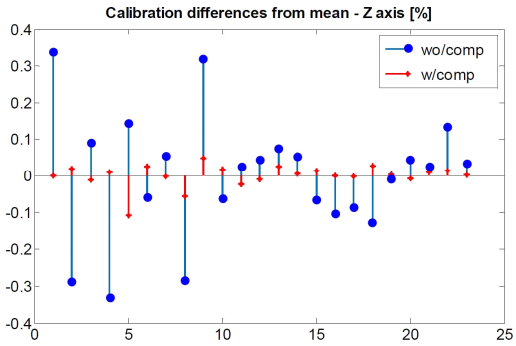

Fig. 5. Differences from the mean (23 estimations of sensitivity) in the case without (circles) and with (crosses) compensations of field variations.

TABLE I

EFFECT OF COMPENSATION ON CALIBRATION

	Direction	w/o compensation	w/ compensation
Standard deviation - relative [ppm]	NS (x)	165	91
	EW (y)	134	108
	vertical	1640	311

TABLE II

CALIBRATION UNCERTAINTY BUDGET—N–S AXIS

Uncertainty source	Uncertainty type	1-σ rel. uncertainty [ppm]
Traceable coil calibration	B	70
Resistor standard	B	15
Voltmeter Solartron 7071	B	14
Coil inhomogeneity in the central 100x100 mm^2 area	B	50
1 degree misalignment (when applicable)	B	(0) 150
Current-source noise and tempco during calibration	A	5
Standard deviation from mean calibration result	A	91
Current-source nonlinearity	B	4
TOTAL	A+B	(181) 318

Table II. It can be seen that the largest effect has the angular deviation of the DUT/coil system which for 1° misalignment causes an additional 150 ppm. If this angular misalignment is calculated [using (1) and (2)] and if the coil-system errors are compensated to about 0.1°, this contribution is negligible. The second highest uncertainty source is the coil-system constants calibration; we aim to decrease this with a new NMR calibration. The total 1 σ uncertainty for the N–S axis sensitivity is thus either 181 ppm (angular deviations corrected/calculated) or 318 ppm (1° misalignment allowance), respectively. Even when allowing for 1° error, the expanded 2 σ uncertainty with 95% probability coverage is below 0.1% for all the three magnetometer axes.

V. CONCLUSION

The main advantage of the presented magnetic calibration system is its small footprint where the reference magnetometer was placed just 2.5 m away from the coil system, which was allowed by using a novel method of sensor alignment and a calibration sequence. In this manner, we were able to cancel the local magnetic disturbance which would be inhomogeneous on a larger scale. Since the system does not utilize a feedback loop, it is possible to calibrate sensors and magnetometers which are themselves producing magnetic fields, affecting the feedback-loop sensor. In all the three axes, we achieved an expanded calibration uncertainty below 0.1%.

ACKNOWLEDGMENT

This work was supported by the Technology Agency of the Czech Republic under Project TE02000202 “Advanced Sensors.”

REFERENCES

[1] J. Merayo *et al.*, “Scalar calibration of vector magnetometers,” *Meas. Sci. Technol.*, vol. 11, no. 2, p. 120, 2000.
[2] P. Brauer, J. M. G. Merayo, O. V. Nielsen, F. Primdahl, and J. R. Petersen, “Transverse field effect in fluxgate sensors,” *Sens. Actuators A, Phys.*, vol. 59, nos. 1–3, pp. 70–74, 1997.
[3] K. Mohamadabadi, C. Coillot, and M. Hillion, “New compensation method for cross-axis effect for three-axis AMR sensors,” *IEEE Sensors J.*, vol. 13, no. 4, pp. 1355–1362, Apr. 2013.
[4] T. Risbo *et al.*, “Ørsted pre-flight magnetometer calibration mission,” *Meas. Sci. Technol.*, vol. 14, no. 5, pp. 674–688, 2003.
[5] H. Kügler, “Performance improvement of the magnetic field simulation facility MFSA,” *Environ. Test. Space Programmes*, vol. 558, pp. 407–414, Jun. 2004.
[6] K.-H. Glassmeier *et al.*, “RPC-MAG the fluxgate magnetometer in the ROSETTA plasma consortium,” *Space Sci. Rev.*, vol. 128, nos. 1–4, pp. 649–670, 2007.
[7] A. Zikmund, M. Janosek, M. Ulvr, and J. Kupec, “Precise calibration method for triaxial magnetometers not requiring Earth’s field compensation,” *IEEE Trans. Instrum. Meas.*, vol. 64, no. 5, pp. 1242–1247, May 2015.
[8] D. S. Batista, F. Granziera, M. C. Tosin, and L. F. de Melo, “Three-axial Helmholtz coil design and validation for aerospace applications,” *IEEE Trans. Aerosp. Electron. Syst.*, vol. 54, no. 1, pp. 392–403, Feb. 2018.
[9] T. Brys *et al.*, “Magnetic field stabilization for magnetically shielded volume by external field coils,” *J. Res. Nat. Inst. Standards Technol.*, vol. 110, no. 3, p. 173, 2005.
[10] P. G. Park, Y. G. Kim, V. Y. Shifrin, and V. N. Khorev, “Precise standard system for low dc magnetic field reproduction,” *Rev. Sci. Instrum.*, vol. 73, no. 8, pp. 3107–3111, 2002.
[11] M. J. Hall, S. A. C. Harmon, and S. Turner, “Magnetic environment and magnetic field standards at NPL for the calibration of low noise magnetometers and gradiometers for cleanliness studies,” in *Proc. ESA Workshop Aerosp. EMC*, May 2012, pp. 1–6.
[12] W. F. Stuart, “Earth’s field magnetometry,” *Rep. Progr. Phys.*, vol. 35, no. 2, p. 803, 1972.
[13] A. Zikmund, P. Ripka, R. Ketzler, H. Harcken, and M. Albrecht, “Precise scalar calibration of a tri-axial Braunbek coil system,” *IEEE Trans. Magn.*, vol. 51, no. 1, Jan. 2018, Art. no. 4000704.
[14] V. Y. Shifrin *et al.*, “Magnetic flux density standard for geomagnetometers,” *Metrologia*, vol. 37, no. 3, p. 219, 2000.
[15] F. I. Skripov, “Nuclear-resonance oscillator operating in the magnetic field of the Earth,” *Dokl. Akad. Nauk SSSR*, vol. 121, no. 6, p. 998, 1958.
[16] B. C. Woo, C. G. Kim, P. G. Park, C. S. Kim, and V. Y. Shifrin, “Low magnetic field measurement by a separated NMR detector using flowing water,” *IEEE Trans. Magn.*, vol. 33, no. 5, pp. 4345–4348, Sep. 1997.
[17] K. Weyand *et al.*, “Final report (draft B) on EUROMET project no. 446: International comparison of magnetic flux density by means of field coil transfer standards,” *Metrologia*, vol. 38, no. 2, p. 187, 2001.
[18] J. L. Kirschvink, “Uniform magnetic fields and double-wrapped coil systems: Improved techniques for the design of bioelectromagnetic experiments,” *Bioelectromagnetics*, vol. 13, no. 5, pp. 401–411, 1992.
[19] M. Ulvr and J. Kupec, “Improvements to the NMR method with flowing water at CMI,” *IEEE Trans. Instrum. Meas.*, vol. 67, no. 1, pp. 204–208, Jan. 2018.
[20] M. Dressler, “Current source for a test coil system,” M.S. thesis, Czech Tech. Univ. Prague, Prague, Czech Republic, 2017. Accessed: Jul. 15, 2018. [Online]. Available: https://dspace.cvut.cz/handle/10467/68554

Precise Calibration Method for Triaxial Magnetometers Not Requiring Earth's Field Compensation

Ales Zikmund, Michal Janosek, Michal Ulvr, and Josef Kupec

Abstract— **A calibration procedure for calibrations of triaxial magnetometers is presented. The procedure uses a triaxial Helmholtz coil system and an Overhauser scalar magnetometer and is performed in the Earth's field range. The triaxial coils are first calibrated with the Overhauser magnetometer, and subsequently, a triaxial magnetometer calibration is performed. As opposed to other calibration approaches, neither Earth's field nulling system nor movements of the magnetometer are needed. A real calibration test was carried out—the extended calibration uncertainty was better than 430 ppm in sensitivity and 0.06° in orthogonality.**

Index Terms— **Calibration, magnetometer, precision, triaxial.**

I. Introduction

A STANDARD way to calibrate triaxial magnetometers is using a compensating system that cancels out any magnetic disturbances [1], [2]. These systems usually utilize 2-m and larger triaxial coils with high homogeneity (a Braunbek configuration) and the field compensation is open loop: it typically uses a triaxial magnetometer placed far away from the building. This triaxial magnetometer is either a standalone where its reading influences the compensating currents or is placed in another smaller triaxial coil system that runs in a local closed-loop system (maintaining zero field): the compensating current is then shared with the coils at the calibrating facility [3]. This approach has many drawbacks. Mainly, the remote triaxial magnetometer and also the coil system have to be aligned and calibrated precisely to establish stable compensation. In addition, the zero magnetic field value is not checked during the calibration and this residual field affects the calibration precision.

The alternative closed-loop systems rely on a zero-detector inside the feedback loop, which is placed in the cancellation coils, i.e., Billingsley APEX-CS. Ultimate precision is allowed using atomic magnetometers in the feedback loop [4], [5]. This principle achieves more precise results but is affected by the influence of the zero detector on the calibrated sensor. Both sensors cannot be ideally placed in the center of the coils where the magnetic field is homogeneous, and so their mutual position can increase uncertainty of the calibration.

Another approach is the scalar calibration [6], [8], which provides very good results. Nevertheless, it relies on rotations of the calibrated triaxial magnetometer in the Earth's field and thus is sensitive not only to disturbances but also to magnetic field gradient, requiring magnetically clean locality, which is not easy to find even in suburban areas. To suppress the effect of magnetic disturbances and diurnal variations of the Earth's magnetic field, the magnetic field should be logged (usually with an Overhauser scalar magnetometer) and its values should be used in the calculations. To achieve an uncertainty below 200 ppm, the residual magnetic field variation during the calibration procedure has to be below 0.5 nT. This is not easy to achieve due to the existing magnetic field gradients between the calibrating site and the place where the magnetic field is logged. Similarly, due to the finite size of the calibrated magnetometer, the magnetic field should be free of gradients in the whole sphere covered by the magnetometer rotations. This measurement is also very time consuming because at least 80 different orientations of the magnetometer are usually measured [6].

II. Motivation

Our motivation, to create an alternative calibrating procedure, is to be able to perform the calibration in a relatively low-cost facility, which would be metrologically traceable to a magnetic field density standard resulting in less than 0.05% (500 ppm) calibration uncertainty. Such technique would be applicable to a wide community of users, as was defined in the European metrology Joint Research Project IND 08 MetMags [7]. In our case, it is necessary only to monitor the Earth's magnetic field variations using the Overhauser magnetometer, and no shielded rooms or field-cancellation loops have to be used. The calibration facility can also be placed in areas with magnetic field gradients that would not allow the scalar calibration method. The basic requirement is that the calibrating facility uses well-calibrated triaxial coils that would enable to create magnetic fields of up to 100 μT–this is rather standard requirement and such coil systems are commercially available.

Manuscript received June 20, 2014; revised December 4, 2014; accepted December 15, 2014. Date of publication March 6, 2015; date of current version April 3, 2015. This work was supported in part by the European Metrology Research Project MetMags under Grant TA01010298 through the Technology Agency of the Czech Republic and in part by Czech Technical University in Prague, Prague, Czech Republic, under Grant SGS12/194/OHK3/3T/13. The Associate Editor coordinating the review process was Thomas Lipe.

A. Zikmund and M. Janosek are with the Department of Measurement, Faculty of Electrical Engineering, Czech Technical University in Prague, Prague 166 36, Czech Republic (e-mail: ales.zikmund@fel.cvut.cz).

M. Ulvr and J. Kupec are with the Department of Electromagnetic Quantities, Laboratory of Fundamental Metrology, Czech Metrology Institute, Prague 150 72, Czech Republic.

Color versions of one or more of the figures in this paper are available online at http://ieeexplore.ieee.org.

Digital Object Identifier 10.1109/TIM.2015.2395531

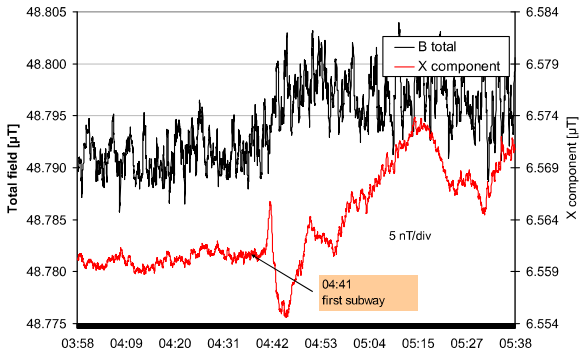

Fig. 1. Noise measurement during traffic strike. The first ongoing subway causes 10-nT p–p noise in horizontal component (approximately E–W).

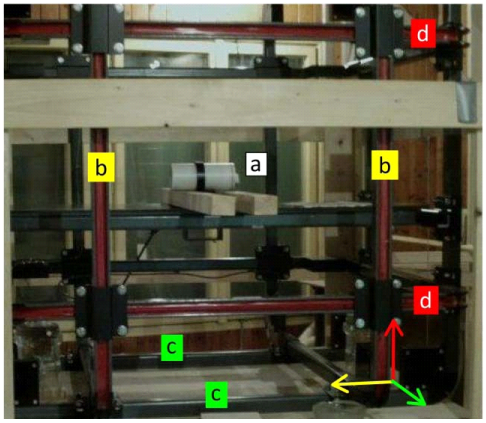

Fig. 2. (a) Overhauser magnetometer sensor placed in the triaxial coil system during calibration—a central position assures low field gradient. (b) Coil pair oriented N–S. (c) Coil pair oriented E–W. (d) Coil pair oriented vertically [12].

III. Calibration

A. Calibration Site

The site, property of the Institute of Geophysics at Academy of Sciences, Czech Republic, has been used till the 1960s as a geomagnetic observatory; however, due to building of dc railways and expanding city borders, it was later converted for paleomagnetic experiments [9]. Although the site is 4 km away from the nearest subway station and 3 km away from dc-electrified railway, the traffic-related noise was observed with disturbances increasing up to 10 nT peak-peak and even the resuming metro operation was identified (Fig. 1). It is clear that during calibration, the magnetic field should be either compensated for or monitored even though averaging might improve the situation but substantially prolonging the calibration time (the time span in Fig. 1 is 1 3/4 h).

The coils used for calibration are the commercially available triaxial coils HELM-3 of Billingsley Aerospace and Defense. The coil system consists of three squared Helmholtz coils whose dimensions are around 1 m. The nominal coil constant as provided by the supplier is 100 μT/A (the coils were originally supposed to be used in a feedback system where coil constants do not have to be precisely known). Orthogonality error of the coils is better than 0.1° for all three axes. The magnetic field uniformity is declared as 0.3% in a centrally located 20-cm sphere. For our purpose, however, the coil constants needed to be calibrated.

The current to the coils was supplied by a custom-built current source to overcome drifts of the coil resistance during calibration caused by self-heating and also ambient temperature. The current source is based on 16-bit digital to analog converters and a voltage-to-current amplifier. Stability of the custom-built current source was measured as ± 10 μA in 1 h while supplying 1 A. To be absolutely independent of the current source stability, current is simultaneously measured using 1-Ω shunts and 6.5-digit voltmeters.

B. Triaxial Coils Calibrations

The procedure uses a scalar Overhauser magnetometer to calibrate the coil constants and the angular alignment of the triaxial Helmholtz coils–the details are described in [10] together with uncertainty analysis in [11]. The details of the setup are shown in Fig. 2. The calibration results express the three coil sensitivities and their respective angular alignment. The results together with the expressed uncertainty are shown in Table I. The resulting coil constants differ from the nominal values about 10% because the producer does need to define these parameters precisely due to using the coils in the feedback system.

TABLE I
Parameters of the Triaxial System

Axis	**Coil constant [nT/A]**	**Combined uncertainty [nT/A]**
X – East West	78787.5	16.1 (204 ppm)
Y – North South	76647.5	13.4 (175 ppm)
Z – Vertical	83016.4	23.7 (286 ppm)
Axes	**Alignment angle**	**Combined uncertainty**
	[deg]	[deg]
X – Y	89.98	0.04
Y – Z	90.01	0.04
X – Z	89.97	0.04

C. Calibration Against Magnetic Flux Density Standard

The aim was to compare the previous calibration results with a traceable calibration. The calibration method is based on a direct comparison with the magnetic flux density (MFD) standard, which is basically a four-section solenoid on a quartz core. The method uses one dc source and is standardized at the Czech Metrology Institute under the procedure code 817-MP-C602 (Fig. 3). The comparison was done for the horizontally located E–W coils only to verify the uncertainty of the coil calibration principle [10].

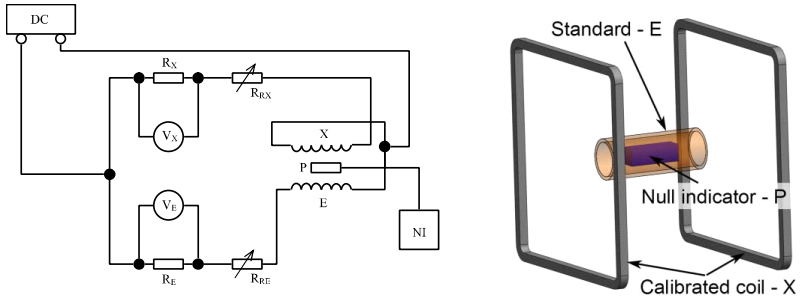

Fig. 3. Calibration procedure based on comparison with a known MFD standard. (a) Electrical circuit. (b) Real arrangement.

The two coils, the unknown X (the E–W-axis of the Helmholtz coils in our case) and the coil standard E were connected in the two branches with variable resistors R_{RX} and R_{RE} (Fig. 3). The currents in these branches, I_X and I_E, were changed in both branches to cancel the flux measured in the middle of the standard coil by the means of zero detector P, which was a single-axis fluxgate magnetometer. The current in the two branches is sensed on the resistor standards R_x and R_E, respectively. When the zero reading at null indicator (NI) was reached, the two currents were recorded and the coil constant K_{BIX} has been calculated as

$$K_{\mathrm{BIX}} = \frac{K_{\mathrm{BIE}} I_E}{I_X} = K_{\mathrm{BIE}} \frac{U_E}{U_X} \frac{R_X}{R_E} \tag{1}$$

where K_{BIE} is the constant of the standard E, U_E is voltage drop on the standard resistor R_E, and U_X is the voltage drop on the standard resistor R_X.

As the voltage source is common for both branches, its instability is suppressed. The resulting uncertainty can be also suppressed by interchanging the sensing resistors R_X and R_E.

The highest uncertainty of 30 ppm had the National flux density standard with a value of 598.827 μT/A. The voltmeters measuring V_X and V_E were of Agilent 34587A type with 8.5 digits of resolution; R_E and R_X were standard resistors of 2- and 5-Ω values, respectively, with an uncertainty of 5.4 ppm.

The cross-calibration result of the x-axis coil X (E–W) was 78795.5 nT/A with an expanded uncertainty of 50 ppm—this agrees well with the calibration results of the x-axis shown in Table I.

D. Triaxial Magnetometer Calibration Principle

The basic idea of the calibration has been described in [12]. A predefined sequence of currents is performed together with measuring the response of the calibrated triaxial magnetometer. The Earth's magnetic field is not cancelled by the coil system, but its scalar value is remotely monitored. All input quantities (coil current, triaxial magnetometer output and the monitored Earth's field scalar value), forming N equations from N calibration steps where the magnetic field in the calibrating coils is changed in its amplitude and direction, are passed to a solver that solves the problem by the Levenberg–Marquardt nonlinear optimization according to [12].

TABLE II
RESULTING PARAMETERS OF THE CALIBRATION

Triaxial magnetometer	**U**	**V**	**W**
Sensitivity	S_U	S_V	S_W
Angle to XY coil plane	α_U	α_V	α_W
Angle in XY coil plane	β_U	β_V	β_W

The remote scalar magnetometer measures the Earth's field and should be in a distance so that the influence of the coil system would be negligible. For our experiment, we supposed that the maximum excited magnetic field is around 100 μT, then according to the magnetic field of a dipole source that falls with $1/r^3$, the scalar Overhauser magnetometer had to be placed at least 40 m away to suppress the coil system influence down to 1.5 nT.

Based on an experience of [12], it was more suitable to approximately align the axes of the calibrated magnetometer with the respective calibrating coil axes, because the nonlinear solver converged faster. From the optimization described above, the sensitivity and two angles with respect to the orthogonal coil system have been obtained for each axis of the calibrated magnetometer. The resulting parameters are summarized in Table II and shown in Fig. 4.

To compare several calibration principles, the mutual orthogonality angles of the calibrated triaxial magnetometer have been expressed according to [6] by simple calculations

$$\begin{aligned} \Delta_1 &= \beta_U + \beta_V \\ \Delta_2 &= \alpha_U + \beta_W \\ \Delta_3 &= \alpha_V + \alpha_W. \end{aligned} \tag{2}$$

IV. CALIBRATION PROCEDURE UNCERTAINTY

The triaxial system's coil constants and their orthogonality are known from the previous calibration—see Table III, which gives their values and uncertainty. Further errors during the calibration can be caused by the variation of the Earth's magnetic field and by environmental noise inherent to the location. However, both are suppressed to a large level by recording the B_E value with a precise Overhauser magnetometer. The field

TABLE III
UNCERTAINTIES OF THE USED INSTRUMENTS

Parameter	Value	Uncertainty
Overhauser magnetometer [nT]	-	0.2 nT
Coil constants X,Y,Z [nT/A]	78788, 76648, 83016	204, 175, 286 ppm
Coil angles XY, YZ, XZ [degree]	90, 90, 90	0.04°
Standard resistors values [Ω]	1.00006, 0.99989, 0.99993	30 ppm
Voltage measurement	1 V nominally	80 ppm

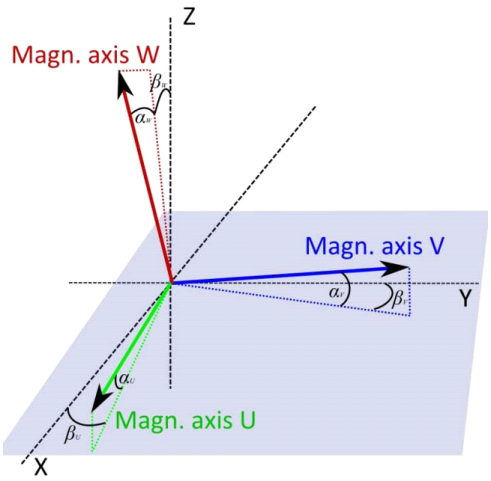

Fig. 4. Resulting angle parameters.

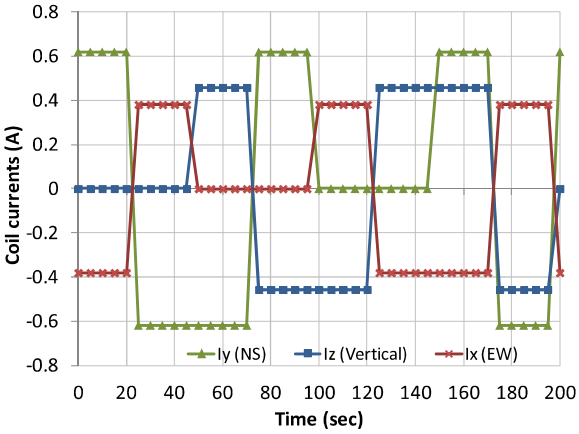

Fig. 5. Current sequence applied to respective coil axes during the calibration of the triaxial magnetometer.

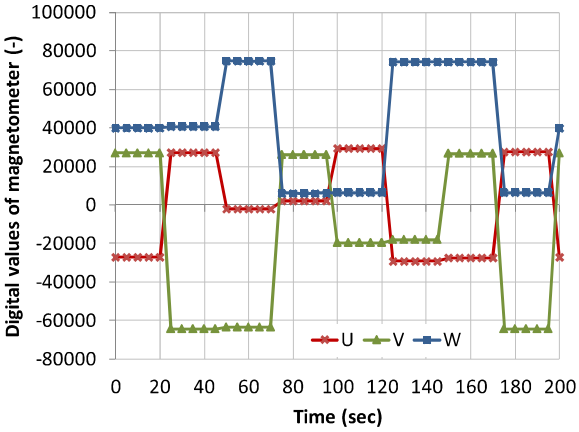

Fig. 6. Digital triaxial magnetometer response on the reference coil excitation.

gradient is subtracted in the measurement and thus the residual error was only considered, which is the gradient noise; this was measured on site as ±5 nT.

We used the Monte Carlo method for estimating the influence of all uncertainties of the input variables (Table III) on the resulting parameters, as opposed to our initial approach in [12]. The measured parameters, being the input to the optimization method, were deviated with a supposed normal noise distribution. The (*B*-type) uncertainty was then expressed as a standard deviation of the set of the solver results. The rather high uncertainty of the voltage measurement was caused by the used voltmeter of Agilent 34401 type.

V. EXPERIMENTAL TEST

The test calibration has been carried out in the former geomagnetic observatory site Pruhonice maintained by the Institute of Geophysics. A triaxial digital magnetometer that was developed in our laboratory was calibrated in the Helmholtz coil system with calibration parameters in Table III. The ambient magnetic field was first measured with the Overhauser magnetometer in the coils without any excitation and then in the remote spot that was 40 m far from the coil system—the scalar gradient of 11 nT, which was then subtracted from the data, was supposed to be stable during the whole measurement time.

A predefined current sequence was applied during the calibration [12] (Fig. 5). The sequence contains current steps designed to have a significant influence on the calibrated magnetometer axes in each orthogonal direction and also to keep the magnetic field well in the magnetometer range. The aim was to obtain a response at least 25 μT in each axis of the calibrated triaxial magnetometer.

The digital output of the calibrated triaxial magnetometer was recorded during the applied current sequence. In Fig. 6,

TABLE IV
UNCERTAINTIES OF THE RESULTS

	Uncertainty B	Uncertainty A	Result with combined uncertainty (k=2)	Scalar method [8]
Offset U ([nT]	2	-	-32.5 ± 4	-30.5
Offset V [nT]	2	-	-37.5 ± 4	-34.4
Offset W [nT]	2	-	-24.0 ± 4	-27.6
Sensitivity U (norm) [-]	88	132	0.9659 ±320 ppm	0.9666
Sensitivity V (norm.) [-]	68	116	0.9431 ±270 ppm	0.9436
Sensitivity W (norm.) [-]	110	185	0.9022 ±430 ppm	0.9021
Angle Δ_1 [°]	0.002	0.016	0.205 ±0.034	0.167
Angle Δ_2 [°]	0.001	0.024	0.531 ±0.048	0.603
Angle Δ_3 [°]	0.003	0.031	0.104 ±0.062	0.107

a time record is shown as a response to the calibrating coils excitation. The magnetic axis orientation is significant because it correlates with the coil excitation. The magnetometer axis W was vertical (coil Z), the axis V was oriented to North–South direction (coil Y) and the magnetometer axis U was approximately aligned with the East–West coil (coil X). The alignment was not ideal due to small cross-field reactions, which can be seen in the record; nevertheless, this did not cause a problem for the calibration algorithm.

The sequence of calibration currents has been repeated 12 times to obtain a minimal statistical set for averaging and calculation of the A-type uncertainty. In the calculation procedure, however, we found higher residuals of the optimization method in some combinations of the current. This was probably caused by vectorial components of ambient magnetic noise that are different—higher residuals were correlated with the situation when the vertical coil was excited. The sensitivities varied maximally of 210 ppm and the angles varied of 0.028°, which were designated as the A-type uncertainty.

The B-type uncertainties have been established by the Monte Carlo simulation using the parameters from Table III. The input parameters were set up according to the real measured quantities and their values were scattered according to their known uncertainties. The worst B-type gain uncertainty of 110 ppm appeared in the W-axis because it was the most affected by magnetic field noise at the location.

The A-type uncertainty was mostly influenced by the noisy magnetic field, which is shown in Fig. 7 (black trace); this is the real data input into the calibration algorithm. The diurnal variation of the Earth's field corresponds to the record of Budkov observatory (INTERMAGNET designation BDV, red trace). In addition, the magnetic field gradient variation (or noise), discussed previously, will affect the measurement uncertainty; however, it cannot be measured at the calibration time.

The combined uncertainty was finally calculated as a norm of the two A and B components and the results are given together with the calibrated parameters of the triaxial magnetometer in Table IV. The same triaxial magnetometer calibrated in this paper was also calibrated by the scalar

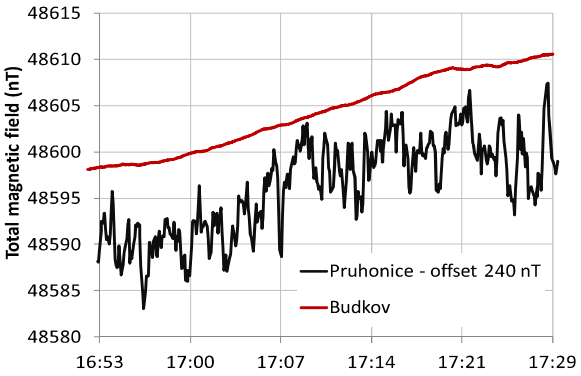

Fig. 7. Noise of ambient magnetic field during calibration compared with the Budkov observatory.

calibration, which is a different technique described in [8]. The results are also presented in Table IV to have a comparison. The data agree well—the scalar calibration results are almost within the calibration uncertainty of the developed method. Assuming that also the scalar calibration has a significant uncertainty, which is usually expressed as a calibration residual [5], [6]—its evaluation is beyond the scope of this paper—we show that our calibration method is at least comparable with the scalar calibration.

VI. CONCLUSION

The presented calibration procedure is advantageous to the currently used methods, because neither an Earth's field cancellation system nor moving a calibrated magnetometer is required to measure the sensitivities and angular misalignments of the respective magnetometer axes. The Earth's magnetic field value was monitored at a distant place with an Overhauser magnetometer and was used in the calibration procedure. The calibration of the triaxial Helmholtz coils system is performed with the same Overhauser magnetometer as during the triaxial magnetometer calibration, preferably before each calibration, to compensate a possible long-term drift of the coil constants. The magnetometer offsets should

be measured separately in a magnetic shielding chamber; this is also the way in which the estimation uncertainty is the lowest [13].

From the Monte Carlo simulations, we have shown that theoretically, the uncertainty of the calibrated parameters should be less than 260 ppm in sensitivity and 0.02° of arc in orthogonality if the environmental gradient noise is below 5 nT and our measurement precision was achieved. A real calibration of a digital triaxial digital magnetometer was done with the proposed procedure. The calibration precision was influenced by gradient noise at the observatory, resulting in the largest combined uncertainty ($k = 2$) of 430 ppm for sensitivity and 0.062° of arc for the orthogonal angle of magnetometer axis.

REFERENCES

[1] H. Kügler, "Simulation of DC magnetic environment on ground," in *Proc. 4th Int. Symp. Environ. Test. Space Programmes*, 2001, p. 263.

[2] T. Risbo *et al.*, "Ørsted pre-flight magnetometer calibration mission," *Meas. Sci. Technol.*, vol. 14, no. 5, pp. 674–688, 2003.

[3] R. Vernier, T. Bonalsky, and J. Slavin, "Goddard space flight center spacecraft magnetic test facility restoration project," NASA Goddard Space Flight Center, NASA, Washington, DC, USA, Tech. Rep. 20050071098, 2004.

[4] V. Y. Shifrin *et al.*, "Magnetic flux density standard for geomagnetometers," *Metrologia*, vol. 37, no. 3, p. 219, 2000.

[5] K. Weyand, "Maintenance and dissemination of the magnetic field unit at PTB," *IEEE Trans. Instrum. Meas.*, vol. 50, no. 2, pp. 470–473, Apr. 2001.

[6] J. M. G. Merayo, P. Brauer, F. Primdahl, J. R. Petersen, and O. V. Nielsen, "Scalar calibration of vector magnetometers," *Meas. Sci. Technol.*, vol. 11, no. 2, pp. 120–132, 2000.

[7] M. J. Hall *et al.*, "Best practice guide for the generation and measurement of DC magnetic fields in the magnetic field range of 1 nT to 1 mT," NPL, Teddington, U.K., NPL Rep. MAT 65, Jun. 2014. [Online]. Available: http://www.npl.co.uk/content/ConPublication/6191

[8] V. Petrucha and P. Kaspar, "Calibration of a triaxial fluxgate magnetometer and accelerometer with an automated non-magnetic calibration system," in *Proc. IEEE Sensors Conf.*, Oct. 2009, pp. 1510–1513.

[9] K. Prihoda, M. Krs, B. Pesina, and J. Blaha, "MAVACS—A new system of creating a non-magnetic environment for paleomagnetic studies," *Cuadernos Geologia Iberica*, vol. 12, pp. 223–250, Dec. 1989.

[10] A. Zikmund and P. Ripka, "Scalar calibration of 3-D coil system," *J. Elect. Eng.*, vol. 61, no. 7/s, pp. 39–41, 2010.

[11] A. Žikmund and P. Ripka, "Uncertainty analysis of calibration of the 3D coil system," *J. Elect. Eng.*, vol. 63, no. 7s, pp. 90–93, 2012.

[12] A. Zikmund and M. Janosek, "Calibration procedure for triaxial magnetometers without a compensating system or moving parts," in *Proc. IEEE Int. Instrum. Meas. Technol. Conf. (I2MTC)*, May 2014, pp. 473–476.

[13] A. Moldovanu, E. Moldovanu, E. D. Diaconu, C. Ioan, B. O. Moldovanu, M. Macoviciuc, "Metrological aspects of the offset evaluation for magnetometric sensors," *Sens. Actuators A, Phys.*, vol. 59, nos. 1–3, pp. 113–118, Apr. 1997.

Ales Zikmund was born in Mostiste in 1985. He received the master's degree from the Faculty of Electrical Engineering, Czech Technical University in Prague, Prague, Czech Republic, in 2009, where he is currently pursuing the Ph.D. degree with the Department of Measurement.

His current research interests include magnetic calibrations by using nonlinear optimizations.

Michal Janosek was born in Varnsdorf, Czech Republic, in 1980. He received the M.Sc. degree in measurement and instrumentation and the Ph.D. degree from the Faculty of Electrical Engineering, Czech Technical University in Prague, Prague, Czech Republic, in 2007 and 2014, respectively.

He has co-authored over 20 journal papers. His current research interests include application of magnetic sensors in gradiometers and magnetometers.

Michal Ulvr was born in Jablonec nad Nisou, Czech Republic, in 1983. He received the master's degree in measuring techniques from Czech Technical University in Prague, Prague, Czech Republic, in 2008.

He has been with the Czech Metrology Institute, Prague, since 2008, where he is currently a Metrologist with the Laboratory of Fundamental Metrology, Department of Electromagnetic Quantities. His current research interests include metrology in the area of magnetic quantities.

Josef Kupec was born in Prague, Czech Republic, in 1940. He received the master's degree in experimental physics from Charles University in Prague, Prague, in 1962, and the C.Sc. (Ph.D. equivalent) degree from Slovak Technical University in Bratislava, Bratislava, Slovakia, in 1984.

He has been with the Czech Metrology Institute, Prague, since 1962, where he is currently a Metrologist with the Laboratory of Fundamental Metrology, Department of Electromagnetic Quantities. His current research interests include metrology in the area of magnetic quantities.

2.2.2 Precise zero field – „magnetic vacuum“

In calibrations of low-level magnetometers with their range less than the minimum range of accurate Overhauser or Proton magnetometers (≪10,000 nT) which are normally used as reference instruments for calibrations [46], fluxgates are used for ambient field and noise cancellation in the coils, either in open or closed-loop [3]−[5]. However, despite their precise once-off calibration, fluxgate offsets are not stable in time, which is increasing the overall calibration uncertainty. The same applies to offsets of current-supplies and/or of the digital-to-analog converters used in the coil system. A well-defined magnetic zero, when initially established and locked-up in the coil system is a promising approach to solve this problem, moreover with a further perspective of integrating a noise-cancelling method. Theoretically, also a SQUID could be employed to establish the field value − in the fundamental, open-loop mode, its „Φ_0-counting“ behaviour lacks the additional uncertainty of a semiconductor-based, feedback-loop current readout circuitry. A “digital feedback” SQUID with higher resolution than one flux quantum could serve this purpose well [47][48].

At IEEE Sensors 2020, the author has presented and subsequently published an approach using rotating AMR and fluxgate sensor, respectively with the title “*Stabilized magnetic vacuum using a rotating fluxgate sensor”* [P3]. The principle is derived from the legacy field cancellation system utilizing rotating search coils installed in the geology laboratory in Pruhonice of the Academy of Sciences of the Czech Republic (ASCR) [49]. The coils however rotate at several thousand revolutions per second and thus have a limited mechanical life, need pressurized air supply etc. Our approach used embedded synchronous demodulation of a rotating AMR/fluxgate, using wireless data transfer overcomes these limitations and is capable, with a single sensor, to perform a total field cancellation (i.e. the horizontal but also the vertical field component).

Further research on utilizing more sensitive fluxgate sensors, an embedded 90 degrees rotating device and a noise cancellation integration is currently ongoing in the scope of a collaboration with the Czech Metrology Institute (CMI) and the South African National Space Agency (SANSA).

[P3] *Stabilized magnetic vacuum using a rotating fluxgate sensor (2020).* **Author contribution:** 50%. Principle proposal, initial device design and measurements, theory and article composition.

Stabilized magnetic vacuum using a rotating fluxgate sensor

Michal Janošek[1], Michal Dressler[1], Elda Saunderson[2]
[1]Dept. of Measurement, Czech Technical University in Prague, Prague, Czech Republic
[2] Directorate Space Science, South African National Space Agency, Hermanus, South Africa
Email: janosem@fel.cvut.cz

***Abstract*— We present an effective zero-field system utilizing a rotating, single-axis fluxgate sensor to establish and maintain a magnetic vacuum in triaxial coils. With the help of a low-noise fluxgate sensor rotating at a frequency of 1 Hz, we were able to set the magnetic zero in the horizontal plane to or below 0.5 nT, which is 10 ppm of the local magnetic field, or 100 dB suppression. With the help of an additional triaxial sensor at a 2.5-m distance, we were able to maintain the magnetic zero to about 1 nT within 30-minutes suppressing field variations and disturbances. Such a system allows for precise magnetic calibrations, paleomagnetic experiments or other tasks where magnetic vacuum is beneficial or required.**

Keywords*— *magnetic field; coil system; vacuum; fluxgate; calibration

I. INTRODUCTION

In the field of calibrations of magnetic sensors, or in paleomagnetism, establishing a zero magnetic field ("magnetic vacuum") in a volume is beneficial.

Paleomagnetic experiments benefit from the zero field for establishing the "frozen" magnetization of the samples and thus indirectly establishing the age of the sample [1]. Calibrating magnetic field sensors will benefit by first nulling the local Earth's field - the desired fields can be then established just by knowing calibration constants of the coils utilized.

In both cases, the problem of the performance of the magnetic sensor used for establishing zero-field in the coils arises. The most precise coil systems use atomic magnetometers of various types [2]-[4], however they cannot be used for zero-fields as their minimum operation is approx. 2000 – 20 000 nT depending on the type of the sensor. Moreover, without special arrangements, they have a scalar response making the nulling system even more challenging.

Readily available sensors which also work in zero magnetic fields would be a fluxgate or anisotropic magnetoresistor (AMR) [5], which can be cheap, small and work at room temperatures. However, the problem arises from their inherent offsets, which is difficult to calibrate for and is not stable in time and temperature. The offset will limit the zeroing ability to about 5-20 nT for a good fluxgate [6] and slightly more for an AMR magnetometer [7].

In this paper, we present an effective approach inspired by the rotating coils of the deprecated magnetic vacuum system "MAVACS" [8], which used high-speed rotating search coils with mercury bearings and pressurized air.

This work was supported by the Grant Agency of the Czech Technical University in Prague, grant No. SGS20/182/OHK3/3T/13.

The system proved as feasible, however the reliability was low. Our system on the other hand, uses a single magnetometer (sensor) rotating in the centre of the coil system, with wireless transfer of the data. Digital signal processing is applied to the signal received to measure the magnetic field regardless of the sensor offset and its offset drift.

II. OPERATING PRINCIPLE

A. *Single-sensor rotating magnetometer*

Let us suppose a magnetic field sensor FS with a sensitivity S in engineering units per unit of field (EU/T) and an offset O in engineering units (EU).

Let us rotate the magnetometer at a frequency f in a plane where the projection of local magnetic field B_a has an arbitrary orientation of φ_a degrees with respect to the initial sensor orientation. We can then write for the raw magnetometer output R (EU) during the rotation:

$$R(t) = B_a \cdot S \cdot \sin(2\pi f t + \varphi_{Ba}) + O \qquad (1)$$

We see from (1) that during the rotation the magnetometer offset O is a constant (or slowly varying) value. However, the amplitude of the magnetic field B_a, which is a projection of the local magnetic field vector B to the plane of rotation, yields a time-varying modulation of the output R at the rotational frequency f.

By minimizing the field B_a, we minimize the raw reading $R(t)$ - its amplitude is proportional to B_a. Because the final aim is a magnetic vacuum, establishing the sensitivity S precisely is not important, unless it would serve as a feedback signal in smart compensating software.

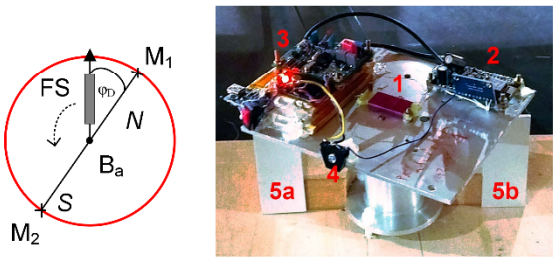

Fig. 1. - The principle (left) and the magnetometer on the rotational support (right). Fluxgate sensor (1) is connected to conditioning electronic (3), values are digitized and transmitted with ESP8266 board (2). Distance sensor (4) senses two markers (5a, 5b) as a reference for demodulation.

978-1-7281-6801-2/20/$31.00 ©2020 IEEE

For signal processing, we will introduce two markers M_1 and M_2 180 degrees apart, which the magnetometer is sensing during the rotation, and a variable demodulator phase φ_D. We can then write for the two intervals between M_1 and M_2, omitting sensitivity and time-independent offset:

$$R_{M1\to M2}(t) \approx B_a \cdot \sin(2\pi ft + \varphi_{Ba} + \varphi_D) \quad (2)$$

$$R_{M2\to M1}(t) \approx B_a \cdot \sin(2\pi ft + \varphi_{Ba} + \varphi_D + \pi) \quad (3)$$

For $\varphi_{Ba} = -\varphi_D$ we get:

$$R_{M1\to M2}(t) = -R_{M2\to M1}(t) \approx B_a \cdot \sin(2\pi ft) \quad (4)$$

The easiest demodulation of (4) would be summing the readings in the two intervals with different signs. We can also create two independent detectors for the in-phase (I) and quadrature (Q) components, having the second detector 90 degrees out of phase (5). We can then detect the parallel and orthogonal components with just one rotating sensor. For example, we can sense the field components in N-S and E-W directions, which simplifies the compensation of the field.

$$R_I(t) \approx B_a \cdot \sin(2\pi ft) \quad R_Q(t) \approx B_a \cdot \cos(2\pi ft) \quad (5)$$

B. *Vertical component*

The above equations work well for a field component in the plane of the rotation, but it might seem that it will not work for the vertical field component. However, it is also possible to measure and minimize the vertical component by tilting the rotating platform as seen in Fig. 2. However, the angle should not be exactly perpendicular to the local inclination (+65° in Prague, -65° in Hermanus).

When compensating the vertical component with the coil system only, the output reacts as follows:

$$R_V(t) \approx B \cdot \sin D \cdot \sin(\beta) = B_{vert} \cdot \sin(\beta) \quad (6)$$

It is evident that for β=0° we cannot measure the effect of nulling the field in the vertical component. However e.g. for a tilt of 30° the sensitivity on changes in horizontal and vertical components is equal.

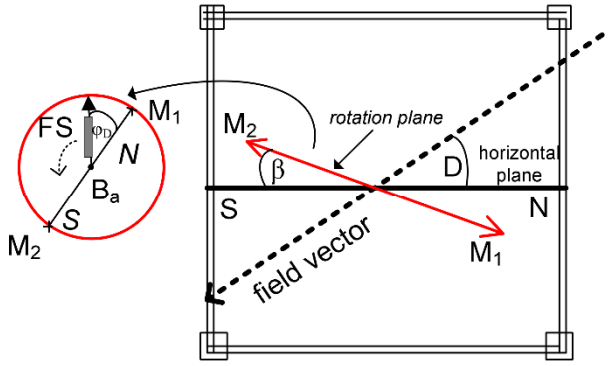

Fig. 2. The proposed placement of the rotational platform in order to measure (compensate) both the horizontal and vertical components of the local magnetic field vector.

III. Components of the System

A. *The coil system and current-source*

We used a 1-m tri-axial Helmholtz coil system of Billingsley Magnetics and a custom current source capable of 1 A output with 10 ppm resolution and stability. The coil system is rotated to the magnetic axes, i.e. in E-W, N-S and vertical - see Fig. 2 and Fig 3. The system is located in a suburb of Prague with ~20 nT p-p man-made disturbances.

B. *The rotating fluxgate magnetometer*

We used a single race-track fluxgate sensor [9] with a simple custom-built analog circuitry (about 5 US$). The analog output was then digitized with ADS1115 A/D converter attached to an ESP8266 wireless microcontroller which served as an access point. The magnetometer was powered from a Li-Ion battery. The sampling speed was 54 sps and sensor noise was about 35 pT/√Hz @ 1 Hz. Electronic components were selected to avoid excessive magnetic signature, however, since the whole assembly rotates and initial permeability of common steel parts is low, the influence on time-varying output will be negligible [10].

C. *The rotating platform and drive motor*

We used a simple rotating platform, driven by a toothed belt via a distant (2.5 m) stepper motor – see Fig. 1 and Fig. 3. By using a toothed belt, we were able to maintain the rotating speed which was beneficial for signal processing. On the rotating platform, we placed two marks (elevated Al plates) 180 degrees apart, which were sensed by a reflex distance-sensor attached to the rotating platform. These marks (M_1 and M_2) served as a reference for demodulation.

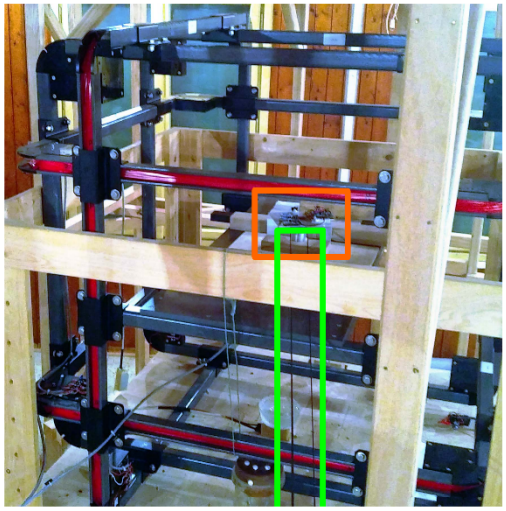

Fig. 3. Helmholtz coils, with the magnetometer (small box) visible in the middle, toothed belt (long box) extends from the coil to the stepper motor.

IV. Results

The system has been built as indicated in Fig. 4. The rotating magnetometer communicated wirelessly with a LabVIEW based data-acquisition and signal processing software. The input signal was first high-pass filtered. With the help of the M_1 and M_2 markers, we could set a coherent sample delay (phase φ_D) in order to measure the N-S

component in the I channel and E-W component in the Q channel of the demodulator. According to the reading obtained, the current source was adjusted manually. Later on, we also relied on stabilizing the field with the help of an auxiliary magnetometer placed close to the coils.

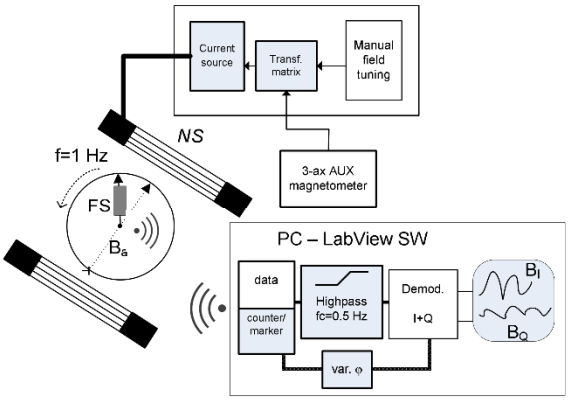

Fig. 4. Fluxgate sensor FS rotates in coils oriented to NS (orthogonal and vertical coils omitted for clarity). Signal is processed in LabVIEW software and used for manually tuning the coil currents.

A. *Time-dependent output*

The time-dependent output is best illustrated in Fig. 5. We can see that the rotational frequency is about 1 Hz. The "zero horizontal" field we managed to set can be established as about 0.5 nT (1 nT p-p), modulated on the constant 172 nT offset (given by fluxgate offset and remanence of electronic parts of the magnetometer and battery). An artificial test field of 6 nT created a clear 12 nT p-p signal – see second 255 and above of the record.

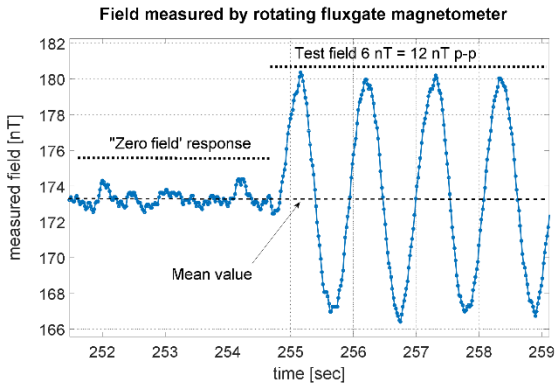

Fig. 5. Time-domain record of the rotating fluxgate magnetometer. A stationary test field of 6 nT is clearly visible in the signal as a sine-wave with the rotational frequency. The sensor offset is just the average (DC) value.

B. *Demodulated output + auxiliary magnetometer*

In Fig. 6 we show a record of three minutes of in-phase (N-S) component as recorded with the rotating magnetometer, together with the output of an auxiliary magnetometer, which was numerically aligned to the same N-S component. For better comparison, its output was low-pass filtered with the same corner frequency as for the rotating magnetometer (0.2 Hz).

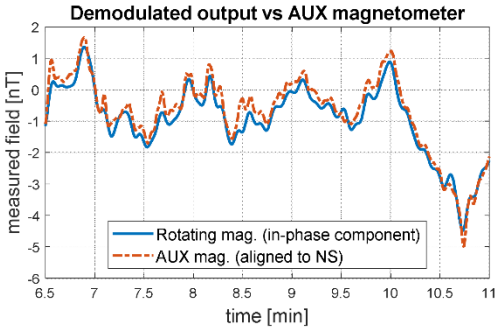

Fig. 6. Demodulated output (NS, in-phase) as compared to the reading of the auxiliary magnetometer (aligned in orientation and offset).

C. *Zero field stabilization*

For precise calibrations in Earth's field range (100 ppm and better), it is necessary to maintain the field to units of nT for minutes up to hours. Establishing a once-off "true" zero is not enough - diurnal variations are up to 50 nT a day; solar storms and urban noise cause further field changes.

To compensate for field changes and "lock" the zero field in the coils, we used a method described in detail in [11]. Since it is an open-loop mechanism, it allows the removal of the rotating sensor while maintaining the magnetic vacuum. In principle, we use numerically recalculated field variations from the AUX-mag to compensate for field changes in the current-source firmware. The variations are small enough not to couple the coils with the AUX magnetometer. When the field in the coils is changed to high values i.e. during the calibrations, the compensation is updated accordingly not to react on the disturbing field from the coils. Fig. 7 shows the stability of the zero field together with the AUX-mag reading. To show the feasibility of the system, a car was parked 10-m away from the coil system, causing a change of only 1.5 nT.

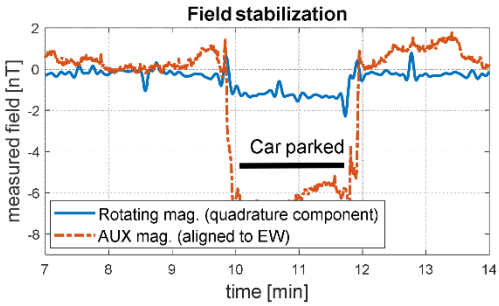

Fig. 7. Time record of stabilized zero-field (E-W). For testing, a car was parked 10-m away from the coils causing only 1.5 nT change. The large peak every 1.5 minutes is caused by wi-fi calibration of the ESP module.

V. Conclusion

We have designed a zero-field system with a rotating fluxgate magnetometer, which to our knowledge is unique in its parameters and simplicity. By creating a wireless fluxgate magnetometer and rotating it, we are able to overcome any offset errors inherent to those magnetometers. We managed to create less than 0.5 nT in 1-m Helmholtz coils, and we were able to keep this magnetic vacuum stable for minutes without a larger deviation than 1 nT.

REFERENCES

[1] R. L. Wilson, "Palaeomagnetism in Northern Ireland. Part 1. The thermal demagnetization of natural magnetic moments in rocks," Geophysical Journal of Royal Astronomical Society, vol. 5, pp. 45–58, 1961.

[2] Shifrin, V. Ya, V. N. Khorev, J. Rasson, and Po Gyu Park, "International comparisons to establish the traceability in the global network of geomagnetic observatories to SI units," Metrologia, vol. 51, Technical Supplement, 2014.

[3] V. Ya. Shifrin, E.B. Alexandrov, T.I. Chikvadze, V.N. Kalabin, N.N. Yakobson, V.N. Khorev and P.G. Park, "Magnetic Flux Density Standard for Geomagnetometers," Metrologia, vol. 37, No. 3, p. 219, 2000

[4] K. Weyand, "Maintenance and dissemination of the magnetic field unit at PTB," IEEE Trans. Instrum. Meas., vol. 50, Issue 2, pp. 470-473, 2001

[5] P. Brown,T. Beek, C.Carr, H. O'Brien, E. Cupido, T. Oddy, TS Horbury. "Magnetoresistive magnetometer for space science applications," Measurement Science and Technology; vol 23(2), p. 025902, 2012.

[6] P. Ripka, M. Pribil and M. Butta, M., "Fluxgate offset study," IEEE Transactions on Magnetics, vol. 50 (11), pp.1-4, 2014.

[7] V. Fúra, V. Petrucha, and A. Platil, "Construction of an AMR magnetometer for car detection experiments," Proc. IOP Conf. Series, Mater. Sci. Eng, vol. 108, 2016.

[8] K. Prihoda, M. Krs, B. Pesina, J. Blaha, "MAVACS-A new system of creating a non-magnetic environment for paleomagnetic studies," Cuadernos de Geología Ibérica, Vol. 12, pp. 223-250, 1989.

[9] M. Janosek, "Parallel fluxgate magnetometers," in High Sensitivity Magnetometers, Springer: Cham, 2017, pp. 41-61

[10] A. Poncelet, A. Gonsette and J. Rasson, "Several years of experience with automatic DI-flux systems: theory, validation and results," Geoscientific Instrumentation, Methods and Data Systems, vol. 6(2), p.353, 2017.

[11] M. Janosek, M. Dressler, V. Petrucha, V. and A. Chirtsov, " Magnetic calibration system with interference compensation. IEEE Transactions on Magnetics,", vol. 55(1), p. 6000104, 2018

2.2.3 Estimating the Overhauser magnetometer accuracy

The Overhauser magnetometer (OVM) is used an for accurate estimate of the total magnetic flux density value F = ||**B**||, i.e. the scalar magnitude of the field vector, based on the measurement of the hydrogen proton precession frequency in magnetic field after an initial polarization [50]. Due to its precision better than 15 pT [51], its high off-the-shelf accuracy and insensitivity to magnetic field gradient –as opposed to proton-precession magnetometers (PPM)– it is widely used in geophysics as a reference instrument at magnetic observatories providing the total field value *F*; for geology; archaeology and exploration [25], and for calibrations of magnetometers and coil systems [52]. Its accuracy is theoretically given only by the frequency measurement accuracy –by the precision of frequency estimation and accuracy of its ovenized reference oscillator– and the agreed value of the gyromagnetic Larmor constant. The precision of frequency measurements [53] in an OVM is higher than for a PPM magnetometer mainly by the superior signal-to-noise-ratio and longer duration of its precession signal [50]. However, similarly to a PPM, OVM accuracy is given also by magnetic cleanliness of the mechanical sensor assembly (threads, bolts, cable, etc.); by the residual heading error[1] and also by any contamination of the proton-rich fluid due to its ageing or leakage. The overall accuracy of a custom-built OVM in [51] has been found as ± 0.25 nT (1σ-uncertainty) including all these effects.

CMI and CTU were participating in an international comparison of a „travelling standard“ OVM [54] in order to verify the calibration capabilities in the geomagnetic field range of the individual participants. This comparison turned out to be useful for establishing the uncertainty of two GSM-19 [59] OVM's of the CTU and CMI. The results in "*Determination of the Overhauser magnetometer uncertainty"* [J13] show up to ± 0.5nT reading difference, i.e. ± 100 ppm, after accounting for the calibration method uncertainty: this is 5× higher than the manufacturer specification. The large reported uncertainties of NPL and PTB seem to be a direct result of uncompensated anthropogenous noise (see Chapter 2.2.1).

[J13] *Determination of the Overhauser magnetometer uncertainty (2015).* **Author contribution:** 16.7% (1/6). Proposal of methodology, data acquisition, and comparison result. **Citations:** 1

[1] – For geophysical measurements with static attitude, i.e. in geomagnetic obseratories, however, the heading error is stable and can be excluded from uncertainty budget when calibrated as an systematic error.

Journal of ELECTRICAL ENGINEERING, VOL 66. NO 7/s, 2015, 26-29

DETERMINATION OF THE OVERHAUSER MAGNETOMETER UNCERTAINTY

Michal Ulvr — Aleš Zikmund* — Josef Kupec** — Michal Janošek* — Michal Vlk*** — Tomáš Bayer*****

Overhauser magnetometers are the basic instruments for scalar measurements; however, their accuracy is determined at the time of manufacture only. Because of various effects affecting the gyromagnetic ratio of the used fluid or the stability of the oscillators in the circuitry, their accuracy should be verified during the instrument lifetime. Specific methodology of data processing and determination of the Overhauser magnetometer uncertainty is described in this paper.

Keywords: Overhauser magnetometer, Earth's magnetic field, comparison, uncertainty

1 INTRODUCTION

The international comparison APMP.EM-S14 [1] was a great opportunity, how to determine the accuracy (the uncertainty) of the Overhauser magnetometer by metrology institutes and geomagnetic observatories. Czech Metrology Institute (CMI) participated on this comparison with Faculty of Electrical Engineering of Czech Technical University in Prague (CTU) and Institute of Geophysics of the Academy of Sciences of the Czech Republic (IG) collaboration in the field of Earth magnetic field measurement. The transfer standard - a modified Overhauser magnetometer type MMPG-1 - was supplied by the pilot laboratory VNIIM, Russia. Its accuracy has been determined with an uncertainty of 0.054 nT [2]. CTU-CMI and IG dispose of a commercial portable quantum magnetometer type GSM-19 based on the Overhauser effect.

Various methods can be used for the comparison. The usual methodology exploits a calibrated coil system, where the magnetometers are compared in an artificial magnetic field generated by the coil. This method is more convenient when the testing of the magnetometers should be carried out in their whole measurement range. However, the coil system, that mostly also cancels the Earth's magnetic field, is very complicated equipment and it brings further uncertainties which have to be considered.

Therefore, we decided to simplify the comparison method and have performed the magnetometer calibration in a very quiet Earth's magnetic field in the nonmagnetic building of Budkov geomagnetic observatory (member of the INTERMAGNET network). The short-time variation of the magnetic field is below 0.1 nT at this place.

2 THEORY

The transfer standard and the compared magnetometer were placed at two distant pillars (designation B and D) to avoid mutual influences (see Fig 1 and Fig. 2). The magnetometers were oriented in the same correct position with respect to the magnetic field vector. The magnetic flux density (MFD) was measured with a repeating time interval of 3 s and later the values were transfered to PC. Unfortunately, the magnetometers could not be perfectly synchronized and so a stable time difference of 1 s occurred, but this was not significant from the statistical point of view.

As a first step, we measured values $B_{F(A)i}$ with CTU-CMI magnetometer (designation F) in position A at time t_i and also the values $B_{V(B)i}$ with VNIIM magnetometer (designation V) in position B at almost the same time t_i . The mutual position of the magnetometers was swapped after about five minutes, so that we obtained values $B_{F(B)j}$ measured with magnetometer CTU-CMI in position B at time t_j and also values $B_{V(A)j}$ measured with magnetometer VNIIM in position A at almost the same time t_j. Measurement (swapping) was repeated by this way several times.

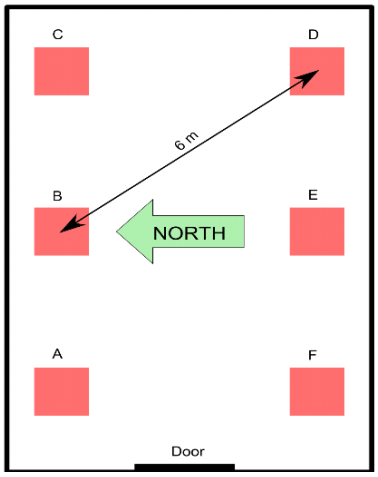

Fig. 1. Position of marble pillars (B and D) in Budkov absolute pavilion

Because of an existing, non-zero gradient between the two pillars A and B (approx. 6 nT) and because of the Earth's field variations, specific methodology for data processing has been used. Differences $B_{F(A)i}$ - $B_{V(B)I}$ at time t_i

* Czech Technical University in Prague, Technická 2, 166 27 Prague, Czech Republic, janosem@fel.cvut.cz, ales.zikmund@fel.cvut.cz, ** Czech Metrology Institute, V Botanice 4, 150 72 Prague, CZ, mulvr@cmi.cz, jkupec@cmi.cz, *** Institute of Geophysics, Academy of Sciences of the Czech Republic, Boční II/1401, 141 31 Prague, CZ, vlk@ig.cas.cz, tbr@ig.cas.cz

ISSN 1335-3632

were calculated together with differences $B_{F(B)j}$ - $B_{V(A)j}$ of opposite series at time t_j . By subtracting these differences we have got a double value of B difference between the two points A and B due to the MFD gradient. If the differences were summed and the result was divided by 2, the difference of the two compared magnetometers was obtained. Let us select n values of $B_{F(A)i}$ - $B_{V(B)i}$ and the same number of values of $B_{F(B)j}$ - $B_{V(A)j}$ that we have assigned randomly to the previous $B_{F(A)i}$ - $B_{V(B)i}$.

Fig. 2. Actual test setup with the compared magnetometers at the pillars B and D

The described calculation corresponds to an equation

$$\Delta_{FVi} = \frac{\left[\left(B_{F(A)i} - B_{V(B)i}\right) + \left(B_{F(B)j} - B_{V(A)j}\right)\right]}{2}, \quad (1)$$

which is a result of one measurement of difference between the CTU-CMI and VNIIM magnetometers. The MFD gradient between the pillars was obtained during the comparison of the magnetometers according to

$$grad_i B_{FV} = \frac{\left[\left(B_{F(A)i} - B_{V(B)i}\right) - \left(B_{F(B)j} - B_{V(A)j}\right)\right]}{2}. \quad (2)$$

The IG magnetometer (designation G) and VNIIM magnetometer were compared by the same way and in the same positions (difference Δ_{GV}). Also CTU-CMI and IG magnetometers were compared by the same way (difference Δ_{FG}), but this comparison was carried out three weeks later. These differences and relevant gradients can be calculated from

$$\Delta_{GVi} = \frac{\left[\left(B_{G(A)i} - B_{V(B)i}\right) + \left(B_{G(B)j} - B_{V(A)j}\right)\right]}{2}, \quad (3)$$

$$\Delta_{FGi} = \frac{\left[\left(B_{F(A)i} - B_{G(B)i}\right) + \left(B_{F(B)j} - B_{G(A)j}\right)\right]}{2}, \quad (4)$$

$$\mathrm{grad}_i B_{GV} = \frac{\left[\left(B_{G(A)i} - B_{V(B)i}\right) - \left(B_{G(B)j} - B_{V(A)j}\right)\right]}{2}, \quad (5)$$

$$\mathrm{grad}_i B_{FG} = \frac{\left[\left(B_{F(A)i} - B_{G(B)i}\right) - \left(B_{F(B)j} - B_{G(A)j}\right)\right]}{2}. \quad (6)$$

We decided to use linear regression (application of method of the least squares) to offset these differences. If the known measured differences are marked as $y_1 = \Delta_{FV}$, $y_2 = \Delta_{VG}$ and $y_3 = \Delta_{GF}$ then

$$y_1 + y_2 + y_3 = k, \quad (7)$$

$$(A_1 + b_1) + (A_2 + b_2) + (A_3 + b_3) = k, \quad (8)$$

where A_1, A_2, A_3 are the correct values of differences, for which following condition is valid where u_γ is the coefficient γ_p of MFD conversion to frequency, u_{grad} is the uncertainty of the influence of vertical and horizontal gradients upon measured difference of B, u_{sysV} is the uncertainty of the influence of systematic uncertainty of measurement with magnetometer VNIIM, u_{sys} is the systematic uncertainty of measurement with magnetometer CTU-CMI or IG, u_h is the uncertainty of the influence of inhomogeneity of B upon measurement of B, u_t is the uncertainty of the influence of non-identical time of measurement of B, and u_m is the uncertainty of the influence of materials of

$$A_1 + A_2 + A_3 = 0, \quad (9)$$

and b_1, b_2, b_3 are the parameters, for which is the following equation valid

$$b_1^2 + b_2^2 + b_3^2 = \min. \quad (10)$$

Equation (10) is valid for following values of b_i

$$b_1 = b_2 = b_3 = \frac{k}{3}. \quad (11)$$

For the measured differences we get from (7) and (8)

$$y_1 = A_1 + b_1, y_2 = A_2 + b_2, y_3 = A_3 + b_3 \quad (12)$$

and by substituting the formula (11) we obtain the correct values A_1, A_2, A_3 as follows

$$A_1 = y_1 - \frac{k}{3}, \quad (13)$$

$$A_2 = y_2 - \frac{k}{3}, \quad (14)$$

$$A_3 = y_3 - \frac{k}{3}. \quad (15)$$

The equations (15,16,17) can be also expressed as

$$A = \frac{2y_1 - y_2 - y_3}{3}, \quad (16)$$

$$B = \frac{2y_2 - y_1 - y_3}{3}, \quad (17)$$

$$C = \frac{2y_3 - y_1 - y_2}{3}. \quad (18)$$

Table 1. Uncertainty budget

Source of uncertainty	Type of uncertainty	Sensitivity coefficient	Standard uncertainty value (nT)
u_γ	B	1	0.015
u_{grad}	B	1	0.100
u_{sysV}	B	1	0.025
u_{sys}	B	1	0.100
u_{h}	B	1	0.050
u_{t}	B	1	0.050
u_{m}	B	1	0.075
Standard deviation of measurement	A	1	0.026
Combined uncertainty	-	-	0.18
Expanded uncertainty (k=2)	-	-	0.36

Table 2. Mean gradient results

	Δ	<MFD> (nT)	σ, k=2 (nT/m)	$<\Delta_T>$ (nT/m/h)
CTU-CMI vs. VNIIM	Δ_{FV}	48582	0.887 ± 0.010	-0.035
IG vs. VNIIM	Δ_{GV}	48587	0.927 ± 0.014	+0.040
CTU-CMI vs. IG	Δ_{FG}	48577	0.784 ± 0.012	+0.060

Table 3. Measurement results (before linear regression)

	Δ (nT)	σ_{EXP}(nT)
Δ_{FV}	-0.144	0.020
Δ_{GV}	-0.496	0.012
$_{FG}$	0.274	0.022

3 UNCERTAINTY ANALYSIS

The A-type uncertainty of the measurement is calculated from

$$u_{sA} = \sqrt{\frac{\sum_{i=1}^{n}\left(x_i - \bar{x}\right)^2}{n\cdot\left(n-1\right)}}, \tag{19}$$

$$\bar{x} = \frac{1}{n}\sum_{i=1}^{n} x_i , \tag{20}$$

where n is the total number of measurements and is the arithmetic mean of the individual measured values x_i.

The B-type uncertainty of the Overhauser magnetometer measurements has several components, as follows

$$u_{sB} = \sqrt{u_\gamma^2 + u_{grad}^2 + u_{sysV}^2 + u_{sys}^2 + u_h^2 + u_t^2 + u_m^2}, \tag{21}$$

where u_γ is the coefficient γ_p of MFD conversion to frequency, u_{grad} is the uncertainty of the influence of vertical and horizontal gradients upon measured difference of B, u_{sysV} is the uncertainty of the influence of systematic uncertainty of measurement with magneto-meter VNIIM, u_{sys} is the systematic uncertainty of measurement with magnetometer CTU-CMI or IG, u_{h} is the uncertainty of the influence of inhomogeneity of B upon measurement of B, u_{t} is the uncertainty of the influence of non-identical time of measurement of B, and u_{m} is the uncertainty of the influence of materials of marble blocks.

The values of all type uncertainties including the expanded uncertainty are presented in Tab. 1.

Magnetometer comparison of the Mean value of < MFD> the Mean gradient of the MDF and its expanded standard deviation σ at k =2, and the Mean time change of gradient during measurement $<\Delta_T>$ - are in Table 2.

4 COMPARISON RESULTS

The arithmetic mean values Δ_{FV}, Δ_{GV}, Δ_{FG} and experimental standard deviations s_{FV} , s_{GV} , s_{FG} for evaluation of type A uncertainty were calculated from n measurement values by chosing several section of measurement (about two hundreds from each section, disregarding the values when the magnetometers were moved). These results of measured differences are presented in Table 3.

Mean values of measured gradients during the comparison are presented in Table 2. The least squares method described above was applied on the results from Table 3 and then the final comparison results were determined as

$$\Delta_{FV} = (-0.17 \pm 0.36)\ \mathrm{nT},$$
$$\Delta_{GV} = (-0.47 \pm 0.36)\ \mathrm{nT},$$
$$\Delta_{FG} = (0.30 \pm 0.36)\ \mathrm{nT}.$$

The final international comparison APMP.EM-S14 results of all participants who used different methods (Overhauser magnetometer, NMR magnetometer and AMR magnetometer) are in Fig. 3

5 CONCLUSIONS

A specific methodology of data processing for the international comparison of MMPG-1 Overhauser magnetometer was described. Also the uncertainty and uncertainty sources analysis of the Overhauser magnetometer measurements were determined during this comparison.

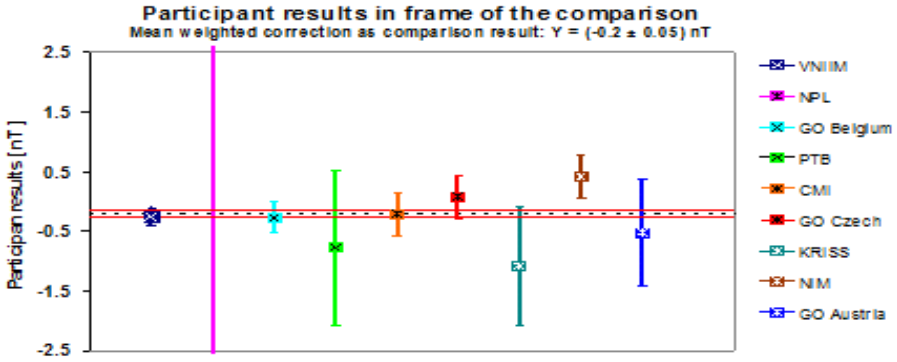

Fig. 3. Final results of APMP.EM-S14 international comparison for nominal value of 50 μT. GO Czech: IG magnetometer results and CMI: CTU-CMI magnetometer results

The final comparison results show that the proposed method was successful – after processing the final comparision results from all participants by the pilot laboratory, the required corrections of our results were only -0.02 nT (F) or 0.28 nT (G), respectively.

REFERENCES

[1] SHIFRIN, V. Ya. - KHOREV, V. N. - RASSON, J. - PARK, P. G.: International comparisons to establish the traceability in the global network of geomagnetic observatories to SI units, In *Metrologia*, 2014, vol. 51, No. 1A, ISSN 1681-7575.

[2] SHIFRIN, V. Ya. - ALEXANDROV, E.B. - CHIVKADZE, T.I - KALABIN, V.N. - JAKOBSON, N.N. - KHOREV, V.N. - PARK, P.G.: Magnetic Flux Density Standard for Geomagnetometers, In *Metrologia*, Vol. 37, No. 3, 2000, pp. 219-227.

[3] SHIFRIN, V. Ya. - KHOREV, V. N. - KALABIN, V. N. - PARK, P. G.: Experimental estimation of the accuracy of modern scalar quantum magnetometers in measurements of the Earth's magnetic field, In *Physics of the Earth and Planetary Interiors*, Vol. 166, No. 3-4, 2007, pp. 147-152.

[4] SHIFRIN, V. Ya. - KHOREV, V. N. - KALABIN, V. N. - PARK, P. G.: Metrological researces of proton and optical pumping eomagnetometers, In Proc. of CPEM 2008, pp. 458-459.

[5] DURET, D. - LEGER, J.M. - FRANCES, M. - BONZOM, J. - ALCOUFFE, F. - PERRET, A. - LLORENS, J.C. - BABY, C.: Performances of the OVH magnetometer for the Danish Oersted satellite, In *IEEE Transactions on Magnetics*, Vol. 32, No. 5, 1996, pp. 4935 - 4937.

[6] PARK, P. G. - KIM WAN-SEOP - KIM MUN-SEOG - SHIFRIN, V. Ya.: Measurement and analysis of earth's magnetic field based on low-magnetic field standards, In Proc. of CPEM 2014, pp. 358-359.

Received 30 November 2015

Michal Ulvr born in Jablonec nad Nisou, Czech Republic, in 1983, graduated with honors in measurement techniques from the Czech Technical University in Prague in 2008. He has been working at the Czech metrology institute since 2008, and is now a metrologist in the Department of Electromagnetic Quantities of the Laboratory of Fundamental Metrology in Prague. His research interest is in metrology in the area of magnetic quantities.

Aleš Zikmund was born in Mostiste in 1985. He received the master's degree from the Faculty of Electrical Engineering, Czech Technical University in Prague, Prague, Czech Republic, in 2009, where he is currently pursuing the Ph.D. degree with the Department of Measurement. His current research interests include magnetic calibrations by using nonlinear optimizations.

Josef Kupec was born in Prague, Czech Republic, in 1940. He received the master degree in experimental physics from Charles University in Prague, Prague, in 1962, and the CSc (PhD) degree from Slovak Technical University in Bratislava, Slovakia, in 1984. He has been with the Czech Metrology Institute, Prague, since 1962, he is currently a Metrologist with Department of Electromagnetic Quantities. His current research interests include metrology in the area of magnetic quantities.

Michal Janošek was born in Varnsdorf, Czech Republic, in 1980. He received the MSc degree in measurement and instrumentation and the PhD degree from the Faculty of Electrical Engineering, Czech Technical University in Prague, Prague, Czech Republic, in 2007 and 2014, respectively. His current research interests include application of magnetic sensors in gradiometers and magnetometers.

Michal Vlk was born in Pečky near Kolín in 1979. He graduated in Communication Engineering in 1998 at secondary technical school in Kutná Hora, received Master degree in Radioengineering in 2005 and PhD degree in Acoustics in 2015; both at the Department of Radioengineering of the Faculty of Electrical Engineering of the Czech Technical University (FEE-CTU) in Prague. He is currently working as observatory technician at the detached workplace (Observatory Budkov) of the Institute of Geophysics of the Czech Academy of Science since 2011. His interests are low-to-mid-frequency low-noise and high-power electronics.

Tomáš Bayer was born in Příbram, Czech Republic, in 1973. He receives the Master degree at the Faculty of Sciences, Comenius University Bratislava, Slovakia, and PhD degree at the Czech Technical University, Faculty of civil Engineering. he worked at Institute for Soil and Water Conservation, Prague. He is specialized for geomagnetic activity forecasting, absolute measurements and geomagnetic field measurement of volcanic residues in west Bohemia.

2.2.4 Uncertainty of angular calibrations

The article „*Estimation of angular deviations in precise magnetometers*“ [J6] focuses on establishing the uncertainties of triaxial magnetometer non-orthogonal angles. The author used a calibrated, non-magnetic, triaxial gimballing / tilting device with electronic readout to confirm and compare the results of multiple magnetometer calibration methods providing the three misalignment angles. The goal was to establish the uncertainty of angular calibrations at SANSA [4], as these are a result of a „scalar calibration“ in the coil system, utilizing an iterative, non-linear solver of the nine non-linear equations describing the magnetometer gains, offset and mutual axes misalignments [55]. The 2.5-m compensated triaxial Helmholtz coil system at SANSA has the additional benefit of very low magnetic noise during the calibration compared to other sites (on a magnetically quiet day, the noise is below 0.5 nT peak-to-peak). The standard deviation of multiple calibration batches was below 1×10^{-3} degree, which is however not yet the final result: it is necessary to include the calibration uncertainty estimate, uncertainty of current sources, etc. The final uncertainty has risen to about 60×10^{-3} degrees and we were able to match the results of direct measurements and scalar calibrations within their uncertainty estimates. Our estimated coil orthogonality uncertainty was probably too pessimistic – in a calibration study of a 50-cm coil system with a NMR magnetometer [56], the orthogonality uncertainty was below 10×10^{-3} degree. We have also shown that the spread of angular alignment in multiple pieces of the same fluxgate magnetometer type follows Gaussian distribution, since the fluxgate sensor alignment and assembly of the researched magnetometer [57] is a manual operation.

Another topic which was researched mainly by the 2nd co-author, was the increase of calibration yield for routine calibrations of large batches of sensors, i.e. an effort to decrease the required calibration time while not compromising the uncertainty. This is of importance e.g. for calibration of spacecraft attitude magnetometers used in large orbital constellations. As the desired calibration result is a matrix including the sensor-to-frame attitude, we proposed a „stopper“ in the coil system: its attitude can be calibrated in few steps. For subsequent calibrations (i.e. during a day) the attitude is deemed constant, the time-consuming procedure of laser-and-mirror alignment to the coil system could be avoided.

[J6] *Estimation of angular deviations in precise magnetometers (2019).* **Author contribution:** 40%. Establishing the uncertainty, supervising the research and experiments; and article composition. **Citations:** 2

Magnetic Instruments

Estimation of Angular Deviations in Precise Magnetometers

Michal Janosek[1*], Elda F. Saunderson[2,3], Michal Dressler[1*], and Daniel J. Gouws[2]

[1]Faculty of Electrical Engineering, Department of Measurement, Czech Technical University in Prague, Praha 16000, Czech Republic
[2]Directorate Space Science, South African National Space Agency, Hermanus 7200, South Africa
[3]Department of Electrical and Electronic Engineering, Stellenbosch University, Stellenbosch 7600, South Africa
* Member, IEEE

Received 1 Aug 2019, revised 1 Sep 2019, accepted 12 Sep 2019, published 26 Sep 2019, current version 22 Oct 2019.

Abstract—Capabilities for calibrations of angular deviations of sensor triplets in precise magnetometers were evaluated in a 2.5 m, triaxial Helmholtz coil facility. The coil system is located in a magnetically quiet environment at SANSA Space Science in Hermanus, South Africa. The angular calibration results obtained from the "thin-shell" calibration procedure were compared with direct measurements on a nonmagnetic tilting/rotational platform. One-year expanded uncertainty of angular deviation calibrations is estimated as 6×10^{-2} degrees of arc; 3×10^{-4} degrees coil orthogonality is possible when doing a numerical recalibration and correction on a short-term basis. In addition, an approach for obtaining body-to-sensor angular calibrations is presented, allowing for speed-up of the calibrations and possibly increasing their accuracy and repeatability by avoiding alignment to the coils with a laser beam and leveling.

Index Terms—Magnetic instruments, magnetometer calibrations, precision, uncertainty.

I. INTRODUCTION

Precise triaxial magnetometers require careful calibration to establish all nine parameters (gains, offsets, nonorthogonal angles) [Olsen 2003]; if the magnetometer is intended for navigation and data fusion with another physical sensor, three further parameters are needed to describe their (mutual) attitude [Primdahl 2002, Vcelak 2009, Figaro 2011].

SANSA Space Science in Hermanus, South Africa operates a square, 2.5 m triaxial Helmholtz coil system for magnetic sensor calibrations (see Fig. 1). With the help of a LEMI-025 magnetometer at a distance of 40 m, it is possible to suppress local magnetic field variations occurring during the calibration run due to the high homogeneity of the Earth's magnetic field at the location (the site houses a magnetic observatory). Moreover, the on-site magnetic noise is less than 10 pT/$\sqrt{\text{Hz}}$ at 1 Hz, even during the day. The coil system is mechanically leveled and calibrated on a periodic basis; the magnetic direction of the east–west axis is aligned with a reference laser.

We present our current approach of calibrating the angular deviations, the results, estimation of the uncertainty, and a novel method of estimating the body-frame-related calibration.

II. MAGNETOMETER MODEL AND CALIBRATION PROCEDURE

A. Magnetometer Model

To express nonorthogonalities between magnetometer axes, we use the typical model as described by Olsen [2003] (see Fig. 2).

In this case, the X-axis is assumed as reference, the nonorthogonal Y'-axis is assumed to be in plane, only rotated by an angle u_1 from the X-axis, i.e., the XY (XY') plane is the reference plane. Then, the Z'-axis is established by two nonorthogonal angles u_2 and u_3 deviating from the ideal Z-axis orthogonal to the XY plane. The effect of nonorthogonality can be then expressed with a matrix $\mathbf{P}$ containing the angular deviations u_1, u_2, and u_3 [Olsen, 2003]

$$\mathbf{P} = \begin{bmatrix} 1 & 0 & 0 \\ -\sin(u_1) & \cos(u_1) & 0 \\ \sin(u_2) & \sin(u_3) & \sqrt{\left(1 - \sin^2(u_2) - \sin^2(u_3)\right)} \end{bmatrix}. \quad (1)$$

We can then establish the magnetic field vector $\mathbf{b}_{\text{mag}}$ from the magnetometer output vector $\mathbf{e}_{\text{mag}}$ by multiplying it by the inverse nonorthogonality matrix $\mathbf{P}^{-1}$ and the inverse sensitivity matrix $\mathbf{S}^{-1}$, after subtracting the offset vector $\mathbf{e}_{\text{o}}$ in arbitrary (engineering) units

$$\mathbf{b}_{\text{mag}} = \left[\text{b}_{\text{mag}X}\ \text{b}_{\text{mag}Y}\ \text{b}_{\text{mag}Z}\right]^{\text{T}} = \mathbf{P}^{-1}\mathbf{S}^{-1}(\mathbf{e}_{\text{mag}} - \mathbf{e}_{\text{o}}). \quad (2)$$

So far the calibration is considered to an X-axis referenced frame ("sensor frame"), which can differ from the mechanical enclosure of

Fig. 1. Square triaxial coil system at SANSA.

Corresponding author: Michal Janosek (e-mail: janosem@fel.cvut.cz). IEEE Magnetics Society Magnetic Frontiers: Magnetic Sensors, Lisbon, Portugal, 24-27 June 2019.
Digital Object Identifier 10.1109/LMAG.2019.2944125

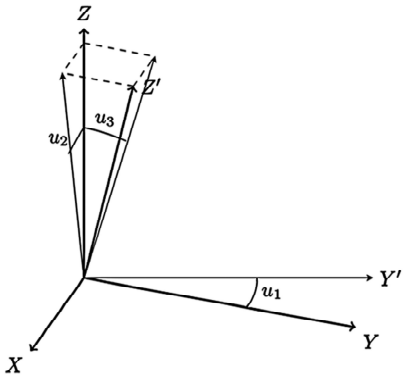

Fig. 2. Triaxial magnetometer sensor frame depicting the nonorthogonal angles u_1, u_2, and u_3 [Olsen 2003].

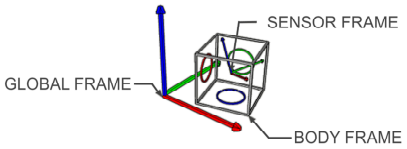

Fig. 3. Definition of the magnetometer sensor frame, magnetometer body frame, and global frame (= coil frame).

the magnetometer ("body frame") (see Fig. 3), which is positioned in the frame of the coil system ("global frame").

To be able to fully describe the measured field with reference to the magnetometer body frame, we need to add an additional rotational matrix **R** describing the rotation of the sensor frame to the body frame. $\mathbf{R}^{-1}$, $\mathbf{P}^{-1}$, and $\mathbf{S}^{-1}$ can be combined to a single matrix **A**

$$\mathbf{b}_{\text{mag}} = \mathbf{R}^{-1}\mathbf{P}^{-1}\mathbf{S}^{-1}(\mathbf{e}_{\text{mag}} - \mathbf{e}_{\mathbf{o}}) = \mathbf{A}(\mathbf{e}_{\text{mag}} - \mathbf{e}_{\mathbf{o}}). \tag{3}$$

B. Calibration Procedure

The calibration procedure relies generally on solving an overdetermined system of (2), i.e., $\mathbf{b}_{\text{mag}}$ is created by the coil system, $\mathbf{e}_{\text{mag}}$ is measured, and the $\mathbf{R}^{-1}\mathbf{P}^{-1}\mathbf{S}^{-1}$ matrix can be established, or even the components of **P** matrix (2) individually to obtain the nonorthogonal angles u_1, u_2, and u_3. The test field vector $\mathbf{b}_{\text{coil}}$ is usually generated with an (almost) constant magnitude but different vector orientations to cover all possible spherical angles.

This "thin-shell" calibration procedure employed with the SANSA Helmholtz coil system uses the spherical harmonic analysis method (**SHM**), and is described in detail by Risbo [2002, 2003]. The magnetometer is currently aligned with the coil system using a laser beam aligned to the magnetic axes of the coil system, reflecting off a mirror attached to magnetometer enclosure. The resulting "sphere" of magnetic field vectors is decomposed using SHM and least squares minimization. The result is a 3×3 matrix related to the magnetometer body frame containing the $\mathbf{A} = \mathbf{R}^{-1}\,\mathbf{P}^{-1}\,\mathbf{S}^{-1}$ matrix.

To obtain nonorthogonal angles from the **A** matrix, we used "*QR*" decomposition to obtain the orthogonal and upper triangular matrix [Anderson 1992]. To obtain the $\mathbf{P}^{-1}$ components, we also used the "scalar-calibration" procedure described in Olsen [2003] on the same thin-shell data (omitting the **R** matrix). In this method, the minimization criteria to find the $\mathbf{P}^{-1}\mathbf{S}^{-1}$ matrix (or its components) are the root-mean-square error (**RMSE**) between the scalar magnitude of the applied vector in the coil system $b_{\text{sca}} = \|\mathbf{b}_{\text{coil}}\|$ and the scalar magnitude of estimated vector $\|\mathbf{b}_{\text{mag}}\|$

$$\text{RMSE} = \sqrt{\frac{1}{N-1}\sum_i^N \left(\|\mathbf{b}_{\text{mag}}(\text{i})\| - b_{\text{sca}}(\text{i})\right)^2}. \tag{4}$$

We verified our results with a different calibration procedure, which is described in Brauer [2001], and we did not find any significant difference in the results of these methods.

Table 1. Results of angular deviation measurements.

	u_1 [°]	u_2 [°]	u_3 [°]	Remark
LEMI-011B #319				
08/2013	–1.71	–0.51	4.94	5 years old
22/10/2018	–1.68	–0.47	4.83	
22/10/2018	–1.64	–0.53	4.75	Direct meas.
24/10/2018	–1.68	–0.47	4.84	
LEMI-011B #379				
05/2017	1.39	–1.42	–0.84	1 year old
15/10/2018	1.38	–1.42	–0.85	
18/10/2018	1.39	–1.41	–0.87	
18/10/2018	1.33	–	–	Direct
19/10/2018	*1.41*	*–1.36*	*–0.94*	*Coils misaligned*
20/10/2018	*1.42*	*–1.37*	*–0.93*	
22/10/2018	*1.41*	*–1.37*	*–0.94*	
22/10/2018	*–*	*–1.32*	*–0.90*	*Direct meas.*

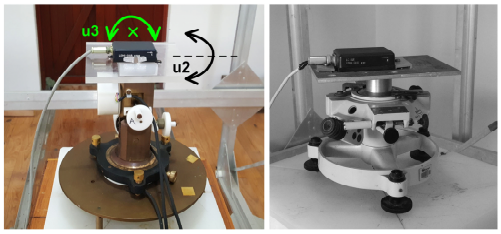

Fig. 4. Tilting jig with optical encoders for u_2 and u_3 measurements (left), Askania circle for horizontal u_1 angle estimation (right).

III. ANGULAR CALIBRATIONS

A. Calibration Results

The results were obtained on a single magnetometer type LEMI-011B [ISR Lviv 2019], serial numbers 319 and 379, respectively (see Table 1). The angles, obtained by the method of Olsen [2003], were compared to a direct measurement using an Askania circle with about $\pm 1.5' = 2.5 \times 10^{-2}$ degrees accuracy, and with a two-axis tilting jig with modified optical encoders (Heidenhain ERO-1324-3600, estimated total system accuracy about $\pm 100'' = 3 \times 10^{-2}$ degrees) (see Fig. 4). The direct measurements were done by minimizing response at the respective axis when energizing the orthogonal coil (by rotation/tilting), and then doing the same for the second axis in pair.

We can see that the short-time spread of calculated angles of about ±0.01° (LEMI-011B #319) increases up to 0.1° for the five-year period, which is more than anticipated. Also, the comparison to the direct measurement was within 0.1°, although the instruments are by far more accurate. In the following section, we will try to derive the sources of this uncertainty. It is evident that the coil calibration is an

Table 2. Result of coil system recalibration.

	u_1 [°]	u_2 [°]	u_3 [°]
Before cal. 10/2018	9.7×10^{-3}	6.4×10^{-2}	2.6×10^{-3}
After cal. 07/2019	2×10^{-4}	-3×10^{-4}	0

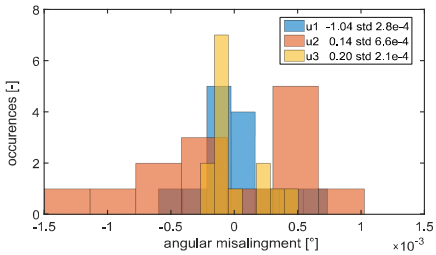

Fig. 5. Histogram with average values and the standard deviation for the calculated nonorthogonal angles (LEMI-011S, 15 runs).

issue, which can be seen in the LEMI-011B #379 results—on October 19, 2018, the coils were misaligned accidentally, which manifested itself in the angular calibration results.

We could verify the coil misalignment by doing a subsequent calibration of the coil system with an Overhauser magnetometer using a modified scalar-calibration procedure [Olsen 2003]. Further details are found in Risbo [2003, p. 677]. The nonorthogonality of the coils was up to 6×10^{-2} degrees and could be suppressed below 3×10^{-4} degrees with the above-mentioned recalibration (see Table 2).

B. Estimating the Uncertainty

To establish the uncertainty of our calibration, we performed 15 consecutive test runs and calculations on a single sensor—the space-qualified LEMI-011S (see Fig. 1). The resulting histogram for the estimation of the three angles is shown in Fig. 5—standard deviation was found below 6.6×10^{-4} degrees. As the measurements were performed over a 12 h span, these statistics also cover the effects of on-site noise and imperfections of the Earth's field cancellation in the coil system. We can consider the standard deviation as a type-A measurement uncertainty U_A [Joint Committee for Guides in Metrology 2008].

As shown previously, we can experience coil nonorthogonality and its instability (see Table 2). This would be the source of type-B calibration uncertainty U_B for both the thin-shell method and direct measurement. The combined uncertainty U ($k = 2$ for 95% probability coverage) is then [Joint Committee for Guides in Metrology 2008]

$$U = 2\sqrt{U_A^2 + U_{B\text{coils}}^2 + U_{B\text{inst}}^2} \tag{5}$$

where U_{Bcoils} is the type-B measurement uncertainty due to coils calibration, U_A is the standard deviation of the results calculated above, and U_{Binst} is the uncertainty of the instrument used in the direct comparison if applicable (either Askania or tilting device).

For numeric calculations from the thin-shell run, we assume the worst case observed standard deviation being U_B and coil misalignment with assumed triangular distribution being U_A

$$U_{\text{calc}} = 2\sqrt{(6.6 \times 10^{-4})^2 + \left(\frac{0.064}{\sqrt{6}}\right)^2} = 5.2 \times 10^{-2}. \tag{6}$$

For the direct measurement, where we have the instrument uncertainty in addition (assuming a uniform distribution of scale error), we can write

$$U_{\text{meas}} = 2\sqrt{(6.6 \times 10^{-4})^2 + \left(\frac{0.064}{\sqrt{6}}\right)^2 + \left(\frac{0.03}{\sqrt{3}}\right)^2} = 6.2 \times 10^{-2}. \tag{7}$$

In Fig. 6, the calculation and measurement results for u_2 on LEMI-011B #379 are plotted, together with uncertainties. The other angles are not displayed because of similarity of the results. We see that our measurements of u_2 fit well within the established uncertainty.

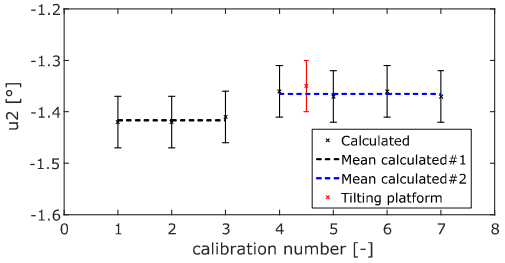

Fig. 6. Calculated u_2 angles (black) with their mean values, together with direct measurement on tilting platform (red). The four points on the right are after the coil calibration changed. LEMI-011B #379 used.

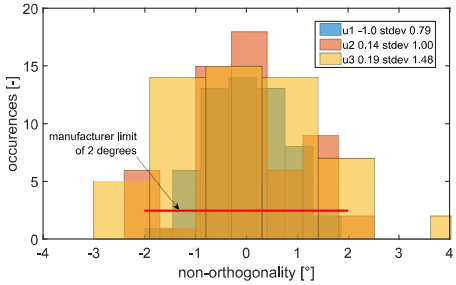

Fig. 7. Statistics on single magnetometer type (LEMI-011B); 57 pieces tested.

C. Statistics on a Single Magnetometer Type

We demonstrate the necessity of angular calibrations on the example of a set of 57 magnetometers (LEMI-011B). From the results in Fig. 7, we see that the datasheet value [LEMI011B] of maximum 2° nonorthogonality is met within one standard deviation. The maximum observed value was +4.5°. This is due to the fact that the precise fluxgate magnetometer sensors are mostly hand assembled.

IV. BODY-FRAME-RELATED CALIBRATIONS

A. Current Method

The alignment of the device under test to the global (coil frame) is performed with a laser aligned to the magnetic axis of the horizontal

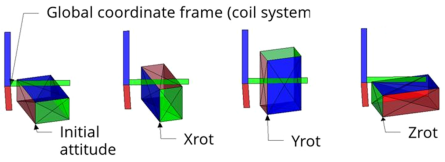

Fig. 8. Four-step rotation to obtain body-frame-referenced calibration.

coil and a precise mirror glued to the magnetometer body. This requires a skilled operator, and thus we propose a novel method for body-frame calibration.

B. Proposed Procedure

The procedure relies on magnetometer calibration in four (or even just three) particular attitudes. The first sensor attitude can be arbitrarily chosen. The three remaining are attitudes with the sensor rotated along its body axis X, Y, and Z, respectively (see Fig. 8). In each step, a thin-shell calibration is performed and a rotation matrix $\mathbf{R}$ is obtained from the calibration matrix result (by QR decomposition).

The rotation matrix from the initial (aligned) position to the first arbitrary position can be written as $\mathbf{R}_0 = \mathbf{R}_{\mathrm{BG}}\mathbf{I}\mathbf{R}_{\mathrm{SB}}$, where $\mathbf{R}_{\mathrm{SB}}$ represents the sensor to body frame rotation, $\mathbf{R}_{\mathrm{BG}}$ is the body frame to global frame (= coil frame) rotation, and $\mathbf{I}$ is unit matrix. The next rotation matrix to a different attitude after rotation in body frame is $\mathbf{R}_g = \mathbf{R}_{\mathrm{BG}}\mathbf{R}_i\mathbf{R}_{\mathrm{SB}}$. We can then obtain the relative rotation $\mathbf{Q}$ between the two attitudes $\mathbf{R}_0$ and $\mathbf{R}_g$ as follows:

$$\mathbf{Q}_i = \mathbf{R}_0^T\mathbf{R}_i = \mathbf{R}_{\mathrm{SB}}^T\mathbf{R}_i^T\mathbf{R}_{\mathrm{SB}}. \tag{8}$$

The eigenvector $\mathbf{v}_x$ of relative rotation describes the axis of rotation in reference to a sensor frame

$$\mathbf{v}_x = \mathrm{eigvec}\left(\mathbf{Q}_x\right) = \mathbf{R}_{\mathrm{SB}}^T\mathrm{eigvec}\left(\mathbf{R}_x^T\right). \tag{9}$$

Then, the rows of rotation matrix $\mathbf{R}_{\mathrm{SB}}$ are the eigenvectors of relative rotations

$$\mathbf{v}_x = \mathbf{R}_{\mathrm{SB}}^T[1\ 0\ 0]^T$$

$$\mathbf{R}_{\mathrm{SB}}^T = \left[\mathbf{v}_x\ \mathbf{v}_y\ \mathbf{v}_z\right]^T.$$

The angles of rotations do not have to be precise as long as the rotation axes are perpendicular. Due to arithmetic imprecision and mostly due to imperfections of rotations axis attitudes, it is better to create $\mathbf{R}_{\mathrm{SB}}$ from each pair of eigenvectors and to calculate the third vector to form a normal basis each time. The spread of rotation angles between each calculated matrix can then be used to evaluate the results. A similar approach to the extraction body frame related calibration is described by Primdahl [2002].

The main advantage of using the reference plane and block to perform the rotation is that once the four-step method is executed for one magnetometer, the reference plane/block (in arbitrary attitude) is also calibrated at the same time. After that, only one-step calibration in the initial position can be used to calibrate other magnetometers, which saves time and reduces possibilities of human error.

C. Procedure Verification

We verified the procedure using a triaxial anisotropic magnetoresistance (**AMR**) magnetometer [Novotný 2019] mounted with respect to the reference block and plane (see Fig. 9). The magnetometer in its square enclosure was then rotated according to Fig. 8. The $\mathbf{R}_{\mathrm{SB}}$ matrices were calculated, and the Euler angles for the sensor frame to body frame rotation (SF2BF) and global frame to body frame (GF2BF) were established.

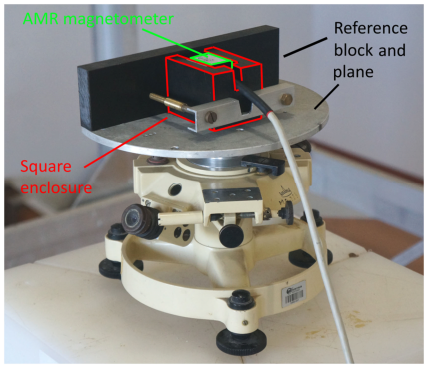

Fig. 9. Magnetometer (triaxial AMR) is fitted in a square enclosure mounted to the reference block and plane.

Table 3. Results of the proposed procedure.

SF2BF	Z [°]	Y' [°]	X'' [°]
initial 0°	−0.90 ± 0.01	−0.52 ± 0.03	−0.34 ± 0.03
initial 20°	−0.94 ± 0.04	−0.55 ± 0.01	−0.22 ± 0.09
initial 60°	−0.96 ± 0.04	−0.55 ± 0.01	−0.23 ± 0.10
mean value	−0.93 ± 0.04	−0.54 ± 0.02	−0.27 ± 0.09
GF2BF diff.	−0.01 ± 0.04	0.08 ± 0.03	0.01 ± 0.11

In Table 3, results for three different initial attitudes (rotation in azimuth about 0°, 20°, and 60°) are given. Ideally, the results would be the same. Z, Y', and X'' are the Euler angles in this order.

The last row shows the differences between alignment to the coil axes as obtained by the current method (leveling and laser alignment) and the new method. We see that both methods agree within 0.1°.

V. CONCLUSION

We show that our one-year expanded ($k = 2$) uncertainty of angular deviation calibrations is about 6×10^{-2} degrees of arc, which we found as the coil-system nonorthogonality, which can improve down to 3×10^{-4} degrees with a numerical coil recalibration. The numerical results were comparable with direct measurements within this uncertainty. We also see that with hand-assembled fluxgate magnetometers, it is crucial to calibrate the orthogonal angles.

The proposed method to obtain body-frame-related magnetometer calibration was verified. Its advantage is not only time saving, but avoidance of tilting and leveling of the device under test, to align it with the coil system, which brings further uncertainties. Even with a nonideal reference block and magnetometer enclosure, the body-frame-referenced calibration resulted in a spread of ±0.1°. Also, the agreement to the current procedure with leveling and laser alignment is within 0.1°, which also corresponds to inclinometer resolution. In order to improve the results, a more precisely machined reference block and reference enclosure are required—with 10 μm manufacturing precision, 6×10^{-3} degrees would be possible.

ACKNOWLEDGMENT

This work was supported by the Czech Technical University through the Ministry of Education Mobility Grant "International Mobility of Researchers in CTU," CZ.02.2.69/0.0/0.0/16_027/0008465.

REFERENCES

Anderson E, Bai Z, Dongarra J (1992), "Generalized QR factorization and its applications," *Linear Algebra Appl.*, vol. 162, pp. 243–271, doi: 10.1016/0024-3795(92)90379-O.

Bonnet S, Bassonpierre C, Godin C, Lesecq S, Barraud A (2009), "Calibration methods for inertial and magnetic sensors," *Sensors Actuators A: Phys.*, vol. 156, pp. 302–311, doi: 10.1016/j.sna.2009.10.008.

Brauer P, Merayo J M G, Risbo T, Primdahl F (2001), "Magnetic calibration of vector magnetometers: Linearity, thermal effects and stability," in *Proc. ESA Conf. SP-490*. [Online]. Available: http://citeseerx.ist.psu.edu/viewdoc/summary?doi=10.1.1.34.2694

Dietrich M R, Bailey K G, O'Connor T P (2017), "Alignment of a vector magnetometer to an optical prism," *Rev. Sci. Instrum.*, vol. 88, 055105, doi: 10.1063/1.4983146

Figaro D, Bryant T, Boeen A (2011), "Spherical calibration and reference alignment algorithms," U.S. Patent 7930148. [Online]. Available: https://patents.google.com/patent/US7930148B1/en

ISR Lviv (2019), "Super-low-power three-components flux-gate magnetometer LEMI-011," National Space Agency of Ukraine and National Academy of Sciences of Ukraine. [Online]. Available: https://www.isr.lviv.ua/lemi011.htm. Accessed on: Aug. 20, 2019.

Joint Committee for Guides in Metrology (2008) "Evaluation of measurement data—Guide to the expression of uncertainty in measurement," International Organization for Standardization, Geneva, Switzerland. [Online]. Available: https://www.bipm.org/utils/common/documents/jcgm/JCGM_100_2008_E.pdf

Novotný D, Petrucha V, Janošek M (2019), "A digitally compensated AMR magnetometer," *IEEE Trans. Magn.*, vol. 55, 4000805, doi: 10.1109/TMAG.2018.2873235.

Olsen N, Tøffner-Clausen L, Sabaka T J, Brauer P, Merayo J M G, Jørgensen J L, Léger J M, Nielsen O V, Primdahl F, Risbo T (2003), "Calibration of the Ørsted vector magnetometer," *Earth, Planets Space*, vol. 55, pp. 11–18, doi: 10.1186/BF03352458.

Pajunpää K, Klimovich E, Korepanov V, Posio P, Nevalinna H, Schmidt W, Genzer M, Harri A-M, Lourenço A (2007), "Accredited vector magnetometer calibration facility," *Geophysica*, vol. 43, pp. 59–76. [Online]. Available: http://www.geophysica.fi/pdf/geophysica_2007_43_1-2_059_pajunpaa.pdf.

Primdahl F, Brauer P, Merayo J M G, Petersen J R, Risbo T (2002), "Determining the direction of a geometrical/optical reference axis in the coordinate system of a triaxial magnetometer sensor," *Meas. Sci. Technol.*, vol. 13, pp. 2094–2098, doi: 10.1088/0957-0233/13/12/339.

Risbo T, Brauer P, Merayo J M G, Nielsen O, Petersen J R, Primdahl F, Olsen N (2002), "Ørsted calibration mission: The thin shell method and the spherical harmonic analysis," in *Proc. ESA Conf. SP-490*.

Risbo T, Brauer P, Merayo J M G, Nielsen O V, Petersen J R, Primdahl F, Richter I (2003), "Ørsted pre-flight magnetometer calibration mission," *Meas. Sci. Technol.*, vol. 14, pp. 674–688, doi: 10.1088/0957-0233/14/5/319.

Vcelak J (2009), *Application of Magnetic Sensors for Navigation Systems*. Aachen, Germany: Shaker Verlag, pp. 77–98.

3 Precise magnetometers in geophysical observations

3.1.1 Race-track fluxgate variometer

The race-track fluxgate sensor has been widely used utilized at author's workplace [U2] [58] and has been improved in terms of noise and size [18]. The advantage of the race-track sensor is its lower demagnetizing factor than of a ring-core, yielding in lower noise for compact dimensions. The article „*Low-noise magnetic observatory variometer with race-track sensors*" [J6] shows 1–Hz noise ASD about 5 pT/√Hz, achieved with 30-mm race-track sensors; the sensor core has been wet-etched and embedded in a fibre-glass sandwich [18]. The as-cast state of the amorphous core was chosen for long-term stability: temporal relaxation of any induced anisotropy –supported by the "easy-axis" magnetization cycles of the 2nd harmonic fluxgate mode– might theoretically introduce long-term parameter drifts.

[J6] *Low-noise magnetic observatory variometer with race-track sensors (2016).* **Author contribution:** 40%. Instrument design – analog part, sensor construction; field testing, data processing and article composition.

3.1.2 The „1-pT" OFM fluxgate magnetometer

The following journal article „*1-pT noise fluxgate magnetometer for geomagnetic measurements and unshielded magnetocardiography"* [J5][2] describes summarization of research and development towards „bridging the gap" between the OFM fluxgate in a laboratory (performing well in an open-loop, with a lock-in amplifier and a magnetic shield); and a practical magnetometer with dynamic range covering full Earth's field vector. The trials at the low-noise site of SANSA proved its low-frequency noise ASD of 1.5 pT/√Hz at 1 Hz, which turned out to be comparable or better than a co-located HTS SQUID. Also, the feasibility of OFM magnetometer for magneto-cardiography (MCG) is shown: its low noise allowed for an unshielded MCG measurement with signal processing limited to just subtracting the reading of a 12-cm distant sensor in transverse gradiometer configuration.

[J5] *1-pT noise fluxgate magnetometer for geomagnetic measurements and unshielded magnetocardiography (2020).* **Author contribution:** 28%. Geophysical part: planning and setting up experiments, data processing and presentation; article composition. **Citations:** 36

[2] Earlier results appear in a preceding a conference publication [P4]; the presented article [J5] is the extended version of it.

Low-noise magnetic observatory variometer with race-track sensors

M Janošek[1], **V Petrucha**[1] **and M Vlk**[2]
[1]Czech Technical University in Prague, Technicka 2, 166 27 Prague, Czech Republic
[2]Institute of Geophysics, Bocni II/140, 141 31 Prague, Czech Republic

E-mail: janosem@fel.cvut.cz

Abstract. We present a low-noise, high-stability observatory magnetometer with race-track sensors, as developed by the Czech Technical University in Prague for National Observatory of Athens. As opposed to the standard instruments, we used our novel race-track fluxgate sensors with planar oval core which were cut by state-of-the art pico-second UV-laser. The noise performance of the complete electronics and sensor chain is below 6 pT/√Hz @ 1 Hz. The electronics uses 24-bit 200-Hz A/D converter with simultaneous sampling and all digital processing is done in FPGA. The variometer with the sensors mounted on a MACOR cube has been successfully calibrated by scalar method.

1. Introduction

The requirements on observatory variometers, as they are in service either officially in IAGA network, or for other purposes, are very demanding. It is necessary to achieve very high stability and low noise to record truly the diurnal Earth's field variations and possible magnetic storms (the IAGA dynamic range requirement is ± 3000 nT). Standard full-field magnetometers can be used for this purpose, if their limited dynamic range (about 130 dB for 24-bit converters) is not a problem. However, if there is a requirement of achieving very low noise, i.e. «20 pT/√Hz @ 1 Hz, compensation of the main Earth's field components (horizontal and vertical in the northern hemisphere) is inevitable [1]. Such low noise variometer, if having suitable bandwidth, can be used for advanced ionospheric or geomagnetic studies (i.e. observing Schumann resonances and other effects). We have implemented a low noise compensation of the main field components, which allowed us to use our low-noise race-track sensors (< 6 pT/√Hz) in the variometer.

2. Magnetometer construction

For the variometer, we used in-house race-track fluxgate sensors with laser-cut cores, slightly modified and downscaled of the heritage CTU sensor [2]. Two of the sensors (N-S and vertical) have an additional coil wound, which is used for main field component offset in the respective direction. For that purpose, we have implemented an ultra-low-noise (< 0.5 pT/√Hz) current source using LTC6655 reference, which feeds the additional coil wound directly on top of the feedback coil of the sensor. In that manner, the possible mutual angular imperfections and mainly their temperature instabilities are minimized. The sensor triplet (each sensor dimension are approx. 30x8x1mm^3) is mounted on a solid MACOR holder maintaining large thermal conductivity and geometric stability,

nevertheless, also the temperature of the holder is monitored – see Fig. 1. The sensor holder is attached to marble base plate, which is to be leveled. The "standard part" of the magnetometer electronics relies on a "standard low-noise magnetometer" manufactured by the CTU and CSRC (Czech Space Research Centre) company, it uses FPGA for signal clock generation and ADC driving and the power supply for the analog part is galvanically isolated. The electronics returns uncalibrated ADC data on RS232 for the three magnetometer axis and also the head temperature measurement. With the help of the low-noise current-source for the NS and vertical field offsets, the baseline noise due to electronics/ADC resolution is less than 1 pT/√Hz@ 1 Hz in the final variometer range of ±3750 nT.

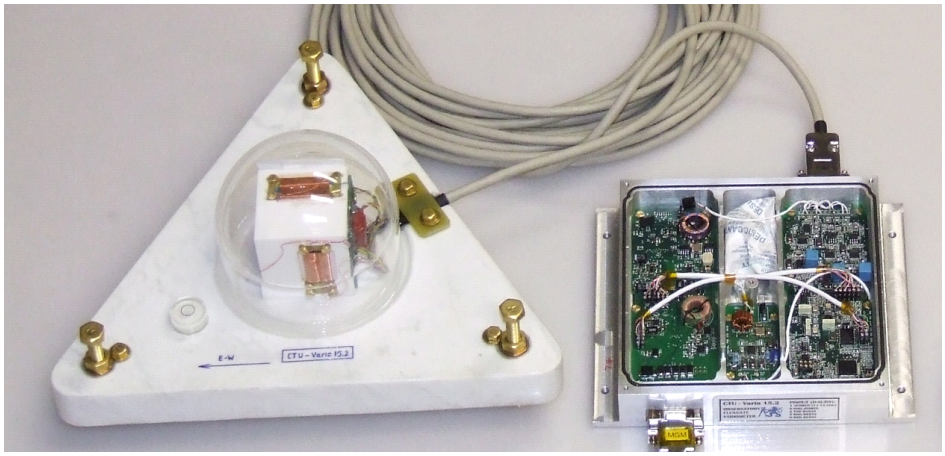

Figure 1. The presented variometer – left: the triaxial race-track fluxgate triplet mounted on MACOR holder on marble base plate, right: the electronics (cover removed).

3. Variometer calibration

A non-trivial task is variometer calibration. We used following approach using scalar calibration technique [3, 4]:

- First, the offset fields have been disabled and the magnetometer has been operated in ±75000 nT range, and a scalar calibration was done. The calibration RMS error was < 2nT.
- After the calibration, the sense resistor (the magnetometer is feedback operated) was measured .
- The resistor has been replaced with 20x larger value (again precisely measured after soldering), and the gain coefficients have been recalculated.
- In this manner, we can use the scalar calibration results, which are comparable or superior to standard techniques utilizing coils and flux density standards [5].

Valuable information has been obtained in trial tests of the magnetometer (before range expansion) during 1-month testing at the Budkov observatory (IAGA BDV). As seen from table 1, we could see ageing of the sense resistors (Vishay PLT thick film series) – the values changed by 250-300 ppm after one-month burn-in. T_c of the gain channels could be also computed: it was 8, 16 and 9 ppm/K, respectively which is a combination of thermal expansion of the compensating coil and sense resistors. From the table, it can be also seen that the mutual angular position was stable with temperature.

From the comparison of the total field computed from the variometer and values from standard instruments at the observatory, we can see that the gains have finally settled after 14 days (Figure 3).

Table 1 – The calibration results – after one month of running and with changed temperature.

Calibration date	temp [℃]	S1 [normalized]	S2 [normalized]	S3 [normalized]	O1 [nT]	O2 [nT]	O3 [nT]	Φ1 [°]	Φ2 [°]	Φ3 [°]
14.12.2014	12	1.2996	1.3068	1.2935	-18.77	-189.59	8.46	0.71	-0.09	0.11
23.1.2015	19	1.2991	1.3064	1.2933	-17.30	-190.25	7.95	0.72	-0.08	0.08
23.1.2015	6	1.2989	1.3062	1.2931	-18.22	-197.94	9.58	0.71	-0.09	0.08

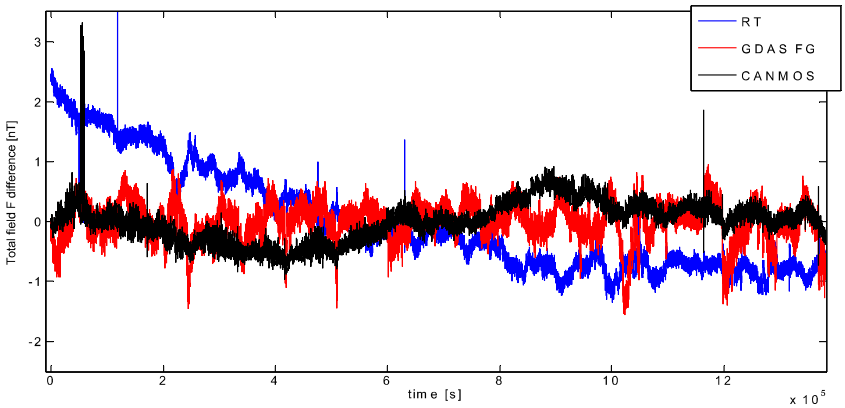

Fig. 3 – Instrument stability (before range expansion and with offsets off) – 14 days of total field (F) are displayed. Blue – CTU variometer, red and black – instruments of BDV observatory

4. Noise performance

Since the sensor head is too large to be tested in our in-house magnetic shield and also because of the need of creating a low-noise counter-acting magnetic field (simulating the NS and vertical Earth's field component), we have decided to do this test in the calm magnetic field at the BDV observatory. Typical record is depicted in the spectrogram on Figure 4: it can be seen that even at the quiet locality, man-made AC noise is present in the low-frequency spectra. AC traction noise at 16 2/3 Hz from Austria / Germany railways is also visible as burst. The source of the 3 Hz noise is still unknown.

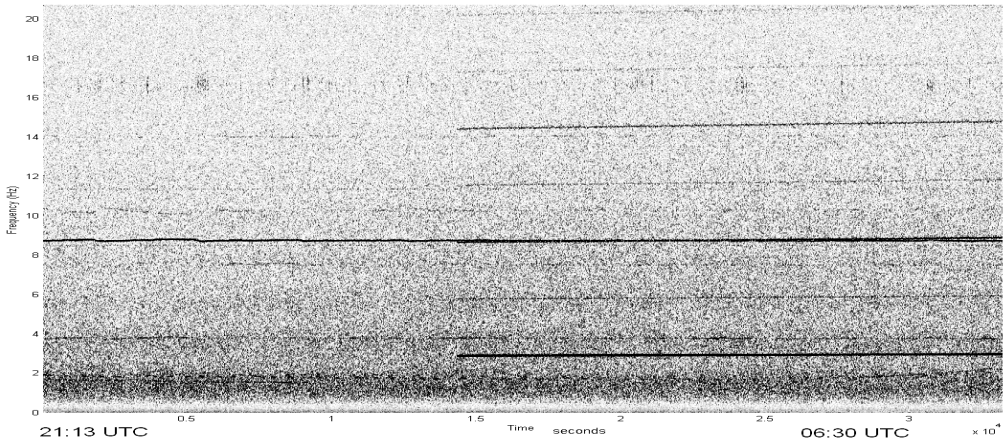

Fig. 4 – The 0.01-20 Hz spectrogram during 8-hours of logging (vertical axis)

If we have chosen a quiet part of the day, we were able to compute noise spectra as depicted in Fig.5: it can be seen, that in the vertical axis, the measured magnetic noise PSD was better than 6 pT/√Hz @ 1 Hz; however the EW and NS axes were noisier which is presumably by the magnetic field noise at the locality since the sensors in the triplet perform equally well.

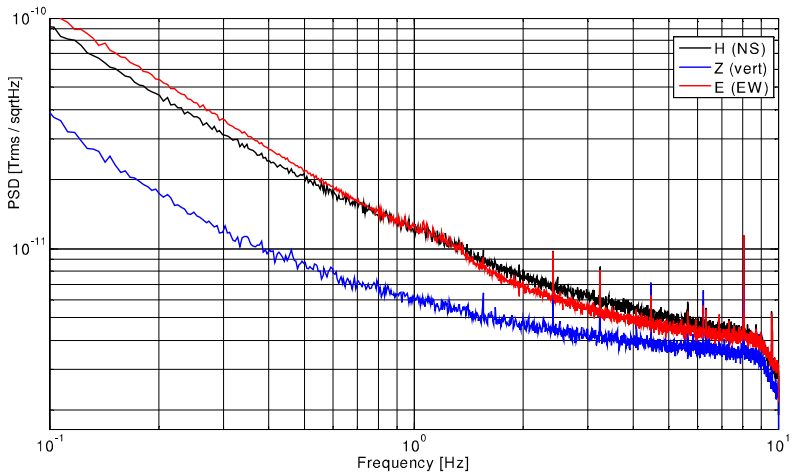

Fig. 5 – The magnetic field noise at the BDV observatory as logged with the variometer.

5. Conclusion

We have successfully built and calibrated a closed-loop operated, observatory variometer with race-track sensors. Its measured noise performance in real conditions of < 6 pT/√Hz @ 1 Hz is up to our knowledge on the state of the art in the field. We have used a simple yet effective calibrating method to obtain the instrument parameters. Further improvements are sought in terms of fluxgate sensors performance with a target of < 3 pT/√Hz. In this case however, from our experience, a large shielded room and low-noise artificial magnetic field generator would be necessary to confirm the instrument performance.

Acknowledgment
This research has been on-contract supported by the National Observatory of Athens. We would like to thank also to Dr. Tomas Bayer from the Budkov observatory for his help during calibrations at the Budkov observatory and Jan Vyhnanek of CTU for participating on the instrument development.

References

[1] Vlk M 2013, Modernisation of the Narod fluxgate electronics at Budkov Geomagnetic Observatory, *EGU General Assembly 2013, Vienna, Austria*, EGU2013-7721
[2] Ripka P 1993, Race-track fluxgate sensors, *Sensors and Actuators A: Physical*, **37** 417-421.
[3] Petrucha V et al 2009, Automated system for the calibration of magnetometers, *Journal of Applied Physics*, **105(7)** 07E704.
[4] Olsen N et al 2003, Calibration of the Ørsted vector magnetometer. *Earth, planets and space*, **55**(1) 11-18.
[4] Zikmund A and Janosek M 2014, Calibration procedure for triaxial magnetometers without a compensating system or moving parts, *IEE International Instrumentation and Measurement Technology Conference (I2MTC) Proceedings*, 473-476

1-pT Noise Fluxgate Magnetometer for Geomagnetic Measurements and Unshielded Magnetocardiography

Michal Janosek, Mattia Butta, Michal Dressler, Elda Saunderson, David Novotny, and Coenrad Fourie

***Abstract*— We present the development of a low-noise, fundamental-mode, orthogonal fluxgate magnetometer with four amorphous, annealed ferromagnetic wires. The 1-Hz noise obtained in the open and closed loop is as low as 0.75 and 1.5 $pT_{rms}/\sqrt{Hz}$, respectively, with the white noise level about 0.6 $pT_{rms}/\sqrt{Hz}$. This is to the best of our knowledge the lowest figure published for a fluxgate magnetometer so far. By using the annealed sensor cores, we also found the offset drift to decrease approximately six times to 2.5 nT/K. We compared the instrument performance to a low-noise observatory magnetometer when doing geomagnetic measurements and show that it is fully suitable for measurements at mHz frequencies, e.g., magnetotellurics. The magnetometer performance enables room-temperature, unshielded magnetocardiography. With a gradiometric arrangement of two sensors, we were able to perform an MCG measurement in ambient field, and even without averaging, the signal could be clearly resolved.**

***Index Terms*— Fluxgate, fundamental-mode, noise.**

I. Introduction

LOW-NOISE fluxgate magnetometers (with amplitude noise density below 10 $pT_{rms}/\sqrt{Hz}$) are mostly built as instruments for measuring weak magnetic fields in the Earth's field range (up to 50 μT). They are used at geomagnetic observatories [1], for navigation and prospection [2], attitude correction, and scientific experiments in aerospace [3], in magnetotellurics [4], [5], nondestructive testing and evaluation [6], nanoparticle detection [7], and in other subjects where vectorial response to magnetic fields and a room-temperature operation are required. Low-noise sensors were used even for shielded magnetocardiography [8], [9]. Fig. 1 shows the requirements for these applications—it is evident that 1-pT performance would be beneficial, together with the desired frequency range of about 1 mHz to 100 Hz.

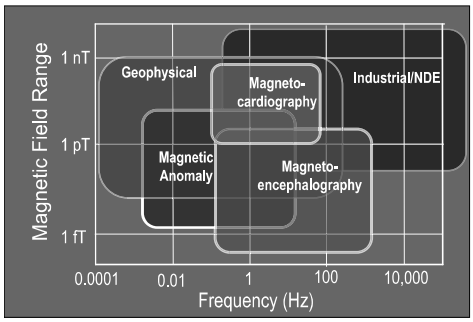

Fig. 1. Overview of applications of 1-pT level sensors [16].

As for parallel-type fluxgates, the state-of-the-art magnetometers exhibit noise levels of about 3–4 $pT_{rms}/\sqrt{Hz}$ at 1 Hz [9]–[12]. The 1-pT noise was obtained with cross correlation measurements and special sensor arrangement in [13]; however, the principle was not exploited any further. Design requirements to use such a low-noise sensor in an observatory variometer were discussed recently in [14].

The other branch of fluxgate sensors, the orthogonal-type, brings low-noise performance only with the fundamental-mode operated fluxgates. They were introduced by Sasada [15] in 2001, and since then, the parameters have continuously improved—the noise decreased from the initial 10 pT down to about 1.5–2 $pT_{rms}/\sqrt{Hz}$ for laboratory devices [17]; with the help of core annealing, sub-pT noise was reported recently [18].

We have to state that the generally accepted disadvantage of fundamental-mode fluxgates is their offset-drift—about 50 nT/K was shown in [17]. This was addressed previously, and the solutions were implemented either in the digital or analog domain [19]–[21], 0.7 nT stability within a 60 °C range was shown in [20]. However, we decided not to use any of these techniques because they tend to increase noise.

In this article, we show the peculiarities of embedding such a low noise fluxgate sensor in a practical magnetometer

Manuscript received August 8, 2019; revised October 2, 2019; accepted October 10, 2019. Date of publication December 24, 2019; date of current version April 7, 2020. This work was supported in part by the Czech Science Foundation (GA ČR) under Grant 16-10591Y (Magnetic Gradiometer Based on Fundamental Mode Orthogonal Fluxgate). The work of M. Janosek was also supported by the Czech Technical University in Prague through the Mobility Grant, International Mobility of Researches in CTU, under Grant CZ.02.2.69/0.0/0.0/16_027/0008465. The Associate Editor coordinating the review process was Boby George. *(Corresponding author: Michal Janosek.)*

M. Janosek, M. Butta, M. Dressler, and D. Novotny are with the Department of Measurement, Czech Technical University in Prague, 16000 Prague, Czech Republic (e-mail: janosem@fel.cvut.cz; buttamat@fel.cvut.cz; dressmic@fel.cvut.cz; novotd12@fel.cvut.cz).

E. Saunderson is with the Directorate Space Science, South African National Space Agency, Hermanus 7200, South Africa (e-mail: esaunderson@sansa.org.za).

C. Fourie is with the Department of Electrical and Electronic Engineering, Stellenbosch University, Stellenbosch 7600, South Africa (e-mail: coenrad@sun.ac.za).

Color versions of one or more of the figures in this article are available online at http://ieeexplore.ieee.org.

Digital Object Identifier 10.1109/TIM.2019.2949205

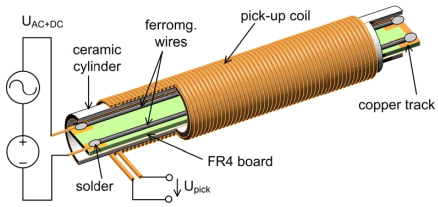

Fig. 2. Sensor structure—two ferromagnetic wires are soldered to an FR-4 printed-circuit-board, forming a "Π shape," and inserted in a ceramic cylinder (silicone filling not shown) with the pickup coil. The excitation voltage U_{ac+dc} is connected to the ferromagnetic wires.

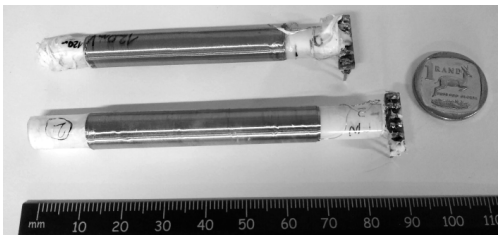

Fig. 3. Photograph of manufactured sensors—both the two-wire, as-cast sensor (top) and the 4-wire, annealed sensor (bottom) are shown.

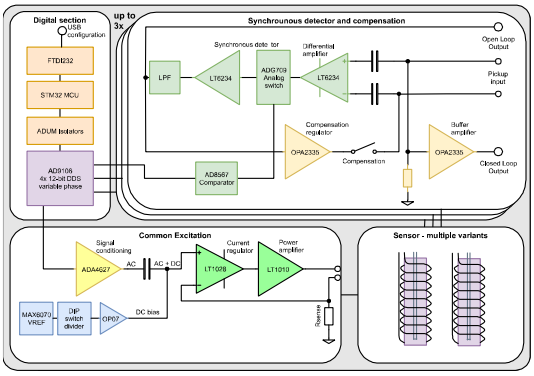

Fig. 4. Block diagram of the magnetometer electronics. A single channel is shown, and the excitation stage is common for all sensors in series.

for real-world measurements out of the laboratory. The noise achieved is actually so low that we were able to perform a magnetocardiography experiment in ambient field.

This article is an extended version of the proceedings article [22] with additional details and results.

II. Sensor Manufacturing

For the fluxgate sensor core, we used Unitika 125AC20 amorphous wires of 125-μm diameter, with the chemical composition $(Co_{0.94}Fe_{0.06})_{72.5}Si_{12.5}B_{15}$.

The sensor was manufactured in two versions: as-cast and joule-annealed [18]—annealing and increasing the effective cross section improved the sensitivity and decreased the magnetic noise (our initial results in [22] used only as-cast, two-wire sensor). The amorphous wires form a "Π-shaped" circuit on an FR-4 printed circuit board (see Fig. 2). In order to further decrease the noise, the FR-4 board with the sensor core was embedded in silicone providing thermal damping [23]. The pickup (also compensation) coil was wound with multiple layers on a ceramic tube, with approximately 1600 and 2000 turns for the as-cast and annealed core, respectively. The core of the annealed sensor was approximately 1-cm longer than that of the as-cast sensor (see Fig. 3). When tuned to the working frequency (cca 47 kHz), and with excitation current of 100-mA p-p and 48-mA ac and dc values, respectively, the sensor sensitivity was about 170 kV/T.

As the fundamental-mode fluxgate operates at a relatively high excitation frequency, the sensor wiring is critical and sensitive to capacitive pickup, e.g., from lights with electronic ballasts. We used subminiature, PTFE insulated cable with two twisted-shielded pairs for excitation and pickup. Balancing and/or shielding the common-mode were found to be critical in the instrument design, as it will be shown later.

III. Electronics Design

A practical magnetometer should meet the noise figures obtained in the laboratory. For the annealed sensors, the laboratory results indicated about 0.7 $pT_{rms}/\sqrt{Hz}$ at 1 Hz [18].

The electronics relies on a precise direct-digital-synthesis (DDS) waveform-generator chip AD9106 and a precise, feedback-loop stabilized power stage. The electronics block diagram is shown in Fig. 4, and its individual parts are thoroughly described in [22].

In the following, we will concentrate on a few critical points and changes in the design that had to be addressed during the transition to annealed, sub-pT sensors.

A. Parasitic Coupling of the Excitation Signal

Because we did not use any push–pull technique for the excitation generator, our excitation is inherently single ended, thus asymmetric with respect to ground. A large ac common-mode voltage (about 3.2 V_{p-p} for annealed wires) is present along the excitation wires, with possible coupling to the wiring of the input coil. This is a disadvantage of first-harmonic fluxgates when compared to second-harmonic types, where the excitation and useful signal are not at the same frequencies simplifying the wiring and balancing. This excitation-to-pickup coupling will, in turn, result in offsets, and their instability will manifest as low-frequency noise. To keep the offsets in the nT-range, we had to use common-mode chokes for decoupling the inputs and the excitation and a fast differential amplifier built with LT6234 for amplifying the input signal.

B. Capacitive Coupling of Ambient Common-Mode Noise

The sensitivity of our sensors is about 200 kV/T at 47 and 100 kHz for the annealed and as-cast sensors, respectively, which for 1 pT results in 7 nV input signal (differential amplifier has a gain of 30). We have found that even when running on batteries, carefully balancing our differential amplifier with

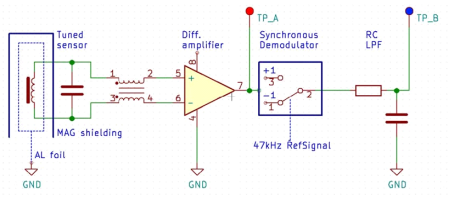

Fig. 5. Detail of the front-end circuitry with a sensor wrapped by a grounded aluminum foil.

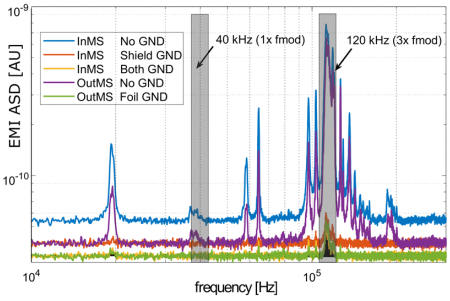

Fig. 6. Spectrum of EMI at the pickup coil (after amplification)—excitation is OFF, and the sensor is an EMI antenna only (TP_A of Fig. 5).

precise resistors, and using common mode chokes and twisted shielded leads, it was finally necessary to shield the sensor with an aluminum foil to obtain 1 $\mathrm{pT_{rms}}/\sqrt{\mathrm{Hz}}$ and better performance. By wrapping the sensor in a thin conductive foil, we were able to suppress most of the capacitive (common-mode) coupling of unwanted signals to the differential amplifier via the sensor wiring—Fig. 5 demonstrates the solution.

We verified this problem by observing the differential amplifier output—TP_A test point shown in Fig. 5—with the excitation switched OFF, i.e., the sensor acted as an antenna only and we were observing only the effect of EMI coupling. Theoretically, with a perfect differential amplifier and infinite common-mode rejection, we would not observe any signal when in the magnetic shield. However, as seen in Fig. 6, connecting the Al foil shield to the instrument ground was necessary to reduce the amplified EMI even in the shielding.

In Fig. 7, we see the noise spectra when such a parasitic signal is demodulated by the synchronous detector of our magnetometer; again, we see that connecting the Al foil shield to the instrument ground is beneficial. Moreover, we could verify that the majority of unwanted noise is due to capacitive coupling; with the sensor in the magnetic shield, the actual noise signal increased because of the metallic shield plates (any EMI induced by magnetic coupling would be eliminated in the shield). Thus, for any further operation, we decided to use the aluminum shielding foil since it does not introduce any significant bandwidth restriction. Also, an alternative excitation frequency should be chosen in areas with high EMI. As the switching synchronous detector behaves as a comb filter on odd harmonics of the switching frequency,

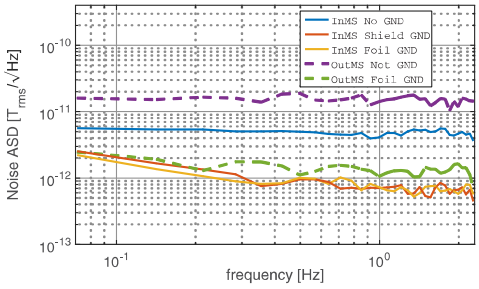

Fig. 7. Demodulated EMI in magnetic units (excitation OFF) in and out of the magnetic shield (In/OutMS)—TP_B of Fig. 5. Various grounding configurations shown—no ground or mag. shield or Al foil was grounded; 0.7 pT limits the magnetometer performance.

therefore, not only the first but also the third-harmonic should stay out of local EMI (see Fig. 6).

C. Closed-Loop Operation

Originally, for closing the feedback loop, we used the OPA2335 amplifier as an integrator [22]. The choice of this particular amplifier was unfortunate because of its high voltage noise despite its excellent dc properties and low bias current. This broadband noise was actually coupled through the pickup/compensation coil itself: the coil constant is about 26 nT/μA. With a 1-kΩ resistor in the feedback loop and anticipated amplification of the error signal $G = 1$, the 60 nV-white amplifier noise results in

$$(60\ \mathrm{nV}/1000\ \Omega)\times(26\ \mathrm{nT}/\mu\mathrm{A}) \cong 1.6\ \mathrm{pT}. \quad (1)$$

By replacing the op-amp with another type (LTC2058) with 5$\times$ lower noise, we would be able to obtain a theoretical noise floor of 0.32 pT. However, as shown later for annealed sensors, this noise limit in a feedback loop was not met, and it is understood to occur due to the imbalance of the pickup coil with respect to ground, which happens when closing the single-ended feedback loop, thus decreasing the achievable CMRR.

D. Output Signal Digitizer

The output of the magnetometer is analog with a $\pm$2.5-V range corresponding to $\pm$12 μT in open-loop (with annealed sensor) or $\pm$25 μT in closed loop (with as-cast sensor).

For the geomagnetic measurements, we used a 24–26-bit DAQ module type "AD-USB24" manufactured by Janascard [24] for data conversion and acquisition. This module uses a custom dual-slope integrating analog-to-digital converter and is galvanically isolated from the USB bus. Moreover, it employs a unique input "chopping" function to avoid the influence of parasitic thermoelectric voltages and uncorrelated noise [25]. The integrating time t_{int} and USB latency limit the bandwidth of the digitized signal; for 80-ms integration time and two samples chopping, our bandwidth was about 2 Hz (220-ms sampling time). When using a gain of 102$\times$ (approximately 100 nT range), the equivalent 1-Hz noise was about 50 $\mathrm{fT}/\sqrt{\mathrm{Hz}}$, whereas, for

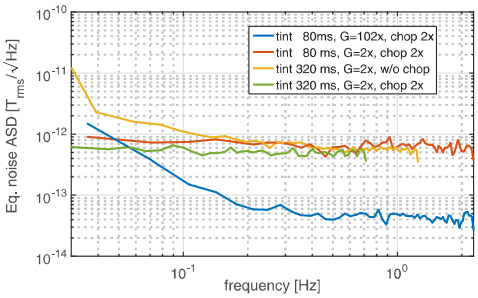

Fig. 8. Equivalent noise of AD-USB24, shown for different gains (2× and 102×), and 80- and 320-ms integration with and without chopping.

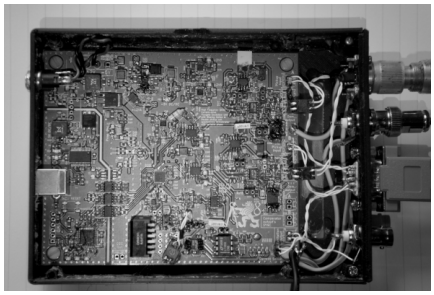

Fig. 9. Magnetometer box shown open. Single printed circuit board with the electronics provides all functions as that of Fig.4.

gain of 2× (full magnetometer range of ±2.5 V), the noise was 0.7 $pT_{rms}/\sqrt{Hz}$ (see Fig. 8). It can be also seen that without chopping, the low-frequency noise increases even with t_{int} =320 ms.

For MCG measurements, where the required bandwidth is higher (about 20 Hz), the outputs of the two channels of the magnetometer were digitized using a NI PXIe-4303 data acquisition card connected to a regular desktop PC. This digitizer features simultaneous 24-bit analog-to-digital converters and a maximum sampling frequency of 51.2 kHz.

E. Final Instrument and Its Noise Performance

The magnetometer in its improved second version compared to [22] is powered by either an external power supply or a 12-V rechargeable battery. Fig. 9 depicts the magnetometer box open to show the electronic board.

The 1-Hz noise of the magnetometer with as-cast sensors was measured in a six-layer shield and was about 1.5 $pT_{rms}/\sqrt{Hz}$ [22]. Noise with the annealed sensors was then measured in a three-layer Permalloy shielding chamber at SANSA Space Science; the shielding factor of about 1000 was enough due to the low ambient field noise, which is below 100 $pT_{rms}/\sqrt{Hz}$ even in a laboratory.

Fig. 10 shows the noise performance with an annealed sensor, as measured with the Janascard DAQ and a gain of 512×. In open loop, the noise was 0.8 $pT_{rms}/\sqrt{Hz}$ at 1 Hz with approximately 0.6-pT noise floor. In closed loop, the 1-Hz noise deteriorated to 1.5 $pT_{rms}/\sqrt{Hz}$; however, at 100 mHz,

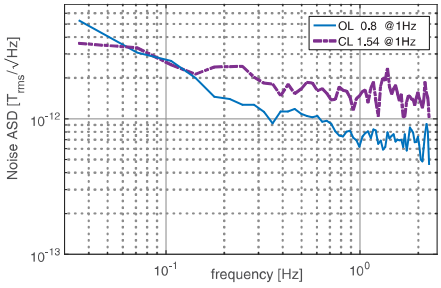

Fig. 10. Noise performance with the annealed sensor in open and closed loops.

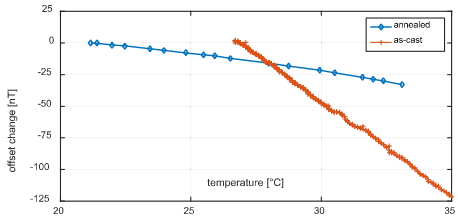

Fig. 11. Offset drift measured in a nonmagnetic thermostated box (sensor head was heated) for the annealed and as-cast sensor.

it is 2.5 $pT_{rms}/\sqrt{Hz}$, which is the same as in open loop. The DAQ noise was negligible on this range (tens of fT $_{rms}/\sqrt{Hz}$).

F. Offset Drifts With Temperature

The temperature drift of the magnetometer offset was established in a nonmagnetic, unshielded chamber, where the sensor head was placed in the E–W direction and temperature swept between room temperature and 33 °C. Because the observed drift was much larger than the change in Earth's field during the measurement, unshielded measurement was sufficient.

The offset temperature coefficient was established as a local derivative of the offset temperature dependencies (see Fig. 11). For the annealed sensor, it was approximately −2.5 nT/K, which is better than −15 nT/K with an as-cast sensor and 50 nT/K reported previously [20].

IV. Geomagnetic Measurements at SANSA Space Science

A. Instruments at SANSA—SQUID and 1-s Observatory Magnetometer LEMI-025

SANSA Space Science, located in Hermanus, South Africa (INTERMAGNET designation HER), operates an unshielded, HTS (LN_2) dc SQUID system, in collaboration with Stellenbosch University and LSBB in Rustrel, Provence, France [26]. Currently, two axes (horizontal and vertical) are running, and the SQUID is measuring geomagnetic field variations [27].

However, as shown previously in our proceedings article [22], the SQUID noise was found to be much higher than anticipated. Even though zero-field cooling and EMI-enhancement techniques were utilized, we were not able to reach the manufacturer noise of 0.3 $pT_{rms}/\sqrt{Hz}$ at

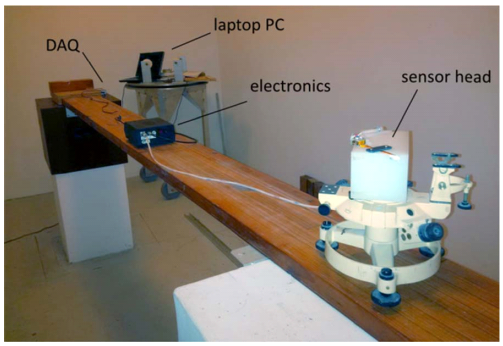

Fig. 12. Sensor placement in the "quiet" hut. The laptop PC with the USB DAQ logger is at a distance of 5 m.

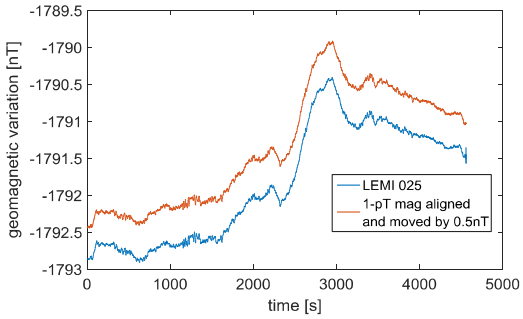

Fig. 13. Alignment of LEMI-025 and 1-pT fluxgate E–W axis sensor. LEMI data offset by 0.5 nT for clarity (17 September, 2018).

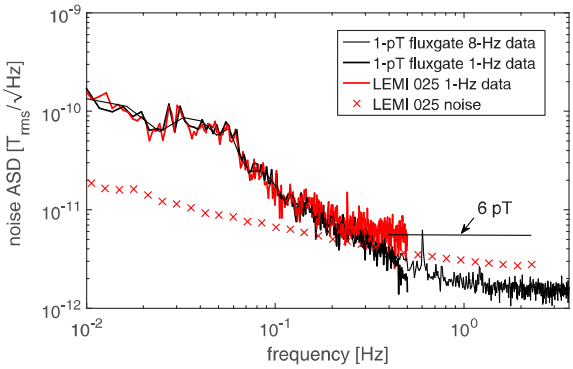

Fig. 14. Geomagnetic field noise spectra as measured with the as-cast sensor and LEMI-025 (17/09/2018). At 1 Hz, 2 $pT_{rms}/\sqrt{Hz}$ was obtained. LEMI-025 noise limit [14] is shown with crosses.

1 Hz; it was actually about 6 and 20 $pT_{rms}/\sqrt{Hz}$ in the X-axis and Z-axis, respectively (Z-axis is noisier due to local disturbances).

For the purpose of a low-noise geomagnetic comparison, we are, thus, comparing our measurements only to the LEMI-025 observatory magnetometer, manufactured by the Institute for Space Research in Lviv, Ukraine, with a sampling frequency of 1 Hz and resolution of 10 pT. The claimed noise level is <10 and 3 $pT_{rms}/\sqrt{Hz}$ at 0.1 and 1 Hz, respectively, which is the state of the art in this field [14], [28].

B. Comparison Methodology

The general difficulty when comparing two vectorial measurements is their alignment. However, for a longer record of the geomagnetic field, diurnal variations and magnetic field fluctuations can be used to mutually align the instruments. The disadvantage of numerical alignment is, however, the propagation of noise from any noisy axis to the other axes. In the case of geomagnetic measurements with anthropogenous noise, the noisiest axis is the vertical one. Thus, numerical "tilting" of the coordinates and noise computation should be avoided, e.g., by precisely leveling the sensor. Numerical rotation in the horizontal plane will not deteriorate the results in terms of noise since the local noise in the E–W and N–S axes is approximately the same.

For this comparison, we used a single sensor mounted on the Askania circle in the "quiet" hut located approximately 50 m away from the next building and 100 m away from the main building area. The magnetometer was powered by batteries, and the USB DAQ unit was connected to a battery-operated laptop PC, approximately 5 m away (see Fig. 12).

The horizontal sensor was rotated to the E–W direction, where the noise at SANSA is lowest. Also, we can then set the gain of our DAQ to 102× (range about ±70 nT) to obtain the noise floor as low as possible. We, thus, rotated it to coincide with the magnetic E–W direction (∼0 nT) since the magnetic field component in the geographic E–W direction is about −4700 nT in Hermanus. The approximate vertical alignment was done with the help of spirit levels.

In order to numerically align the axis of the 1-pT magnetometer to LEMI-025, the following optimization problem has been solved:

$$B_R = [\sin(\theta)\cos(\varphi) \quad \sin(\theta)\sin(\varphi) \quad \cos(\theta)] \begin{vmatrix} B_{25x} \\ B_{25y} \\ B_{25z} \end{vmatrix} \tag{2}$$

$$B_R - B_{1px} - O_{1px}(1 + \tau_x * t) = \min \tag{3}$$

where $\mathbf{B}_{25}$ is the magnetic flux density (x, y, and z components) as measured with LEMI-025 and B_R is the rotated horizontal (EW) field vector component. B_{1px} is the x-axis component as measured with the 1-pT instrument, O_{1px} is its initial offset, and τ_x is the offset temperature coefficient in this axis. In addition to our initial results in [22], we also added the tilting angle θ because the sensor was not perfectly horizontal. However, for the reasons described earlier, for noise calculations, we assumed that the tilting angle is to be $\theta = 0$ not to introduce any noise from the noisy vertical component into the comparison.

As we see in (3), because we were not able to measure the temperature of the sensor head without disturbing the magnetic field, we assumed that the offset drift within a 3-h recording window is linear, and we were fitting on the sample time rather than temperature. The fit coefficient τ was about 0.2 pT/s.

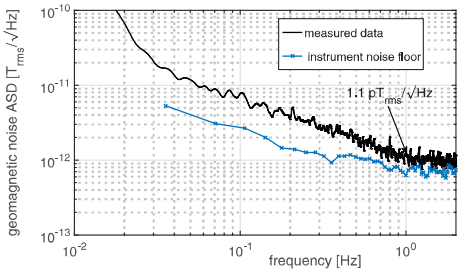

Fig. 15. Night-time (04 August, 2019, 02–03 A.M.) geomagnetic measurement with the 1-pT magnetometer and an annealed sensor; instrument noise floor also shown, using the same data as that of Fig. 10.

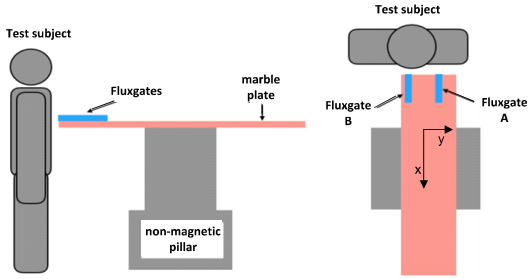

Fig. 16. Arrangement of the two fluxgate sensors for gradiometric MCG measurement. The gradiometric base was 12 cm.

The optimization problem was solved in MATLAB with *fminsearch* function, and the resulting alignment is shown in Fig. 13. From that result, we can conclude that even when the sensor drifts in its offset inherently, we can compensate for it and use it even for ultralow frequency (mHz) measurements.

C. Geomagnetic Measurement—As-Cast Sensor

The results of geomagnetic measurements with the as-cast sensor are shown in Fig. 14 (night-time data were used because of the anthropogenous noise during the day). The 1-pT sensor was placed in the "quiet hut," as shown in Fig. 12. From the comparison with simultaneously obtained observatory magnetometer data, we see that the LEMI-025 noise is limited by about 6 $pT_{rms}/\sqrt{Hz}$ for frequencies above 0.3 Hz. This can be either due to the instrument noise itself or by higher field noise at the LEMI-025 position—its "instrument bunker" is about 100 m from other buildings that might generate local noise. For lower frequencies, measurement with both instruments results in the same noise (about 15 $pT_{rms}/\sqrt{Hz}$ @ 100 mHz).

D. 1-pT Geomagnetic Measurement—Annealed Sensor

We repeated the geomagnetic measurements once more with an annealed sensor to verify the possibility of (sub) pT geomagnetic measurements. The measurement was done between 12 P.M. and 4 A.M. in the same quiet location as in part C, and the same methodology was used to verify that the geomagnetic measurement was comparable to LEMI-025.

Fig. 15 shows the geomagnetic field noise spectral density as measured by the magnetometer with an annealed sensor; we can see that in a low-noise location, it is actually possible to obtain 1 $pT_{rms}/\sqrt{Hz}$ at 1 Hz, which is an interesting result, e.g., for magnetotelluric applications.

V. Magnetocardiography Experiment

In order to perform measurements of the magnetic field of a human heart, we placed two magnetometer sensors on a marble plate located on top of a nonmagnetic pillar. The measurements took place at the Budkov geomagnetic observatory of the Academy of Sciences of the Czech Republic, in South Bohemia. The two sensors were arranged as a transverse, dB_x/dy gradiometer (with x denoting the sensor axis), and the y-distance—or gradiometric base—was 12 cm (see Fig. 16).

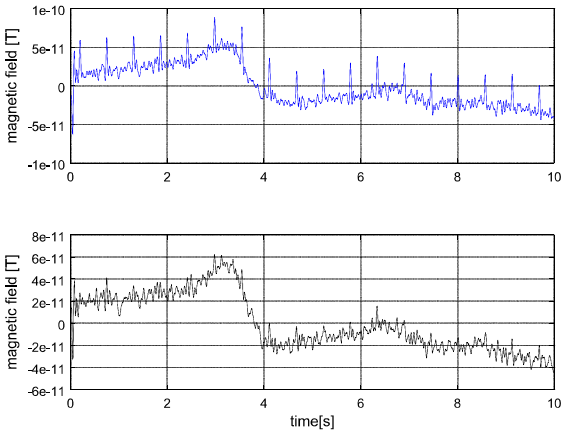

Fig. 17. Top: signal recorded by channel A (in front of the heart). Bottom: signal recorded by channel B.

The first sensor was located at chest level and the approximate heart position of the subject freely standing in front of it, whereas the second sensor was located toward the left side. Chest-to-sensor tip distance was about 4–5 cm.

The magnetometer was located at a distance of 1.5 m and powered by batteries. The magnetometer outputs were connected to the NI PXIe-4303 data acquisition module by 2-m-long coaxial cables. In order to minimize the noise due to the digitizer, we selected the ±0.1-V input range that corresponds to ±450 nT. For this reason, the sensors were placed in the E–W direction in front of the subject. Following the digitization of the magnetometer output at a 1-kHz sampling rate, we applied a 30-Hz digital low-pass filter, which is enough for the signal of a human heartbeat and removes 50 Hz effectively. The signals of both magnetometer channels (sensors) are shown in Fig. 17: the top trace corresponds to the sensor A (i.e., the sensor in front of the heart), whereas the bottom trace corresponds to the reference sensor B.

As we can see, both signals share a common variation of the magnetic field corresponding to the noise in the environment where the measurements took place. In addition to that, the first sensor also shows the peaks corresponding to

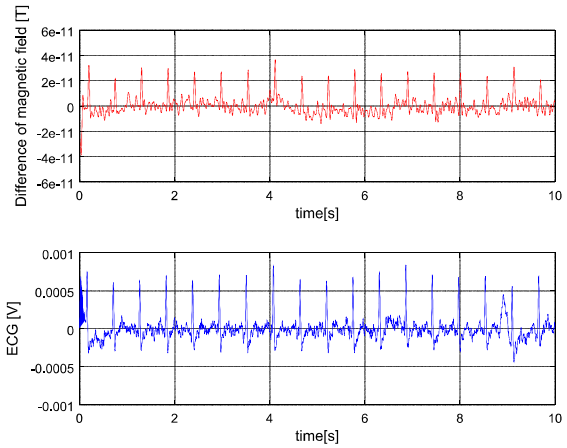

Fig. 18. Top: MCG signal obtained subtracting the recorded signals shown in Fig. 17. Bottom: ECG used a validation reference to confirm the heart origin of the MCG signal.

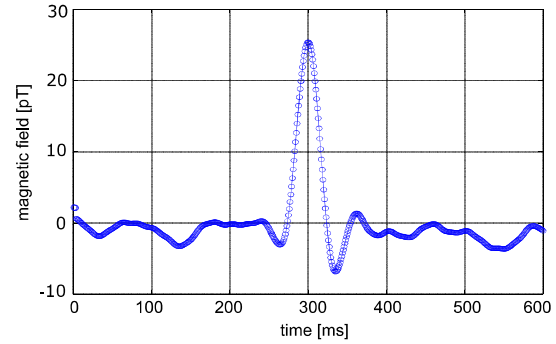

Fig. 19. MCG signal obtained when averaging 30 peaks.

the heart's magnetic field, which are missing in the signal measured by the second sensor.

When the signals from the two sensors are subtracted, the common variation of the magnetic field due to environmental noise is suppressed and the MCG signal is eventually revealed. In order to be sure that the peaks of the magnetic field corresponded to the heartbeat, we simultaneously acquired ECG on the third channel of the data acquisition module, by connecting two copper plates to the test subject's hands. As we can see in Fig. 18, the MCG signal obtained as difference of the two channels A and B corresponds to the ECG signal.

It must be noted that the MCG signal shown in Fig. 18 has been obtained without applying averaging, as opposed to other systems that rely on averaging in order to reduce the noise. We should also note that the subject was not secured to any support and, therefore, was free to move. Despite the best effort to be stable, his/her position oscillated about 3 cm. In order to prevent the chest from touching the sensor, we, therefore, had to keep the sensors about 4–5 cm from the chest of the test subject. This made the signal from the heart

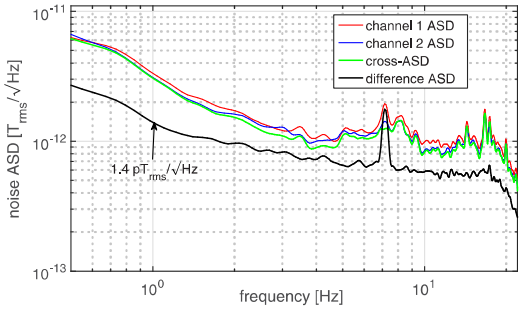

Fig. 20. Noise ASD spectra of both individual channels and their difference (sensor arrangement as that of Fig. 16). Also, the cross-power spectrum is shown (in amplitude units), indicating that most of the observed noise is correlated, i.e., homogenous.

just about 20–25-pT peak when, typically, it can even reach 100 pT. Therefore, with a better arrangement, we expect the signal-to-noise ratio to increase by a factor of four to five.

The signal-to-noise ratio is commonly improved by averaging at the cost of losing the dynamic information in a single-beat cycle. For instance, Fig. 19 shows a peak of MCG signal obtained by averaging 30 peaks recorded by our fluxgate gradiometer, without the use of any synchronization by ECG (the peaks are large enough to allow easy detection and selection for averaging). We can identify not only the main peak but also the negative peak, which reaches −7 pT.

The efficiency of the gradiometer arrangement to suppress the environmental noise is illustrated in Fig. 20. The graph shows the spectral density of the fluxgate outputs without the MCG signal (the test subject was not present, while the sensors were kept in the same arrangement). Both sensors show noise components that are removed in their difference. Notably, the spikes above 10 Hz are very efficiently suppressed. Unfortunately, however, the spike at 7.1 Hz is almost not affected by the gradiometric arrangement. We believe that it originated from the magnetic field gradient signature of the electronic circuits (for instance the fan of the PXI frame) or from local EMI that coupled in a different way to both sensors.

This was confirmed by the cross-spectral analysis (green trace in Fig. 20) that suppresses the signal at this particular frequency. A better arrangement of the instrument is expected to improve the rejection of this signal.

The noise density of the difference of the two channels is about 1.4 $pT_{rms}/\sqrt{Hz}$ at 1 Hz, which is slightly higher than the noise of the individual channels multiplied by $\sqrt{2}$ (1.41×0.75 $pT_{rms}/\sqrt{Hz}$, see Fig. 10)—we assume uncorrelated noise in both channels. This indicates that the suppression of the noise obtained by gradiometric configuration and numerical subtraction is not yet perfect, probably because of the nonperfect alignment and calibration of the two probes. This might pose a problem in environments where the sources of local noise are larger and exhibit larger gradient.

VI. Conclusion

We have described the design of a portable magnetometer, based on a fundamental-mode, orthogonal fluxgate sensor,

where 0.6-pT_{rms} white noise and 0.75-pT_{rms} noise density at 1 Hz can be achieved with an annealed sensor. This is to the best of our knowledge so far the lowest published noise of a room-temperature vector magnetometer.

Even when considering the inherent sensor offset drift of −2.5 nT/K for the annealed sensor, the magnetometer can be utilized in a range of applications including biomedical measurements, where the frequency range of 10 mHz–25 Hz is sufficient. We have also shown later that the offset drift can be successfully numerically compensated with the help of an additional stable magnetometer, allowing even for geomagnetic measurements at much lower frequencies.

We have tested the instrument side-by-side to a state-of-the-art observatory magnetometer LEMI-025 and verified its low-noise performance during geomagnetic measurements. A comparison to HTS SQUID was also done; however, in this case, the SQUID exhibited high noise in the X-axis.

We have successfully demonstrated the applicability of the instrument in a room-temperature, unshielded magnetocardiography experiment, where the MCG signal is clearly discernible even without averaging. After the initial MCG experiment with search coils [29] 56 years ago, magnetocardiography measurements were mostly limited to shielded rooms with SQUID magnetometers [30] because, until now fluxgate magnetometers did not achieve noise figures better than few $pT_{rms}/\sqrt{Hz}$ at 1 Hz. Recently, optically pumped magnetometers (OPM) have been used for MCG with noise figures of about 50–300 $fT_{rms}/\sqrt{Hz}$ at 1 Hz [31]. Despite the noise of our fluxgate magnetometer still being higher than that of OPM devices, we believe in broadening the MCG usability not only by avoiding the necessity for cryogenic operation and expensive magnetic shields but also by providing a simple and affordable sensor and electronics. However, when judging our MCG results, noisier environments than that of the magnetic observatory has to be expected in reality and the common-mode rejection should be further improved. One possibility would be adding a (noisy, cheap) triaxial magnetometer close by.

As the HTS SQUID sensors currently available state $0.2-0.6$ $pT_{rms}/\sqrt{Hz}$ at 1 Hz [32], it is evident that the instrument presented meets HTS SQUID performance at least in terms of low-frequency noise. The future improvement of the 1-pT fluxgate magnetometer lies in its electronics where the closed-loop performance should be improved. Also, as we have shown, by further improving the input stage common-mode rejection, with better shielding and differential amplification, we should be able to further decrease at least the noise of the electronics, if not of the complete magnetometer.

ACKNOWLEDGMENT

The authors would like to thank V. Petrucha for providing a part of the electronic design. M. Janosek would like to thank D. Gouws for the support at the South African National Space Agency (SANSA) and E. Nahayo for the observatory data.

The results of the magnetocardiography experiments were presented at the Frontiers 2019 conference.

REFERENCES

[1] L. W. Pedersen and L. Merenyi, "The FGE magnetometer and the INTERMAGNET 1 second standard," *J. Ind. Geophys. Union*, vol. 2, pp. 30–36, Jan. 2016.

[2] P. Ripka and A. Zikmund, "Precise magnetic sensors for navigation and prospection," *J. Supercond. Novel Magn.*, vol. 28, no. 3, pp. 1077–1080, 2014.

[3] Å. Forslund, S. Belyayev, N. Ivchenko, G. Olsson, T. Edberg, and A. Marusenkov, "Miniaturized digital fluxgate magnetometer for small spacecraft applications," *Meas. Sci. Technol.*, vol. 19, no. 1, Dec. 2007, Art. no. 015202.

[4] A. D. Chave, and A. G. Jones, *The Magnetotelluric Method: Theory and Practice*. New York, NY, USA: Cambridge Univ. Press, 2012, p. 445.

[5] R. Bazinet, A. Jacas, G. A. B. Confalonieri, and M. Vazquez, "A low-noise fundamental-mode orthogonal fluxgate magnetometer," *IEEE Trans. Magn.*, vol. 50, no. 5, May 2014, Art. no. 6500103.

[6] I. Mohanty, R. Nagendran, A. V. T. Arasu, R. Baskaran, and A. Mani, "Correlation of defect depth with diffusion time of eddy currents for the defects in conducting materials using transient eddy current NDE," *Meas. Sci. Technol.*, vol. 29, no. 10, Aug. 2018, Art. no. 105601.

[7] B. W. Ficko, P. M. Nadar, P. J. Hoopes, and S. G. Diamond, "Development of a magnetic nanoparticle susceptibility magnitude imaging array," *Phys. Med. Biol.*, vol. 59, no. 4, pp. 1047–1071, Feb. 2014.

[8] S. Harada, I. Sasada, and F. Hang, "Development of a one-dimensional fluxgate array and its application to magnetocardiogram measurements," *Electron. Commun. Jpn.*, vol. 98, no. 4, pp. 20–26, Apr. 2015.

[9] C. Dolabdjian, S. Saez, A. R. Toledo, and D. Robbes, "Signal-to-noise improvement of bio-magnetic signals using a flux-gate probe and real time signal processing," *Rev. Sci. Instrum.*, vol. 69, no. 10, pp. 3678–3680, Jul. 1998.

[10] C. Hinnrichs, J. Stahl, K. Kuchenbrandt, and M. Schilling, "Dependence of sensitivity and noise of fluxgate sensors on racetrack geometry," *IEEE Trans. Magn.*, vol. 37, no. 4, pp. 1983–1985, Jul. 2001.

[11] M. Janosek, J. Vyhnánek, A. Zikmund, P. Butvin, and B. Butvinová, "Effects of core dimensions and manufacturing procedure on fluxgate noise," *Acta Phys. Polonica A*, vol. 126, no. 1, pp. 104–105, 2014.

[12] V. Korepanov and A. Marusenkov, "Flux-gate magnetometers design peculiarities," *Surv. Geophys.*, vol. 33, no. 5, pp. 1059–1079, Sep. 2012.

[13] R. H. Koch and J. R. Rozen, "Low-noise flux-gate magnetic-field sensors using ring- and rod-core geometries," *Appl. Phys. Lett.*, vol. 78, no. 13, pp. 1897–1899, Feb. 2001.

[14] A. Marusenkov, "Possibilities of further improvement of 1s fluxgate variometers," *Geosci. Instrum., Methods Data Syst.*, vol. 6, no. 2, pp. 301–309, Aug. 2017.

[15] I. Sasada, "Orthogonal fluxgate mechanism operated with DC biased excitation," *J. Appl. Phys.*, vol. 91, no. 10, p. 7789, 2002.

[16] D. P. Pappas. (2008). *High Sensitivity Magnetic Field Sensor Technology Overview*. [Online]. Available: ftp://ftp.boulder.nist.gov/pub/pappas/MagneticSensors/Sensors.ppt

[17] M. Butta, S. Yamashita, and I. Sasada, "Reduction of noise in fundamental mode orthogonal fluxgates by optimization of excitation current," *IEEE Trans. Magn.*, vol. 47, no. 10, pp. 3748–3751, Oct. 2011.

[18] M. Butta and B. P. Schutte, "Low-noise orthogonal fluxgate using flipped current joule annealing," *IEEE Trans. Magn.*, vol. 55, no. 7, Jul. 2019, Art. no. 4002906.

[19] E. Weiss and E. Paperno, "Noise investigation of the orthogonal fluxgate employing alternating direct current bias," *J. Appl. Phys.*, vol. 109, no. 7, p. 07E529, 2011.

[20] M. Butta and I. Coroli, "Low offset drift–low-noise orthogonal fluxgate with synchronized polarity flipping," *IEEE Trans. Magn.*, vol. 53, no. 4, Apr. 2017, Art. no. 4001406.

[21] N. Murata, H. Karo, I. Sasada, and T. Shimizu, "Fundamental mode orthogonal fluxgate magnetometer applicable for measurements of DC and low-frequency magnetic fields," *IEEE Sensors J.*, vol. 18, no. 7, pp. 2705–2712, Apr. 2018.

[22] M. Janosek, M. Butta, M. Dressler, E. Saunderson, D. Novotny, and C. Fourie, "1 pT-noise fluxgate magnetometer design and its performance in geomagnetic measurements," in *Proc. IEEE Int. Instrum. Meas. Technol. Conf. (I2MTC)*, May 2019, pp. 1–5.

[23] M. Butta and M. Janosek, "Very low frequency noise reduction in orthogonal fluxgate," *AIP Adv.*, vol. 8, no. 4, 2018, Art. no. 047203.

[24] Janascard. *AD24USB/AD24ETH—Data Acquisition Modules*. Accessed: Nov. 20, 2018. [Online]. Available: http://www.janascard.cz/aj_Vyrobky.html

[25] Janascard. *Noise Reduction in AD24USB*. Accessed: Aug. 1, 2019. [Online]. Available: http://www.janascard.cz/PDF/AD24USBNoise.pdf

[26] G. Waysand *et al.*, "Seismo-ionosphere detection by underground SQUID in low-noise environment in LSBB-Rustrel, France," *Eur. Phys. J. Appl. Phys.*, vol. 47, no. 1, Jul. 2009, Art. no. 12705.
[27] L. J. J. van Vuuren *et al.*, "Implementation of an unshielded SQUID as a geomagnetic sensor," in *Proc. IEEE AFRICON*, Pointe-Aux-Piments, Mauritius, Sep. 2013, pp. 908–912.
[28] S. Hong, J. H. Kim, A. Marusenkov, L. Hegymegi, and A. Csontos, "The temperature stability of LeMI-025 1-second variometer: Case study in the icheon observatory," *J. Indian Geophys. Union*, vol. 2, pp. 42–46, Jan. 2016.
[29] G. Baule and R. Mcfee, "Detection of the magnetic field of the heart," *Amer. Heart J.*, vol. 66, no. 1, pp. 95–96, Jul. 1963. doi: 10.1016/0002-8703(63)90075-9.
[30] D. Cohen *et al.*, "Magnetocardiograms taken inside a shielded room with a superconducting point-contact magnetometer," *Appl. Phys. Lett.*, vol. 16, no. 7, p. 278, 1970.
[31] O. Alem *et al.*, "Fetal magnetocardiography measurements with an array of microfabricated optically pumped magnetometers," *Phys. Med. Biol.*, vol. 60, no. 12, p. 4797, Jun. 2015.
[32] T. Technlogies. *General Geophysical Devices*. Accessed: Nov. 26, 2018. [Online]. Available: http://tristantech.com/general

Michal Janosek received the M.Sc. and Ph.D. degrees from Czech Technical University in Prague, Prague, Czechia, in 2007 and 2014, respectively, all in low-noise magnetometers and gradiometer.

From 2018 to 2019, he was a Post-Doctoral Fellow with the Stellenbosch University, Stellenbosch, South Africa. He is currently an Assistant Professor with the Faculty of Electrical Engineering, Department of Measurement, Czech Technical University in Prague. His current research interests include low-noise magnetic sensors, gradiometers, magnetometers, and magnetic measurements.

Mattia Butta received the M.Sc. degree from the Politecnico di Milano, Milan, Italy, in 2005, and the Ph.D. degree from Czech Technical University in Prague, Prague, Czechia, in 2010, with a focus on magnetic sensors based on microwires.

From 2010 to 2012, he was a JSPS Fellow with Kyushu University, Fukuoka, Japan. In 2019, he spent 12 months at the Institute of Material Science-CSIC, Madrid, Spain, working on the development of low-magnetostriction amorphous magnetic wires. He is currently an Associate Professor with the Faculty of Electrical Engineering, Department of Measurement, Czech Technical University in Prague. His current research interests include low-noise magnetic sensors, mainly orthogonal fluxgate.

Michal Dressler received the M.Sc. degree from Czech Technical University in Prague, Prague, Czechia, in 2019, with a focus on coil system for magnetometer calibrations with interference compensation. He is currently pursuing the Ph.D. degree in gradiometer based on magnetic microwires with the Faculty of Electrical Engineering, Department of Measurement, Czech Technical University in Prague.

His current research interests include precise magnetometer calibrations and development of magnetometer electronics.

Elda Saunderson received the M.Sc. degree from Stellenbosch University, Stellenbosch, South Africa, in 1995, where she is currently pursuing the Ph.D. degree with a focus on the feasibility of using low -frequency geomagnetic measurements by SQUID magnetometers for space weather and hazard prediction.

She is currently a Specialist Engineer with the Directorate Space Science, Applied Science and Technology Group, South African National Space Agency (SANSA), Hermanus, South Africa. Her current research interests include magnetism and electromagnetism, mainly magnetic measurements and integration and calibration of magnetic sensors.

David Novotny received the M.Sc. degree from Czech Technical University in Prague, Prague, Czechia, in 2018, with a focus on magnetic gradiometer for car detection and speed measurements. He is currently pursuing the Ph.D. degree with Faculty of Electrical Engineering, Department of Measurement, Czech Technical University in Prague.

His current research interests include low-noise magnetic sensors, mainly anisotropic magnetoresistors (AMR) and digital signal processing methods and low-noise electronics.

Coenrad Fourie received the B.Eng. degree in electronic engineering and the Ph.D. degree in superconducting electronics from Stellenbosch University, Stellenbosch, South Africa, in 1998 and 2003, respectively.

In 2001, he joined Stellenbosch University as a Lecturer, where he is currently a Professor with the Department of Electrical and Electronic Engineering. His current research interests include superconducting electronics, superconducting quantum interference device sensor applications, and the development of extraction, simulation, and verification software for superconducting integrated circuits.

3.1.3 Increasing accuracy of geomagnetic observations

As stated in previous chapters, not only calibration sites but also magnetic observatories [22] are subject of increasing urban noise, unless the planning of their layout was well planned at the time construction – i.e., the INTERMAGNET HER observatory of SANSA has its instruments in a square, 16-ha site, serving as *cordon sanitaire*. However, this might not be enough in the long term: the ever-increasing demand for new on-site instruments and development is increasing the noise, too. Also, with the recent introduction of fast (1-s) data requirement for geomagnetic observatories [31], disturbances which would be suppressed by the previously used 1-minute filtering, start to appear in observatory data.

In the article *Improving Earth's magnetic field measurements by numerical corrections of thermal drifts and man- made disturbances* [J10], the author studied increasing accuracy of observations at two localities: the station POLOM operated jointly by the Institute of Geophysics ASCR and by the Office of Military Geography and Hydrometeorology (VGHMUR), with a fluxgate variometer at ambient temperatures; and an experimental underground station with the same sensor, temperature-stable but close to a busy road. For the latter case, a „moving-dipole-fitting" algorithm was proposed, in order to correct for the disturbances by car traffic without losing the original information. Further, the feasibility of running the POLOM instrument at ambient temperatures is shown, only with light thermal shielding and damping by the sensor enclosure / hut, but with numerical corrections. The fitted linear temperature sensitivity coefficients were enough to suppress the temperature effect by at least one magnitude; better results require much larger thermal-damping [60].

The second article *Identification of geomagnetic pulsations in SQUID data for Space Weather research* [J1] shows the research towards utilizing an HTS SQUID magnetometer for determining the occurrence of sub-nT geomagnetic effects even at a noisy location. The SQUID not only sensed the anthropogenous noise but also generated additional noise due to its sensitivity to thermal oscillations in the cryostat. By cross-correlating the data with a remote observatory, however, we were able to detect weak pulsations [29] due to the fact that the Earth's magnetic field and its natural perturbations are homogenous on a large scale.

[J10] *Improving Earth's magnetic field measurements by numerical corrections of thermal drifts and man- made disturbances.* **Author contribution:** 60%. Algorithms, data processing and presentation, article composition. **Citations:** 3

[J1] *Identification of geomagnetic pulsations in SQUID data for Space Weather research.* **Author contribution:** 40%. Method proposal, data and algorithms.

Hindawi
Journal of Sensors
Volume 2018, Article ID 1804092, 10 pages
https://doi.org/10.1155/2018/1804092

Research Article

Improving Earth's Magnetic Field Measurements by Numerical Corrections of Thermal Drifts and Man-Made Disturbances

Michal Janošek,[1] **Mattia Butta**,[1] **Michal Vlk**,[2] **and Tomáš Bayer**[2]

[1]*Department of Measurement, Faculty of Electrical Engineering, Czech Technical University in Prague, Czech Republic*
[2]*Institute of Geophysics, Czech Academy of Sciences, Prague, Czech Republic*

Correspondence should be addressed to Michal Janošek; janosem@fel.cvut.cz

Received 20 June 2018; Accepted 6 August 2018; Published 15 October 2018

Academic Editor: Luca De Stefano

This contribution deals with challenges encountered in real-world geomagnetic measurements and is focused on improving the performance of two variometer stations of Kelčany and Polom, which have been recently established in the Czech Republic. It is shown that a carefully designed full-field instrument, despite lacking temperature stabilization, can provide vectorial and scalar data accurate to a few nT, if the raw data were postprocessed by compensating for gain temperature coefficients—we show how this can be obtained by a precise calibration and long-term scalar measurements. We also show a method for suppressing nT-level spikes in the data due to nearby car traffic, by utilizing gradiometric measurement for detecting the car occurrences and by employing a linear optimization problem in order to find the parameters of the moving magnetic dipole and compensate for it. In this manner, we were able to reduce the anthropogenous noise due to car traffic while keeping as much original information as possible.

1. Introduction

Vectorial magnetometers which serve for monitoring of Earth's field variations due to diurnal field changes, geomagnetic storms, etc., are standard instruments deployed at geomagnetic observatories and variation stations; they are mostly based on fluxgate sensors [1]. To achieve the best magnetometer (variometer) performance, it will usually be installed in a temperature-stabilized environment, either by the use of an active and magnetically clean heating-system or by selecting a highly temperature-stable location, preferably underground. This approach is of course demanding on the site selection and/or the necessary infrastructure. However, the variometer performance improved recently not only in terms of noise (the current state-of-the-art noise limit of fluxgate sensors is about 3–5 pT/$\sqrt{\text{Hz}}$ @ 1 Hz) but also in temperature stability [1–3]. Also, with the advent of dc-precise 24-bit A/D converters, it is possible to build a "full-field" instrument which not only can monitor the magnetic field variations but also can provide the vector magnitude (scalar) from the three vector components. To achieve this, precise magnetometer calibrations are needed [4, 5], and the calibration parameters need to be long-term stable. The calculated total field value can be further used for temperature compensations.

An important aspect of real-world deployment of variometers is the anthropogenous noise at the selected site, which is at least in the Central European region difficult to obey by placing the instrument in a remote locality—due to extensive urban development, DC-railways, pipelines, etc. [6]. Thus, the anthropogenic noise should be estimated and, if a better location is not viable, a compensating or at least a detection method should be developed; the latter is the case mainly if the occurring disturbances are on local-scale, i.e., car traffic—we will show this is the case of one of our localities.

The following results were obtained from magnetometers running at three different localities in the Czech Republic. The reference low-noise data was obtained from the established INTERMAGNET geomagnetic observatory Budkov (BDV) in Southern Bohemia, which employs passive and active temperature stabilization. Two variometer stations were recently established—Polom (PLM) in Eastern

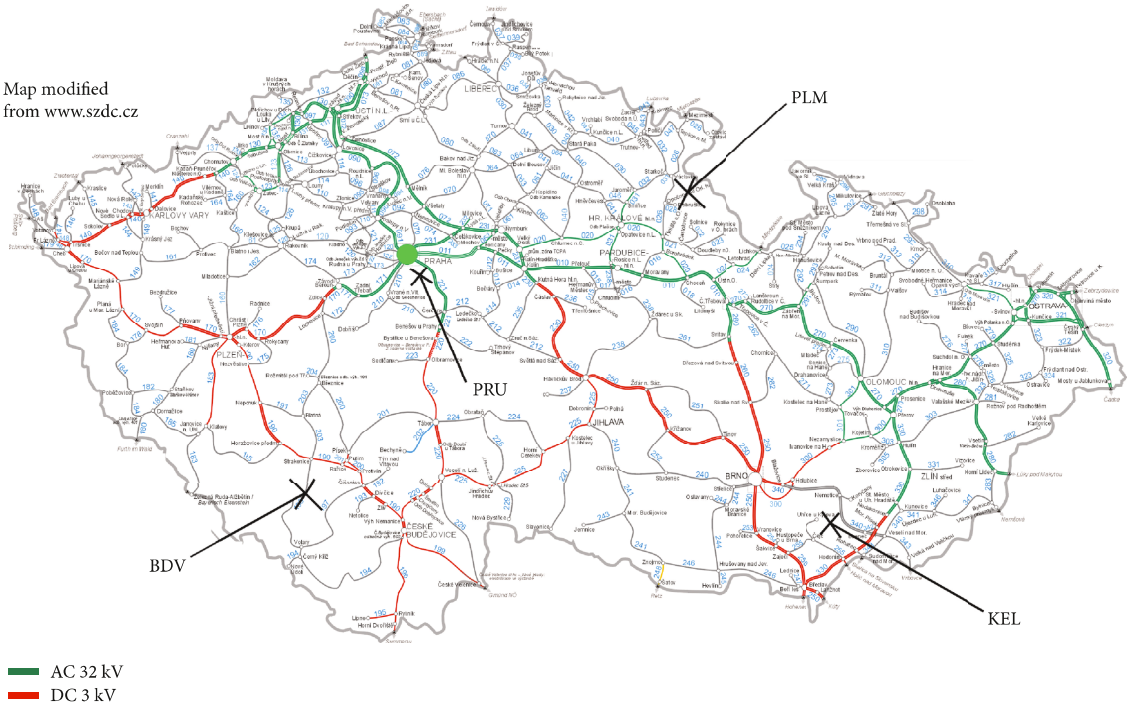

Figure 1: Budkov (BDV), Polom (PLM), and Kelčany (KEL) sites location. The background image is the Czech railway network electrification—green is DC traction; red is AC 50 Hz (modified from [7]). Ex-observatory site Průhonice (PRU) is shown to illustrate moving away from human-made noise.

Bohemia at the Czech-Polish border and Kelčany (KEL) in south Moravia—see Figure 1. The motivation to have all three stations is clear—first, having data redundancy is important for magnetic field observations, forecasts, and data services; moreover, from the three measurements, it would be theoretically possible to suppress the anthropogenous noise which occurs on local-scale—the only correlated information is the Earth's field variation, which is homogeneous enough across the three stations span (100–200 km). From Figure 1, it is evident that mainly the DC railways (which are far away from BDV observatory) will have a detrimental effect on anthropogenic noise on both variometers running at PLM and KEL. The site of Průhonice (PRU) just at the outskirts of Prague is also shown; it served as a geomagnetic observatory station from 1946 to 1967, when the magnetic observations have been moved to a much quieter location of Budkov.

2. Instrument Setup and Site Limitations of PLM and KEL Stations

The station of Polom (PLM) has been in service since late 2016. The site is a property of Czech Army and is being run in collaboration with the Institute of Geophysics, CAS and provides important seismic, meteorological, and geodetic data [8]. CTU and IG CAS took the opportunity to install a fluxgate variometer instrument [4] in the already magnetically prescreened and prepared locality. Because of the recent installation, the temperature-stabilized hut is not yet available, and therefore, the variometer sensor and also electronics are operating at ambient temperatures, although protected from the elements. The site is also equipped with nonmagnetic pillars for obtaining "absolute" magnetic measurements, i.e., measurements of local inclination and declination hand-to-hand with total field intensity, which are usually obtained using a portable Overhauser magnetometer [9].

The station of Kelčany (KEL) is privately owned and is being run by the members of Magnetic Laboratory at the Department of Measurement, FEE CTU Prague. The advantage of the site compared to PLM is the underground location of the sensor and electronics (in a dual-purpose wine-cellar), which allows for less than ±5°C yearly temperature variation. Careful magnetic mapping has been done before installation, the site was cleaned of ferromagnetic objects and a nonmagnetic pillar for the instrument was built. The site is running since 2015 and is, advantageously, on roughly the same latitude as the BDV observatory. The data are publicly available [10].

The magnetometers installed both at KEL and PLM stations were manufactured at the CTU using low-noise race-track fluxgate sensors, exhibiting ~20 pT digital noise

(a) (b)

Figure 2: (a) The triaxial sensor head (1) at PLM station is placed in an unheated hut made of PVC (3) and is surrounded by nonmagnetic white bricks to increase the thermal mass. The hut is painted with special sun-reflecting paint. (b) The sensor at KEL variation station is located 6 m underground.

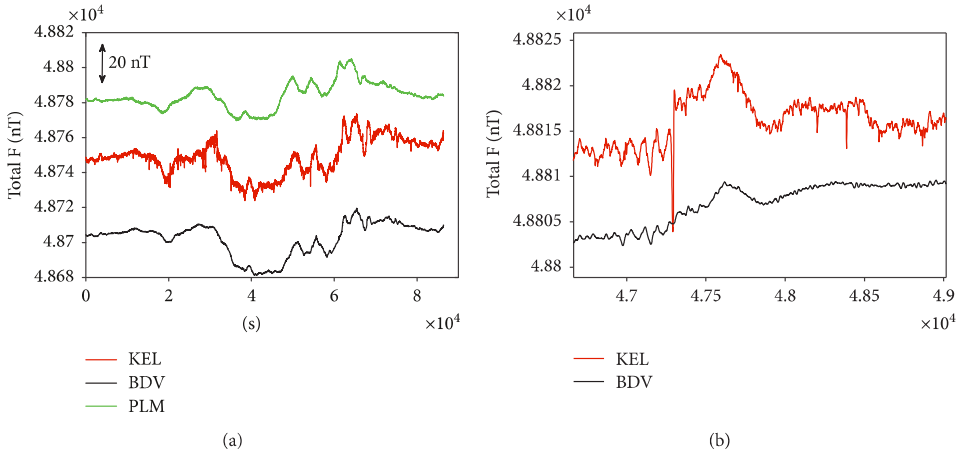

(a) (b)

Figure 3: (a) 1-day total field variation recorded at Budkov (BDV: black), Polom (PLM: green), and Kelčany (KEL: red). It is clearly seen that lowest-noise occurs at BDV, followed by PLM showing distant anthropogenic noise and KEL exhibiting large, fast spikes, most probably from car traffic. Offsets are caused by different site geology and instrument calibrations. (b) KEL and BDV in detail.

floor and showing high geometrical and temperature stability. The triaxial sensor head at PLM is moreover made from MACOR machinable ceramics; the head is further fixed on a marble plate [3]—see Figure 2. Neither KEL nor PLM facilitate a scalar magnetometer; thus, the total field data are calculated from the three orthogonal field components.

After initial trials at the PLM station, where the ambient temperature can change from −20°C to +40°C, we decided to orient the sensor to the "UVZ" orientation [11]. This means that the two horizontal axes are oriented ±45° from local meridian—in this manner, both horizontal axes are measuring roughly the same magnetic field (about 15,000 nT at our location). The NEZ or HDZ components are computed numerically [9], so the offset drifts and mechanical instability in azimuth are of less significance than if measuring the E or D component directly. Also, the compensating current in all axes is large enough (few mA) not to be influenced by cable leakage currents. The UVZ orientation is also beneficial for obtaining a simple thermal drift model as shown later.

A comparison of anthropogenous noise observed at BDV, KEL, and PLM stations is shown in time-domain in Figure 3, where the calculated total field from both KEL and PLM vectorial readings is compared to total field measurements at BDV observatory provided by Overhauser magnetometer.

The anthropogenous noise at both PLM and KEL is larger than at the BDV observatory (about 0.2 nT peak-peak); however, at KEL also isolated peaks occur with an amplitude

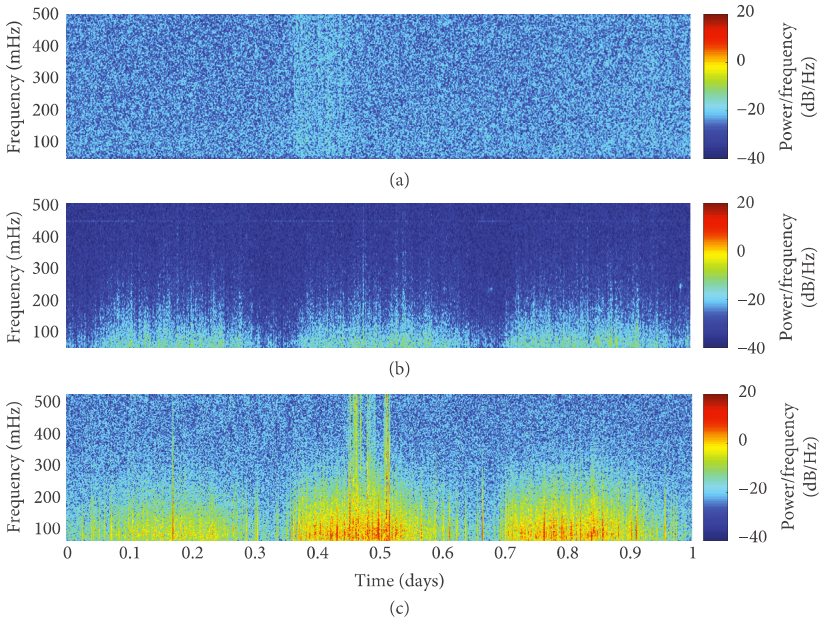

Figure 4: The power spectral density of 1 Hz magnetic data (vertical component, diurnal variation removed) at BDV (a), PLM (b), and KEL (c) shows that the anthropogenic repeats on a daily-scale, with quiet night periods and noise bursts in the daytime.

up to several tens of nT p-p, which have been later traced down to be caused by nearby car traffic, as further shown in Section 2.1.

Figure 4 further shows aligned spectrograms from three days of 1-second data obtained at all three sites (21–23/7/2017). At PLM, the clean nights are alternated with noisy daytime periods due to the ~40 km distant DC railway and light urban rail. Although the noise at BDV station is very low, the used instrument (DMI fluxgate variometer) has large intrinsic noise, so actually, during the quiet night periods (with almost no electric train traffic), the PLM data are less noisy due to the used variometer. The KEL data on the other hand suffer from increased anthropogenic noise even during the night, since the sensor is located in a residential location—the broadband daytime noise is another 10 dB above PLM. Another 10–20 dB noise increase in short bursts has been traced down as local car traffic.

2.1. Car Traffic and Magnetic Noise. To confirm the origin of the excess-noise at KEL site, the passing cars (the local street is about 25 m away from the sensor location) have been observed by a web-camera and by a cellphone video recording, respectively, and compared to magnetic data—a sketch displaying the actual setup at KEL site is shown in Figure 5.

To be able to detect, mark, and possibly remove the passing car's magnetic signature, an axial (dB_y/dy) fluxgate gradiometer has been created in N-S direction by placing a second sensor coaxial to the variometer head. This second sensor has been placed approx. 5 m away from the variometer (position 1), closer to the street; later also a short-baseline gradiometer was placed at position 2. The peaks obtained from the axial

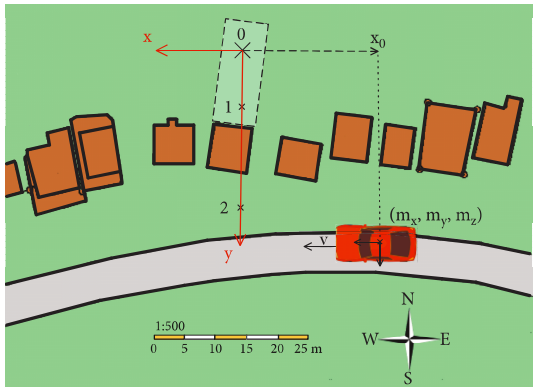

Figure 5: Sketch of the situation at KEL station: the variometer sensor (0) is located approximately 25 m from a frequent local street, which is running roughly in E-W (x) direction. The car occurrences were measured at the central line in the N-S direction, thus in the magnetic sensor "y" coordinate. Positions 1 and 2 show the locations of the second sensor and gradiometer, respectively.

gradient data correspond with the peaks of the variometer data; however, the gradiometer noise floor is still high for detecting spikes less than about 5 nT p-p.

In Figure 6, the vehicle occurrences have been drawn into the magnetic field recorded. Axial gradient (in N-S direction) and magnetic field (N-S component) are shown—the recorded spikes are in the order of tens nT p-p (even larger for vans/busses); we show that there is a clear correlation of the spikes and car traffic.

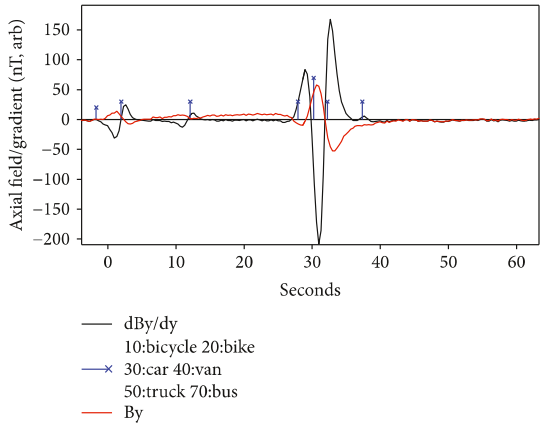

FIGURE 6: The vehicle occurrences and magnetic field/axial gradient in the N-S direction. The strongest disturbance occurs for a bus running in the closer lane—about 110 nT p-p.

3. Methods of Improving the Real-World Performance at KEL and PLM Stations

At KEL and PLM sites, we are experiencing two difficulties: temperature drifts due to seasonal and diurnal changes of the ambient temperature (PLM) and large noise due to car occurrences (KEL). It should be noted that the car-induced spikes cannot be simply filtered out with a low-pass filter since the peaks in the individual axes are not bipolar, thus any low-pass filtration would introduce artefacts in the measured data. Moreover, for a strong magnetic source (e.g., a bus-coach), the disturbance occurs even for 20 seconds.

3.1. Correcting for Temperature Drifts (PLM). It is obvious that if the temperature coefficients of the sensor are known (i.e., offset and gain temperature coefficient), one could recalculate and obtain drift-free data. However, the temperature drift in a fluxgate magnetometer (assuming that the electronic is drift-free) is caused by multiple effects [12], e.g., by the temperature of the excitation tank capacitor, by the dimensional expansion of the feedback/pick-up coil, or due to the expansion of the triaxial holder material and its base. Moreover, it is difficult to calibrate the whole setup as the sensor, and its base are quite bulky. As we have selected the UVZ orientation of the sensor, the ~20–30 ppm·K^{-1} sensitivity drifts dominate in all axes, simplifying further modeling of thermal response (With NEZ orientation, the E axis drift would be dominated by the offset drift which is a combination of electronic and sensor drifts; however, the electronics and sensor head are in our case at different positions and temperatures and exhibit different thermal mass. With HDZ orientation, the D component (~2000 nT) would be influenced both by the offset and gain drifts. In both NEZ and HDZ cases, also mechanical directional instability would have to be modeled.). The predicted sensitivity drift is 0.4 nT·K^{-1} for each horizontal axis and 1.1 nT·K^{-1} for the vertical axis, respectively. Utilizing a "full-field" variometer, thus measuring in a feedback loop all the three vector components of the magnetic field at once, allows us for calculation of the total magnetic field (the scalar vector magnitude). Both variometers at PLM and KEL have been calibrated with the "scalar method" [4] for their offsets, gains, and orthogonalities, so the only difference to a drift-free scalar measurement from an Overhauser magnetometer are then the magnetometer drifts itself.

We did this for the PLM variometer by comparing the Overhauser readings obtained at BDV observatory to the calculated total field from PLM—in this case, we assume that on the local scale, the measurements at the two localities, which do not exhibit geologic anomalies, will differ only by a stable offset $\mathbf{B}_{\mathrm{Off}}$. This was also verified during multiple onsite measurements with an Overhauser magnetometer at different times and temperatures (we could not yet perform a long-term scalar measurement due to the lacking infrastructure).

To find the actual variometer drifts in all three axes, we have utilized a least-squares fitting method, which generally minimizes the difference B_{Diff} between the scalar reading B_{BDV} at the BDV observatory and the calculated scalar value at PLM from the three individual components B_1, B_2, B_3. Thus we try to minimize B_{Diff} from a large set of following equations:

$$B_{\mathrm{BDV}} - \sqrt{[(1+\alpha\theta)\cdot B_{1\mathrm{PLM}}]^2 + [(1+\beta\theta)\cdot B_{2\mathrm{PLM}}]^2 + [(1+\gamma\theta)\cdot B_{3\mathrm{PLM}}]^2} - B_{\mathrm{Off}} = B_{\mathrm{Diff}}. \quad (1)$$

The solution of equation (1) was found with a constrained *fminsearch* function in MATLAB R2015 [13], and the offset B_{off} agreed well with the one obtained from onsite Overhauser measurements. After correcting on the obtained drift constants α, β, and γ [T·K^{-1}], we were able to largely suppress the temperature drifts in all three axes. The dataset we have used was from February 2018, which allowed for large temperature span between +17°C and −12°C, see Figure 7.

We could improve the results even further by introducing a lag of 800 s which was experimentally obtained by calculating the cross-correlation between the total field differences and temperature—this delay is believed to originate from the fact that the temperature measurements occur at the MACOR cube where the sensors are located, but significant part of the drifts can be caused by the excitation capacitor temperature coefficient [14]—the capacitor is heated only by radiation, since it is thermally connected to the MACOR

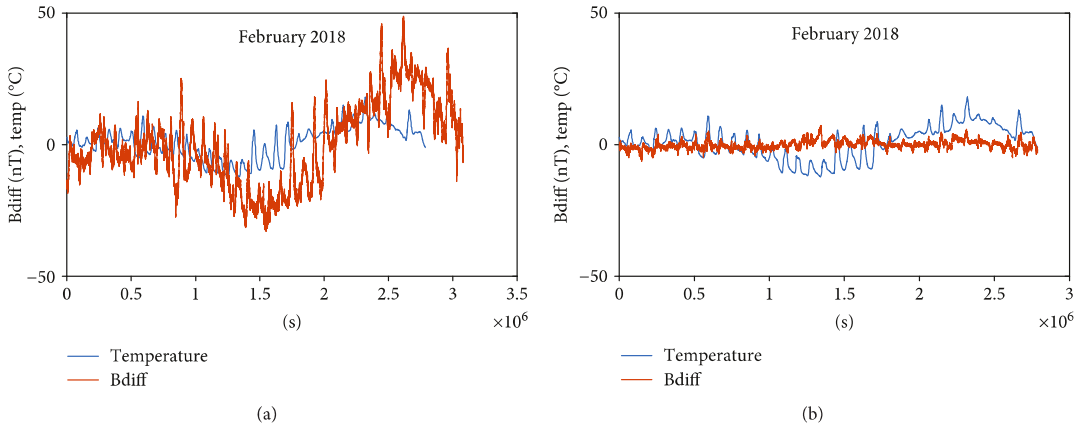

FIGURE 7: (a) Without temperature compensation, the difference between PLM and BDV scalar values (B_{Diff}) is temperature-dependent and varying between −30 nT to +50 nT. (b) After temperature compensation, the B_{Diff} decreased one order of magnitude (to about 5 nT maximum during the freezing temperatures). The data were obtained in February with −12 to +17°C temperature swing.

cube only by its thin leads. After introducing this delay, the calculated values were the following:

$$\alpha = 1.11,\ \beta = -2.5, \gamma = 0.37\left[\text{nT}\cdot\text{K}^{-1}\right],\ B_{\text{off}} = 417[\text{nT}]. \tag{2}$$

The value of α roughly corresponds to the 30 ppm predicted drift (vertical axis measuring approx. 44,000 nT). Also, the γ value corresponds to an expected value for a horizontal sensor. However, the obtained value of β is unexpected, since both horizontal sensors should exhibit the same values or at least the same order of magnitude. We cannot currently offer other explanation than a faulty sensor deployed at this position.

After rotating the temperature-compensated PLM vector readings with a 3×3 matrix, which reorients the sensor at PLM to the orientation at BDV, we were able to show that the temperature compensation was successful also in the individual components, see Figure 8.

3.2. Suppressing the Car-Induced Disturbances (KEL). As we have shown in paragraph 2.1, there is a clear correlation between the disturbances occurring at KEL and the car traffic. Thus we decided to create a simple model, assuming the following simplifications:

(1) The car at the ~25 m+ distance can be well modeled as a single magnetic dipole

(2) We neglect the road curvature and assume it in E-W direction (x-axis)

(3) The magnetic moment magnitude and orientation are stable during the car passage, since it keeps its orientation to the Earth's magnetic field

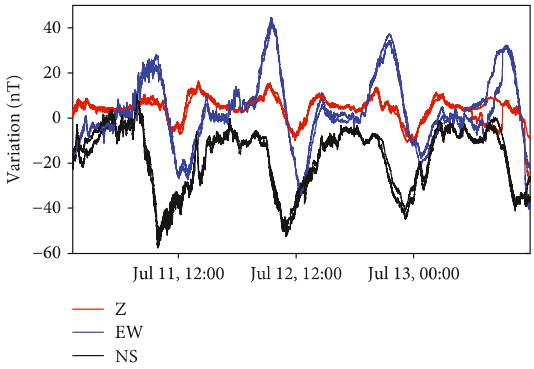

FIGURE 8: Comparison of aligned BDV and PLM magnetometer readings (the mean is removed to show only Earth's field variations) during three days in July 2017. The difference is well below 5 nT during the observed 14°C ambient temperature swing. The divergences near the dataset end were caused by false temperature readings.

(4) The occurrence of the maximum axial gradient in the y-axis, which occurs when the car radial distance to the sensor is smallest, defines the symmetry point of the car movement

(5) The maximum axial gradient in the y-axis (N-S component) occurs defines symmetry of the car movement

(6) The car does not change its speed significantly

(7) In 10 seconds, the car is distant enough not to give any significant (>0.1 nT) disturbance

(8) During the ~20 s car passage, the Earth's magnetic field changes only linearly

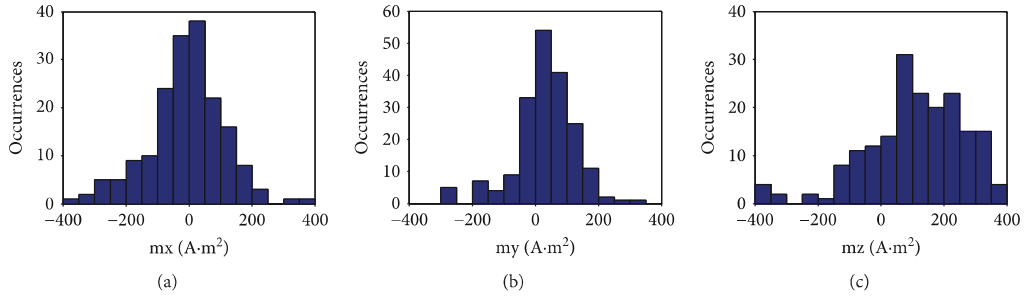

FIGURE 9: Histogram of magnetic moment components—m_x (a), m_y (b), and m_z (c). The vertical m_z component is statistically larger and unipolar, i.e., it does not change its sign depending on car trajectory orientation.

(9) The occurrences of cars in both lanes are not frequent.

Thus when fulfilling the above assumptions, we can write for the vectors of observed field $B_{\text{Obs}} = [B_x, B_y, B_z]$ and vector of car disturbance field $B_{\text{car}} = [B_{\text{cx}}, B_{\text{cy}}, B_{\text{cz}}]$ utilizing the well-known equation for magnetic field of a magnetic dipole with magnetic moment $\mathbf{m}\,[m_x, m_y, m_z]$ position vector $\boldsymbol{r}\,[r_x, r_y, r_z]$ and an (orthogonal) rotation matrix $\mathbf{R}$:

$$\vec{B}_{\text{Obs}} = \vec{B}_{\text{Earth}} + \vec{B}_{\text{Car}} = \vec{B}_{\text{Earth}} + R\frac{\mu_0}{4\pi}\left[\frac{3\vec{r}\left(\vec{m}\cdot\vec{r}\right)}{r^5} - \frac{\vec{m}}{r^3}\right], \tag{3}$$

where the position vector size (radial distance) r is calculated as

$$r = \sqrt{r_x^2 + r_y^2 + r_z^2}. \tag{4}$$

The position vector coordinates of equations (3) and (4) are aligned with the magnetic moment coordinates of the dipolar source (hence the need for rotational matrix $\mathbf{R}$ to align with the $\mathbf{B}_{\text{Obs}}$ coordinates). However, we are not interested in the real orientation of the magnetic moment vector in this case, so there is no need to calculate for $\mathbf{R}$, which would further complicate the problem.

To find the "true, disturbance-free" $\mathbf{B}_{\text{Earth}}$ of equation (3), we have implemented a least-squares fitting-based algorithm, which relies on reading from a gradiometer placed close to the street, allowing for detection of the passing cars through the "point of symmetry". In other words, we are trying to fit the magnetic field $\mathbf{B}_{\text{Obs}}$ at every sampling point using equation (3). To achieve this, we implement a set of equations which describe the magnetic field during the short disturbance, which occurs due to the moving magnetic moment. The dataset for the optimization is centered at the gradient peak and is usually 10 + 10 seconds long (Figure 4). Since we assume a simple trajectory as of Figure 4, we are trying to find position components x and y, whereas the only changing is the x, since y is constant and z equals zero in our case. Due to the constant sampling time, we can express x as a linear function of time t and vehicle speed v, both of which we assume constant. Since the sensor at KEL is sampling at 206.5 samples·s^{-1}, there are enough equations during the car passage, even after FIR filtering of the data (to remove 50 Hz mains disturbances) and smoothing. The optimization result of equation (3) is then the "true" Earth's field vector $\mathbf{B}_{\text{Earth}}$, the magnetic moment vector $\mathbf{m}$, the car speed $\mathbf{v}$, the initial position x_0, and the constant y distance together with the time-derivative of the Earth's magnetic field during the fitting period.

The optimization started only when the G_{yy} gradient amplitude in the observed interval crosses a preset threshold in order to run only for disturbances significantly larger than overall system noise. In our case, the threshold has been set to 2 nT·m^{-1}. The algorithm also contains bounds and tests to compensate only using the expected values (car speed ~ 5–20 m·s^{-1}, y between 20 and 30 meters, fitted |m| below 600 A·m^2). For details of the algorithm and used functions, see Appendix.

3.2.1. Webcam-Trial: Magnetic Moment Statistics. We applied the compensating algorithm on the dataset from the verification video trial (see Chapter 2.1) in order to check the feasibility of our model. In the 50-minute dataset, we had ~270 car passages: 2 bus-coaches, 4 vans, and 17 motorbikes and the rest were passenger cars (see Figure 6 for the induced disturbances); they were evenly distributed in the close and far lane (130 vs. 133 occurrences). The resulting "typical" magnetic moment for passenger cars and busses was found as 250 ± 50 A·m^2 and 520 ± 50 A·m^2, respectively (the compensating algorithm did not start for the motorbikes due to the gradient threshold). In Figure 9, we show statistics of the individual magnetic moment components (only passenger cars shown), from which it is evident that the largest component is the vertical one which tends to be oriented along the magnetic flux lines, i.e., the m_z component does not change its sign depending on car trajectory orientation.

3.2.2. Compensating the Disturbances. An example result for compensating a single car disturbance is shown in Figure 10—the original data, the fitted dipole from moving the car, and the data after disturbance compensation are

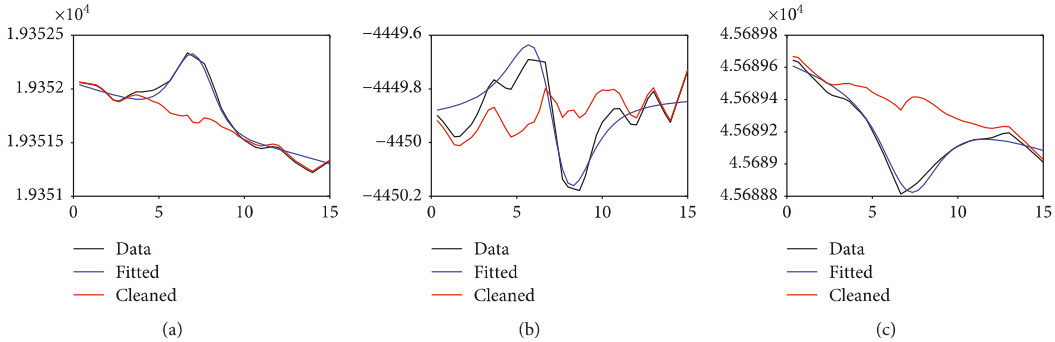

FIGURE 10: The original data (black), the fitted curve (blue), and the resulting cleaned-up data (red) for the NS-y (a), EW-x (b), and vertical-z component (c) of the magnetic field, respectively. The car passage occurs at $t = 7.5$ s. Fitted values were $x_0 = 56$ m, $v = -7.8$ m·s^{-1}, $y = 19.8$ m, $m = [7, 23.6, 43.5]$ A·m^2.

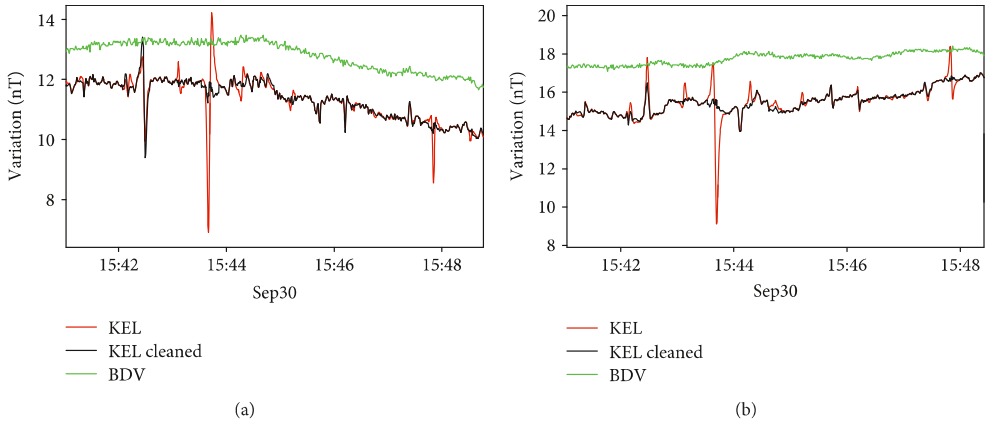

FIGURE 11: The original (red) and cleaned (black) KEL data compared to the aligned BDV data (5 minutes shown). (a) NS-y component, (b) EW-x component. The 15:42 (left) peak is not being well compensated, since it occurred when two cars were passing in adjacent lanes and our model fails to find the correct solution. The small uncompensated peaks (about 15:46) did not fit the gradient threshold and/or result tests (see text).

shown for x, y, and z field components. The noise clearly decreased in the cleaned-up dataset—see Figure 11 for a close-up of time-domain and Figure 12 for two spectrograms of 14-hour data.

4. Conclusion

We show an approach on how to deal with (1) unstabilized ambient temperature and (2) man-made disturbances occurring at two variometric stations. Whereas the first problem is usually solved by temperature stabilization—active or passive [15]; our approach shows that a "moderate" performance can be achieved even at ambient temperatures. Although the presented method seems straightforward, we are not aware of other ambient-temperature magnetic field stations utilizing such long-term calibration and compensation. The overall maximum residual drift of 5 nT p-p during 30°C temperature swing was achieved, which is even in accordance with INTERMAGNET standards [16], where the instrument should keep 0.25 nT·C^{-1} for vectorial readings, but it still does not fulfill the required 1 nT accuracy for scalar values. However, for our purposes, this approach brings fast and reliable results as we can really choose the ambient-run site at PLM as a redundant source of magnetic data. The steps and results shown here can be beneficial to many "repeat" stations, which usually run at ambient temperatures and which are supplementing the magnetic observatories. Even better results can then be expected if the sensor is, i.e., buried at 1-2 meters to avoid such large temperature fluctuations, and of course, when utilizing at least a moderate temperature stabilization (±2°C), the residual drifts after fitting would be one order of magnitude less than those presented.

As for the second problem, fitting and cleaning of a 14-hour 1-second dataset took less than 60 seconds on a Core-i7 PC using MATLAB R2015, so *off-line* postprocessing of daily data could be viable even in embedded systems running Linux and using Python fitting libraries. The fitting speed and accuracy can be improved by having an a priori

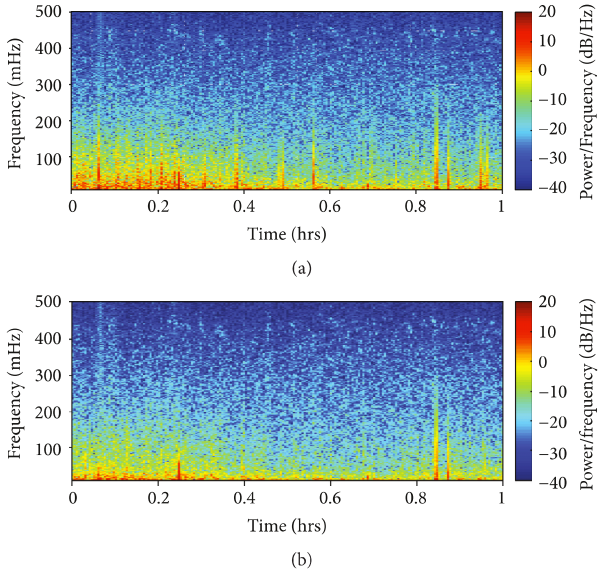

Figure 12: Spectrograms of 14 hours of KEL data (NS-y)—original data with car disturbances (a) and after disturbances compensation (b).

```
function F = field-fit(x,t)
    x0 = x(1); % initial x-distance [m]
    v = x(2); % car speed [m/s]
    y = x(3); % y-distance [m]
    m1 = x(4); % magnetic moment components [A·m2]
    m2 = x(5); %
    m3 = x(6); %
    Bx = x(7); % Earth's field components [nT]
    By = x(8); %
    Bz = x(9); %
    dBdtX = x(10); % Earth's field variation (linear) during the disturbance
    dBdtY = x(11); %
    dBdtZ = x(12);%
[bbx,bby,bbz] = dip2B(x0 + t*v,y,0,[m1,m2,m3]); %% calculating the disturbing field by
                                                    %% moving dipole along x-coord.
    F(:,1) = Bx + bbx + dBdtX*t;
    F(:,2) = By + bby + dBdtY*t;
    F(:,3) = Bz + bbz + dBdtZ*t;
end
    x = lsqcurvefit(@field-fit, guess, xdata, Bobs, lb, ub)
```

Algorithm 1: Appendix - Matlab code.

knowledge of the target y-distance (i.e., knowing the lane) and/or the car speed. For achieving this, distance calculation from axial gradiometer reading [17] or speed measurement with magnetic sensor [18] could be used. Also, improved detection of the passing cars can be facilitated with a short-baseline gradiometer placed as close to the street as possible, which also results in a better approximation of the gradient by the calculated field difference. As for the problem with two cars passing in adjacent lanes, it could be possibly solved by employing a second order model with two car trajectories and vector summation of the magnetic signature; for detection of this situation could symmetrically deploy two short-baselines along the street and observe their output in time.

We again emphasize that this method, when compared to the usual ways—disregarding or interpolating the data heavy low-pass filtering [9, 19]—allows not only to keep the true DC value but also does not destroy the "high frequency" component originating from various physical phenomena (field oscillations, solar storm onsets, etc.).

Appendix

The basic MATLAB function utilized in the optimization problem for car-induced disturbances cancelling is shown in this appendix. The *field-fit* function enters the least-squares curve-fitting algorithm *lsqcurvefit* of the Optimization Toolbox (MATLAB 2015) with a guess of the values and lower and upper bounds, where *xdata* is the time vector and B_{Obs} is the vector of the observed magnetic field. The function *dip2B* to calculate the field from a point-like dipolar source follows the dipolar term in equation (3); an example implementation can be accessed, e.g., in [20].

Data Availability

The geomagnetic data used to support the findings of this study are available from the corresponding author upon request.

Conflicts of Interest

The authors declare no conflict of interest.

Authors' Contributions

Conceptualization, investigation, software, methodology, data curation, and visualization was provided by M. J.; writing was performed by M. J., M. V., and T.B.; resources and data collection were provided by M. B., M. J., M. V., and T. B.

Acknowledgments

We would like to thank the Military Geographic and Hydrometeorologic Office of the Czech Army for the possibility to work and acquire data at the Meteorologic and Seismic station Polom, including the complimentary accommodation. We would also like to thank Jaroslav Pokorný for his logistic and technical support during onsite measurements.

References

[1] L. W. Pedersen and L. Merenyi, "The FGE magnetometer and the Intermagnet 1 second standard," *Journal of Indian Geophysical Union*, vol. 2, pp. 30–36, 2016.

[2] A. Marusenkov, "Possibilities of further improvement of 1 s fluxgate variometers," *Geoscientific Instrumentation, Methods and Data Systems*, vol. 6, no. 2, pp. 301–309, 2017.

[3] M. Janošek, V. Petrucha, and M. Vlk, "Low-noise magnetic observatory variometer with race-track sensors," *IOP Conference Series: Materials Science and Engineering*, vol. 108, article 012026, 2016.

[4] V. Petrucha, P. Kaspar, P. Ripka, and J. M. Merayo, "Automated system for the calibration of magnetometers," *Journal of Applied Physics*, vol. 105, no. 7, article 07E704, 2009.

[5] N. Olsen, L. Tøffner-Clausen, T. J. Sabaka et al., "Calibration of the Ørsted vector magnetometer," *Earth, Planets and Space*, vol. 55, no. 1, pp. 11–18, 2003.

[6] N. Kompein, R. Pleschberger, R. Egli, B. Leichter, and R. Leonhardt, "A comparison between Conrad Observatory and the old Wien Cobenzl observatory: insights into anthropogenic ground currents," in *Book of Abstracts - XVII IAGA Workshop on Geomagnetic Observatory Instruments, Data Acquisition and Processing*, p. 83, Dourbes, Belgium, 2016.

[7] "SŽDC-operation of infrastructure," June 2018, http://provoz.szdc.cz/PORTAL/ViewArticle.aspx?oid=594598.

[8] L. Laža, "Four decades of the Polom station, Vojenský geografický obzor 2014," vol. 2, pp. 4–33, 2014, June 2018, http://www.vgo.army.cz/sites/vgo.army.cz/files/dokumenty/zakladni-stranka/vgo_2014_02.pdf.

[9] J. Jankowski and C. Sucksdorff, *Guide for Magnetic Measurements and Observatory Practice*, International association of Geomagnetism and Aeronomy, Boulder, 1996, June 2018, http://www.iaga-aiga.org/data/uploads/pdf/guides/iaga-guide-observatories.pdf.

[10] "Geomagnetic observatory of Kelčany," June 2018, https://maglab.fel.cvut.cz/geomagnetic.

[11] G. Schultz, "Geomagnetic results Wingst, 2001- Yearbook No. 47," in *Yearbook Magnetic Results 2001, 2002, 2003*, H. J. Linthe, Ed., p. 59, GfZ Potsdam, 2007.

[12] Y. Nishio, F. Tohyama, and N. Onishi, "The sensor temperature characteristics of a fluxgate magnetometer by a wide-range temperature test for a mercury exploration satellite," *Measurement Science and Technology*, vol. 18, no. 8, pp. 2721–2730, 2007.

[13] J. D'Errico, "Bound constrained optimization using fminsearch," *Math Works-File Exchange*June 2018, https://www.mathworks.com/matlabcentral/fileexchange/8277-fminsearchbnd–fminsearchcon.

[14] A. Cerman, J. M. Merayo, P. Brauer, and F. Primdahl, "Self-compensating excitation of fluxgate sensors for space magnetometers," in *2008 IEEE Instrumentation and Measurement Technology Conference*, pp. 2059–2064, Victoria, BC, Canada, May 2008.

[15] M. Korte, M. Mandea, H. J. Linthe, A. Hemshorn, P. Kotzé, and E. Ricaldi, "New geomagnetic field observations in the South Atlantic anomaly region," *Annals of Geophysics*, vol. 52, no. 1, pp. 65–81, 2009.

[16] B. J. St-Louis, E. A. Sauter, and R. L. Coles, "INTERMAGNET technical reference manual, version 4.6, INTERMAGNET 2012," June 2018, http://www.intermagnet.org/publications/intermag_4-6.pdf.

[17] M. Janošek, A. Platil, and J. Vyhnánek, "Simple estimation of dipole source z-distance with compact magnetic gradiometer," *IOP Conference Series: Materials Science and Engineering*, vol. 108, no. 1, article 012025, 2016.

[18] V. Markevicius, D. Navikas, A. Idzkowski, A. Valinevicius, M. Zilys, and D. Andriukaitis, "Vehicle speed and length estimation using data from two anisotropic magneto-resistive (AMR) sensors," *Sensors*, vol. 17, no. 8, p. 1778, 2017.

[19] J. J. Curto, S. Marsal, J. M. Torta, and E. Sanclement, "Removing spikes from magnetic disturbances caused by trains at Ebro Observatory," in *Proceedings of XIII IAGA workshop on geomagnetic observatory instruments, data acquisition and processing*, pp. 60–66, Boulder, CO, USA, 2009, US Geological Survey Open File Report 1226.

[20] University of British Columbia, "Potential fields in Earth and planetary sciences," June 2018, https://www.eoas.ubc.ca/~malasad/EOSC450.

Identification of Geomagnetic Pulsations in SQUID Data for Space Weather Research

Elda F. Saunderson, *Member, IEEE*, Michal Janošek, *Member, IEEE*, Michal Dressler, *Member, IEEE*, Amoré E. Nel, Stefan I. Lotz, and Coenrad J. Fourie, *Senior Member, IEEE*

***Abstract*—A High Temperature Superconductor (HTS) SQUID magnetometer is located at the INTERMAGNET Hermanus Magnetic Observatory (HER) site in South Africa. The LN_2-cooled SQUID is operated unshielded and records the geomagnetic field continuously. If validated, the SQUID may be used as a space weather instrument. The SQUID records small geomagnetic variations such as pulsations, which are short period fluctuations of the geomagnetic field at ULF frequencies. Although the SQUID magnetometers are about 10× more sensitive than fluxgate magnetometers, it is running in an urban environment contaminated by anthropogenous noise. It was also found that one of the SQUIDs is prone to thermally induced oscillations due to thermo-acoustic oscillations in the dewar. To distinguish pulsations from uncorrelated noise, the SQUID data is correlated with fluxgate data from the two closest INTERMAGNET observatories, Hartebeesthoek (HBK) and Keetmanshoop (KMH), both located more than 1000 km away. Man-made noise and SQUID oscillations should give low coherence between SQUID/KMH and SQUID/HBK pairs. Coherence higher than 0.9 was found when pulsations were present in the data and the algorithm has also proven effective on data contaminated with the thermal SQUID oscillations.**

***Index Terms*—Geomagnetic field, pulsations, space weather, SQUID, thermal oscillations.**

I. Introduction

A HIGH Temperature Superconductor (HTS) SQUID magnetometer is located at the Hermanus Magnetic Observatory (HER) in South Africa and has been in operation for the past 13 years, with near continuous operation (95%) during the past 3 years. The LN_2-cooled SQUID is operated unshielded and records the three components of the geomagnetic field continuously [1], including small geomagnetic variations such as pulsations.

The HER observatory in South Africa also boasts a 24/7 space weather prediction centre, and it is with this application in mind that the SQUID is investigated as a space weather instrument, which is a novel application for SQUIDs - similar studies in remote locations were done with He-cooled, shielded, Low Temperature SQUIDs [2], [3] but were not aimed at a long-term operation as a geophysical instrument.

The SQUID magnetometer utilized in this study is co-located with observatory grade fluxgate magnetometers which validate the SQUID data. The SQUID magnetometer is an order of magnitude more sensitive than the fluxgate magnetometers, but operates in a semi-urban environment where it suffers from anthropogenous noise. The monitoring of geomagnetic pulsations using the SQUID magnetometer would be an excellent space weather application, however, the surrounding anthropogenous noise often falls within the same frequency range as the geomagnetic events, mainly for sub-nanotesla magnitudes. This paper investigates the possibility of identifying the SQUID recorded pulsations in the presence of anthropogenous noise by correlating the data with magnetic observatories some distance away, where the anthropogenous noise will not be correlated to the SQUID.

We show that the most sensitive SQUID magnetometer suffers from thermal noise due to an apparent high temperature coefficient of the instrument, coupled to thermal oscillations in the LN_2 bath. The frequency of these oscillations is unfortunately close to that of the geomagnetic pulsations under investigation, creating a significant challenge. The oscillation effect is presented as well as an algorithm for coherence calculations, which was shown as effective to mitigate this parasitic effect, allowing us to use the full SQUID data, not only the "quiet days" without temperature oscillations.

II. Background

A. Geomagnetic Pulsations

Geomagnetic pulsations are small fluctuations of the near-Earth magnetic field typically falling within the ultra-low frequency (ULF) range between about 1 mHz to 1 Hz [4], [5], [6]. ULF pulsations can be driven by various types of mechanisms in the magnetosphere and the upstream solar wind. The nature of the plasma instabilities and the efficiency of coupling with different plasma populations and their transfer

Manuscript received 26 September 2023; revised 4 December 2023; accepted 10 December 2023. Date of publication 8 January 2024; date of current version 6 February 2024. This work was supported by South African National Research Foundation (NRF) under Grant ERT22062728110. *(Corresponding author: Elda F. Saunderson.)*

Elda F. Saunderson is with South African National Space Agency, Hermanus 7200, South Africa, and also with Stellenbosch University, Stellenbosch 7600, South Africa (e-mail: esaunderson@sansa.org.za).

Michal Janošek and Michal Dressler are with Czech Technical University in Prague, Prague 16000, Czechia (e-mail: janosem@fel.cvut.cz; dressmic@fel.cvut.cz).

Amoré E. Nel and Stefan I. Lotz are with South African National Space Agency, Hermanus 7200, South Africa (e-mail: anel@sansa.org.za; slotz@sansa.org.za).

Coenrad J. Fourie is with Stellenbosch University, Stellenbosch 7600, South Africa (e-mail: coenrad@sun.ac.za).

Color versions of one or more figures in this article are available at https://doi.org/10.1109/TASC.2024.3350597.

Digital Object Identifier 10.1109/TASC.2024.3350597

to the inner magnetosphere and ionosphere is dependent on prevailing conditions in the solar wind and magnetosphere. ULF waves show oscillations with a quasi-sinusoidal waveform (Pc) or irregular waveforms (Pi), which are further divided into period bands that isolate a specific type of pulsation. The geomagnetic pulsations most commonly observed at low to middle latitudes during local daytime are Pc3 (22–100 mHz) and Pc4 (7–22 mHz) quasi-sinusoidal continuous pulsations [5] with amplitudes of up to a few nT. Pc3 and Pc4 waves are routinely caused by waves in the upstream solar wind propagating into the magnetosphere where wave power is transferred to the ionosphere. The ULF wave signals detected at ground level provide information about the region it has propagated through, rather than from the region (magnetosphere) it was generated.

Historically the spectral structure of Pi, Pc3 and Pc4 ULF pulsations [7], [8] has been studied using low latitude ground-based stations in South Africa, which usually consisted of 1 Hz induction magnetometer data. These have been replaced in 2013 by LEMI-025 fluxgate magnetometers [9].

Geomagnetic storms are multi-day events characterized by the impact and subsequent disturbance of the geomagnetic field by fast, dense solar wind plasma, typically originating from coronal mass ejections (CME) [10]. The disturbance of the geomagnetic field can cause various negative impacts on technological systems on the Earth and in space [11]. Geomagnetic pulsations can serve to indicate the current state of the magnetosphere during the onset, expansion and recovery phases of a geomagnetic storm, as different types of wave-particle interactions are indicative of different coupling and recovery processes. Pulsation events are heavily affected by any change in orientation of the interplanetary magnetic field or an increase in solar wind velocity [5], [12]. Pi2 pulsations (6–25 mHz) occur during magnetospheric substorm onsets and intensifications [13] in mid- or low latitudes on the nightside [14], which makes it a good indicator of substorms [15] and an important tool in space weather monitoring and forecasting [9], [11]. The high fidelity of SQUID observations would enable increased sensitivity and time resolution of Pc and Pi pulsation events.

B. SQUID Setup at the Observatory Site

The three-axis HTS SQUID magnetometer has an M2700 SQUID from Star Cryoelectronics (25 nT/Φ_0, <300 fT/$\sqrt{\text{Hz}}$) as vertical axis and both horizontal axes are HTM-8 SQUIDs from FZ Jülich (4.5 nT/Φ_0, <45 fT/$\sqrt{\text{Hz}}$). The SQUID magnetometer is LN_2-cooled in a 34-litre unpressurised dewar and operated unshielded. The LN_2 dewar is manually refilled every 3.5 weeks due to the high boil-off rate, limited by the selected dewar and losses due to the SQUID installation. The SQUID magnetometer is located in a non-magnetic building and co-located (2 m) with a low noise triaxial fluxgate magnetometer from the Czech Technical University, as well as the HER observatory DMI FGE [16] fluxgate magnetometer (70 m); both are used as references for the SQUID that is a relative instrument [17]. The SQUID magnetometer is generally at least 10× more sensitive to changes in the magnetic flux density than the reference fluxgate magnetometers.

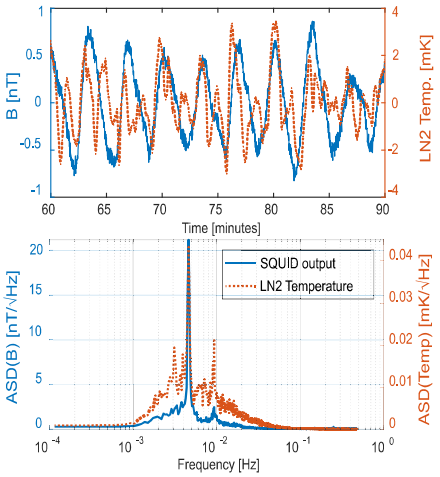

Fig. 1. 5 mHz SQUID and LN_2 temperature oscillations, time domain (top), and amplitude spectrum (bottom).

The 16 ha HER magnetic observatory site [18], where the SQUID is located, is magnetically clean to INTERMAGNET standards. However, it is located in a semi-urban environment where it is surrounded by a general residential area, three hospitals, a light industrial area, and located 400 m from the Atlantic Ocean. These factors add to the increased anthropogenous noise present.

The final purpose of the SQUID magnetometer as additional space weather instrument would be to add sensitivity and higher temporal resolution to space weather measurements [1].

III. Thermal Oscillations in the Dewar

During installation of the horizontal HTM-8 SQUIDs it was observed that these SQUIDs exhibit excess noise as a low frequency oscillation up to 2 nT_{pp}, T ≈ 200 s or f ≈ 5–6 mHz. Unfortunately, this falls well within the frequency range of geomagnetic pulsations, which are the subject of this study, and is very close to Pc pulsation frequencies.

All possible sources of oscillations were investigated, including monitoring during an unrelated complete absence of electricity grid supply at the site and surrounding town; the observed oscillations persisted. A non-magnetic resistive temperature sensor was inserted in the LN_2 bath, and 6 mK_{pp} temperature oscillations were recorded at 5–6 mHz [19]. Correlation between the oscillations on the SQUIDs and the temperature oscillations measured implied that 6 mK_{pp} temperature oscillations yield 2 nT_{pp} SQUID oscillations (Fig. 1). After additional tests in an alternative dewar of similar shape and volume [19] it was concluded that the temperature oscillation in the LN_2 bath is caused by irregular boil off rate [20] and the specific thermal resonance is determined by dewar shape, heat influx and pressure changes.

The LN_2 dewar is refilled every 3.5 weeks, when the level drops to 42 cm below the neck. The dewar is refilled into the neck to the top completely, so for the first 24 hours after refill the LN_2 does not fall below the shoulder of the dewar. Long term

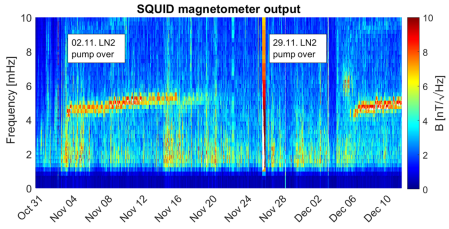

Fig. 2. Frequency spectra of HTM-8 oscillations.

data has shown that the amplitude and frequency of oscillations changes slightly as the level of the LN_2 decreases, implying that the increasing volume of vapor phase in the dewar plays a role. Fig. 2 shows the change in the 5 mHz oscillations, also showing that the oscillations disappear towards end of LN_2 refill period and 1 day thereafter. Thus, initially the use of horizontal SQUID data for geomagnetic pulsations was limited to these thermally quiet days.

IV. Coherence of Magnetic Data

A. Pulsations Vs. Anthropogenous Noise

In order to identify geomagnetic pulsations in SQUID data, it is necessary to distinguish pulsations from anthropogenous noise. Although the SQUID utilizes two on-site fluxgate magnetometers as references, these magnetometers would suffer from the same or similar man-made noise. Thus, we correlated the SQUID data with fluxgate data from INTERMAGNET magnetic observatories located far away, where anthropogenous noise correlation is not expected. The SQUID data were correlated with fluxgate data from the Hartebeesthoek (HBK) observatory, with 9° difference in both longitude and latitude (1400 km NE), as well as the Keetmanshoop (KMH) observatory 1000 km North of HER. The lower sensitivity and higher noise of HBK and KMH magnetometers do not affect the coherence calculation.

B. SQUID and Observatory Data Processing

The 4 Hz SQUID data is down-sampled using a digital filter to 1 Hz to compare with 1 Hz INTERMAGNET observatory data. The data from both the SQUID and KMH/HBK magnetometers are bandpass filtered between 3–250 mHz with a 20th order infinite impulse response (IIR) filter to remove the diurnal geomagnetic field variation and higher frequency signals not of interest. Coherence using the Welch method estimation of the power spectral density (PSD) [21] is computed using MATLAB software and "mscohere" package [22]. Coherence is calculated in a sliding window with 30 or 60 minutes length, 93% overlap, using a fast Fourier transform (FFT) of 1024 points. Coherence throughout the day is plotted in a "coherogram".

C. Coherence in Z: SQUID and HBK

The advantage of the Z-axis (B_z, vertical) SQUID is its immunity to the oscillations in the dewar, so first trials were done using the Z component of the magnetic field. Fig. 3 shows data from 2022-10-04. The difference between the SQUID and HBK

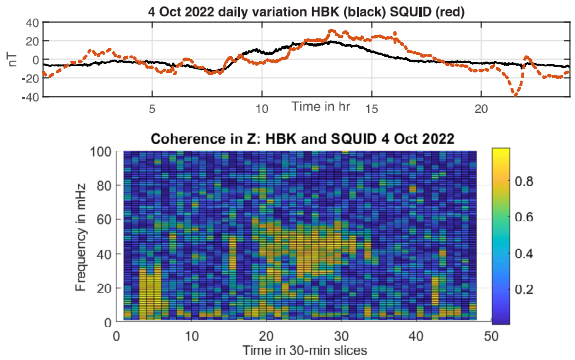

Fig. 3. Time domain and coherence SQUID and HBK: Z axis.

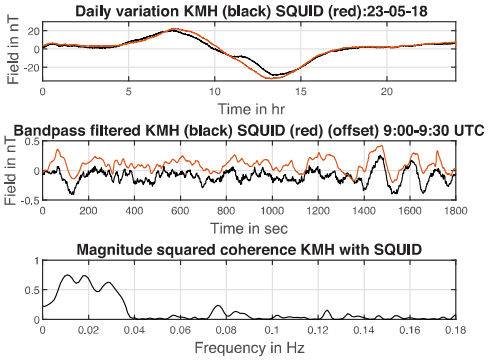

Fig. 4. Raw data, filtered data and coherence in H axis.

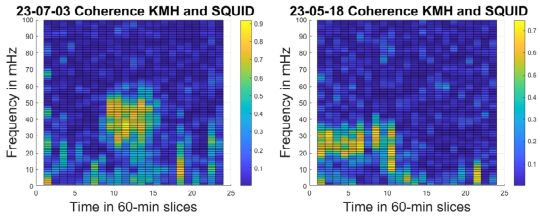

Fig. 5. Coherence in the H axis: SQUID and KMH, 2 days.

data is mainly due to anthropogenous noise in Z at the SQUID location. As depicted in the spectrograph, during the daytime Pc3 pulsations were observed in the SQUID and HBK data sets with coherence higher than 0.9 at 36, 41 and 44 mHz. During night-time Pi pulsations were observed in both data sets with coherence of 0.97 at 12.7 to 22.5 mHz. During the remainder of the 24 hours coherence between the data sets were around 0 with peaks up to 0.17.

D. Coherence in H: SQUID and KMH, Before and After Refill

For coherence in the H axis (B_H, local magnetic north) two days with observed pulsations are presented (Figs. 4 and 5), which are oscillation free (1 day before and after refill).

Pulsations are observed in both KMH and SQUID data both on 2023-05-18 and 2023-07-03 with coherence about 0.62 to 0.93,

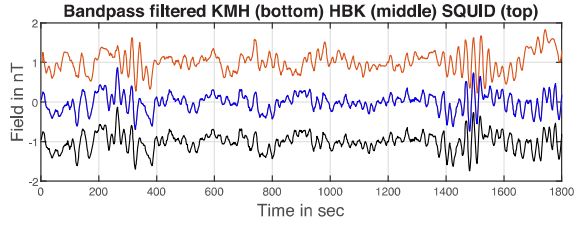

Fig. 6. Bandpass filtered data, ± 1 nT offset for visibility.

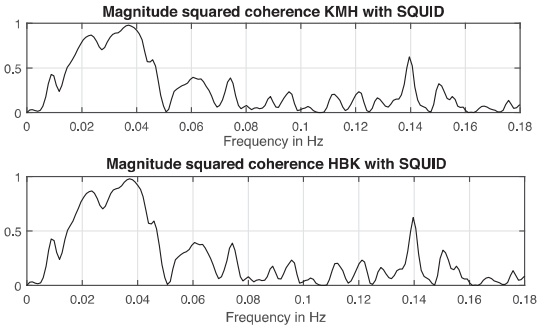

Fig. 7. Coherence with HBK and KMH; low 5 mHz amplitude.

between 11–46 mHz. The time-domain plot in Fig. 4 with pulsation amplitudes of only ∼0.1 nT shows the advantage of our method. In the time domain one could not identify anthropogenous noise from pulsations with certainty, especially given that these levels are on the edge of the KMH fluxgate magnetometer resolution, as opposed to the SQUID which has much higher sensitivity.

E. Coherence in H: SQUID and KMH, 3 Days Before Refill

Coherence results in the H axis are shown for 2023-03-04 at 14:00–14:30 UTC; 3 days before refill. Although the 5 mHz oscillations were still present, the amplitude is already low. Fig. 6 shows the bandpassed time-domain data. The pulsations recorded on the SQUID show excellent correlation with both HBK and KMH (Fig. 7). The results, which show almost no coherence at 5 mHz, indicated that this method could be feasible for remaining days with 5 mHz oscillations present.

F: Coherence in H: SQUID and KMH, High 5 mHz Oscillation

We are showing results for 2023-09-20 with clearly observed pulsations as well as 5 mHz oscillations in the time domain (Figs. 8 and 9). During the first 30 minutes the SQUID data coincides with the KMH data, but during the last 30 minutes the inherent 5 mHz SQUID temperature induced oscillations are evident. The SQUID shows excellent correlation with both HBK and KMH for pulsation frequencies, and with minimal coherence at 5 mHz (theoretically it would be zero).

V. Conclusion

Coherence calculations between unshielded SQUID and fluxgate data from magnetic observatories located 1000–1500 km

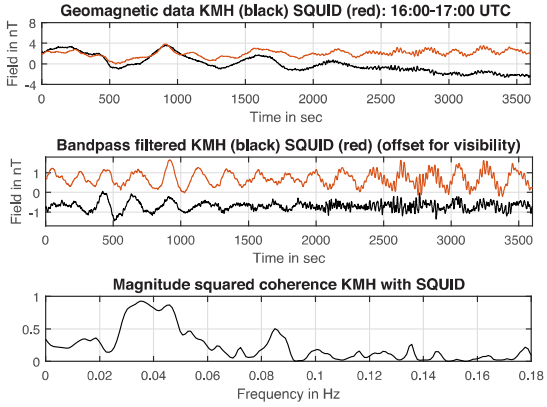

Fig. 8. Coherence with KMH, 5 mHz visible in time domain but suppressed in the coherence graph.

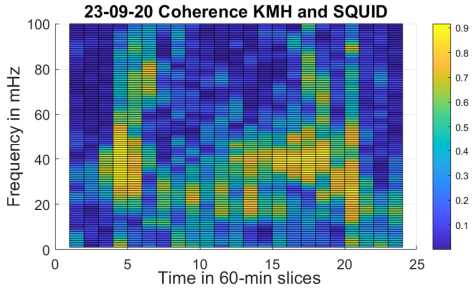

Fig. 9. Coherence SQUID and KMH, 5 mHz not visible.

away was shown as a useful tool to obtain information on whether we are observing anthropogenous noise or actual geomagnetic signal. We are able to confirm Pc and Pi geomagnetic pulsations both in the vertical and horizontal axes. Pulsations even smaller than 0.1 nT in amplitude were successfully detected, which would not be possible with a single observatory fluxgate magnetometer.

In the H axis, where the more sensitive SQUID is installed, the data is contaminated with its response to a 5 mHz thermal oscillation in the LN_2 bath. Envisioned solutions to mitigate the oscillations range from keeping the LN_2 dewar 100% full all the time to keeping the system below atmospheric pressure to stabilize the temperature well below the critical temperature of the SQUIDs. Also, alternative dewars with extended holding times may be available, but their thermo-acoustic properties would need to be investigated. However, we have shown that calculating the coherence is useful not only to suppress the man-made noise, but also the SQUID thermal oscillations.

The data and solution presented indicate that an unshielded HTS SQUID magnetometer could be generally useful as a space weather instrument for detecting low-amplitude Pc and Pi pulsations. Given its high resolution, an improvement in forecasting of geomagnetic storms should also be possible.

References

[1] T. K. Matladi, C. J. Fourie, T. J. Phiri, E. F. Saunderson, D. J. Gouws, and C. Kwisanga, "Correlation between fluxgate and

SQUID magnetometer data-sets for geomagnetic storms," in *Proc. I-DUST Inter Disciplinary Underground Sci. Technol. Conf.*, 2014, pp. 1–5, doi: 10.1051/e3sconf/20140402002.

[2] J. Kawai, M. Miyamoto, M. Kawabata, M. Nosé, Y. Haruta, and G. Uehara, "Characterization and demonstration results of a SQUID magnetometer system developed for geomagnetic field measurements," *Superconductor Sci. Technol.*, vol. 30, 2017, Art. no. 084002, doi: 10.1088/1361-6668/aa733f.

[3] S. Henry, E. Pozzo di Borgo, and A. Cavaillou, "Tracking geomagnetic fluctuations to picotesla accuracy using two superconducting quantum interference device vector magnetometers," *Rev. Sci. Instrum.*, vol. 84, 2013, Art. no. 024501, doi: 10.1063/1.4790715.

[4] J. A. Jacobs, *Geomagnetic Pulsations*. New York, NY, USA: Springer, 1970.

[5] E. Kozlovskaya and A. Kozlovsky, "Influence of high-latitude geomagnetic pulsations on recordings of broadband force-balanced seismic sensors," *Geosci. Instrum. Method Data Syst.*, vol. 1, pp. 85–101, 2012.

[6] P. R. Sutcliffe, B. Heilig, and S. Lotz, "Spectral structure of Pc3–4 pulsations: Possible signatures of cavity modes," *Annales Geophysicae*, vol. 31, pp. 725–743, 2013.

[7] J. A. Jacobs, Y. Kato, S. Matsushita, and V. A. Troitskaya, "Classification of geomagnetic pulsations," *J. Geophys. Res.*, vol. 69, pp. 180–181, 1964, doi: 10.1029/JZ069i001p00180.

[8] B. Heilig et al., "Empirically modelled Pc3 activity based on solar wind parameters," *Annales Geophysicae*, vol. 28, pp. 1703–1722, 2010, doi: 10.5194/angeo-28-1703-2010.

[9] P. B. Kotzé, P. J. Cilliers, and P. R. Sutcliffe, "The role of SANSA's geomagnetic observation network in space weather monitoring: A review," *Space Weather*, vol. 13, pp. 656–664, 2015, doi: 10.1002/2015SW001279.

[10] W. D. Gonzalez et al., "What is a geomagnetic storm?," *J. Geophys. Res.*, vol. 99, pp. 5771–5792, 1994, doi: 10.1029/93JA02867.

[11] M. Vallée, L. Newitt, I. R. Mann, M. Mouhamed, R. Dumont, and P. Keating, "The spatial and temporal characteristics of PC3 geomagnetic activity over Canada in 2000, as a guide to planning the times of aeromagnetic surveys," *Pure Appl. Geophys.*, vol. 164, pp. 161–176, 2007.

[12] R. L. McPherron, "Magnetic pulsations: Their sources and relation to solar wind and geomagnetic activity," *Surv. Geophys.*, vol. 26, pp. 545–592, 2005, doi: 10.1007/s10712-005-1758-7.

[13] P. R. Sutcliffe, "Substorm onset identification using neural networks and Pi2 pulsations," *Annales Geophysicae*, vol. 15, pp. 1257–1264, 1997.

[14] M. Nosé et al., "Automated detection of Pi2 pulsations using wavelet analysis: 1 Method and an application for substorm monitoring," *Earth Planets Space*, vol. 50, pp. 773–783, 1998.

[15] T. K. Saito, K. Yumoto, and Y. Koyama, "Magnetic pulsation Pi2 as a sensitive indicator of magnetospheric substorm," *Planet. Space Sci.*, vol. 24, pp. 1025–1029, 1976.

[16] A. Csontos, L. Hegymegi, and B. Heilig, "Temperature tests on modern magnetometers," *Pub. Inst. Geophys., Polish Acad. Geophys.*, vol. 99, 2007, Art. no. 171.

[17] M. Janošek, D. Novotny, M. Dressler, and E. Saunderson, "Low frequency noise investigation of pT-level magnetic sensors by cross-spectral method," in *Proc. IEEE Sensors Conf.*, 2021, pp. 1–4, doi: 10.1109/SENSORS47087.2021.9639875.

[18] P. B. Kotzé, "Hermanus magnetic observatory: A historical perspective of geomagnetism in Southern Africa," *Hist. Geo- Space Sci.*, vol. 9, pp. 125–131, 2018, doi: 10.5194/hgss-9-125-2018.

[19] M. Janošek, M. Dressler, and E. F. Saunderson, "Excess ULF noise in HTS SQUID magnetometer caused by cryostat temperature oscillations," presented at the XIII Eur. Magn. Sens. Actuat. Conf., Madrid, Spain, July 5–8, 2022.

[20] D. J. Blundell and B. W. Ricketson, "The temperature of liquid nitrogen in cryostat dewars," *Cryogenics*, vol. 19, pp. 33–36, Jan. 1979.

[21] P. Stoica and R. Moses, *Spectral Analysis of Signals*. Upper Saddle River, NJ, USA: Prentice Hall, 2005, pp. 25–26.

[22] The MathWorks, Inc. "Signal Processing Toolbox Reference Documentation." Accessed: Sep. 26, 2023. [Online]. Available: https://www.mathworks.com/help/signal/ref/mscohere.html

Conclusions

The author presents selected topics of his research in the field of precise, room-temperature magnetometers (parallel and orthogonal fluxgate), and a high-temperature-superconductor quantum magnetometer (SQUID), with the emphasis on their metrology and geophysical applications. As the overall magnetometer accuracy is given not only by its precision −mainly governed by magnetometer noise− but also by the calibration uncertainty, relevant publications on both of the topics are presented.

After a brief discussion of the limitations of parallel fluxgate magnetometers, it is shown that the (ultra-) low-frequency noise of the orthogonal, fundamental-mode (OFM) fluxgate magnetometer could be decreased below 1 pT/√Hz at 1 Hz, which brings a new state-of-the-art and a prospect for its use in geophysical exploration, possibly replacing search- coils and even HTS SQUIDs (in the ultra-low-frequency range).

Metrological aspects of magnetometer calibration procedures were covered, e.g. establishing the real-world uncertainties of angular calibrations, creating and maintaining a precise magnetic zero and suppressing the effects of anthropogenous noise on the calibration uncertainty. The latter topic is of increasing importance: the ever escalating man-made noise at legacy metrological installations results in higher uncertainties than anticipated. Several procedures for compensation and/or suppression of anthropogenous noise were presented with the aim to reduce the calibration uncertainty below 100 ppm, even at a sub-urban location.

The magnetometer noise at mHz frequencies is also affected by its parasitic temperature sensitivity (be it due to the magnetometer sensor or its electronics) - it was shown that this is not only the case of the OFM fluxgate, but also a property of a HTS SQUID, where any temperature oscillations in the cryostat (Dewar flask) can result in significant parasitic signal if the SQUID's temperature sensitivity is high enough. Further decreasing the OFM fluxgate magnetometer temperature sensitivity, which is currently about one order of magnitude greater than for a parallel fluxgate, is a current topic. Also, another low-frequency effect was discovered while investigating the temperature properties of the OFM fluxgate − an excess offset drift due to uncompensated field changes, which is however different from perming because of its reversibility − the underlying physics of this effect is still under active research.

References

[1] SHIRMOHAMMADI, S.; MARI, L.; PETRI, D. On the commonly-used incorrect visual representation of accuracy and precision. *IEEE Instrumentation & Measurement Magazine*, 2021, **24**(1), 45-49. 10.1109/MIM.2021.9345597

[2] ISO 10012:2003(en). Measurement management systems — Requirements for measurement processes and measuring equipment. ISO, International Organization for Standardization, 2003. Available from: https://www.iso.org/obp/ui/en/#iso:std:iso:10012

[3] HALL, M.J.; HARMON, S.A. C.; TURNER, S. Magnetic environment and magnetic field standards at NPL for the calibration of low noise magnetometers and gradiometers for cleanliness studies. In: *2012 ESA Workshop on Aerospace EMC*. IEEE, 2012. ISBN:978-92-9092-266-7. Available from: https://ieeexplore.ieee.org/document/6232578

[4] SAUNDERSON, E.F.; GOUWS, D.J. Evaluation of the effect of ambient temperature variation on the calibration of a Large Helmholtz Coils System, employed for the calibration of space qualified magnetometers. In: 2018 *SpaceOps Conference*. 2018. p. 2374. 10.2514/6.2018-2374

[5] SCHULZ, L.; HEINISCH, P.; RICHTER, I. Calibration of off-the-shelf anisotropic magnetoresistance magnetometers. *Sensors*, 2019, **19**(8), 1850. 10.3390/s19081850.

[6] PAJUNPÄÄ, K., et al. Accredited vector magnetometer calibration facility. *Geophysica*, 2007, **43**(1-2), 59-76.

[7] SHIFRIN, V. Ya, et al. A standard quantum measuring system for reproduction and measurement of low direct magnetic field in the range 0.1/spl mu/T-1.5 mT. *IEEE Transactions on Instrumentation and Measurement*, 2005, **54**(2), 727-729. 10.1109/TIM.2005.843578.

[8] PARK, P.G., KIM, Y. G.; SHIFRIN, V. Ya. Maintenance of magnetic flux density standards on the basis of proton gyromagnetic ratio at KRISS. *IEEE Transactions on Instrumentation and Measurement*, 2005, **54**(2), 734-737. 10.1109/TIM.2005.843566

[9] WEYAND, K. Final Report of CCEM Key Comparison CCEM. M-K1: Magnetic flux density by means of transfer standard coil. *Metrologia*, 2005, **42** (1A), 01006. 10.1088/0026-1394/42/1A/01006

[10] WEYAND, K. Maintenance and dissemination of the magnetic field unit at PTB. *IEEE Transactions on Instrumentation and Measurement*, 2001, **50**(2): 470-473. 10.1109/19.918168

[11] RIPKA, P. (ed.). Fluxgate Sensors. *Magnetic sensors and magnetometers*. Artech house, 2021. ISBN 9781630817428

[12] STUTZKE, Nathan A., et al. Low-frequency noise measurements on commercial magnetoresistive magnetic field sensors. *Journal of Applied Physics*, 2005, **97**(10), 10Q107. doi.org/10.1063/1.1861375

[13] LEITNER, S., et al. Design of the Magnetoresistive Magnetometer for ESA's SOSMAG Project. *IEEE Transactions on Magnetics*, 2015, **51**(1): 4001404. 10.1109/TMAG.2014.2358270

[14] FESCENKO I,et al. Diamond magnetometer enhanced by ferrite flux concentrators. *Physical review research*, 2020, **2**(2), 023394. 10.1103/PhysRevResearch.2.023394

[15] JODKO-WŁADZIŃSKA, A., et al. Compensation system for biomagnetic measurements with optically pumped magnetometers inside a magnetically shielded room. *Sensors*, 2020, **20**(16), 4563. 10.3390/s20164563

[16] LI, J., et al. Miniature wide-range three-axis vector atomic magnetometer. *IEEE Sensors Journal*, 2021, **21**(21), 23943-23948. 10.1109/JSEN.2021.3112522

[17] MARUSENKOV, A. Possibilities of further improvement of 1 s fluxgate variometers. *Geoscientific Instrumentation, Methods and Data Systems*, 2017, **6**(2): 301-309. 10.5194/gi-6-301-2017

[18] PETRUCHA, V. and M. BUTTA. Race-track fluxgate sensor scaling versus noise. In: *IEEE SENSORS 2021 proceeding*. IEEE SENSORS 2021, Sydney, 2021-10-31/2021-11-04. Irvine, CA: IEEE Sensors, 2021. ISSN 1930-0395. ISBN 978-1-7281-9501-8. 10.1109/SENSORS47087.2021.9639560.

[19] KOCH, R. H.; ROZEN, J. R. Low-noise flux-gate magnetic-field sensors using ring- and rod-core geometries. *Applied Physics Letters*, 2001, **78**(13), 1897-1899. 10.1063/1.1358852

[20] SASADA, I. Orthogonal fluxgate mechanism operated with dc biased excitation. *Journal of Applied Physics*, 2002, **91**(10): 7789-7791.10.1063/1.1451899

[21] BUTTA, M.; SCHUTTE, B.P. Low-noise orthogonal fluxgate using flipped current Joule annealing. *IEEE Transactions on Magnetics*, 2019, **55**(7), 4002906. 10.1109/TMAG.2019.2894302

[22] LINGALA, M.; NELAPATLA, P. Ch.; ARORA, K. Evaluating the effect of noise from traffic on HYB Magnetic Observatory data during COVID-19 lockdown. *Applied Sciences*, 2022, **12**(5), 2730. 10.3390/app12052730

[23] RAMDAS, V; SETHUNADH, R. A magnetic sensor calibration system based on a closed-loop tri-axial field simulator. *IEEE Access*, 2022, **10**, 81846-81855. 10.1109/ACCESS.2022.3195130

[24] KORTE, M.; MANDEA, M. Geomagnetism: From Alexander von Humboldt to current challenges. *Geochemistry, Geophysics, Geosystems*, 2019, **20**(8), 3801-3820. 10.1029/2019GC008324

[25] MANDEA, M.; KORTE, M.(ed.). *Geomagnetic observations and models*. Springer Science & Business Media, 2010. ISBN 978-90-481-9857-3. 10.1007/978-90-481-9858-0

[26] NAHAYO, E.; KORTE, M. A regional geomagnetic field model over Southern Africa derived with harmonic splines from Swarm satellite and ground-based data recorded between 2014 and 2019. Earth, Planets and Space, 2022, **74**(8). 10.1186/s40623-021-01563-5

[27] LOVE, J.J.; CHULLIAT, A. An international network of magnetic observatories. *Eos, Transactions American Geophysical Union*, 2013, **94**(42), 373-374. 10.1002/2013EO420001

[28] SAITO, T. Geomagnetic pulsations. *Space Science Reviews*, 1969, **10**(3), 319-412. 10.1007/BF00203620

[29] HEYNS, M. J.; LOTZ, S. I.; GAUNT, C. T. Geomagnetic pulsations driving geomagnetically induced currents. *Space Weather*, 2021, **19**(2), e2020SW002557. 10.1029/2020SW002557

[30] PEDERSEN, L. W.; MERENYI, L.. The FGE magnetometer and the INTERMAGNET 1 second standard. *J. Ind. Geophys. Union*, 2016, **2**, 30-36.

[31] BRUNKE, H.-P, IDMER-SCHNIDRIG, R.; KORTE, M. Merging fluxgate and induction coil data to produce low-noise geomagnetic observatory data meeting the INTERMAGNET definitive 1 s data standard. *Geoscientific Instrumentation, Methods and Data Systems*, 2017, **6**(2), 487-493. 10.5194/gi-6-487-2017

[32] KHOMUTOV, S.Y., et al. Noise in raw data from magnetic observatories. *Geoscientific Instrumentation, Methods and Data Systems*, 2017, **6**(2), 329-343. 10.5194/gi-6-329-2017

[33] CHAVE, A.D.; JONES, A.G. (ed.). *The magnetotelluric method: Theory and practice*. Cambridge University Press, 2012. ISBN 978-1-139-02013-8. 10.1017/CBO9781139020138

[34] STOLZ, R., et al. SQUIDs for magnetic and electromagnetic methods in mineral exploration. *Mineral Economics*, 2022, **35**(3), 467-494. 10.1007/s13563-022-00333-3

[35] STOLZ, R., et al. Superconducting sensors and methods in geophysical applications. *Superconductor Science and Technology*, 2021, **34**(3), 033001. 10.1088/1361-6668/abd7ce

[36] FANTAYE, T. Magnetotelluric and transient electromagnetic methods in geothermal exploration with examples from the Krysuvik area, SW-Iceland. *United Nations University 'Geothermal Training Programme' reports*, 2010, **12**, 151-182.

[37] LE ROUX, C.; MACNAE, J. SQUID sensors for EM systems. In: *Proceedings of Exploration*. 2007. p. 417-423. In: Exploration '07: Exploration in the New Millennium : Proceedings of the Fifth Decennial International Conference on Mineral Exploration. Toronto, Canada, 9-12 September 2007

[38] KAWAI, J., et al. Characterization and demonstration results of a SQUID magnetometer system developed for geomagnetic field measurements. *Superconductor Science and Technology*, 2017, **30**(8), 084002. 10.1088/1361-6668/aa733f

[39] KAWAI, J., et al. Improvement of performance of SQUID magnetometer system for highly sensitive geomagnetic field measurements. *IEEE Transactions on Applied Superconductivity*, 2018, **28**(8), 1602607. 10.1109/TASC.2018.2874425

[40] KOREPANOV, V.; MARUSENKOV, A. Flux-gate magnetometers design peculiarities. *Surveys in geophysics*, 2012, **33**(5), 1059-1079. 10.1007/s10712-012-9197-8

[41] BUTTA, M. Orthogonal Fluxgate Magnetometers. In: GROSZ, A, M.J HAJI-SHEIKH, and S. MUKHOPADHYAY, eds. *High Sensitivity Magnetometers*. Basel: Springer, 2016. p. 63-102. Smart Sensors, Measurement and Instrumentation. **19**. ISSN 2194-8402. ISBN 978-3-319-34070-8. 10.1007/978-3-319-34070-8.

[42] CHO, H.-M., et al. Low-frequency noise in field-cooled, directly coupled magnetometers. *IEEE transactions on applied superconductivity*, 1999, **9**(2), 3294-3297. doi.org/10.1109/77.783733

[43] PRIMDAHL, F., et al. Demagnetising factor and noise in the fluxgate ring-core sensor. *Journal of Physics E: Scientific Instruments*, 1989, **22**(12), 1004. 10.1088/0022-3735/22/12/009

[44] RIPKA, P.; PRIBIL, M.; BUTTA, M. Fluxgate offset study. *IEEE Transactions on Magnetics*, 2014, **50**(11),4006804. 10.1109/TMAG.2014.2329777

[45] ZIKMUND, A. *Magnetic calibration by using non-linear optimization method*. 2014. PhD Thesis. 2014, Czech Technical University, FEE, Dept. Of Measurement.

[46] MERAYO, J.MG, et al. Scalar calibration of vector magnetometers. *Measurement science and technology*, 2000, **11(**2), 120. 10.1088/0957-0233/11/2/304

[47] WANG, Y., et al. Wide Range SQUID Amplifier With Proportional Feedback for Flux Quanta Counting Scheme. *IEEE Transactions on Applied Superconductivity*, 2020, **30**(5), 1600505. 10.1109/TASC.2020.2976596

[48] REICH, T.; ORTLEPP, Th; UHLMANN, F. H. New approach for a highly sensitive magnetometer utilizing a multi-stage digital SQUID. *Superconductor Science and Technology*, 2006, **19**(5), S276. 10.1088/0953-2048/19/5/S23

[49] PŘÍHODA, K. MAVACS-A new system creating a non-magnetic environment for paleomagnetic studies. *Cuad. Geol. Iberica.*, 1989, **12**, 223-250.

[50] GONG, X.; CHEN, Sh.; ZHANG, Sh. *JOM-4S Overhauser magnetometer and sensitivity estimation*. Sensors, 2021, **21**(22), 7698.10.3390/s21227698

[51] DURET, D., et al. Performances of the OVH magnetometer for the Danish Oersted satellite. *IEEE Transactions on Magnetics*, 1996, **32**(5), 4935-4937. 10.1109/20.539293

[52] ZIKMUND, A., et al. Precise scalar calibration of a tri-axial Braunbek coil system. *IEEE Transactions on Magnetics*, 2015, **51**(1), 4000704. 10.1109/TMAG.2014.2357783

[53] TAN, Ch., WANG, J.; LI, Z. A frequency measurement method based on optimal multi-average for increasing proton magnetometer measurement precision. *Measurement*, 2019, **135**, 418-423. 10.1016/j.measurement.2018.10.016

[54] SHIFRIN, V. Ya, et al. International comparisons to establish the global network of geomagnetic observatories to SI units. *Metrologia*, 2014, **51**(1A), 01015-01015. 10.1088/0026-1394/51/1A/01015

[55] OLSEN, N., et al. Calibration of the Ørsted vector magnetometer. *Earth, planets and space*, 2003, **55**(1), 11-18. 10.1186/BF03352458

[56] ROTT, N., et al. Three-dimensional coil system for the generation of traceable magnetic vector fields. *Journal of Sensors and Sensor Systems*, 2022, **11**(2), 211-218. 10.5194/jsss-11-211-2022

[57] MATANDIROTYA, E., et al. Evaluation of a Commercial-Off-the-Shelf Fluxgate Magnetometer for Cube Sat Space Magnetometry. *Journal of Small Satellites*, 2013, **2**(1), 133-146. Available from: https://digitalknowledge.cput.ac.za/handle/11189/5894

[58] RIPKA, P. Race-track fluxgate sensors. *Sensors and Actuators A: Physical*, 1993, **37**, 417-421. 10.1016/0924-4247(93)80071-N

[59] Gem Systems, Inc., Overhauser Magnetometers, 2018. Available from: https://www.gemsys.ca/rugged-overhauser-magnetometer/

[60] KORTE, Monika, et al. New geomagnetic field observations in the South Atlantic Anomaly region. Annals of Geophysics, 2009, **52** (1), 65-81. ISSN 2037-416X.

List of author's publications

[Q1] JANOŠEK, Michal. A Precise Gradiometer Suitable for Space Applications. 2014. PhD Thesis. Czech Technical University, FEE, Dept. Of Measurement. Avaiable online: https://dspace.cvut.cz/handle/10467/60803

I. Articles in Impacted Journals - B08

[J1] ▶ SAUNDERSON, E.F., et al. Identification of geomagnetic pulsations in SQUID data for Space Weather research. *IEEE Transactions on Applied Superconductivity*. 2024, 34(3), 10.1109/TASC.2024.3350597.

[J2] ▶ BUTTA, M., M. DRESSLER, and M. JANOŠEK. Offset drift in orthogonal fluxgate and importance of closed-loop operation. *Sensors and Actuators A: Physical*. 2022, **342**, 10.1016/j.sna.2022.113583.

[J3] BUTTA, M., et al. An Improved Composition of CoFeSiB Alloy for Orthogonal Fluxgates. *SENSORS*. 2022, **22**(6), 10.3390/s22062162.

[J4] ▶ DRESSLER, M., M. JANOŠEK, and M. BUTTA. Reduction of magnetic noise limits of orthogonal fluxgate sensor. *AIP Advances*. 2021, **11**(1), 10.1063/9.0000231.

[J5] ▶ JANOŠEK, M., et al. 1-pT noise fluxgate magnetometer for geomagnetic measurements and unshielded magnetocardiography. *IEEE Transactions on Instrumentation and Measurement*. 2020, **69**(5), 2552-2560, 10.1109/TIM.2019.2949205

[J6] ▶ JANOŠEK, M., et al. Estimation of Angular Deviations in Precise Magnetometers. *IEEE Magnetics Letters*. 2019, **10**, 10.1109/LMAG.2019.2944125.

[J7] ▶ JANOŠEK, M., et al. Magnetic Calibration System With Interference Compensation. *IEEE Trans. Magn*. 2019, **55**(1), 10.1109/TMAG.2018.2874169.

[J8] NOVOTNÝ, D., V. PETRUCHA, and M. JANOŠEK. A Digitally Compensated AMR Magnetometer. *IEEE Trans. Magn*. 2019, **55**(1), 10.1109/TMAG.2018.2873235.

[J9] BUTTA, M., et al. Effect of Amorphous Wire Core Diameter on the Noise of an Orthogonal Fluxgate. *IEEE Trans. Magn*. 2018, **54**(11), 10.1109/TMAG.2018.2850905.

[J10] ▶ JANOŠEK, M., et al. Improving Earth's magnetic field measurements by numerical corrections of thermal drifts and man- made disturbances. *Journal of Sensors*. 2018, **2018**, 180409. 10.1155/2018/1804092.

[J11] BUTTA, M. and JANOŠEK, M. Orthogonal Fluxgate Gradiometer With Multiple Coil Pairs. *IEEE Trans. Magn*. 2018,**54**(1), 10.1109/TMAG.2017.2758680.

[J12] ▶ BUTTA, M. and JANOŠEK, M. Very low frequency noise reduction in orthogonal fluxgate. *AIP Advances*. 2018, **8**(4), 047203-1, 10.1063/1.4994208.

[J13] ▶ ULVR, M., et al. Determination of the Overhauser magnetometer uncertainty. *Journal of Electrical Engineering*. 2015, **66**(7), 26-29.

[J14] JANOŠEK, M., et al. Compact Full-tensor Fluxgate Gradiometer. *Journal of Electrical Engineering*. 2015, **66**(7/s), 146-148. ISSN 1335-3632.

[J15] SARKAR, P., et al. Study of Stress-Induced Anisotropy in METGLAS 2714. *IEEE Transactions on Magnetics*. 2014, **50**(11), 10.1109/TMAG.2014.2329992.

[J16] JANOŠEK, M., A. PLATIL, and J. VYHNÁNEK. The Effect of Sensor Size on Axial Gradiometer Performance. *IEEE Transactions on Magnetics*. 2015, **51**(1), 10.1109/TMAG.2014.2359960.

[J17] ▶ ZIKMUND, A., et al. Precise calibration method for triaxial magnetometers not requiring Earth's field compensation. *IEEE Transactions on Instrumentation and Measurement*. 2015, **64**(5), 1250-1255, 10.1109/TIM.2015.2395531.

[J18] BUTTA, M., et al. Electroplated FeNi ring cores for fluxgates with field induced radial anisotropy. *Journal of Applied Physics*. 2015, **117**(17), 10.1063/1.4914874.

[J19] BUTTA, M., et al. Influence of Magnetostriction of NiFe Electroplated Film on the Noise of Fluxgate. *IEEE Trans. Magn*. 2014, **50**(44), 10.1109/TMAG.2014.2327105.

[J20] PETRUCHA, V., M. JANOŠEK, and M. A. AZPÚRUA. Vector Feedback Homogeneity and Inner Layout Influence on Fluxgate Sensor Parameters. *IEEE Trans. Inst. Meas*. 2015, **64**(5), 1293-1299, 10.1109/TIM.2014.2362831.

[J21] RIPKA, P., et al. AMR Proximity Sensor With Inherent Demodulation. *IEEE Sensors Journal*. 2014, **14**(9), 3119-3123, 10.1109/JSEN.2014.2325406.

[J22] BUTTA, M., et al. Fine Smoothing of Conductive Substrate for Permalloy Layer Electroplating. *Acta Physica Polonica A*. 2014, **126**(1), 150-151. ISSN 0587-4246, 10.12693/APhysPolA.126.150.

[J23] ► JANOŠEK, M.,et al. Effects of Core Dimensions and Manufacturing Procedure on Fluxgate Noise. *Acta Physica Polonica A*. 2014, **126**(1),104-105, 10.12693/APhysPolA.126.104

[J24] PLATIL, A., et al. Magnetopneumography Using Optical Position Reference. *Sensor Letters*. 2013, **11**(1), 69-73. 10.1166/sl.2013.2805.

[J25] BUTTA, M., SASADA, I. and JANOŠEK, M. Temperature Dependence of Offset and Sensitivity in Orthogonal Fluxgate Operated in Fundamental Mode. *IEEE Transactions on Magnetics*. 2012, **48**(11), 4103-4106.10.1109/TMAG.2012.2202383.

[J26] TOMEK, J., et al. Magnetopneumography - Incorporation of Optical Position Reference. *Journal of Electrical Engineering*. 2012, **63**(7s), 122-125.

[J27] BUTVIN, P.B., et al. Field Annealed Closed-path Fluxgate Sensors Made of Metallic-glass Ribbons. *Sensors and Actuators*. 2012, **2012**(184), 72-77. 10.1016/j.sna.2012.07.001.

[J28] VYHNÁNEK, J., JANOŠEK, M. and RIPKA, P. AMR Gradiometer for Mine Detection. *Sensors and Actuators*. 2012, **186** 100-104.10.1016/j.sna.2012.03.007

[J29] VYHNÁNEK, J., JANOŠEK, M. and RIPKA, P. AMR Gradiometer for Mine Detection and Sensing. *Procedia Engineering*. 2011, **25** 362-366. 10.1016/j.proeng.2011.12.089

[J30] TOMEK, J., et al. Suppression of Environmental Noise in Magnetopneumography by the use of Higher Order Gradients. *IEEE Transactions on Magnetics*. 2012, **48**(4), 1317-1319. ISSN 0018-9464. 10.1109/TMAG.2011.2172200.

[J31] JANOŠEK, M., et al. Single-core fluxgate gradiometer with simultaneous gradient and homogeneous feedback operation. *Journal of Applied Physics*. 2012, **111**(7), 07E328-1-07E328-3. 10.1063/1.3676238.

[J32] RIPKA, P., et al. Crossfield Effect in Commercial Fluxgate and AMR Sensors. *Journal of Electrical Engineering*. 2010, **61**(7/s), 13-16. Available from: http://iris.elf.stuba.sk/JEEEC/data/pdf/7s_110-05.pdf

[J33] JANOŠEK, M. and RIPKA, P. PCB Fluxgate Gradiometer Measuring dBx/dy. *Journal of Electrical Engineering*. 2010, **2010**(7/s), 7-9. Available from: http://iris.elf.stuba.sk/JEEEC/data/pdf/7s_110-03.pdf

[J34] BUTTA, M., JANOŠEK, M. and RIPKA, P. Field-Programmable Gate Array-based fluxgate magnetometer with digital integration. *Journal of Applied Physics*. 2010, **107**(9), 09E714. 10.1063/1.3360773.

[J35] PRIBULA, O., JANOŠEK, M. and FISCHER., J. Optical Position Sensor Based on Digital Image Processing: Magnetic Field Mapping Improvement. *Radioengineering*. 2011, **2011**(20), 55-60. ISSN 1210-2512. 10.13164/re

[J36] RIPKA, P. and JANOŠEK, M. Advances in Magnetic Field Sensors. *IEEE Sensors Journal*. 2010, **10**(6), 1108-1116. 10.1109/JSEN.2010.2043429.

[J37] JANOŠEK, M., BUTTA, M. and RIPKA, P. Two Sources of Cross-field Error in Racetrack Fluxgate. *Journal of Applied Physics*. 2010, **107**(09E714),1-3. 10.1063/1.3337721.

[J38] JANOŠEK, M. and RIPKA, P. Current-Output of Printed Circuit Board Fluxgates. *Sensor Letters*. 2009, **7**(3), 299-302. 10.1166/sl.2009.1064.

[J39] RIPKA, P., M. JANOŠEK, and M. BUTTA. Crossfield Sensitivity in AMR Sensors. *IEEE Transactions on Magnetics*. 2009, **45**(10), 4514-4517. 10.1109/TMAG.2009.2022051.

[J40] JANOŠEK, M., P. RIPKA, and A. PLATIL. Magnetic Markers Detection Using PCB fluxgate array. *Journal of Applied Physics*. 2009, **105**(7),7E717. 10.1063/1.3074780.

[J41] JANOŠEK, M. and P. RIPKA. PCB Sensors in Fluxgate Magnetometer with Controlled Excitation. *Sensors and Actuators*. 2009, **151**(2), 141-144. 10.1016/j.sna.2009.02.002.

[J42] KUBÍK, J., JANOŠEK, M. and RIPKA, P. Low-power Fluxgate Signal Processing Using Gated Differential Integrator. *Sensor Letters*. 2007, **5**(1), 149-152. 10.1166/sl.2007.046.

[J43] KUBÍK, J., JANOŠEK, M. and RIPKA, P. Magnetometer with Pulse-Excited Miniature Fluxgate Sensor. *Journal of Electrical Engineering*. 2006, **57**(8/S), 80-83. ISSN 1335-3 632.

II. Proceedings articles (indexed conferences) - B12

[P1] BUTTA, M., et al. Orthogonal fluxgate sensor noise depends on annealing-induced magnetostriction of the core. *IEEE SENSORS 2021 proceeding*. IEEE SENSORS 2021, Sydney, 2021-10-31/2021-11-04. Irvine, CA: IEEE Sensors, 2021. ISSN 1930-0395. ISBN 978-1-7281-9501-8. 10.1109/SENSORS47087.2021.9639470.

[P2] ▶JANOŠEK, M., et al. Low frequency noise investigation of pT-level magnetic sensors by cross-spectral method. *IEEE SENSORS 2021 proceeding*. IEEE SENSORS 2021, Sydney, 2021-10-31/2021-11-04. Irvine, CA: IEEE Sensors, 2021. ISSN 1930-0395. ISBN 978-1-7281-9501-8. 10.1109/SENSORS47087.2021.9639875.

[P3] ▶JANOŠEK, M., DRESSLER, M. and SAUNDERSON, E. Stabilized magnetic vacuum using a rotating fluxgate sensor. *2020 IEEE SENSORS Proceedings*. IEEE Sensors 2020, Rotterdam, 2020-10-25/2020-10-28. Orlando, Florida: IEEE Sensors Council, 2020. ISSN 2168-9229. ISBN 978-1-7281-6801-2. 10.1109/SENSORS47125.2020.9278793.

[P4] BUTTA, M., et al. Effect of amorphous wire core diameter on the noise of an orthogonal fluxgate. *Proceedings IEEE International Magnetics Conference (INTERMAG)*. INTERMAG 2018, Singapore, 2018-04-23/2018-04-27. New Jersey: IEEE, 2018. ISBN 978-1-5386-6425-4. 10.1109/INTMAG.2018.8508815.

[P5] JANOŠEK, M., et al. 1 pT-noise fluxgate magnetometer design and its performance in geomagnetic measurements. *2019 IEEE International Instrumentation and Measurement Technology Conference - proceedings*. 2019 IEEE International Instrumentation and Measurement Technology Conference, Auckland, 2019-05-20/2019-05-23. New York: IEEE, 2019. ISSN 2642-2077. ISBN 978-1-5386-3460-8. 10.1109/I2MTC.2019.8826956.

[P6] BUTTA, M. and JANOŠEK, M. Orthogonal fluxgate gradiometer with multiple coil pairs. *2017 IEEE International Magnetics Conference (INTERMAG)*. IEEE International Magnetics Conference, Dublin, 2017-04-24/2017-11-28. San Francisco: American Institute of Physics and Magnetic Society of the IEEE, 2017. ISSN 2150-4601. ISBN 978-1-5386-1086-2. 10.1109/INTMAG.2017.8007976.

[P7] BUTTA, M. and JANOŠEK, M. Magnetic gradiometer with self compensation of offset drift. *2016 IEEE SENSORS Proceedings*. IEEE SENSORS 2016, Orlando, 2016-10-

30/2016-11-02. Orlando, Florida: IEEE Sensors Council, 2017. ISSN 2168-9229. ISBN 978-1-4799-8287-5. 10.1109/ICSENS.2016.7808502.

[P8] JANOŠEK, M., PLATIL, A. and VYHNÁNEK, J. Simple estimation of dipole source z-distance with compact magnetic gradiometer. *Proceedings of 5th International Conference on Materials and Applications for Sensors and Transducers (IC-MAST2015)*. 5th International Conference on Materials and Applications for Sensors and Transducers, Mykonos, 2015-09-27/2015-09-30. Bristol: IOP Institute of Physics, 2016. IOP Conference Series: Materials Science and Engineering. ISSN 1757-899X. 10.1088/1757-899X/108/1/012025.

[P9] ►JANOŠEK, M., PETRUCHA, V. And VLK, M. Low-noise magnetic observatory variometer with race-track sensors. *Proceedings of 5th International Conference on Materials and Applications for Sensors and Transducers (IC-MAST2015)*. 5th International Conference on Materials and Applications for Sensors and Transducers, Mykonos, 2015-09-27/2015-09-30. Bristol: IOP Institute of Physics, 2016. IOP Conference Series: Materials Science and Engineering. ISSN 1757-899X. 10.1088/1757-899X/108/1/012026.

[P10] JANOŠEK, M., VYHNÁNEK, J. and PLATIL, A. Compact magnetic gradiometer and its astatization. *Procedia Engineering Special Issue Eurosensors 2015*. Eurosensors 2015, Freiburg, 2015-09-06/2015-09-09. Oxford: Elsevier Ltd, 2015. p. 1249-1252. ISSN 1877-7058. 10.1016/j.proeng.2015.08.841.

[P11] BUTTA, M., JANOŠEK, M. and RIPKA, P. Electroplated Multi-ring Core Planar Fluxgate. *28TH EUROPEAN CONFERENCE ON SOLID-STATE TRANSDUCERS (EUROSENSORS 2014)*. Eurosensors 2014, Brescia, 2014-09-07/2014-09-10. Amsterodam: Elsevier, 2014. p. 1176-1179. ISSN 1877-7058. 10.1016/j.proeng.2014.11.376.

[P12] ZIKMUND, A. and JANOŠEK, M. Calibration procedure for triaxial magnetometers without a compensating system or moving parts. *Proceedings of Instrumentation and Measurement Technology Conference (I2MTC) 2014*. 2014 IEEEE International Instrumentation and Measurement Technology Conference, Montevideo, 2014-05-12/2014-05-15. Vail, Colorado: IEEE Instrumentation and Measurement Society, 2014. p. 473-476. ISSN 1091-5281. ISBN 978-1-4673-6385-3. 10.1109/I2MTC.2014.6860790.

[P13] PETRUCHA, V., JANOŠEK, M. and AZPURUA, M.A. Fluxgate magnetometer vector feedback homogeneity and its influence on sensor parameters. *Proceedings of*

Instrumentation and Measurement Technology Conference (I2MTC) 2014. IEEE International Instrumentation and Measurement Technology Conference, Montevideo, 2014-05-12/2014-05-15. IEEE Instrumentation and Measurement Society, 2014. p. 460-463. ISSN 1091-5281. ISBN 978-1-4673-6385-3. 10.1109/I2MTC.2014.6860787.

[P14] JANOŠEK, M., et al. Dual-core fluxgate gradiometer with gradient feedback. In: IEEE Sensors 2013 - Proceedings. IEEE Sensors 2013, Baltimore, 2013-11-03/2013-11-06. Piscataway: IEEE, 2013. p. 1-3. ISSN 1930-0395. ISBN 978-1-4673-4640-5. 10.1109/ICSENS.2013.6688287.

[P15] RIPKA, P., et al. AMR Proximity Sensor with Inherent Demodulation. In: *2013 IEEE Sensors Proceedings*. IEEE Sensors 2013, Baltimore, 2013-11-03/2013-11-06. Piscataway: IEEE, 2013. p. 655-658. IEEE Sensors. ISSN 1930-0395. ISBN 978-1-4673-4640-5. 10.1109/ICSENS.2013.6688289.

[P16] VYHNÁNEK, J., JANOŠEK, M. and RIPKA, P. Low frequency noise of anisotropic magnetoresistors in DC and AC-excited metal detectors. In: *Sensors & Their Applications XVII*. Sensors & their Applications XVII, Dubrovník, 2013-09-16/2013-09-18. Bristol: IOP Publishing Ltd, 2013. p. 1-5. Journal of Physics Conference Series. ISSN 1742-6588. 10.1088/1742-6596/450/1/012031.

[P17] TOMEK, J., et al. Magnetopneumography - Real-World Phantom Inversion. In: *OIPE 2012 - 12th International Workshop on Optimization and Inverse Problems in Electromagnetism*. Ghent, 2012-09-19/2012-09-21. Gent: University of Gent, 2012. p. 248-249. ISBN 978-94-6197-069-5.

[P18] JANOŠEK, M., VYHNÁNEK, P. and RIPKA, P. CW Metal Detector Based on AMR Sensor Array. In: *IEEE Sensors 2011 - Proceedings*. IEEE SENSORS 2011 Conference,Limerick, 2011-10-28/2011-10-31. Limerick:IEEE Sensors Council, 2011. p.1515-1517. ISSN 1930-0395. ISBN 978-1-4244-9288-6.10.1109/ICSENS.2011.6127370.

[P19] BUTTA, M., JANOŠEK, M. and RIPKA, P. Coil-less Fluxgate Operated in Feedback Mode by means of DC Current. In: *IEEE Sensors 2010 - Proceedings*. The 9th Annual IEEE Conference on Sensors, IEEE Sensors 2010 Conference, Waikoloa, Hawaii, 2010-11-01/2010-11-04. Stoughton, Wisconsin: IEEE Sensors Council, 2010. p. 639-642. ISSN 1930-0395. ISBN 978-1-4244-8168-2. 10.1109/ICSENS.2010.5690109.

[P20] JANOŠEK, M. and ĎAĎO, S. Single-lockin Detection of AC Magnetic Fields by Fluxgate Sensor. In: *Proceedings of the 12th Biennial Baltic Electronics Conference*. BEC2010 - 12th Biennial Baltic Electronic Conference, Tallin, 2010-10-04/2010-10-06. Tallin: Tallin University of Technology, 2010. p. 223-226. ISSN 1736-3705. ISBN 978-1-4244-7357-1. 10.1109/BEC.2010.5631591

[P21] RIPKA, P., JANOŠEK, M. and NOVÁČEK, P. Depth Estimation of Metal Objects. In: *EUROSENSORS XXIV - Proceedings*. Eurosensors XXIV, Linz, 2010-09-05/2010-09-08. Linz: Elsevier BV, 2010. p. 280-283. ISSN 1877-7058. 10.1016/j.proeng.2010.09.102.

[P22] RIPKA, P., et al. Crossfield Effect in Magnetic Sensors. In: *IEEE SENSORS 2009 - The Eighth IEEE Conference on Sensors*. IEEE SENSORS 2009 Conference, Christchurch, 2009-10-25/2009-10-28. Christchurch: IEEE Sensors Council, 2009. p. 1860-1863. ISSN 1930-0395. ISBN 978-1-4244-4548-6. 10.1109/ICSENS.2009.5398405

[P23] JANOŠEK, M. Detection of Magnetic Markers Using Array of PCB Fluxgate Sensors. In: *Workshop 09 CTU REPORTS*. Workshop 2009, Praha, 2009-02-16/2009-02-20. Praha: Czech Technical University in Prague, 2009. ISBN 978-80-01-04286-1.

[P24] JANOŠEK, M. and PRIBULA, O. Optically Referenced 2D Magnetic Field Mapping. In: *EUROSENSORS XXII 2008*. EUROSENSORS 2008, Dresden, 2008-09-07/2008-09-10. Dresden: Eurosensors, 2008. p. 247-249. ISBN 978-3-00-025217-4.

[P25] PLATIL, A., et al. Short-range Navigation of Minesweeping Detector. In: *EUROSENSORS XXII 2008*. EUROSENSORS 2008, Dresden, 2008-09-07/2008-09-10. Dresden: Eurosensors, 2008. p. 508-511. ISBN 978-3-00-025217-4

III. Book chapters -B05

[B1] ►JANOŠEK, M. Parallel Fluxgate Magnetometers. In: GROSZ, A, M.J HAJI-SHEIKH, and S. MUKHOPADHYAY, eds. *High Sensitivity Magnetometers*. Basel: Springer, 2016. p. 41-61. Smart Sensors, Measurement and Instrumentation. vol. 19. ISSN 2194-8402. ISBN 978-3-319-34070-8. 10.1007/978-3-319-34070-8_2.

IV. Patents – BX17, BX18

[X1] ČVUT v Praze. *ORTHOGONAL FLUXGATE SENSOR*. Inventors: M. JANOŠEK and M. BUTTA. European Patent Office. Patent EP3460499. 2020-06-24.

[X2] ČVUT v Praze. *Vehicle presence detector*. Inventors: M. JANOŠEK and A. PLATIL. European Patent Office. Patent EP3315919. 2019-10-09.

[X3] České vysoké učení technické v Praze. *Ortogonální feromagnetická sonda*. Inventors: M. JANOŠEK and M. BUTTA. Czech Republic. Patent CZ 307319. 2018-04-18.

[X4] České vysoké učení technické v Praze - fakulta elektrotechnická. *Detektor přítomnosti vozidla*. Inventors: M. JANOŠEK and A. PLATIL. Czech Republic. Patent CZ 307060. 2017-11-08.

[X5] ČVUT FEL. *Fluxgate sensor circuit for measuring the gradient of a magnetic field*. Inventors: M. JANOŠEK and P. RIPKA. European Patent Office. Patent EP2388608. 2013-08-09.

[X6] České vysoké učení technické v Praze - fakulta elektrotechnická, Praha 6, CZ. *Zapojení feromagnetické sondy pro měření gradientu magnetického pole*. Inventors: M. JANOŠEK and P. RIPKA. Czech Republic. Patent CZ 302564. 2011-06-02.

V. Utility models – BX19

[U1] URC Systems, spol. s r.o., Česká republika; České vysoké učení technické v Praze, Česká republika. Detektor nesených feromagnetických částí. Inventors: J. ČECHÁK, et al. Czech Republic. Utility Model CZ 33608. 2020-01-21.

[U2] České vysoké učení technické v Praze, Fakulta elektrotechnická, CZ. *Feromagnetická sonda*. Inventors: M. JANOŠEK and V. PETRUCHA. Czech Republic. Utility Model CZ 27638. 2014-12-18.

[U3] ČVUT FEL. *Gradiometr se dvěma feromagnetickými sondami*. Inventors: M. JANOŠEK. Czech Republic. Utility Model CZ 23385. 2012-02-06.

[U4] ČVUT FEL. *Zapojení feromagnetické sondy pro měření gradientu magnetického pole*. Inventors: M. JANOŠEK and P. RIPKA. Czech Republic. Utility Model CZ 21161. 2010-08-16.